Understanding and Design of Long-Term Stable Liquid-Infused Surfaces

Dissertation

zur Erlangung des Grades

“Doktor der Naturwissenschaften”

im Promotionsfach Chemie

am Fachbereich Chemie, Pharmazie, und Geowissenschaften der Johannes Gutenberg-Universität Mainz.

Philipp Baumli,
Geb. in Frauenfeld (TG), Schweiz

Mainz, März 2020

This dissertation was undertaken at the Max Planck Institute for Polymer Research from November 2016 until spring 2020 under the supervision of [redacted] To the best of my knowledge and conscience, I assure the reader that original research is presented, and no plagiarism has been committed. Sources are acknowledged to the best of my knowledge. Material originating from other publications has been reproduced with the corresponding permissions.

Mainz, March 2020

Diese Dissertation wurde von November 2016 bis zum Frühjahr 2020 am Max-Planck-Institut für Polymerforschung unter der Leitung von [redacted] Nach bestem Wissen und Gewissen versichere ich, dass die Forschung im Original vorliegt und kein Plagiatismus begangen wurde. Die Quellen wurden nach bestem Wissen und Gewissen anerkannt und zitiert. Bildmaterial und Resultate die aus anderen Publikationen stammen, wurde mit den entsprechenden Genehmigungen reproduziert.

Mainz, März 2020

1. Berichterstatter: [redacted]

2. Berichterstatter: [redacted]

Tag der mündlichen Prüfung: 03. Juni 2020

Dissertation an der Johannes Gutenberg-Universität Mainz

„To pick the stars, you have to see the sky.“

Korean Proverb

Table of Contents

1 Abstract

Liquid-infused surfaces are two-component surface coatings consisting of a scaffold and a tethered liquid stabilized within and by the scaffold. The most prominent example of liquid-infused surfaces is a porous or textured solid infused with a chemically compatible oil-based lubricant. The scaffold is not limited to solid textured surfaces, though. Polymeric networks can also serve as a scaffold. Upon infusion with a compatible liquid, liquid-infused polymer films, organogels, or hydrogels are obtained.

In general, liquid-infused surfaces are prepared in two steps: the fabrication of the scaffold followed by subsequent infusion with liquid. Liquid-like surfaces are a sub-class of liquid-infused polymer films. They consist of flexible polymer chains covalently attached to a substrate.

Liquid-infused surfaces are candidates for liquid-repellent surfaces used as self-cleaning surfaces, anti-(bio)fouling coatings, and anti-icing coatings. In the first part of the thesis, transparent liquid-like surfaces are prepared. Methyl-terminated polydimethylsiloxane (PDMS) spontaneously binds to substrate surfaces displaying silicon oxide surface chemistry. The surfaces show excellent liquid-repellency towards non-polar and polar liquids as well as minimal ice adhesion strengths.

The documented properties and the proposed applications of liquid-infused surfaces are based on allowing easy removal of contaminants in contact with the surface. The most common contaminant encountered is drops of water, which is the reason why most liquid-infused surfaces employ oil as their lubricant since it is immiscible with water. However, the interactions of a drop with a liquid-infused surface and, in particular, the friction of drops on liquid-infused surfaces are not fully understood yet. The mobility of a drop on a liquid-infused surface, in particular, the friction encountered by the drop, is determined by a feature that is specific for liquid-infused surfaces: the annular meniscus formed around the deposited drop. The dimensions of the meniscus for a scaffold-liquid combination establishing a liquid-infused surface depend on the degree of liquid-infusion and the thickness of the infused liquid film. On liquid-like surfaces, the size of the meniscus is in the nanometer range. On liquid-infused porous substrates, the size of the meniscus is in the micrometer range. The meniscus can be separated into advancing and receding parts. The receding parts of the meniscus are modeled within the framework of the Landau-Levich formalism. In this thesis, the dynamic nature of the advancing parts of the meniscus is confirmed and characterized by utilizing laser scanning confocal microscopy. Furthermore, a universal scaling behavior of the friction force of drops moving on liquid-infused surfaces is evidenced. It is found that the friction force does universally scale with the power of 2/3 of the speed of drops moving on liquid-infused surfaces. This result can be generalized to the cases of drops contained in Hele-Shaw cells and bubbles rising on a liquid-infused surface submerged in a water bath.

A critical drawback of liquid-infused surfaces potentially limiting their applicability as coatings are flow-induced shear forces leading to the depletion of lubricant. Previous works investigated lubricant-depletion on grooved surfaces. In the presence of a lubricant-reservoir, a so-called steady-state length of the liquid-infused surface remains lubricated despite persistent shear-flows. Furthermore, it has been found that rough textures can hold more lubricant than smooth textures. The third part of the thesis deals with lubricant-depletion on liquid-infused surfaces on which the conventional roles of water and oil are reversed. The lubricant is now water. Water-lubricated liquid infused surfaces offer the possibility to prepare biocompatible liquid-infused surfaces since most natural systems are based on water. The water is stabilized within the texture by a hydrogel-coating attached to the rough solid

substrate. This approach combines gels and a rough texture. The swollen hydrogel is subjected to a shear flow of oil. The loss of water is monitored with the help of laser scanning confocal microscopy for different flow conditions and lubricant viscosities for two different kinds of hydrogel-coatings. The lubricant-depletion progresses linearly and independent of the nature of the hydrogel and the flow conditions. The depletion kinetics is quantitatively described with the help of an extended diffusion model. The underlying mechanism is the diffusion of water into the oil-phase. Performing the same depletion experiments with water-saturated oil does not lead to progressive depletion.

The depleted lubricant has to be replenished to maintain the functionality of the liquid-infused surface coating. As of this writing, lubricant-replenishment strategies are limited to *ex-situ* methods, such as lubricant baths and spraying, or rely on built-in lubricant-reservoirs. In the fourth part of the thesis, a novel strategy to overcome the shear-induced lubricant depletion is presented. The lubricant is replenished from the flow of oil-in-water emulsions across the texture. Laser scanning confocal microscopy reveals the attachment and coalescence of oil drops from the emulsion at the features of the substrate above a threshold velocity, leading to the gradual filling of the structure with the lubricant. The liquid-infused surfaces created under flow in that way are stable since the flow-induced lubricant-replenishment prevails over the shear-induced depletion. This strategy of flow-induced lubrication of textures can be generalized to a broad range of lubricant-solid combinations using minimal amounts of oil.

Flüssigkeitsinfiltrierte Oberflächen sind zweikomponentige Oberflächenbeschichtungen, die aus einem Gerüst und einer eingebundenen Flüssigkeit, dem Schmiermittel, bestehen, die im und durch das Gerüst stabilisiert wird. Das prominenteste Beispiel für flüssigkeitsinfiltrierte Oberflächen ist eine poröse oder strukturierte Feststoffoberfläche, die mit einem chemisch verträglichen Schmiermittel auf Ölbasis infiltriert ist. Das Gerüst ist jedoch nicht auf feste, strukturierte Oberflächen beschränkt. Auch Netzwerke aus Polymeren können als Gerüst dienen. Nach Infusion mit einer kompatiblen Flüssigkeit erhält man flüssigkeitsinfiltrierte Polymerfilme, Organogele oder Hydrogele.

Im Allgemeinen werden flüssigkeitsinfiltrierte Oberflächen in zwei Schritten hergestellt: die Herstellung des Gerüsts und die anschließende Infusion mit Flüssigkeit. Flüssigkeitsähnliche Oberflächen sind eine Unterklasse von flüssigkeitsinfiltrierten Polymerfilmen. Sie bestehen aus flexiblen Polymerketten, die kovalent an ein Substrat gebunden sind.

Flüssigkeitsinfiltrierte Oberflächen sind Kandidaten für flüssigkeitsabweisende Oberflächen, die als selbstreinigende Oberflächen, Anti-(Bio)Fouling-Beschichtungen und Anti-Eis-Beschichtungen verwendet werden. Im ersten Teil der Arbeit wird die Herstellung von transparenten flüssigkeitsähnlichen Oberflächen vorgestellt. Methyl-terminiertes Polydimethylsiloxan (PDMS) bindet spontan an Substratoberflächen, die eine Siliziumoxid-Oberflächenchemie aufweisen. Die Oberflächen zeigen eine ausgezeichnete Flüssigkeitsabweisung gegenüber unpolaren und polaren Flüssigkeiten sowie minimale Haftungsstärken von Eis.

Die dokumentierten Eigenschaften und die vorgeschlagenen Anwendungen von flüssigkeitsinfiltrierten Oberflächen basieren auf der einfachen Entfernung von Verunreinigungen, die mit der flüssigkeitsinfiltrierten Oberfläche in Kontakt kommen. Die am häufigsten angetroffene Verunreinigung sind Wassertropfen. Deshalb verwenden die meisten flüssigkeitsinfiltrierten Oberflächen Öl als Schmiermittel, da es mit Wasser nicht mischbar ist. Die Wechselwirkungen eines Tropfens mit einer flüssigkeitsinfiltrierten Oberfläche und insbesondere die Reibung von Tropfen auf flüssigkeitsinfiltrierten Oberflächen sind jedoch noch nicht vollständig verstanden. Die Beweglichkeit eines Tropfens und die Reibung eines Tropfens auf einer flüssigkeitsinfiltrierten Oberfläche werden durch ein für flüssigkeitsinfiltrierte Oberflächen spezifisches Merkmal bestimmt: den ringförmigen Meniskus, der sich um den aufgetragenen Tropfen bildet. Die Größe und Abemessungen des Meniskus für eine gegebene Gerüst-Flüssigkeits-Kombination, die eine flüssigkeitsinfiltrierte Oberfläche bildet, hängen vom Grad der Flüssigkeitsinfiltration und der Dicke des infiltrierten Flüssigkeitsfilms ab. Bei flüssigkeitsähnlichen Oberflächen liegt die Größe des Meniskus im Nanometerbereich. Auf flüssigkeitsinfiltrierten porösen Substraten liegt die Größe des Meniskus im Mikrometerbereich. Der Meniskus kann in einen vor- und einen zurückweichenden Teil getrennt werden. Die zurückweichenden Teile des Meniskus werden im Rahmen des Landau-Levich-Formalismus modelliert. Im zweiten Teil dieser Arbeit wird der dynamische Charakter der vorrückenden Teile des Meniskus bestätigt und durch den Einsatz der konfokalen Laserscanmikroskopie charakterisiert. Darüber hinaus wird ein universelles Skalierungsverhalten der Reibungskraft von Tropfen, die sich auf flüssigkeitsinduzierten Oberflächen bewegen, nachgewiesen. Es wird festgestellt, dass die Reibungskraft universell mit der Potenz von 2/3 der Geschwindigkeit von Tropfen, die sich auf flüssigkeitsgefüllten Oberflächen bewegen, skaliert. Dieses Ergebnis kann auf die Fälle von Tropfen in Hele-Shaw-Zellen und Blasen, die auf einer mit Flüssigkeit durchtränkten Oberfläche in einem Wasserbad aufsteigen, verallgemeinert werden.

Ein Nachteil flüssigkeitsgefüllter Oberflächen, der möglicherweise ihre Anwendbarkeit einschränkt, sind Fluss-induzierte Scherkräfte, die zu einer Verarmung der als Schmiermittel dienenden Flüssigkeit führen. In früheren Arbeiten wurde die Schmiermittelverarmung auf gerillten Oberflächen untersucht.

In Gegenwart eines Schmiermittelreservoirs bleibt eine so genannte stationäre Länge der flüssigkeitsgefüllten Oberfläche trotz anhaltender Scherströmungen geschmiert und infiltriert mit Flüssigkeit. Darüber hinaus wurde festgestellt, dass raue Oberflächen mehr Schmiermittel aufnehmen können als glatte Oberflächen. Auf der Grundlage dieser Erkenntnisse wurden Strategien zur Verzögerung der Schmiermittelverarmung entwickelt. Der dritte Teil der Arbeit befasst sich mit der Schmiermittelverarmung auf flüssigkeitsgefüllten Oberflächen, auf denen die konventionellen Rollen von Wasser und Öl vertauscht sind. Das Schmiermittel ist nun Wasser. Mit Wasser geschmierte, flüssigkeitsinfiltrierte Oberflächen bieten die Möglichkeit, biokompatible, flüssigkeitsinfiltrierte Oberflächen herzustellen, da die meisten natürlichen Systeme auf Wasser basieren. Das Wasser wird innerhalb der Textur durch eine Hydrogel-Beschichtung stabilisiert, die auf dem rauen festen Substrat angebracht und chemisch gebunden ist. Dieser Ansatz kombiniert Gele und eine raue feste Textur. Das gequollene Hydrogel wird einem Scherstrom von Öl ausgesetzt. Der Wasserverlust wird mit Hilfe der konfokalen Laserrastermikroskopie für verschiedene Fließbedingungen und Viskosität des Schmiermittels für zwei verschiedene Arten von Hydrogel-Beschichtungen untersucht. Der Schmiermittelverlust verläuft linear und unabhängig von der Art des Hydrogels und den Strömungsbedingungen. Der Verlauf der Schmiermittelverarmung wird mit Hilfe eines erweiterten Diffusionsmodells quantitativ beschrieben. Der zugrunde liegende Mechanismus ist die Diffusion von Wasser in die Ölphase. Die Durchführung der gleichen Experimente zur Schmiermittelverarmung mit wassergesättigtem Öl führt nicht zu einer progressiven Schmierstoffverarmung.

Das Schmiermittel das der flüssigkeitsinfiltrierten Oberfläche verloren ging muss wieder aufgefüllt werden, um die Funktionalität der flüssigkeitsgefüllten Oberflächenbeschichtung aufrechtzuerhalten. Zum Zeitpunkt der Abfassung dieser Arbeit beschränken sich die Strategien zum Nachfüllen des Schmiermittels auf *Ex-Situ*-Methoden wie Schmiermittelbäder und Besprühen mit Schmiermittel oder auf in die Oberflächenbeschichtung eingebaute Schmiermittelreservoirs. Im vierten Teil der Arbeit wird eine neue Strategie zur Überwindung der scherbedingten Schmiermittelverarmung vorgestellt. Das Schmiermittel wird durch den Fluss von Öl-in-Wasser-Emulsionen über die Textur wieder aufgefüllt. Konfokale Laserrastermikroskopie zeigt die Anhaftung und Koaleszenz von Öltröpfchen aus der Emulsion an den Merkmalen des Substrats oberhalb einer Schwellengeschwindigkeit, was zu einer allmählichen Füllung der Struktur mit dem Schmiermittel führt. Die auf diese Weise unter der Strömung entstandenen flüssigkeitsinfiltrierten Oberflächen sind stabil, da die strömungsinduzierte Schmiermittelauffüllung gegenüber der scher-induzierten Schmiermittelverarmung überwiegt. Diese Strategie der Fluß-induzierten Schmierung von Texturen lässt sich auf ein breites Spektrum von Schmiermittel-Feststoff-Kombinationen mit minimalen Ölmengen verallgemeinern.

2 Introduction

This chapter gives an introduction to liquid-infused surfaces. The terminology, concepts, and previously published research results, which are relevant to the subsequent chapters, are introduced. After a brief overview (section 2.1), fabrication strategies (section 2.2) of liquid-infused surfaces are presented. Applications of liquid-infused surfaces (section 2.3) are briefly discussed thereafter. Next, liquid-infused surfaces established on a solid texture are described in terms of a physical model (section 2.4). Next, the state of the art of published research work addressing the mobility of drops on liquid-infused surfaces is discussed. The scenarios of drops at rest (section 2.5) and drops moving (section 2.6) on liquid-infused surfaces are treated separately. Subsequently, the topics of lubricant-depletion (section 2.7) and lubricant-replenishment (section 2.8) are addressed. The chapter closes with a summary of the thesis in which the contributions of the author are explained (section 2.9) and concludes with a brief outlook.

2.1 Overview

Liquid-Infused Surfaces (LIS), or Lubricant-impregnated slippery surfaces (LubISS), also called Slippery Liquid-Infused Porous Surfaces (SLIPS) had attracted a lot of attention since their first appearance in the research literature[1,2]. A liquid-infused surface is a combination of two components: a liquid tethered to a scaffold stabilizing the liquid[3]. Liquid-infused surfaces are of a dual nature: the scaffold in combination with the infiltrated liquid.

The most common and "classic" case of a liquid-infused surface encountered in literature is the combination of a solid rough and/or textured substrate (black in Figure 2.1.1) with micro- and nanoscale topography infiltrated by an oil-based lubricant (yellow in Figure 2.1.1). The restriction to solid scaffolds (solid textures) and oil-based tethered liquids would define liquid-infused surfaces too narrowly, though (section 2.2). Very often, liquid-infused surfaces are used as surface coatings aiming at liquid-repellency or low physical and chemical interaction of contaminants with the coating (section 2.3)[3]. The most common liquids to be repelled are water-based (*e.g.* raindrops). Hence, solid scaffolds and liquids immiscible with water are the preferred and the most prominent combination for a liquid-infused surface. The conditions under which a stable liquid-infused surface can be established have to be carefully elucidated (section 2.4).

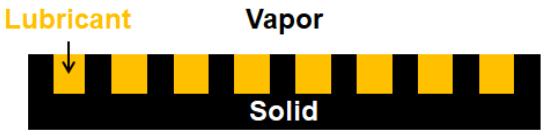

Figure 2.1.1: Schematic of a Liquid-Infused Surface.

A drop deposited onto such a liquid-infused surface (Figure 2.1.2) is a complex 4-phase system involving the (textured solid) scaffold, the impregnating lubricant, the liquid drop, and the surrounding vapor. Visual inspection (green circles in Figure 2.1.2) reveals an essential and typical feature encountered on liquid-infused surfaces accommodating immiscible liquid drops: the so-called wetting ridge or meniscus. It is an annular ridge of oil situated around the drop.

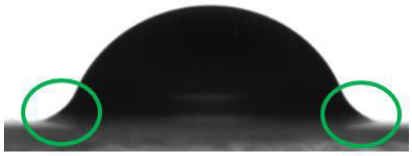

Figure 2.1.2: A drop placed onto a liquid-infused surface. The green circles highlight the annular ridge, *i.e.* the wetting ridge, of oil surrounding the drop. Courtesy of Dr. William Wong (Max Planck Institute for Polymer Research, Mainz, Germany).

Many factors, most notably the wetting ridge, affect the mobility of drops placed on liquid-infused surfaces (section 2.5 and 2.6). The high mobility and low (lateral) adhesion of drops (and other contaminants) on liquid-infused surfaces is the basis of their promising applications (section 2.3). The lack of lubricant, the depletion of lubricant, or an excess of lubricant can be situations arising due to different reasons (section 2.7). The amount of lubricant present within the texture influences the dynamics of drops placed on liquid-infused surfaces, and the integrity of the surface. There are (albeit few) strategies pursued to replenish depleted lubricant (section 2.8).

Liquid-infused surfaces have existed long before their treatise in research endeavors conducted by humankind. Liquid-infused surfaces are also found in nature. A prominent example of such a non-adhesive surface found in nature is the carnivorous pitcher plants (Figure 2.1.3) belonging to the genus of *Nepenthes*[4-6]. The (upper) pitcher of the *Nepenthes* pitcher plants is bounded by the so-called peristome, which consists of a rough and anisotropic structure. The micro-rough structure of the peristome displays a very strong affinity to water. The peristome contains nectaries and glands to secrete nectar. In combination with rain and the humid environment (abundant in the tropical habitat of the plant species), the nectar and water constitute the fluid infusing the texture of the peristome. In this wetted state, insect prey suffers the same fate as drops placed on liquid-infused surfaces (section 2.6). They can no longer get any grip on the peristome (aquaplaning), and they fall into the pitcher and are subsequently digested by the plant.

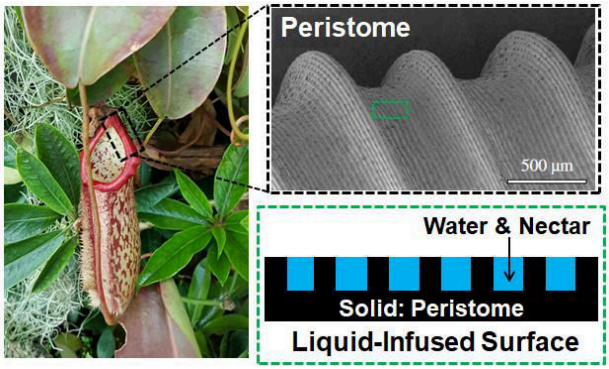

Figure 2.1.3: *Nepenthes* pitcher plant (left, picture taken by the author at the Singapore Botanic Garden, Singapore, May 2017). The upper rim of the pitcher, the peristome – a liquid-infused surface (top right: Scanning electron micrograph, adapted and reproduced with permission from Bauer, Bohn, and Federle[5] Copyright © 2008 The Royal Society of Chemistry, schematic: bottom right) - is a rough anisotropic structure, which is a lethal trap for insect prey under wet conditions.

2.2 Fabrication of Liquid-Infused Surfaces

Liquid-infused surfaces are functional surface coatings. Liquid-infused surfaces can be created, starting from an extremely broad spectrum of scaffolds and liquids. The role of the scaffold material is to stabilize the tethered fluid[7]. In most cases, the scaffold is a solid texture made of metals, ceramics, or polymers[8]. The cases of *liquid-like* surfaces and *infused gels* will be introduced at the end of the section. The focus of this section lies on liquid-infused surfaces based on solid scaffolds infused with oil-based lubricants. This is the most prominent scaffold-liquid combination constituting a liquid-infused surface encountered in literature.

The general workflow concerning the fabrication of liquid-infused surfaces is to start with the preparation of the solid textured substrate or template followed by the impregnation with a chemically compatible and suitable lubricant (section 2.4).

There is no generally valid classification of substrates used for the fabrication of liquid-infused surfaces. One can distinguish regular surface textures from irregular ones. As an alternative, one can distinguish between bottom-up and top-down approaches[8]. Yet, another classification approach can be based on how porosity on the substrate is obtained.

Solid substrates which are inherently porous upon fabrication without additional steps include substrates prepared via colloidal approaches based on inverse opal scaffolds (Figure 2.2.1 a)[9,10], porous fiber networks (Figure 2.2.2 b)[2,11-14], porous polymer (including Teflon[15] and polypropylene[16]) substrates[17], porous portland cement[18], mesoporous alumina[19,20], and randomly wrinkled polymeric substrates[21-23].

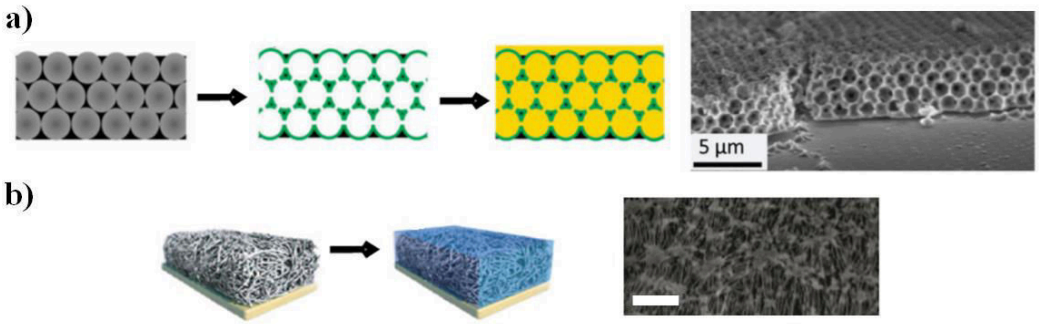

Figure 2.2.1: Preparation of liquid-infused surfaces from inherently porous substrates. a) Left: Colloidal approach based on inverse opal scaffolds. A glass substrate is vertically lifted out of an aqueous dispersion containing polystyrene particles and silica nanoparticles[10]. Subsequently, the polystyrene template is removed by calcination[10]. The inverse opals were then hydrophobized by chemical vapor deposition (CVD) with perfluorooctyl-trichlorosilane (green) and subsequently infiltrated with a lubricant (yellow)[10]. Adapted with permission from Schellenberger *et al.*[10] Copyright © 2015 The Royal Society of Chemistry. Right: Scanning electron micrograph of the inverse opal texture prepared via the colloidal approach (Adapted with permission from Schellenberger *et al.*[10] Copyright © 2015 The Royal Society of Chemistry) b) Left: non-ordered random fibrous networks which are subsequently infused with lubricant. Right: Scanning electron micrograph of the Teflon-based porous nanofiber network[2], scale bar: 5 µm. Adapted with permission from Wong *et al.*[2] Copyright © 2011 Springer Nature.

There is a wide variety of flat substrates that can readily be rendered rough to the degree these substrates can stabilize lubricating fluid (Figure 2.2.2). Such substrates can be prepared with the help of wet etching[24-26], by sandblasting of metal (steel) substrates[27], or by laser texturing (silicon)[28].

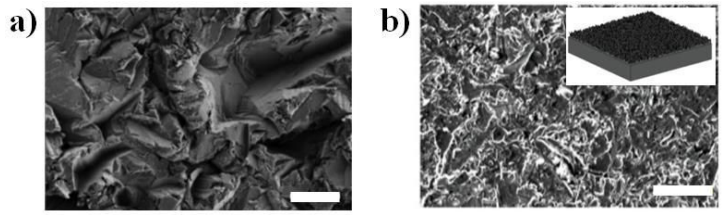

Figure 2.2.2: Preparation of liquid-infused surfaces from flat substrates rendered porous. a) Scanning electron micrograph of sandblasted aluminum (Reproduced with permission from Kim *et al.*[25] Copyright (2013) American Chemical Society). Scale bar: 50 μm b) Scanning electron micrograph of sandblasted steel (Adapted with permission from Subramanyam *et al.*[27] © 2014 WILEY-VCH Verlag GmbH & Co. KGaA, Weinheim). Sketch in the inset, scale bar: 50 μm.

The fabrication of porous substrates can also be achieved via decorating surfaces with discrete micro-rough features, which are regular and uniform. These fabrication approaches are the most labor-intense and time-consuming routes to prepare substrates suitable for liquid-infused surfaces. A very prominent example of such a fabrication route is regular and uniform micropillar arrays prepared by photolithography protocols[10,29,30] coating a substrate. The popularity of this approach lies in the possibility to make apposite comparisons to models and theoretical predictions (section 2.4, 2.5, and 2.6). In this thesis, chapters 4, 5, and 6 make use of regular and uniform micropillar arrays. In addition to photolithography, imprinting strategies (vascularization based on encasing or direct embedding)[31], sol-gel protocols[12,13,32-34], spray-coating[35], or layer-by-layer assembly approaches[36-41] are being followed.

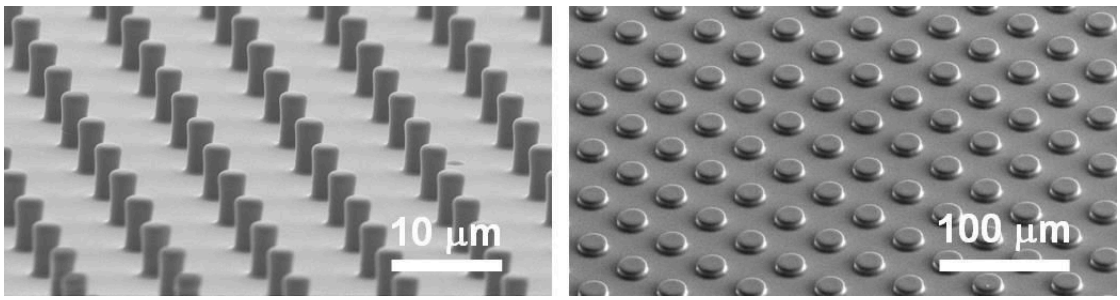

Figure 2.2.3: Fabrication of a liquid-infused surface by decorating the substrate with micropillars prepared by photolithography. There is great flexibility in the choice of micropillar geometries. (left: SEM image taken by Dr. F. Geyer, Max Planck Institute for Polymer Research, right: SEM image taken by A. Sharifi-Aghili, Max Planck Institute for Polymer Research). Regular and uniform micropillar arrays can be hydrophobized and subsequently infused with lubricating oils.

Oil-based lubricants are in widespread use in industry to lubricate solid-solid contacts[42]. Oil-based lubricants are less corrosive to metal components, less volatile, and typically show higher temperature stability compared to water-based lubricants[43].

Water-based lubricants are preferred in fields dealing with biological systems such as tissue engineering[44]. Whereas water is prevalent in naturally occurring liquid-infused surfaces (*Nepenthes* pitcher plant, section 2.1), commonly employed lubricants for artificially created liquid-infused surfaces are not aqueous lubricants but are mostly oil-based and include silicone oils (Polydimethylsiloxane, PDMS), perfluoroethyl ether, fluorinated lubricants (*e.g.* Fomblin® PFPE), biocompatible almond oil[41], and perfluorinated lubricants like Krytox®, or Fluorinert™ (*e.g.* FC-40 or FC-70).

The texture´s surface chemistry and the chemical nature of the lubricant must match (section 2.4 & 2.5). Only hydrophobic textures or textures rendered hydrophobic will be preferentially wetted by oil. Rendering a texture hydrophobic can be achieved via coating the texture with low surface energy silanes, *e.g.* octadecyltricholorsilane (OTS)[45] . Resin- and silicone-based microstructures are completely wetted by silicone oil[45].

Infusing the texture with lubricant has to be done in a controllable and reproducible way. The three most common impregnation methods applied are *spontaneous impregnation*, *dip-coating*, and *spin-coating*.

Spontaneous impregnation[46,47] describes the process in which an inclined or vertically held texture is placed into contact with a reservoir of compatible lubricant along one of its rims/ends. The reservoir may be a trace of oil deposited onto the rim of the texture or a lubricant bath. Following the process of hemiwicking (section 2.2), the lubricant will spontaneously infuse the texture.

During the process of dip-coating, the texture is dipped into a bath of lubricant and slowly retracted at a controlled speed[48]. The process works analogously to the classical case of flat substrates[49-52], albeit in the case of liquid-infused surfaces, the substrate/texture is rough.

When lubricating texture by means of spin-coating, an excess quantity of lubricant is deposited onto the rough texture. Spinning (rotation) of the texture and/or flows of pressurized air/nitrogen forces the excess lubricant off the texture due to the presence of external shear forces. Spin-coating is faster and simpler than the former two methods[2,15,24,53-55]. When impregnating a texture with the help of spontaneous impregnation or dip-coating, excess quantities of lubricant and excess lubrication are avoided.

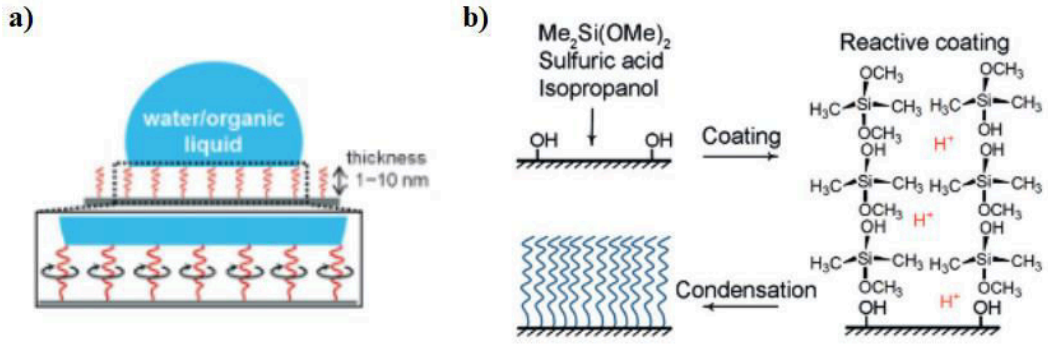

Figure 2.2.4: a) Schematic of liquid-like surfaces, flexible polymer chains grafted to a substrate provide the lubrication properties. Modified with permission from Wooh and Vollmer[56] Copyright © 2016 WILEY-VCH Verlag GmbH & Co. KGaA, Weinheim. b) Preparation of a liquid-like surface by covalent grafting of polydimethylsiloxane (PMDS) via acid-catalyzed polycondensation. Modified with permission from Wang and McCarthy[57] Copyright © 2016 WILEY-VCH Verlag GmbH & Co. KGaA, Weinheim.

Polymer brushes consisting of flexible polymer chains that are chemically (covalently) grafted to a surface can establish a so-called *liquid-like surface*. On liquid-like surfaces, the scaffold and the liquid establishing the liquid-infused surface can be the same component. Alternatively, lubricant different from the grafted polymer molecules is supplied from an external source[53,58]. A prominent example of a liquid-like surface is based on the covalent attachment of polydimethylsiloxane (PDMS) to a substrate[57,59-61]. The flexibility of the siloxane repeating group (-O-Si-O-) provides the high flexibility of the grafted polymer molecules, which allows considering them liquid-like (Figure 2.2.4)[56]. Furthermore, the grafted polymer chains may contain reactive groups providing additional functionality to the liquid-like surface[62].

In contrast to more conventional liquid-infused surface coatings, whose thickness is in the range of tens of nanometers, the thickness of coatings based on liquid-like surfaces is in the range of 1 – 10 nm[56]. Within the framework of this thesis, the possibility of creating liquid-infused surfaces in the form of liquid-like surfaces at room temperature in one step by grafting methyl-terminated polydimethylsiloxane to materials with silicon oxide surface chemistry without the help of solvents and the creating of by-products is explored further and their potential to repel polar and nonpolar liquids as well as ice is assessed (Chapter 3).

Liquid-infused surfaces can also be prepared from infused gels, which consist of a liquid entrapped in a 3D cross-linked polymer network acting as the scaffold stabilizing the liquid[63-67]. They show extraordinary liquid sorption and retention capabilities; the liquid content can reach up to 99%[8]. When the infused liquid is organic, one refers to such swollen gels as *organogels*. If the infused liquid is water, one speaks of *hydrogels*.

This category of liquid-infused surfaces will be dealt with more extensively in section 2.8. Within the framework of this thesis, a hydrogel-coating will be covalently attached to a micropillar array, and the depletion characteristics of the infused water will be investigated under shear flows of oil (Chapter 5). In particular, this part of the thesis combines liquid-infused surfaces relying on a solid substrate with gel-based liquid-infused surfaces.

2.3 Applications of Liquid-Infused Surfaces

The extremely low (lateral) adhesion of fluids (immiscible with the lubricant) and solids on liquid-infused surfaces and consequentially their high mobility (section 2.6) make such surfaces up-and-coming candidates for a wide variety of applications as non-adhesive surfaces in very diverse fields. Furthermore, there are virtually limitless possibilities of solid-lubricant combinations which can be adjusted to the agent whose adhesion shall be prevented.

Liquid-infused surfaces display self-cleaning properties (Figure 2.3.1)[1,2,68,69]. Provided there is no contact line pinning, any contaminant placed on a liquid-infused surface is highly mobile, and can thus be easily removed, *e.g.* by tilting the liquid-infused surface. Other possibilities to remove contaminants from liquid-infused surfaces include acoustic waves[70] or thermal gradients[53,71]. It has to be noted that contact line pinning resulting in negligible contact angle hysteresis can, in general, not completely avoided[10], or requires additional measures to do so (section 2.6).

The ability of liquid-infused surfaces to repel a wide variety of contaminants, including blood and viscous pastes[9], offers a lot of potential in the cosmetics industry and food industry[72].

The perspective of minimizing the loss of cosmetic products due to adhesion of the product to its container and minimizing food waste is fascinating despite the fact that the production of liquid-infused surfaces is difficult to upscale. Appropriate commercial positioning of possible products and solutions has to be left to economists and marketing specialists. Furthermore, the shelf life of cosmetic and food products can be quite long, which requires the stability and integrity of such commercially used liquid-infused surfaces to be quite long.

Figure 2.3.1: Self-cleaning surfaces, a 20 μL water drop deposited carries away silica particles (particle size ranges from 0.2 mm to 0.5 mm) deposited onto a liquid-infused surface lubricated with silicone oil inclined by 20°. Reproduced with permission from Lafuma and Quéré, 2011, *EPL*, 96, 56001. Copyright ® 2011 IOP Publishing, all rights reserved.

Liquid-infused surfaces have repeatedly been identified as candidates for anti-biofouling coatings[58,73-78], also in a marine environment[79-81]. For such applications, including surgical instruments[73] and catheters[75], it is often sufficient to provide a temporary solution against bacterial adhesion and biofilm formation or to delay the aforementioned significantly, so the requirements concerning stability and integrity of the liquid-infused surfaces are often limited to shorter time spans not exceeding a couple of hours to days (Figure 2.3.2).

The (also economical) feasibility of liquid-infused surfaces as internal coatings of tubing[75] may be only limited, due to the presence of infusion gradients and more competitive approaches not requiring any lubricant[82]. However, the potential of surgical instruments (albeit often single-use and disposable only)[73] or endoscopy camera lenses[37] coated by a liquid-infused surface seem very promising, also owed to the increased sophistication and added value of such products. However, it remains to elucidate to which degree the anti-(bio)fouling properties on liquid-infused surfaces is owed to the presence of excess lubricant ("overfilling with lubricant").

Liquid-infused surfaces have also been proposed as anti-icing coatings[83-90]. Anti-icing can mean the reduction of the adhesion strength of ice[84] or the reduction of ice accumulation[83]. The anti-icing performance of liquid-infused surfaces might be owed to the presence of excess lubricant and that frost formation can deplete the infused lubricant (section 2.7)[85].

Other proposed applications of liquid-infused surfaces including corrosion resistance[91-93], drag reduction/fluid mobility[28,45,47,54,94-102] including turbulent flow conditions[103,104], (enhanced) condensation (water recovery)[105-108], fog harvesting[109,110], optics[111-114], selective membranes[115], and active surfaces[35,116] including in the context of electrowetting[117-119].

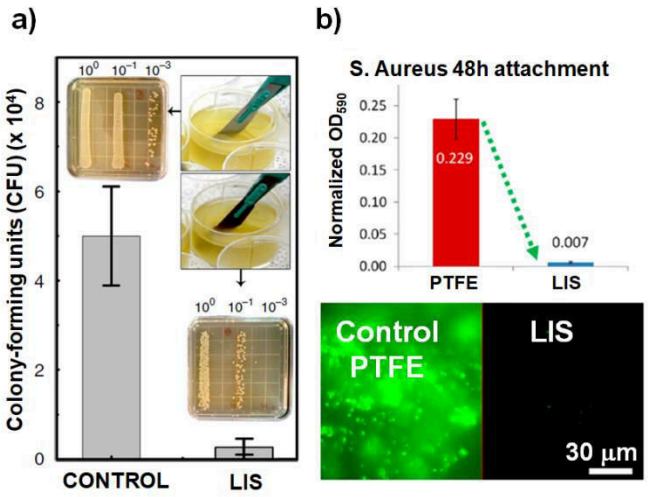

Figure 2.3.2: Applications of liquid-infused surfaces as anti-biofouling coatings. a) Colony-forming unit (CFU) count at different dilution factors for untreated (control) scalpel blades consisting of stainless steel and infused (Krytox® GPL-K103/perfluorodecaline) tungsten oxide-modified (hence textured) stainless steel-based scalpel blades after dipping in a concentrated culture of *E. Coli* (photographs) followed by a brief rinse in deionized water (reprinted with permission from Tesler *et al.*[73], Copyright © 2015, Springer Nature). b) Biofilm attachment reduction by a liquid-infused surface extends to highly pathogenic *S. Aureus*, compared to the PTFE control, the liquid-infused surface (LIS)-coating strongly reduces biofilm attachment, evidenced by CFU counting (top) and fluorescence imaging (bottom)[15]. Adapted with permission from Epstein *et al.*[15] Copyright © 2012, National Academy of Sciences.

Despite the many promising fields of application of liquid-infused surfaces, the critical issue lubricant-depletion persists (section 2.7). The depletion of lubricant is synonymous with the loss of the functionality of the liquid-infused surface. Therefore, to pave the way for the industrial application of liquid-infused surfaces, strategies to replenish the depleted lubricant have to be devised (section 2.8).

2.4 Existence of Liquid-Infused Surfaces

In the following, a solid textured substrate is considered. The case of an infused texture in contact with deposited drops is treated in separate sections (sections 2.5 and 2.6).

The fluid has to be efficiently trapped and stabilized within the solid substrate[120-125]. The chemical compatibility of the lubricant with the substrate and degrees of surface roughness are essential to establish a liquid-infused surface.

For the sake of simplicity, we assume a regular and uniform array of micrometer-sized pillars (micropillars, in the following, called pillars, Figure 2.4.1). The geometrical parameters of importance are the pillar diameter (d), the edge-to-edge distance between pillars (p), and the height of the pillars (h)[126].

The fluid can form a stable fluid film within the solid texture if it is energetically favorable for the fluid to spread into the texture instead of resting on the texture in the form of a discrete drop of fluid[45,120,123,126]. In the following, we develop the terminology and concepts necessary to understand the existence of a stable fluid film within a texture enabling the establishment of a stable liquid-infused surface with the help of Figure 2.4.1.

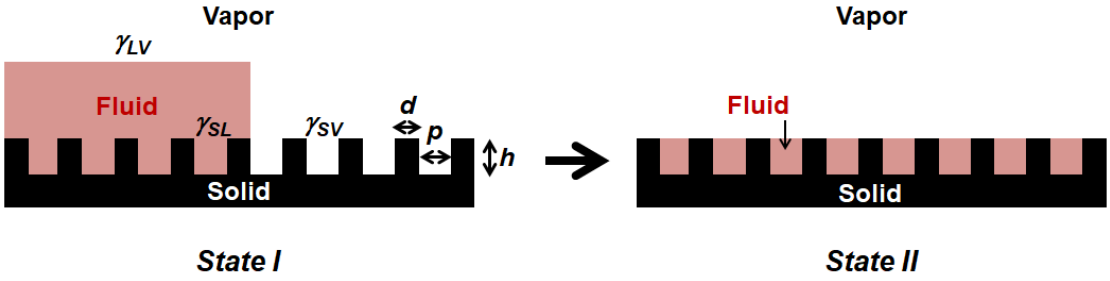

Figure 2.4.1: Stable fluid film within a texture surrounded by vapor ("air"). When the energy associated with *State II* is lower than the energy associated with *State I*, the fluid (red) can be stabilized within the solid texture (black) forming a fluid film. Adapted with permission from Quéré[126] Copyright © 2008 by Annual Reviews. All rights reserved.

The binding environment and the associated potentials are asymmetric for molecules and atoms close to a surface or an interface. Molecules and atoms close to a surface or interface, therefore, have higher energies than atoms or molecules in the bulk of a specific material. This additional surface energy can be quantified in terms of the so-called ***surface tension*** or ***interfacial tension*** γ. This quantity has the dimensions of force per length or energy per area. Intuitively, the surface tension can be understood as the resistance of a fluid interface to deformation. The smaller the surface tension, the easier the fluid interface in question can be deformed. The interfacial tensions to be considered (Figure 2.4.1) are associated with the fluid ("liquid")-vapor interface (γ_{LV}), the solid-vapor interface (γ_{SV}), and the solid-fluid ("liquid") interface (γ_{SL}).

In the following, the change in energy per unit area upon the transition from *State I* to *State II* is expressed in terms of the relevant interfacial tensions and the geometrical parameters characterizing the surface texture.

We define the so-called *roughness factor* (r) and the fraction of the surface decorated with micropillars, the so-called *feature fraction* (ϕ), often also called *pillar density*[126]. The roughness factor is defined as the ratio of the real surface area to the projected surface area[126]. The pillar density defines the ratio of the areas of the pillars´ tops to the projected surface area[126]. By definition, the roughness factor is greater or equal to unity ($r \geq 1$), and the feature fraction is smaller or equal than unity ($\phi \leq 1$)[126].

The transition from *State I* to *State II* suppresses solid-vapor interface but creates additional fluid-vapor interface and fluid-solid interface[126]. Let the energy per unit area associated with *State I* be E_I. Then, the energy associated with *State II* (denoted by E_{II}) per unit area is given by[126]:

$$E_{II} = E_I - (r - \phi) \cdot \gamma_{SV} + (r - \phi) \cdot \gamma_{SL} + (1 - \phi) \cdot \gamma_{LV} \qquad (2.4.1)$$

The first term in equation 2.4.1 is the energy (per unit area) of *State I*, the second term is the amount of suppressed solid-vapor interface, the third term describes the additional solid-fluid interface, and the

fourth term is the amount of additional fluid-vapor interface[126]. It is assumed that the pillars´ top faces are not wetted by the liquid, which, in general, does not necessarily need to be the case (section 2.5 and section 2.6).

The change in energy (per unit area) when passing from *State I* to *State II* is hence given by:

$$\Delta E = E_{II} - E_I = (1 - \phi) \cdot \gamma_{LV} + (r - \phi) \cdot \gamma_{SL} - (r - \phi) \cdot \gamma_{SV} \qquad (2.4.2)$$

The transition from *State I* to *State II* associated with the establishment of a stable fluid film within the texture is only energetically favorable if $\Delta E < 0$. Hence, rearranging gives:

$$(1 - \phi) \cdot \gamma_{LV} + (r - \phi) \cdot \gamma_{SL} - (r - \phi) \cdot \gamma_{SV} < 0 \Leftrightarrow$$

$$(1 - \phi) + (r - \phi) \cdot \frac{(\gamma_{SL} - \gamma_{SV})}{\gamma_{LV}} < 0 \qquad (2.4.3)$$

Equation 2.4.3 can be simplified and rearranged further. For that purpose, it is helpful to introduce the concept of the (equilibrium) *contact angle* to understand the contact between a solid and a fluid.

Consider a drop of a fluid placed on a solid substrate. The contact angle θ is defined at the so-called three-phase *contact line*, where the fluid phase (*L*), the vapor phase ("air", *V*), and the solid phase (*S*) meet[126].

The equilibrium contact angle is given by *Young's equation*[127] (Figure 2.4.2) describing the equilibrium contact angle θ:

$$\cos\theta = \frac{\gamma_{SV} - \gamma_{SL}}{\gamma_{LV}} \qquad (2.4.4)$$

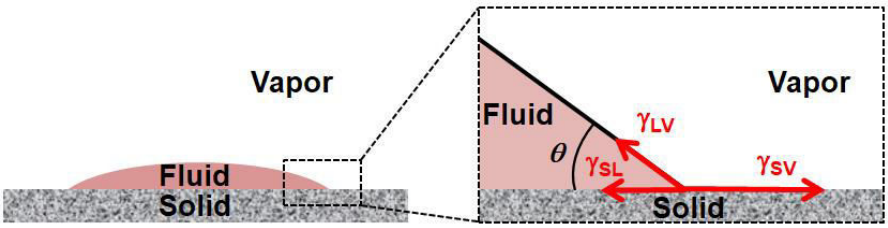

Figure 2.4.2: Young´s equation. The drop is at equilibrium and rest. There is a force balance between the interfacial forces representing the interfaces at stake. Note that the wetting is only partial. The contact angle θ is determined by the balance of the interfacial tensions.

Next to the restriction of equilibrium conditions, the applicability of Young`s equation has further limits[126]. The equilibrium contact angle θ is not necessarily consistent with the experimentally observed so-called *apparent contact angle* θ_{app}. On non-ideal surfaces (not considered in Young´s equation), the equilibrium contact angle (static) θ ranges between the *advancing contact angle* θ_a and the *receding contact angle* θ_r. The advancing contact angle is defined as the angle at the point where the contact line of the drop starts to advance when the volume of the drop is increased[128]. Likewise, the receding contact angle is defined as the angle at the point where the contact line of the drop starts to recede when the volume of the drop is decreased[128]. The advancing angle is higher than the receding contact angle, *i.e.* $\theta_a > \theta_r$. The difference between the advancing and receding contact angle $\Delta\theta = \theta_a - \theta_r$ is defined as the *contact angle hysteresis*[128]. On any non-ideal surface, a contact angle hysteresis exists.

Young´s equation does not deal with spreading drops. For a fully spreading liquid, a vanishing contact angle ($\theta = 0°$) is assigned. A surface having high surface energy associated with a high surface tension γ_{SV} gets immediately contaminated since virtually everything placed onto such a surface lowers the surface energy. The spreading drop creates new solid-liquid (*SL*) interface, suppresses solid-vapor (*SV*) interface, and creates new liquid-vapor (*LV*) interface[126].

With the help of the surface tensions involved, the so-called *Spreading Parameter* (2.4.5), also called *spreading coefficient*, can be defined:

$$S := \gamma_{SV} - (\gamma_{SL} + \gamma_{LV}) = \gamma_{SV} - \gamma_{SL} - \gamma_{LV}. \qquad (2.4.5)$$

For a positive spreading parameter ($S > 0$), the liquid will spread ($\theta = 0°$); it will form a lens otherwise[126]. In the latter case, the liquid lens will display a finite and well-defined contact angle with the solid. A surface on which the equilibrium contact angle θ exceeds 90° is referred to as hydrophobic. It is referred to as hydrophilic otherwise ($\theta < 90°$).

With the help of Young´s equation (equation 2.4.4), although addressing equilibrium, it is now possible to rewrite equation 2.4.3:

$$(1-\phi) + (r-\phi)\cdot\frac{(\gamma_{SL}-\gamma_{SV})}{\gamma_{LV}} < 0 \overset{Young}{\Longleftrightarrow} (1-\phi) - (r-\phi)\cdot\cos\theta < 0 \quad (2.4.6)$$

The energy is lowered upon transition from *State I* into *State II*, *i.e.* $\Delta E < 0$, if

$$\Delta E < 0 \Leftrightarrow \cos\theta < \frac{1-\phi}{r-\phi} \qquad (2.4.7)$$

We now define:

$$\cos\theta_c := \frac{1-\phi}{r-\phi} \quad (2.2.8) \quad \text{or} \quad \theta_c := arccos\left(\frac{1-\phi}{r-\phi}\right) \quad (2.4.9)$$

It is defined as the *critical contact angle*[126]. The propagation of the liquid within the solid is energetically favorable if the contact angle θ of the fluid on the solid texture is smaller than the critical contact angle θ_c, *i.e.* $\theta < \theta_c$. It is an artificial angle given by the design of the surface; θ_c depends exclusively on the design of the solid[120,129]; it does not depend on γ_{LV}. The consequence of this concept (equations (2.4.7) – (2.4.9)) is that tuning the roughness (affects the roughness factor *r* and typically also the pillar fraction ϕ) of a solid substrate affects the infiltration of that solid substrate with liquid[126].

The impregnation of texture via the transition from *State I* to *State II* is also described in the literature as *hemiwicking*[126]. The rougher a solid substrate, the more likely *hemiwicking* occurs, as the critical contact angle θ_c is the larger, the more rough, *i.e.* larger *r*, is[126]. The energy considerations developed with the help of Figure 2.4.1 and the formalism of hemiwicking developed with the help of equations 2.4.1 – 2.4.9 explain the existence of stable liquid-infused surfaces (on a rough solid substrate) on which a fluid film is stabilized. The criteria addressing the stability of the liquid film in contact with a deposited drop (assumed immiscible with the impregnating fluid) are discussed separately (section 2.5).

The driving force of the hemiwicking process is counteracted by viscous dissipation, *i.e.* resistance to flow[126], and *pinning* of the contact line. The viscous dissipation depends on the product of the fluid viscosity, the impregnated distance, and the velocity of the flow. This is why viscous liquids take much longer to impregnate a porous substrate than liquids having very low viscosities. The contact angle hysteresis determines the degree of pinning[130]. The larger the contact angle hysteresis, the stronger contact line pinning occurs[130]. The contact line is pinned at so-called *pinning sites*. Pinning sites may have their origin in surface roughness, chemical heterogeneities, or deposited substances acting as contaminants of the surface[130].

2.5 Drops Placed onto Liquid-Infused Surfaces at Rest

As already mentioned (section 2.1), a drop positioned on a Liquid-Infused Surface (LIS) is a complex 4-phase system, involving the solid texture ("solid"), the impregnating lubricant ("oil"), the liquid drop ("water"), and the surrounding vapor ("air"). In the following, it is assumed that the drop deposited on the liquid-infused surface is immiscible with the impregnating lubricant, which is non-aqueous. In the following, the drop is referred to as water, the lubricant is referred to as oil, the textured surface is referred to as solid, and the surrounding vapor is called air. The following considerations assume a solid substrate consisting of regular and uniform micropillars. It has to be kept in mind that the choice of drops and lubricants are not limited to water and oils, respectively.

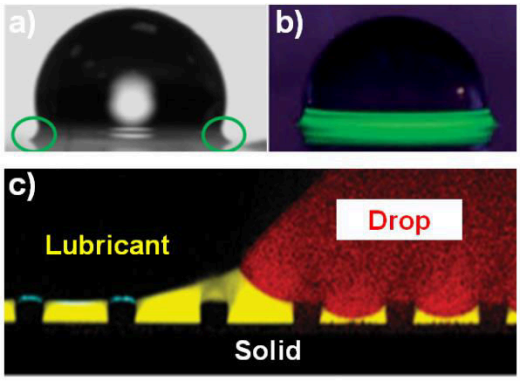

Fig. 2.5.1: Drops immiscible with the lubricant placed onto a liquid-infused surface. a) Water drop deposited on a liquid-infused surface (Adapted with permission from Vogel *et al.*[9] Copyright © 2013 Springer Nature). A feature specific to liquid-infused surfaces is the wetting ridge (green circles). b) Wetting ridge formed by lubricant in the presence of a deposited immiscible drop. Photograph (under UV illumination, fluorescent dye dissolved in the lubricant) of the annular wetting ridge around a water drop (adapted with permission from Smith *et al.*[45] Copyright © 2013, The Royal Society of Chemistry). c) Drop (water, red) deposited on infused (yellow: lubricant) micropillar array[10] (black, pillar diameter: 10 μm, pillar height: 10 μm, edge-to-edge distance between micropillars: 30 μm). Note that the surrounding air does also appear black. Adapted with permission from Schellenberger *et al.*[10] Copyright © 2015 Published by the Royal Society of Chemistry.

Visual inspection of a drop deposited onto a liquid-infused surface hints at a deviation from the idealized shape of a spherical cap[131]. More advanced methods, other than just "looking" at the drop,

such as laser scanning confocal microscopy (LSCM), reveal features not found for drops deposited onto "dry " surfaces[9].

The *wetting ridge* is encountered on liquid-infused surfaces accommodating immiscible drops (Figure 2.5.1). Synonymous terms to wetting ridge include *meniscus*, *wedge*, *oil skirt*, or *oil foot*. This annular ridge of oil situated around the drop that is pulled onto the drop in order to satisfy the vertical force balance of the interfacial tensions[45]. The vertical component of the surface tension of water pulls up the meniscus from the oil[45]. Any drop placed on a liquid-infused surface is surrounded by a wetting ridge. Wetting ridges can also be observed close to the wetting front on other non-rigid solid surfaces[132-134]. The meniscus is also maintained in dynamic situations in which drops move on liquid-infused surfaces (see section 2.6)[10]. The wetting ridge is a low-pressure region. The wetting ridge grows by lubricant flowing into the ridge from the surrounding area[55].

The deviation of the drop´s shape from the idealized shape of a spherical does also depend on the degree of filling of the microtextures[10]. As a consequence, the real contact angle can strongly deviate from the observed contact angle[10]. The relative size of the deposited drop compared to the surrounding wetting ridge formed by the infused lubricant influences the drop shape in terms of the apparent contact angle[135].

In the case of a positive spreading coefficient ($S > 0$, section 2.4), the drop may be covered by a thin lubricant layer, the so-called ***cloaking layer***[45] also called *wrapping layer*. The cloaking layer may reach thicknesses in the range of tens of nanometers[108]. For a given targeted contaminant liquid, the lubricant can be selected to avoid cloaking[136].

In Figure 2.5.2, a schematic of a drop deposited on a liquid-infused surface is presented. In addition to the textured surface (the "solid"), the liquid lubricant (the "oil"), and the surrounding vapor (the "air"), the cloaking layer, and especially the wetting ridge are features to take into consideration when addressing drops on liquid-infused surfaces.

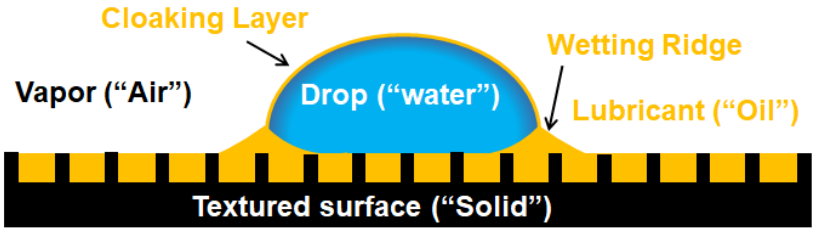

Figure 2.5.2: Schematic of a drop at rest on a liquid-infused surface.

For a cross-section (two-dimensional representation) through the drop and the liquid-infused surface considering the water-air-oil interface, it is possible to calculate the angles established at the *triple point* (where oil, water, and air meet, green dot in fig. 2.5.3). In the full three-dimensional picture, the triple point corresponds to the *liquid-triple-point-contact-line* (TPCL)[135]. However, the interfacial tensions between the individual fluid phases need to be known, and the drop shall not be cloaked by oil. The so-called *Neumann-triangle* is spanned by the interfacial tensions at the triple point. In equilibrium, these interfacial tensions add to zero when summated (vector sum)[137]. The Neumann angles are the angles between the individual interfacial tensions (Figure 2.5.3).

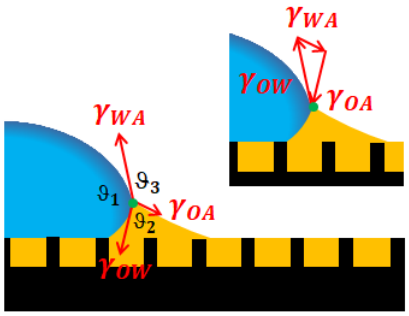

Figure 2.5.3: Neumann angles (ϑ_1, ϑ_2, and ϑ_3) and Neumann triangle.

The Neumann angles (ϑ_1, ϑ_2, and ϑ_3) can be calculated from the known interfacial tensions and the laws of sinus and cosine[138]. The Neumann angles are given by the following expressions:

$$\cos \vartheta_1 = \frac{\gamma_{OA}{}^2 - \gamma_{WA}{}^2 - \gamma_{OW}{}^2}{2\gamma_{OW}\gamma_{WA}} \qquad (2.5.1)$$

$$\cos \vartheta_2 = \frac{\gamma_{WA}{}^2 - \gamma_{OA}{}^2 - \gamma_{OW}{}^2}{2\gamma_{OW}\gamma_{OA}} \qquad (2.5.2)$$

$$\cos \vartheta_3 = \frac{\gamma_{OW}{}^2 - \gamma_{WA}{}^2 - \gamma_{OA}{}^2}{2\gamma_{WA}\gamma_{OA}} \qquad (2.5.3)$$

Smith *et al.*[45] established a thermodynamic framework explaining different wetting configurations of drops deposited on a liquid-infused surface based on a solid substrate consisting of regular and uniform micropillar arrays. This work provides classifications of thermodynamic configurations in which a static drop on a liquid-infused surface can exist. Configurations underneath the drop are distinguished from configurations outside the drop[45]. The configurations outside the deposited drop (in the air environment) are a dry texture which is not impregnated (called *A1*), an impregnated texture with emerging features corresponding to a not overfilled texture (called *A2*), and a texture submerged in oil (impregnated with submerged features, encapsulated texture, called *A3*)[45]. Outside the drop, the liquid-infused surface is in an air-environment[45]. Underneath the drop, the liquid-infused surface is in a water-environment[45]. Underneath the drop, the drop can displace the impregnating lubricant, corresponding to the impalement of the drop (called *W1*). In addition, the configurations of an impregnated texture with emerging features (called *W2*) and a texture submerged in oil (called *W3*) are also possible to obtain underneath the drop[45]. The configuration realized is the configuration associated with the lowest total surface energy[45]. Figure 2.5.4 summarizes these possible wetting configurations.

The total interfacial energy per unit area can be computed for each configuration in terms of the relevant interfacial tensions γ, roughness factor r, and fraction ϕ of micro-features (micropillars) present on the surface by summing up the individual interfacial energy contributions[45].

Table 2.5.1 presents the interfacial energies per unit area associated with each configuration. The full picture of possible thermodynamic states of a water (aqueous) drop placed on a liquid-infused surface is then obtained by taking into account whether there is the cloaking of the water drop by the oil (spreading coefficient $S > 0$) or not ($S < 0$)[45]. in total, there are 12 possible configurations[45].

The configuration with the lowest total interfacial energy per unit area is the configuration realized for a given system[45].

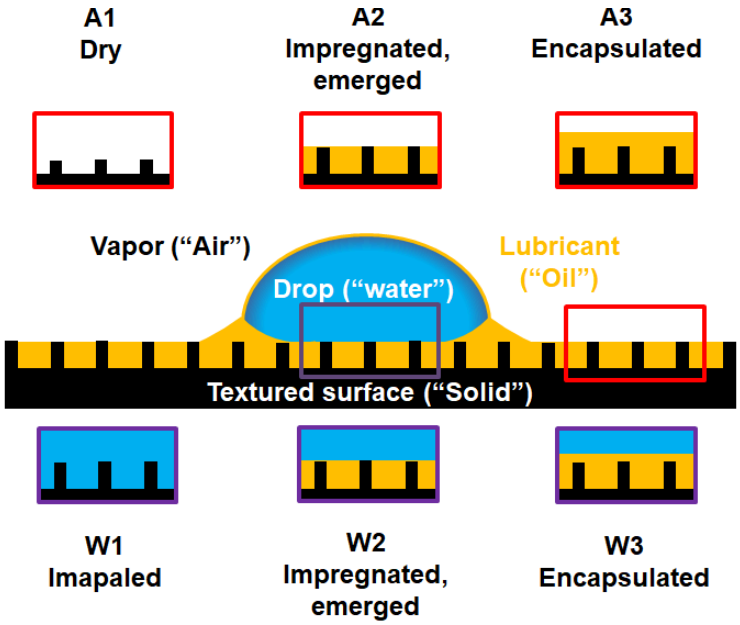

Figure 2.5.4: Possible wetting configurations outside (*A1-A3*) or underneath (*W1-W3*) the drop deposited on the liquid-infused surface. Adapted with permission from Smith *et al.*[45] Copyright © 2013 The Royal Society of Chemistry.

Table 2.5.1: Interfacial energies per unit area for the possible wetting configurations outside the drop (*A1-A3*) and underneath the drop (*W1-W3*). Adapted with permission from Smith *et al.*[45] Copyright © 2013 The Royal Society of Chemistry.

	Configuration	Total interfacial energy per unit area
A1	Dry	$E_{A1} = r \cdot \gamma_{SA}$
A2	Impregnated, emerged	$E_{A2} = (r - \phi) \cdot \gamma_{OS} + \phi \cdot \gamma_{SA} + (1 - \phi) \cdot \gamma_{OA}$
A3	Encapsulated	$E_{A3} = \gamma_{OA} + r \cdot \gamma_{OS}$
W1	Impaled	$E_{W1} = r \cdot \gamma_{SW}$
W2	Impregnated, emerged	$E_{W2} = (r - \phi) \cdot \gamma_{OS} + \phi \cdot \gamma_{SW} + (1 - \phi) \cdot \gamma_{OW}$
W3	Encapsulated	$E_{W3} = \gamma_{OW} + r \cdot \gamma_{OS}$

In table 2.5.2, the criteria according to which a specific configuration (*A1 - A3 & W1 - W3*) will be realized according to the lowest possible interfacial energy (table 2.5.1) are presented. There are two possibilities to express these criteria. The first possibility is to express the criteria in terms of the spreading coefficients obtained for the solid-lubricant/oil configuration in the presence of air ($S_{OS(A)}$, configurations *A1-A3*), or water environment ($S_{OS(W)}$, configurations *W1-W3*).

The other possibility is to express the criteria in terms of the contact angles in the air- or water environment ($\theta_{OS(A)}$ and $\theta_{OS(W)}$)[45].

Table 2.5.2: Equivalent criteria for the stability of possible wetting configurations outside the drop (*A1-A3*) and underneath the drop (*W1-W3*). Adapted with permission from Smith *et al.*[45] Copyright © 2013 The Royal Society of Chemistry.

	Configuration	Equivalent Criteria for the realization of a configuration	
A1	Dry	$S_{OS(A)} < -\gamma_{OA} \cdot \left(\frac{r-1}{r-\phi}\right)$	$\theta_{OS(A)} > \theta_C$
A2	Impregnated, emerged	$-\gamma_{OA} \cdot \left(\frac{r-1}{r-\phi}\right) < S_{OS(A)} < 0$	$0 < \theta_{OS(A)} < \theta_C$
A3	Encapsulated	$S_{OS(A)} \geq 0$	$\theta_{OS(A)} = 0$
W1	Impaled	$S_{OS(W)} < -\gamma_{OW} \cdot \left(\frac{r-1}{r-\phi}\right)$	$\theta_{OS(W)} > \theta_C$
W2	Impregnated, emerged	$-\gamma_{OW} \cdot \left(\frac{r-1}{r-\phi}\right) < S_{OS(W)} < 0$	$0 < \theta_{OS(W)} < \theta_C$
W3	Encapsulated	$S_{OS(W)} \geq 0$	$\theta_{OS(W)} = 0$

In the two *encapsulated* configurations (*A3* and *W3*), the thickness of the impregnating oil film exceeds the height of the micropillars. There is oil on the top of the micropillars. Consequently, a drop deposited onto a liquid-infused surface in an encapsulated configuration is separated by a thin film of oil, the so-called *intercalated film*, separating the drop from the solid texture. Chemical functionalization[54] of the micropillar array or the presence of a hydrophobic nanoroughness on the micropillar arrays (coatings with nanobeads) can ensure the presence of oil on the pillar tops (section 2.6)[47].

It is assumed that the stability of a lubricant film underneath a deposited drop is determined by the competition between the capillary pressure, which is trying to drain/squeeze out the lubricant underneath the drop and the stabilization of the lubricant film due to van der Waals forces[54].

The stability of the lubricant films in the *encapsulated configuration*s (*A3* & *W3*) in the absence of deposited drops (*A3*), *i.e.* in the absence of external destabilizing forces, is given by a positive spreading parameter ($S = \gamma_{SV} - \gamma_{SL} - \gamma_{LV} > 0$)[1,45]. When a drop is deposited onto the lubricant film (configuration *W3*), a positive spreading parameter is a necessary but not sufficient condition for a stable lubricant film.

The capillary pressure *P* describes the pressure difference across a curved interface of two static immiscible fluids. It can be described with the help of the *Young-Laplace equation*:

$$P = \gamma \left(\frac{1}{R_1} + \frac{1}{R_2}\right) \qquad (2.5.4)$$

where γ is the interfacial tension, R_1 and R_2 are the principal radii of curvature[139].

The pressure inside the deposited drop P_{drop} is given by:

$$P_{drop} = P_{atm} + \frac{2\gamma}{R} \qquad (2.5.5)$$

where P_{atm} is the atmospheric pressure, R the radius of the drop (radius of curvature) and $\gamma = \gamma_{LA}$ (no cloaking) or $\gamma = \gamma_{LO} + \gamma_O$ (cloaking) with γ_{LA} describing the drop ("liquid", *L*)-air (*A*) interface, γ_{LO} the interfacial tension at the drop - lubricant ("oil", *O*) interface, and γ_O the surface tension of the oil[54].

The pressure in the intercalated lubricant film P_{film} is equal to the pressure in the drop P_{drop} since the hydrostatic pressure is ignored ($\rho gR << \gamma/R$)[54].

Therefore, assuming the drop is cloaked by the lubricant, there is a pressure difference ΔP trying to squeeze out lubricant from underneath the drop given by[54]:

$$\Delta P \sim \frac{\gamma_{LO}+\gamma_O}{R} \qquad (2.5.6)$$

For drops not cloaked with lubricant, the surface tension of the liquid constituting the deposited drop (γ_{LA}) has to be used in equation 2.5.5[10,45].

The stabilization of the lubricant film underneath a deposited drop (and the cloaking layer of a drop) due to van der Waals forces can be expressed in terms of the *disjoining pressure*[140]. Intuitively, it can be interpreted as the difference between the pressure within a film between two interfaces and the pressure in the bulk phase[141].

The disjoining pressure $\Pi(h)$ is given by:

$$\Pi(h) = \frac{A}{6\pi h^3} \qquad (2.5.7)$$

where A is the *Hamaker constant* and h is the thickness of the lubricant film[54]. To stabilize the lubricant film through van der Waals forces within the lubricant film, the disjoining pressure has to be positive, being a condition which requires a positive Hamaker constant ($A > 0$)[142]. In addition, the thickness of the lubricant film does also depend on the amount of lubricant present in the system. Textures depleted of lubricant (section 2.7) will hardly facilitate stable lubricant films between drops and texture. The formalism above implicitly assumes that there is sufficient lubricant and that there is no lubricant-depletion (section 2.7). Note that in the criteria presented in tables 2.5.1 and 2.5.2 (Smith *et al.*[45]), the disjoining pressure is ignored.

The equilibrium lubricant film thickness h_{eq} results from the equality of the disjoining pressure with the pressure at which lubricant is being squeezed out from underneath the deposited drop. By equating equation 2.5.6 with equation 2.5.7 we obtain:

$$\Pi(h) \sim P \Leftrightarrow \frac{A}{6\pi h^3} \sim \frac{\gamma_{LO}+\gamma_O}{R} \Rightarrow h_{eq} \sim \left(\frac{R \cdot A}{\gamma_{LO}+\gamma_O}\right)^{1/3} \qquad (2.5.8)$$

The criterion for a stable lubricant film underneath a deposited drop (and the cloaking layer of a drop) is thus given by a positive spreading coefficient ($S > O$) and a positive Hamaker constant ($A > 0$, $|A| \approx 10^{-21}$J)[54]. The Hamaker constant can be estimated within the framework of the Lifshitz theory[141]. If one of these conditions is not met, the lubricant film is not stable and may partially or fully dewet, in the sense that the deposited drop may partially or fully displace the lubricant. In the case of partially dewetting lubricant, discrete pockets of lubricant are formed underneath the deposited drop.

Independent of whether the solid substrate is ideally flat or decorated with micro-and nanostructures, there are three possible lubrication states to be found. Either there are stable intercalated films[54], corresponding to the encapsulated configurations *A3* and *W3* (Figure 2.5.4 and Table 2.5.1 and Table 2.5.2)[45], or discrete micron-sized lubricant-pockets are found on the texture, corresponding to partial dewetting of the lubricant[45,54], or the complete displacement (dewetting) of lubricant from the solid texture by the deposited drop penetrating the texture[54], corresponding to the impaled configuration *W1* (Figure 2.5.4 and Table 2.5.1 and Table 2.5.2)[45].

2.6 Drops in Motion on Liquid-Infused surfaces

A drop moving on a liquid-infused surface is a very complex system (section 2.1) due to the interplay of the four different phases present (solid, lubricant, drop, and air) and the features specific and typical to liquid-infused surfaces, namely the meniscus. A multitude of different factors influences and determines the motion of drops on liquid-infused surfaces.

Drops roll on (confirmed via the addition of tracer particles) and eventually off liquid-infused surfaces[45]. Liquid-Infused surfaces (LIS) show very low contact angle hysteresis ($\Delta\theta$ = few °)[143] and very low roll-off angles of drops (≈ few °) deposited onto them[45]. Drops placed onto a liquid-infused surface are highly mobile, showing very low lateral adhesion[45,47].

The motion of drops placed on liquid-infused surfaces is discussed, considering the published works most relevant to this thesis. The works of Smith *et al.*[45] is the foundation of the work of Keiser *et al.*[47], whose findings are crucial for the further course of this thesis. The work of Daniel *et al.*[54] provided data complementary to the data obtained in Keiser *et al.*[47].

The system we consider is a drop moving at a ***steady-state velocity*** V on a liquid-infused surface parallel to the plane of the surface (shown schematically in Figure 2.6.1).

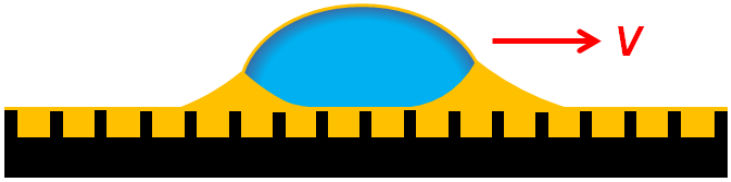

Figure 2.6.1: Drop moving on liquid-infused surfaces at a steady-state velocity *V*.

In the work of Smith *et al.*[45] and Keiser *et al.*[47], the *steady-state velocity V* is set by tilting the liquid-infused surface (Figure 2.6.2). In this case, it is a steady-state descending velocity. In the work of Daniel *et al.*[54] (Figure 2.6.8), the steady-state velocity is controlled by holding the drop in place with the help of a cantilever and moving the substrate. For the sake of clarity and simplicity, the *steady-state velocity* is referred to as *velocity*.

In Keiser *et al.*[47] the steady-state descending velocities V of drops moving onto inclined (tilted) liquid-infused surfaces are measured for different driving forces (modulated by varying the drop volume Ω and the inclination angle α) across a large parameter space (Table 2.6.1) by following the trajectories of the drops with high-speed imaging (Figure 2.6.2) and the extraction of scaling laws[45,47].

The geometrical parameters of the texture to consider are the height of the micropillars (h), subsequently called pillars, and the pillar density (ϕ, section 2.4)[47]. The drop viscosity (η_w) is varied with the help of water-glycerol mixtures[144,145].

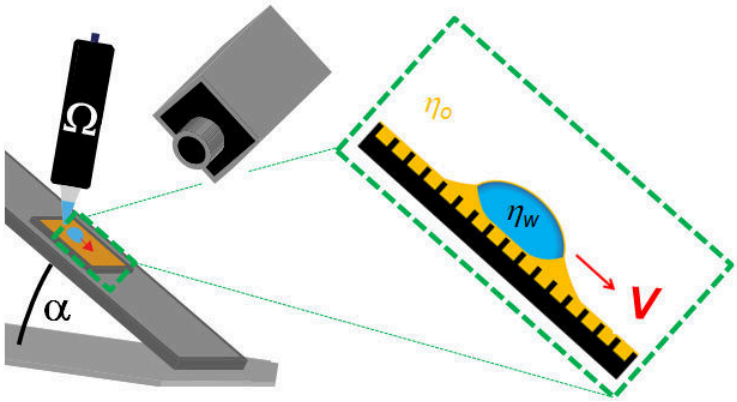

Figure 2.6.2: Experimental setup used by Smith *et al.*[45] and Keiser *et al.*[47] (Courtesy of Dr. Armelle Keiser ESPCI/EPFL, modified by author).

The texture consisted of micropillar arrays made of SU-8 on silicon wafers prepared by photolithography[47]. The lubricant was silicone oil. Impregnation has been accomplished by spontaneous impregnation, thereby ensuring that there is no excess lubricant (section 2.2)[47].

If excess lubricant is present, the tops of roughness features, *e.g.* tops of micropillars, are completely submerged in lubricating oil (*encapsulated* configurations *A3* and *W3* in section 2.5, Figure 2.5.4). The strength of contact line pinning, represented by the roll-off angle α^* should, in principle, be reduced in these configurations. In contrast, when there is no excess lubricant, on the tops of asperities which are not submerged in oil but emerge from the oil without being covered by oil (*impregnated, emerged* configurations A2 and W2 in section 2.5, Figure 2.5.4), non-negligible pinning of the contact line occurs[10,146,147], resulting from the contact angle hysteresis of two contact lines (oil-air-solid contact line and oil-water-solid contact line)[45].

Table 2.6.1: Parameters and parameter spaces investigated in Keiser *et al.*[47]

Parameter	Range
Oil viscosity η_o	10 – 1000 mPa·s
Drop viscosity η_w	1 – 1000 mPa·s
Height of micropillars ("pillar height") h	20 ± 3 µm
Edge length of micropillars a	18 -185 µm
Edge-to-edge spacing b	15 - 40 µm
Density of micropillars ("pillar density") ϕ	23% - 67%
Drop volume (Ω)	1 – 40 µL (1-20 µL)
Inclination angle α	5° - 70° (1°-70°)
Coating of micropillar array with nanobeads	Yes/No

In Keiser *et al.*[47] the height of the micropillars is kept constant. Within the framework of this thesis, the influence of the micropillar height on the descending velocity of drops moving on liquid-infused surfaces is studied in more detail (Chapter 4).

On inclined liquid-infused surfaces, deposited drops experience gravitational forces[45]. The driving force (F_M) is the component of the gravitational force acting on the drop parallel to the plane on which the drop moves[47]. The gravitational forces must overcome the pinning forces to set the drop in motion. Only at inclination angles (α) exceeding the roll-off angle (α^*), *i.e.* $\alpha > \alpha^*$, the drop is set in motion[47]. During the rolling process, the gravitational potential energy is transformed into kinetic energy associated with the drop motion[45]. Energy is dissipated due to contact line pining and viscous effects.

The driving force (F_M) is expressed as[47]:

$$F_M = \rho g \Omega (\sin\alpha - \sin\alpha^*) \qquad (2.6.1)$$

where ρ is the density of the drop and g the acceleration of gravity.

It is possible to establish experimental conditions for which the roll-off angle approaches 0° (see below). In this case, equation 2.6.1 simplifies to[47]:

$$F_M = \rho g \Omega (\sin\alpha - \sin\alpha^*) \cong \rho g \Omega \sin\alpha \qquad (2.6.2)$$

For the remainder of this section, equation 2.6.2 is used to express the driving force (F_M).

Therefore, the descending velocities V in the stationary regime are given by the balance of gravitational and dissipative forces. The dissipative forces are subsequently also referred to as friction forces. The stationary regime is quickly reached; after a few centimeters, the drop has moved on the inclined liquid-infused surface[47]. Viscous dissipation, or friction, may occur in the drop as well as in the lubricating oil. Dissipation (friction) occurring in the oil may, in principle, take place in the lubricating oil underneath the drop and the wetting ridge[45,47].

Functionalizing a regular and uniform micropillar array with nanobeads (made of polystyrene, size of nanobeads ≈ 30 nm), so-called *Glaco-treatment*, reduces contact line pinning on the pillar tops since the lubricating oil also impregnates the nanoroughness features created by the nanobeads[47]. Thereby, the aqueous drop is separated from the microtexture by establishing an oil film[148]. A thin film of oil is stabilized at the pillar tops[47]. This configuration is reminiscent of the *encapsulated* configurations *A3* and *W3* (section 2.5, Figure 2.5.4) in which the micropillars are completely submerged in oil. As a consequence, the roll-off angles and contact angle hysteresis are strongly reduced and approach non-measurable values ($\alpha^* \approx 0°$) and are independent of the viscosity of the impregnating oil (η_o) and the characteristic spacing between the micropillars[45,47]. Without nanobead-coating (Glaco-treatment), the roll-off angle depends on the pillar density (ϕ)[47]. Furthermore, non-negligible pinning of the contact line occurs[10,146,147], resulting from the contact angle hysteresis of two contact lines (oil-air-solid contact line and oil-water-solid contact line)[45]. Therefore, the friction behavior of drops on the liquid-infused surfaces depends on the presence or absence of nanobeads on pillar tops/roughness features on the microscale[47,148].

To obtain the relationship between friction force and measured velocities, one first considers situations of extreme viscosity ratios. Figure 2.6.3 evidences that the origin of the predominant contribution to friction and dissipation, *i.e.* the nature of friction, is determined by the ratio of the drop viscosity (η_w) to the oil viscosity (η_o)[47], *i.e.* η_w/η_o.

At constant oil viscosity (η_o) and for a given drop volume (Ω), inclination angle (α), and pillar density (ϕ), the steady-state velocity depends on the drop viscosity (η_w) as is evidenced in Figure 2.6.3.

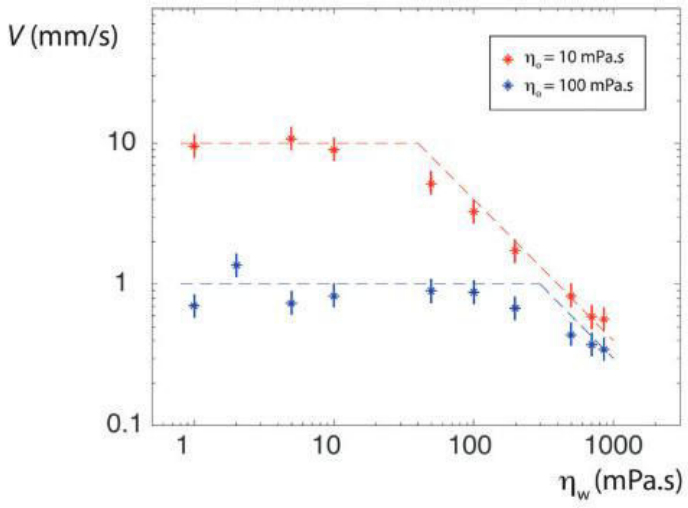

Figure 2.6.3: Descending velocity V in dependence of drop viscosity (η_w) for two different oil viscosities (η_o, red: 10 mPa·s, blue: 100 mPa·s). The other parameters were kept constant (drop volume Ω = 20 µL, pillar density ϕ = 23%, pillar height h = 20 µm, tilting angle α = 5°). The micropillar array was coated with nanobeads (Glaco Mirror Coat, Soft 99). Hence, the roll-off angle α^* approaches 0°. Reprinted with permission from Keiser *et al.*[47] Copyright © 2017 The Royal Society of Chemistry.

In Figure 2.6.3, it is evidenced that there are two different regimes of friction at work, depending on the drop viscosity (η_w). For drop viscosities much smaller than the viscosity of the impregnating oil ($\eta_w << \eta_o$), the steady-state drop descending/shedding velocity is independent of the drop viscosity (η_w) for each selected oil viscosity (η_o)[47]. The velocity becomes a factor of approximately 10 smaller when the oil viscosity (η_o) is increased by a factor of 10 (Figure 2.6.3)[47]. This suggests that in this regime, the viscous dissipation does mainly take place in the oil. In the other extreme case, when the drop viscosity (η_w) greatly exceeds the oil viscosity (η_o), *i.e.* $\eta_w >> \eta_o$, the steady-state drop descending/shedding velocity is inversely proportional to the drop viscosity (η_w)[47]. In this regime, the dissipation of energy mainly occurs in the drop[47]. Hence, two different regimes of friction behavior can be clearly identified by considering the extreme cases of obtainable viscosity ratios.

In the following, we consider the first case of an extreme viscosity ratio: the drop viscosity greatly exceeding the oil viscosity ($\eta_w >> \eta_o$). In this regime of viscosity ratio, viscous dissipation does predominantly occur in the drop[47]. It is found that the measured velocities linearly depend on the driving force (Figure 2.6.4)[47]. The measured descending velocities do not depend on the pillar density (ϕ)[47].

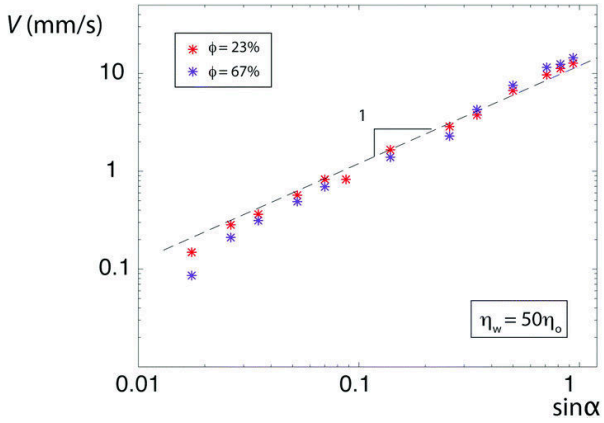

Figure 2.6.4: Drop speed V as a function of the driving force (represented by driving parameter $sin\alpha$, for η_o = 10 mPa·s, η_w = 500 mPa·s ($\eta_w >> \eta_o$), pillar height h = 20 µm, and Ω = 20 µL. The dashed line has a slope 1. The two series of data correspond to pillar densities ϕ = 23% (red data) or ϕ = 67% (purple data)[47]. Reprinted with permission from Keiser *et al.*[47] Copyright © 2017 The Royal Society of Chemistry.

Slip is favored at the oil-water interface due to the existence of an oil film underneath the drop[47]. The friction law in this regime can be understood by considering the continuity of the viscous stress at the oil-water interface between the oil film and the drop (Figure. 2.6.5)[47].

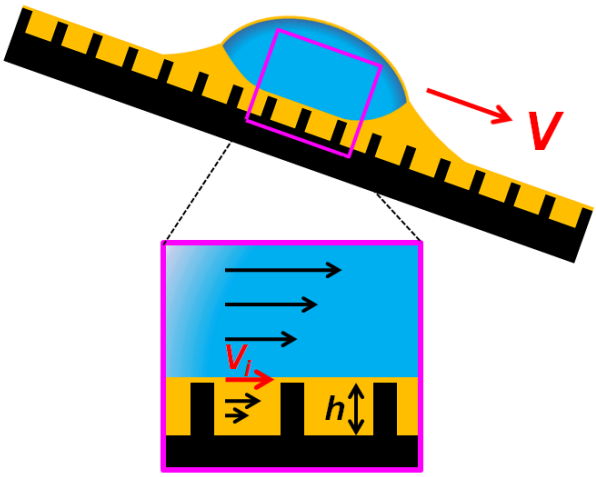

Figure 2.6.5: Oil-water interface between the drop and oil film underneath the drop. The interfacial velocity V_i is obtained from the continuity of the viscous stress across the interface[47]. Adapted with permission from Keiser *et al.*[47] Copyright © 2017 The Royal Society of Chemistry.

The scaling law for the continuity of the viscous stress across the oil-water interface reads as[47]:

$$\eta_w \frac{(V-V_i)}{R} \sim \eta_o \frac{V_i}{h} \Leftrightarrow V_i \sim \frac{V}{1+\frac{\eta_o R}{\eta_w h}} \qquad (2.6.3)$$

In equation 2.6.3, V_i is the interfacial velocity, R is the characteristic drop size (assuming a hemispherical drop geometry, it is the drop radius), and h is the thickness of the oil film[47].

Owed to the underlying assumption that the characteristic drop size greatly exceeds the thickness of the oil film, *i.e.* $R >> h$, and the velocity gradients within the drop and the pillars minimizing slip, the interfacial velocity V_i is significantly smaller than the steady-state velocity V ($V_i << V$)[47].

Hence, equation 2.6.3 simplifies to[47]:

$$\eta_w \frac{(V-V_i)}{R} \cong \eta_w \frac{V}{R} \sim \eta_o \frac{V_i}{h} \qquad (2.6.4)$$

The friction force in this regime (F_η) can then be expressed by integrating the right-hand side of equation 2.6.4 over the drop area (A)[47], which scales with R^2.

$$F_\eta \sim \int \eta_w \frac{V}{R} dA = \eta_w RV \qquad (2.6.5)$$

Balancing equation 2.6.5 with the gravitational driving force (equation 2.6.2) gives the scaling law for the steady-state descending velocity in this regime (recalling that the drop volume Ω scales with R^3, *i.e.* $\Omega \sim R^3$)[47]:

$$F_\eta \sim F_M \Leftrightarrow \eta_w RV \sim \rho g \Omega \sin\alpha \Rightarrow V \sim \frac{\rho g R^2}{\eta_w} \sin\alpha \qquad (2.6.6)$$

This expression accurately captures the scaling behavior of the drop velocity in this regime. In this regime, equation 2.6.5 evidences that the friction force (F_η) is of a Stokes´ type nature.

In the following, we pass to the second case of an extreme viscosity ratio: the drop viscosity being very small compared to the oil viscosity ($\eta_w << \eta_o$), where viscous dissipation does mainly occur in the oil (Figure 2.6.6)[47]. The work of Smith *et al.*[45] postulates that the dominant contribution to friction taking place in the oil-phase originates from the viscous dissipation in the meniscus (wetting ridge). Furthermore, comparing the results obtained for drops shed from inclined liquid-infused surfaces[45,47] to the results obtained for rolling solid spheres on thin films of viscous liquids revealed[149,150], that viscous dissipation primarily occurs in the wetting ridge.

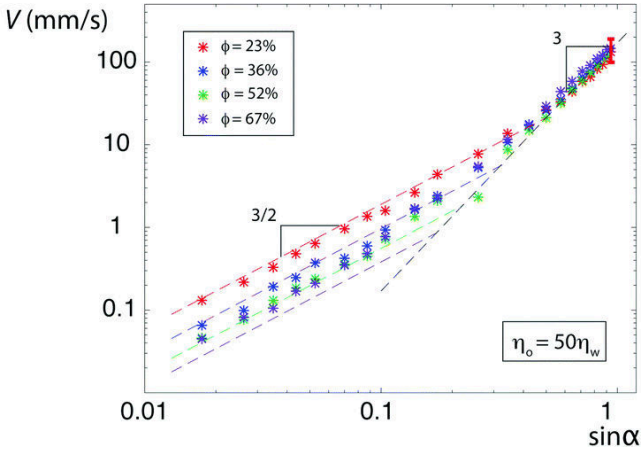

Figure 2.6.6: Viscous dissipation predominantly taking place in the oil[47]. A drop (η_w = 2 mPa·s, Ω = 20 µL) runs down a liquid-infused surface (pillar height h = 20 µm) impregnated with silicone oil whose viscosity greatly exceeds the viscosity of the drop (η_o = 100 mPa·s). At small inclination angles ($\alpha < 30°$), the drop velocity scales with the inclination angle elevated by 3/2, *i.e.* $V \sim sin^{3/2}\alpha$. Furthermore, the drop velocities depend on the pillar density ϕ. Higher pillar densities decrease the velocities. For larger inclination angles (exceeding 30°), the drop velocities scale with the third power of the driving force, *i.e.* $V \sim sin^3\alpha$. Reproduced with permission from Keiser *et al.*[47] Copyright © 2017 The Royal Society of Chemistry.

The measured velocities do not depend linearly on the driving force (Figure 2.6.6). Two different non-linear relationships between drop velocity and driving force are found (Figure 2.6.6) depending on the inclination angle (driving force). The two different non-linear dependencies evidence that the dominant contribution to friction taking place in the oil-phase does not originate from the subjacent film, which would suggest a linear dependence of velocity instead[47].

In the following, viscous dissipation in the meniscus is assessed. For that purpose, a 2D-approach is pursued. Although the oil meniscus is an annular continuum around the deposited drop (section 2.5, Figure 2.5.1b), it is a valid approach to separate the meniscus into two parts, namely, the front and the back meniscus[151]. The deposited aqueous drop is assumed immiscible with the oil. Hence, the front and back menisci consist of two parts each, an advancing, and a receding part (Figure 2.6.7)[47].

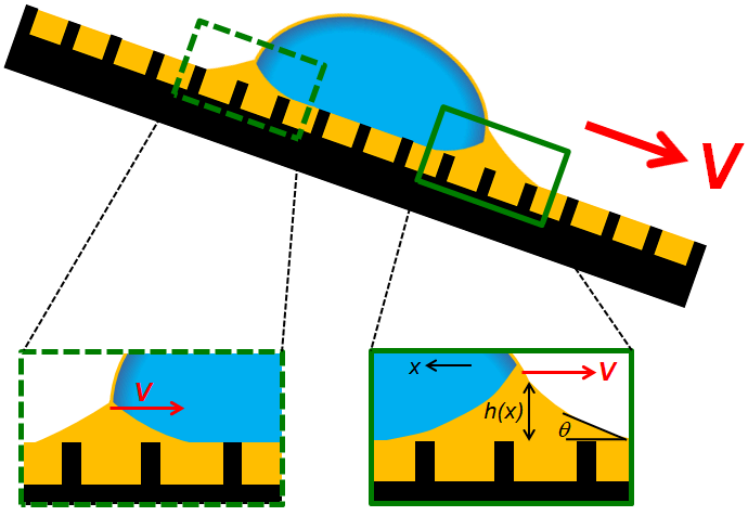

Figure 2.6.7: 2D representation of a 3D annular meniscus consisting of front (solid green box) and back meniscus (dashed green box). The front and back menisci consist of an advancing part and a receding part each[47]. Adapted with permission from Keiser *et al.*[47] Copyright © 2017 The Royal Society of Chemistry.

In the following, we shall characterize the friction in each of these four parts of the meniscus, discussed in more detail elsewhere[47,152]. The meniscus is assumed to be dynamic[47]. It is assumed that the advancing parts of the front and back meniscus are analogous and that likewise, the two receding parts are analogous[47]. In the two advancing parts, dynamic angles are formed, and they increase in value upon increasing velocity[47]. The receding parts of the meniscus deposit a thin film of oil after their passage. Furthermore, it is assumed that the viscous stress deforms the dynamic meniscus, with respect to the equilibrium shape[47].

In the following, a scaling law for the friction force in the advancing part of the front meniscus (Figure 2.6.7, solid green box) of the oil meniscus is derived.

The friction force is the viscous stress integrated over the surface of the meniscus in contact with the substrate, *i.e.* the pillar tops. Only the contributions originating from the displacement of the meniscus on the pillar tops are considered. The oil meniscus wets the oil in-between pillars completely[47]. On pillar tops, a no-slip condition is assumed[47]. Between the pillars, the meniscus slips on the oil film, a condition associated with negligible dissipation, since the characteristic size of the meniscus is in the same range as the characteristic size of the micropillars[47]. In the 2D model, the meniscus successively

displaces on the pillar tops and the oil film. The friction force hence depends on the pillar density[47] ϕ. A velocity gradient *V/h(x)* (Figure 2.6.7) is established within the meniscus[47]. On average, the meniscus is moving at speed V [47].

The friction force F_η is expressed as follows:

$$F_\eta \sim \phi \int_\varepsilon^L \frac{\eta_o V R}{h(x)} dx \qquad (2.6.7)$$

Where the cut-off length ε describes the typical thickness of the oil layer on which the meniscus glides (given by the size of the nanobeads coming from Glaco-treatment ≈ 30 nm), L the characteristic size (= lateral extension) of the meniscus (≈ tens of microns), R the drop size, and *h(x)* the height of the meniscus (Figure 2.6.7)[47].

Assuming small angles θ (Figure 2.6.7), describing the dynamic angle at the front of the meniscus, the height of the meniscus *h(x)* can be approximated (Huh-Scriven approximation[153]) by:

$$h(x) = x \cdot \sin\theta \approx x \cdot \theta \qquad (2.6.8)$$

Hence one obtains for the friction force (equation 2.6.7):

$$F_\eta \sim \phi \int_\varepsilon^L \frac{\eta_o V R}{h(x)} dx \approx \phi \int_\varepsilon^L \frac{\eta_o V R}{x\theta} dx = \frac{\phi \eta_o V R}{\theta} ln\left(\frac{L}{\varepsilon}\right) = \frac{\beta \phi \eta_o V R}{\theta} \qquad (2.6.9)$$

where the logarithmic factor (constant) $\beta = ln(L/\varepsilon) \approx 10$ is accounting for the very weak slip on the pillar tops and the singular dissipation at the front of the meniscus[47]. Without the introduction of the cut-off length ε the friction force F_η would diverge.

In the next step, the dynamic contact angle θ shall be expressed in the form of a scaling law.

The friction force in the advancing part of the front meniscus is destabilizing the oil-water interface. On the other hand, the capillary force (F_c) is opposing this deformation of the interface[47].

The capillary force is expressed in terms of the drop radius (R), the surface tension of the oil (γ_o), and the dynamic angle θ, and reads as[47]:

$$F_c \sim \gamma_o R(1 - \cos\theta) \approx \frac{\gamma_o R \theta^2}{2} \qquad (2.6.10)$$

In the last step, the Taylor approximation for $cos\theta$ has been used, which is justified since only small angles θ are considered[47]. Note that the consideration of small angles θ constitutes an assumption.

The dynamic angle θ can now be rewritten via balancing the friction force in the advancing part of the front meniscus (F_η) with the capillary force (F_c), which yields *Tanner´s Law*[47,154]. We also introduce the capillary number *Ca*, which denotes the ratio of viscous forces to interfacial forces.

$$F_\eta \sim F_c \Leftrightarrow \frac{\beta \phi \eta_o V R}{\theta} \sim \frac{\gamma_o R \theta^2}{2} \xRightarrow{Ca := \frac{\eta_o V}{\gamma_o}} \theta \sim (\phi \beta Ca)^{1/3} \qquad (2.6.11)$$

Tanner´s law implies that the geometry of the meniscus strongly depends on the velocity of the drop. The dynamic angle increases with increasing speed. Within the framework of this thesis, the shape-dependence of the meniscus is investigated and visualized with the help of laser scanning confocal microscopy (Chapter 4).

Substituting Tanner´s law (equation 2.6.11) into the expression for the friction force in the advancing part of the front meniscus (equation 2.6.9) yields[47]:

$$F_\eta \sim \frac{\beta\phi\eta_o VR}{\theta} \sim \gamma_o R(\phi\beta Ca)^{2/3} \qquad (2.6.12)$$

The steady-state drop descending velocity is subsequently obtained by balancing the friction force (equation 2.6.12) with the driving force (equation 2.6.2)[47]:

$$F_\eta \sim F_M \;\Leftrightarrow\; \gamma_o R(\phi\beta Ca)^{2/3} \sim \rho g \Omega \sin\alpha \overset{\Omega\sim R^3}{\Longrightarrow} V = \frac{\gamma_o}{\beta\phi\eta_o}\left(\frac{\rho g R^2}{\gamma_o}\right)^{3/2} sin^{3/2}\alpha \qquad (2.6.13)$$

The 3/2-power-law dependence of the drop velocity on the driving force is contained in this formalism and correctly captured (Figure 2.6.6).

For the advancing part of the back meniscus, the surface tension of the oil (γ_o) has to be replaced by the interfacial tension at the oil-water interface (γ_{ow})[47]. Otherwise, the same formalism applies.

In the following, the friction originating from the receding part of the back meniscus (Figure 2.6.7) is characterized.

It is assumed that the receding parts of the meniscus deposit a thin film of thickness ε upon their passing and behave like in the case of the Landau-Levich (also called Landau-Levich-Derjaguin) experiment (dip-coating, section 2.2), where the menisci connect the vertically retracted plate to the fluid bath[47,49,50]. It is recognized that the viscous stress deforms the meniscus with respect to its static shape[47]. However, it is assumed that the length λ across which the static meniscus is deformed is small compared to the characteristic size (lateral extension) of the meniscus (L)[47], *i.e.* $\lambda << L$.

Analogous to the advancing parts of the meniscus, the capillary forces oppose this deformation[47]. The thickness ε of the deposited film and the length scale λ across which the meniscus is deformed with respect to its static shape is given by the competition between the capillary pressure and the viscous stress in the deformed zone[47]:

$$\frac{\eta \cdot V}{\varepsilon^2} \sim \frac{\gamma}{\lambda \cdot L} \qquad (2.6.14)$$

The term on the left-hand side describes the viscous stress per unit length, and the right-hand side describes the capillary pressure gradient[47].

Furthermore, there is an asymptotic relationship between the curvature of the static meniscus and the curvature of the dynamic meniscus[47]:

$$\frac{\varepsilon}{\lambda^2} \sim \frac{1}{L} \qquad (2.6.15)$$

The left-hand side expresses the curvature of the dynamic meniscus, and the right-hand side expresses the curvature of the static meniscus[47].

With the help of these two relationships (equation 2.6.14 and 2.6.15), it is possible to obtain expressions for the film thickness ε and the length λ across which the meniscus is dynamically deformed due to the viscous stress with respect to its static shape[47].

One obtains:

$$\lambda \sim LCa^{1/3} \qquad (2.6.16)$$

$$\varepsilon \sim LCa^{2/3} \qquad (2.6.17)$$

The scaling behavior of these two quantities relies on the assumption that $\varepsilon << \lambda << L$, which is the case for the small capillary numbers ($Ca < 10^{-3}$) found in the oil, for small inclination angles ($\alpha < 30°$)[47].

The viscous stress integrated over the surface area over which shearing takes place ($\sim \lambda R$) gives the friction force.[47] It is expressed as[47]:

$$F_\eta \sim \frac{\eta_o V}{\varepsilon} \lambda R \qquad (2.6.18)$$

Substituting equations 2.6.16 and 2.6.17 into equation 2.6.18 yields the scaling law for the friction force originating from the receding part of the back meniscus:

$$F_\eta \sim \gamma_o R Ca^{2/3} \qquad (2.6.19)$$

To obtain the scaling law for the receding part of the front meniscus, the surface tension of the oil (γ_o) has to be replaced by the interfacial tension at the oil-water interface (γ_{ow})[47]. The same scaling behavior ($F_\eta \sim Ca^{2/3}$) as for the advancing parts of the meniscus is obtained.

Equating equation 2.6.19 with the driving force (equation 2.6.2) yields the scaling behavior of the drop velocity[47]:

$$F_\eta \sim F_M \;\Leftrightarrow\; \gamma_o R Ca^{2/3} \sim \rho g \Omega \sin\alpha \overset{\Omega \sim R^3}{\Longrightarrow} V = \frac{\gamma_o}{\eta_o}\left(\frac{\rho g R^2}{\gamma_o}\right)^{3/2} sin^{3/2}\alpha \qquad (2.6.20)$$

Note that for the friction originating from the receding parts of the meniscus, there is no dependence on the pillar density. Furthermore, this contribution to the overall friction is reduced compared to the contribution originating from the advancing parts, owed to the absence of the logarithmic factor $\beta \approx 10$, *i.e.* the absence of a singularity[47].

The friction force in the receding parts of the meniscus relies on the dynamic deposition of a thin film[47]. Seiwert *et al.*[48] showed that on rough substrates (microstructured), there is no film thickness below a critical velocity V^* of the drop.

Recently, Keiser *et al.*[155] have investigated the dynamics of bubbles on rough substrates in confinement (textured Hele-Shaw cell). They found that when there is no film deposition (for velocities below the critical velocity V^*), friction in the receding parts of the meniscus is strongly reduced[155] and rendered negligible compared to the contribution to friction originating from the advancing regions of the meniscus[47].

So far, only small inclination angles α (low velocities V) have been considered. At large inclination angles ($\alpha > 30°$), the velocity scales with the third power of the driving force (Figure 2.6.6)[47], *i.e.* $V \sim sin^3\alpha$. Tanner´s law suggests that the Huh-Scriven approximation of a small dynamic contact angle is no longer valid. The friction does not depend on the pillar density ϕ (Figure 2.6.6), which could be explained by a fully dynamical meniscus[47]. The oil constituting the meniscus is constantly extracted from the texture by the surface tension of the drop and reinjected into the texture at a velocity of the

order of the drop velocity V [47]. The meniscus s not given sufficient time to form[47]. In this regime, the dynamic meniscus deposits a thick dynamic film of oil lubricating the drop following the Landau-Levich scaling behavior and thereby erasing the influence of the underlying texture[47].

In summary, when viscous dissipation predominantly takes place in the oil, the drop dynamics are dominated by the behavior of the oil meniscus. By adopting a 2D-representation of the meniscus, the front and back meniscus contain an advancing and receding part each. In total, there are 4 distinct parts of the meniscus[47]. The two advancing parts are characterized by a dynamic contact angle described by Tanner´s law[147,153,154]. The two receding parts deposit an oil film upon their passage across their texture, provided the drops´ velocity exceeds a threshold velocity[47]. The film deposition is described within the framework of the Landau-Levich theory originally developed for the classical experiment of dip-coating[48-50]. For both the advancing and receding regions, the friction force shows the same scaling law, namely a 2/3-power-law dependence on the capillary number in the oil, *i.e.* $F_\eta \sim \gamma_o RCa^{2/3}$. The shape of the wetting ridge depends on the thickness of the lubricant film[156]. The thicker the lubricant film, the larger the wetting ridge[10]. The thickness of the oil film between the drop and the micropillars is essential to understand and influence the friction and dynamics of drops moving on liquid-infused surfaces.

The work of Daniel *et al.*[54] also characterizes friction on liquid-infused surfaces. The experimental setup (Figure 2.6.8) allows measuring the friction force directly[54]. A cantilever is introduced into the deposited drop. The surface underneath the deposited drop is set in motion at speed U. The speed U at which the surface is moving corresponds to the steady-state drop descending velocity (V) in Keiser *et al*[47]. The movement of the surface causes a deflection of the cantilever (spring constant k) holding the drop. The displacement of the cantilever (Δx) allows measuring the friction force (called dissipative forces) F_d directly at a precision estimated to be 0.1 µN with the help of Hooke´s law ($F_d = k \cdot \Delta x$)[54].

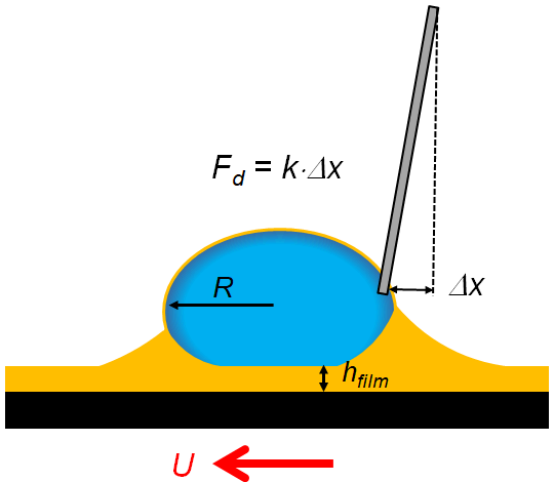

Figure 2.6.8: Experimental setup in Daniel *et al.*[54] Direct measurement of the friction force via the deflection of the cantilever holding the drop on a liquid-infused surface moving at speed U. White-light interferometry is used to assess the thickness of the deposited lubricant film. Adapted with permission from Daniel *et al.*[54] Copyright © 2017 Springer Nature.

At small velocities (U), the setup is very precise. The level of precision in the setup used in Daniel *et al.*[54] is inaccessible with the setup used in Keiser *et al.*[47], owed to the imprecision in the inclination angle of ± 1°. However, at higher velocities U, the drop may detach from the cantilever, making

friction force measurements impossible[54]. At high velocities, the setup used by Keiser *et al.*[47] is more reliable. In Daniel *et al.*[54], white-light interferometry is used to measure the thickness of the deposited film underneath the drop, the *intercalated film* (corresponding to the receding part of the front meniscus in Keiser *et al.*[47], Figure 2.6.7), separating the solid substrate from the deposited drop, under static and dynamic conditions[157-159].

With increasing velocity, the thickness of the lubricant film (h_{film}) is increasing[54]. On flat liquid-infused surfaces, the thickness of the intercalated lubricant film (h_{film}) under a moving drop obeys the Landau-Levich law (h_{LL})[49,50,54], *i.e.*

$$h_{film} = h_{LL} \sim R \cdot Ca^{2/3} \qquad (2.6.21)$$

For substrates equipped with micropillars but otherwise identical surface chemistry, the Landau-Levich law is obeyed, provided the height of the texture features does not exceed the lubricant film thickness predicted by the Landau-Levich law[54]. If the height of the texture features (micropillars) exceeds the thickness of the Landau-Levich film, *i.e.* $h_p > h_{LL}$, the thickness of the lubricant film is determined by the height of the texture features[54], *i.e.* $h_{film} = h_p$.

In the work of Daniel *et al.*[54] the thickness of the lubricant film thickness depends on the height of the micropillars decorating the underlying solid substrate. Hence, there are two different oleoplaning states. In the case of $h_{film} = h_{LL}$ (flat substrates and substrates with $h_p \leq h_{LL}$), the dissipative force increases nonlinearly with the capillary number[54], namely with $F_d \sim Ca^{2/3}$. In contrast, for $h_{film} = h_p$ (textured substrates with texture size exceeding h_{LL}), the dissipative force increases linearly with the capillary number[54], *i.e.* $F_d \sim Ca$.

Hence, in Daniel *et al.*[54], friction forces show two different scaling behaviors in dependence of the height microtexture features. In contrast, in Keiser *et al.*[47], it is postulated that the friction force (for viscous dissipation localized in the oil) of drops moving on liquid-infused surfaces obeys a single scaling behavior only. Within the framework of this thesis, it is aimed at resolving this contradiction (Chapter 4). The influence of the texture feature height is thoroughly investigated. Furthermore, the generality of the observed scaling behavior is tested for additional configurations, including a confined Hele-Shaw cell geometry. It is speculated that new friction behavior might be triggered due to the fact that the size of the drop is reduced due to the confinement[47].

The role of the wetting ridge concerning the mobility of drops on liquid-infused surfaces, in particular, viscous dissipation and contact line pinning at the wetting ridge, has also been investigated for partially wetting lubricants with the help of ternary free-energy lattice-Boltzmann numerical methods[160].

In the simulation work, the lubricant is only partially wetting (including pinning and depinning effects)[160], whereas, in Keiser *et al.*[47], the lubricant is fully wetting the texture (vanishing contact angle). The size of the wetting ridge compared to the size of the drop is larger in the simulation than in the actual experiments[160]. Furthermore, the simulations are in quasi-3D instead of full 3D (experiments)[47,160].

Despite the differences between the simulations and the experiments, there is considerably good agreement between simulation results and experimental data presented by Keiser *et al.*[47]. The regimes of viscous dissipation predominantly occurring within the deposited drop and viscous dissipation predominantly occurring within the wetting ridge are identified and reproduce experimental data[160].

2.7 Lubricant-Depletion on Liquid-Infused Surfaces

On liquid-infused surfaces, the desired non-adhesive and liquid-repellent properties (section 2.3 and 2.6) are based on the presence and stability of chemically compatible lubricant within the porous texture. The durability and functionality of liquid-infused surfaces are impeded and limited due to the loss of lubricant, so-called lubricant-depletion, which degrades the non-adhesive properties of liquid-infused surfaces.

Lubricant-depletion on liquid-infused surfaces has been assessed and quantified using a wide variety of experimental approaches and techniques. Techniques and experimental approaches involving fluorescence intensity[23,161,162], fluorescence macrophotography[97], laser scanning confocal microscopy[163], interference microscopy[164], and white light interferometry[54] are limited to transparent substrates and are diffraction-limited. Other works quantified lubricant-depletion with the help of weight changes[25,34], pressure changes (Figure 2.7.2)[97,98,165,166], or gas chromatography[31].

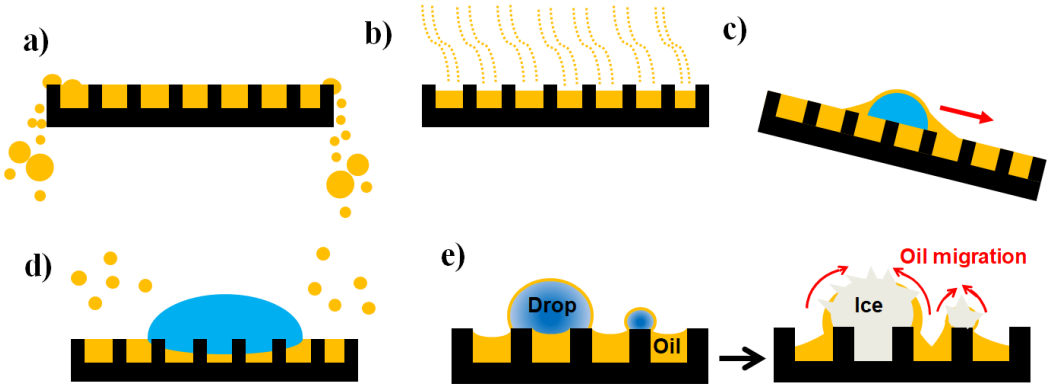

Figure 2.7.1: Mechanisms contributing to lubricant-depletion. a) gravitational drainage – the lubricant flows out of the texture, b) wetting ridge and cloaking layer shedding lubricant-drops from the surface, c) evaporation, d) drop impact, e) frost growth via drop condensation and frosting[85] (adapted with permission from Rykaczewski *et al.*[85] Copyright © 2013, American Chemical Society).

In addition to mechanical damage to the texture, gravitational drainage of the lubricant (Figure 2.7.1a)[162,167], solubilizing of the lubricant, contact with other absorbing material[66,168], and evaporation (Figure 2.7.1b)[31 169], lead to progressive loss of lubricant from the infused textured surface. The wetting ridge (and cloaking) can significantly contribute to lubricant depletion as a drop is shed from an inclined infused surface[55] (Figure 2.7.1c). As the drops depart the surface, the lubricant is taken along and lost to the surface. Drops moving with a high capillary number deplete less lubricant than slow-moving drops on less viscous lubricants[55]. Drops moving across the surface with a higher driving force (*e.g.* gravity on inclined liquid-infused surfaces) and correspondingly higher shear rates deplete less lubricant than slower-moving drops[55]. Impacting drops (Figure 2.7.1d) can displace the lubricant contributing to lubricant-depletion given sufficiently strong impact conditions[170,171]. Lubricant can also be lost due to frosting (Figure 2.7.1e)[38,85] because lubricant impregnates the porous ice. The extent of water penetration and lubricant-depletion depends on the degree of overfilling of the texture and the dimensions of the substrate[84,85].

In addition to the mechanisms mentioned above (Figure 2.7.1), flow conditions due to external shear flows imposing shear stresses onto the lubricant-film are a challenge. In a naïve picture, it is expected

that the capillary forces are keeping the lubricant stable within the texture. However, when liquid-infused surfaces are immersed in a dynamic fluid environment, such as wind or working fluids (immiscible with the lubricant) flowing across the infused texture, exerted shear forces on liquid-infused surfaces lead to shear-induced lubricant-depletion[97,98,161,163,166] on portions of the liquid-infused surface, owed to the continuity in interfacial velocities and stresses. The working fluid penetrates the textures and displaces and, therefore, removes the lubricant from the infused texture. Displaced lubricant may also overflow the textured surface[163].

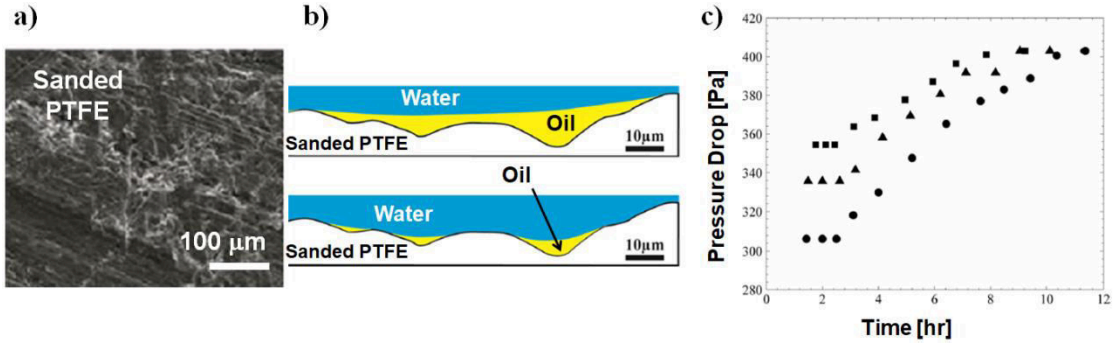

Figure 2.7.2: a) Sanded PTFE-sample subsequently infused with lubricant establishing a liquid-infused surface (in a microchannel)[166]. b) Sketch of lubricant-depletion on sanded infused PTFE-samples[166]. c) Quantification of lubricant-depletion on infused sanded PTFE-samples with the help of pressure drop measurements (squares: root mean square (RMS) roughness 15.4 µm, circles: RMS roughness 13.7 µm, triangles: RMS roughness 10.9 µm, flow velocity: 0.4 mm/s, capillary number $Ca = 10^{-3}$)[166]. Adapted with permission from Kim and Rothstein[166] Copyright © 2016, Springer Nature.

In general, rough texture can withhold more lubricant than smooth surfaces under shear flow conditions[161]. Although liquid-infused surfaces suffer from lubricant-depletion due to shear conditions, they can remain stable over a certain fraction of their infused length parallel to the flow of the working fluid[97,98]. The portion of the length of the texture remaining lubricated is defined as the so-called *steady-state length* (L_∞)[97,98]. It is the characteristic length scale of drainage and lubricant retention[97].

In the following, it is explained how such a finite length of the infused texture, *i.e.* the steady-state length, remains infused with lubricant under persistent shear flow conditions.

Surfaces consisting of epoxy-based micro-fabricated grooves[97,98,162,163] on silicon wafers oriented towards the flow direction (streamwise) of the working fluid were contained in a microfluidic flow cell containing a reservoir of lubricant[97]. The infused surfaces were subjected to an aqueous flow (of flow rate Q) imposing a shear stress[97] τ_{yx} (Figure 2.7.3a). The shear stress τ_{yx} is given by:

$$\tau_{yx} = \frac{6\mu_{aq}Q}{WH^2} \qquad (2.7.1)$$

where H denotes the height of the flow cell, W the width of the flow cell, and μ_{aq} the viscosity of the aqueous working fluid[97].

It is assumed that the flow profile is uniform (in width) and parabolic (in depth)[97]. The viscosity of oil significantly exceeds the viscosity of the aqueous phase ($\mu_o >> \mu_w$)[97]. Hence, the shear stress imposed is not changed by the oil[97]. Furthermore, it is assumed that gravity and inertial effects are negligible[97].

Fluorescence Macrophotography evidenced and followed the drainage of the oil-phase[97]. Oil depletion initiated at the upstream portions of the flow channel and progressed downstream under the influence of the imposed shear stress[97]. The propagation of the dewetting front is initially taking place rapidly, but eventually slows down and comes to a halt at a steady-state position (Figure 2.7.3b)[97]. The distance between the lubricant-reservoir (downstream and in close vicinity to the outlet of the flow cell) and the steady-state position of the dewetting front corresponds to the steady-state length[97] L_∞. Along the steady-state length, the lubricant is retained inside the grooves[97]. The length of the surface or the length along which the surface is infused (length of the flow channel containing the infused surface L) with lubricant in general greatly exceeds the steady-state length, *i.e.* $L_\infty << L$.

Laser scanning confocal microscopy observations reveal that the oil-aqueous interface is curved inwards in the cross-sectional planes perpendicular to the flow direction (yz-plane, Figure 2.7.3c)[97]. The interfacial deflection δ (measured in the center of the groove, laser scanning confocal micrographs presented on the right-hand side of Figure 2.7.3c) is largest at the dewetting front and decreases linearly with the distance along the channel in the downstream direction ($\delta(x) \sim x$)[97]. The radius of curvature is smallest at the onset of the steady-state length (r_{min} at the dewetting front, Figure 2.7.3c) and increases in the downstream direction, eventually reaching infinity at the oil reservoir close to the outlet (Figure 2.7.3c, there, the oil-water interface is assumed to be flat)[97]. The steady-state length is much longer than the width and height of the grooves. Hence, the cross-sectional curvatures of the oil phase dominate the curvature in the streamwise direction[97]. Therefore, the pressure within the oil-phase increases in the downstream direction[97]. This pressure gradient counteracts external shear stress. It is thereby responsible for the establishment of a steady-state length along which oil is retained within the grooves by driving oil recirculation in the upstream direction[97]. The downstream flux of oil is driven by the imposed shear stress due to the flow of the aqueous phase[97]. The upstream flux of oil is driven by the pressure gradient based on varying curvatures of the oil-water interface[97]. In other words, the shear stress imposed by the external flow is counteracted by a Laplace-pressure gradient (capillary pressure gradient) originating from deformations of the fluid-fluid interface[97].

The quantitative model explaining the lubricant-retention along the steady-state length L_∞ is based on the volume-conservation equation for the flux of oil out of the grooves[97]. The steady-state length L_∞ is given by[97]:

$$L_\infty = \left(\frac{c_p h}{c_s r_{min}}\right)\frac{\gamma}{\tau_{yx}} \qquad (2.7.2)$$

Here c_p, c_s are hydrodynamic resistance constants depending on the aspect ratio of the grooves. The height of the grooves is denoted by h, and the interfacial tension between the oil and the aqueous phase is given by γ.

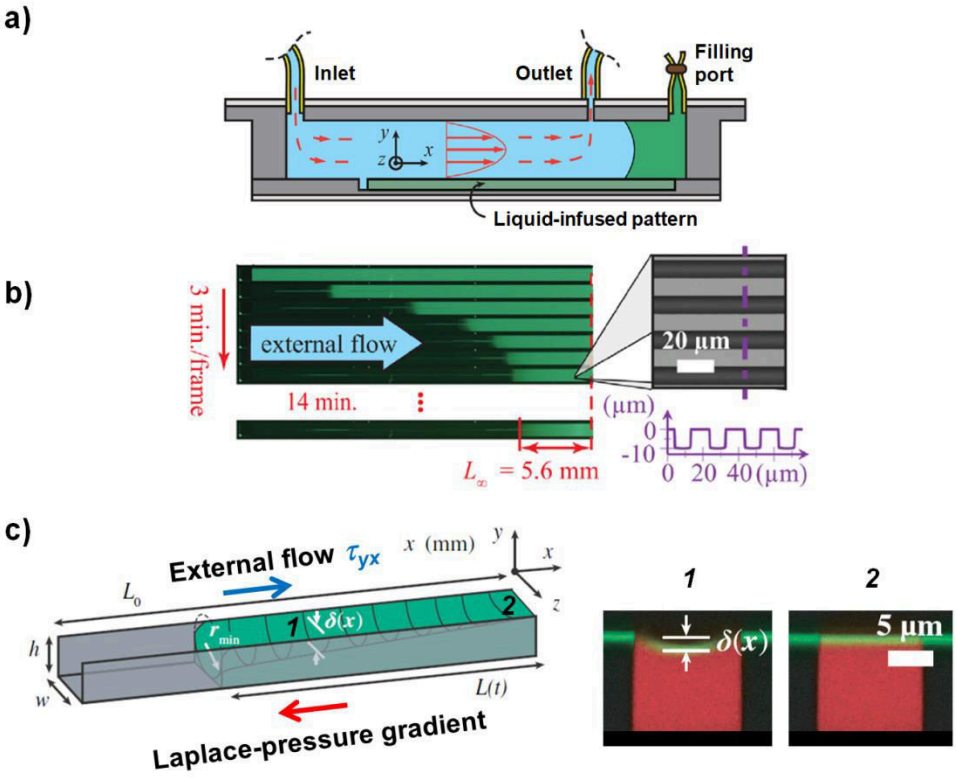

Figure 2.7.3: The establishment of a *steady-state length* L_∞ across which lubrication remains intact despite the persistence of shear flows. a) Cross-section (*xy*-plane) of a microfluidic flow cell at the beginning of the experiment (modified with permission after Wexler, Jacobi, and Stone[97] Copyright © 2015 American Physical Society). The aqueous working fluid (blue) flows from left to right. The grooves are filled with oil (green). The oil within the grooves is connected to an oil reservoir close to the outlet of the flow cell. b) Time-evolution of shear-driven drainage experiment (volumetric flow rate Q = 2 mL/min, shear stress τ_{yx} = 5.2 Pa) showing lubricant-depletion and the establishment of a steady state in which lubricant is retained across the steady-state length (L_∞)[97]. Micrograph (top view, *xz*-plane) and profile (*yz*-plane) of grooves on the right (reproduced with permission after Wexler, Jacobi, and Stone[97] Copyright © 2015 American Physical Society). c) Schematic of one groove, showing the geometric parameters and the shape of the interface (laser scanning confocal micrographs on the right-hand side), modified with permission after Wexler, Jacobi, and Stone[97] Copyright © 2015 American Physical Society.

The steady-state length does not depend on the viscosity of the impregnating oil (equation 2.7.2)[97]. The narrower and deeper the grooves are, the larger the steady-state length is[97]

The establishment of a steady-state length has also been observed on liquid-infused surfaces consisting of randomly arranged micropillars[97]. Furthermore, the steady-state length can be tuned via the addition of surfactant due to Marangoni stresses assisting in counteracting the shear stress imposed by the flow of the working fluid[163].

In a refined model introducing slip at the fluid-fluid interface which induces a slip-driven flow at the interface, the influence of the viscosity ratio of the viscosity of the working fluid (μ_w) to the viscosity of the lubricating oil (μ_o), *i.e.* $N = \mu_w/\mu_o$, has been investigated[98,166]. So far, the considerations presented above were limited to the extreme case of $N << 1$. Large viscosity ratios N delay the depletion of lubricant[166]. For a given viscosity ratio N the steady-state length L_∞ is inversely proportional to the flow rate Q[98]. For a constant oil viscosity μ_o and constant flow rate Q, the steady-

state length L_∞ increases for decreasing viscosity ratios N[98]. Less viscous working fluids lead to less lubricant-depletion and less drainage due to lower applied shear stresses[98].

The establishment of a Laplace-pressure gradient counteracting shear-induced drainage and driving a backflow of oil (thereby establishing a steady-state length L_∞) relies on the presence of a reservoir of excess lubricant at the terminus of the flow cell. It remains to investigate drainage behavior in the absence of a lubricant-reservoir.

Placing non-wettable zones by chemical patterning (spray-coating, UV-exposure) onto solid substrates periodically separated by the distance smaller or equal to steady-state length for given flow conditions can improve lubricant-retention under shear conditions (Figure 2.7.4)[162]. These portions acting as sacrificial zones are preferentially wetted by the working. Hence, they remain free of lubricant. The continuous nature of the impregnated lubricant is broken by these patches. The lubricant is still displaced by the working fluid. However, it does not leave the surface; since it accumulates at the edges of the non-wettable zones[162].

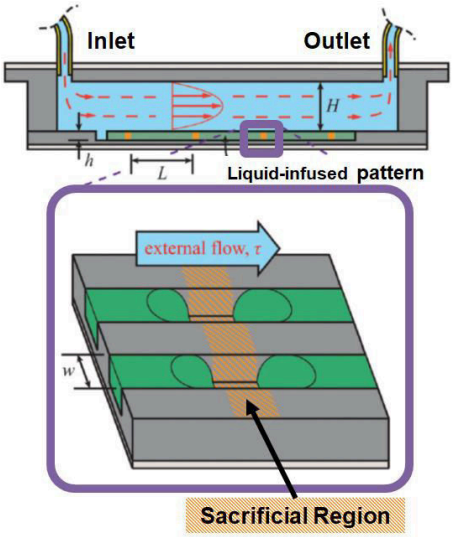

Figure 2.7.4: Sacrificial regions preferentially wetted by the working fluid separated by a periodicity smaller or equal to the steady-state length L_∞ reduce lubricant-depletion[162]. Modified with permission after Wexler *et al.*[162] Copyright © 2015 The Royal Society of Chemistry.

The disadvantage is that the sacrificial regions will not show the favorable non-adhesive properties normally associated with liquid-infused surfaces. These sacrificial regions might act as pinning sites or suffer from biofouling. Furthermore, it is questionable if lubricant-depletion will still not occur if the time horizon significantly exceeds the time scales of tens of minutes considered in these works[97,162].

In addition to delaying lubricant-depletion with the help of sacrificial zones (Figure 2.7.4), or tuning the viscosity ratio and geometry of the texture (aspect ratio), lubricant-depletion can also be delayed with the help of built-in lubricant-reservoirs (section 2.8).

2.8 Lubricant-Replenishment on Liquid-Infused Surfaces

Lubricant-replenishment summarizes the endeavors to (re-)supply a texture with lubricant to re-establish lubrication and a fully functional liquid-infused surface with its desired non-adhesive and liquid-repellent properties. It is often encountered in the literature that lubricant-replenishment is not clearly distinguished from delaying lubricant-depletion (section 2.7).

Delaying lubricant-depletion relying on lubricant reservoirs present within the structure is a strategy often pursued. Substrates having a self-similar structure, such as infused mesoporous alumina composites[19,20], infused inverse opal scaffolds[9,10], or infused fibrous networks[2], remain lubricated upon damage inflicted to the top layers of the surface. Hence, they are self-replenishing owed to their self-healing capabilities. Polymeric matrices can be swollen in the lubricant (Figure 2.8.1)[13,17,35,39,41,66,172,173].

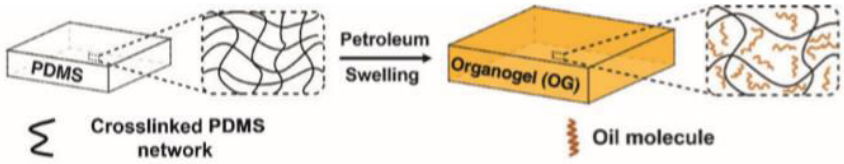

Figure 2.8.1: Crosslinked polydimethylsiloxane (PDMS)-matrix swollen in petroleum. The lubricant (petroleum) is established by the diffusion of petroleum molecules into the polymer matrix (Reproduced with permission from Yao *et al.*[65] © 2015 The Authors. Published by Wiley-VCH Verlag GmbH & Co. KGaA (open access article under the terms of the Creative Commons Attribution Non-Commercial License).

The lubricant reservoir can also consist of shell-less lubricant drops stored inside a gel-matrix[64,168,174]. Organogel- or hydrogel-based systems, such as systems based on crosslinked poly(dimethylsiloxane) (PDMS) or other crosslinked elastomers, with the ability to release lubricant due to a variety of stimuli, have been proposed[67,175-177]. Rough polymer coatings, prepared by a solution casting method, which can release lubricant, have been developed[64,174]. Lubricating oil is stored in discrete drops distributed within the texture consisting of a supramolecular polymer matrix based on urea-PDMS copolymers[174]. These coatings show mechano-responsiveness and release lubricant upon mechanical loading (local pressing by 50kPa)[174], mimicking the secretion behavior of earthworms (epidermal glands), enabling them to move through the soil (Figure 2.8.2). It is expected that lubricant-replenishment in response to stimuli is more effective than relying on lubricant-reservoirs, which are not responsive to stimuli.

All approaches relying on the presence of a built-in lubricant reservoir have in common that there is only a finite and limited amount of lubricant present in such a reservoir, which, in general, cannot be replenished *in-situ*. The favorable properties of liquid-infused surfaces are only maintained for as long as the stock of lubricant lasts.

Within the framework of this thesis, lubricant-depletion is investigated quantitatively on a liquid-infused surface consisting of a swollen hydrogel-coating covalently attached to a micropillar array (Chapter 5). The swollen hydrogel is subjected to a shear flow of neat oil. It is assessed to which degree the surface remains lubricated despite persistent shear flows.

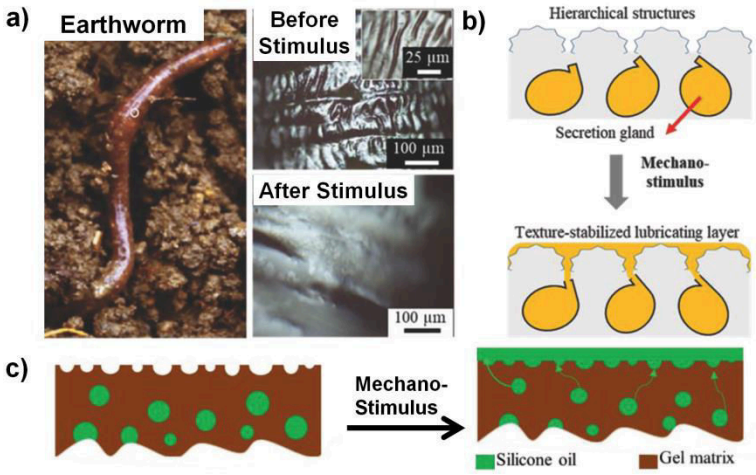

Figure 2.8.2: Mechano-responsive urea-PDMS-based liquid-infused surface mimicking epidermal glands of earthworms[174]. a) The secretion behavior under extra stimulation: live earthworm moving out from moist soil (left); image of earthworm's skin before (upper right) and after mechano-stimulus (lower right); b) Schematic for earthworm surface texture and secretion mechanism[174]. c) Schematic of the stimuli-responsive release of the gel film[174]. Adapted with permission from Zhao *et al.*[174] © 2018 WILEY-VCH Verlag GmbH & Co. KGaA, Weinheim.

The aqueous lubricant of the carnivorous *Nepenthes* pitcher plant´s peristome[4-6] (section 2.1, Figure 2.1.3) is replenished by rain (and ambient humidity) and/or nectaries (glands). The lubricated peristome of the pitcher plant is self-replenishing.

Succeeding in replenishing lubricant without relying on built-in lubricant-reservoirs on porous substrates with roughness features on the micron-scale employed by humankind rely on expensive energy- and time-consuming (hemiwicking, section 2.2) and potentially environmentally hazardous procedures, such as spraying (Figure 2.8.3a) or soaking in baths of lubricant (Figure 2.8.3b). A lubricant bath requires excessive and unsustainable quantities of lubricant. The amounts of lubricant needed to establish liquid-infused surfaces are typically limited. Still, the bath dimensions need to be excessively large, given the dimensions of the surface features that need to be covered with lubricant. Spraying has an effect similar to rain when lubricating the peristome of the pitcher plant. Disadvantages of spraying include the health hazards posed by aerosols[178,179]. Build-in lubricant reservoirs are more sustainable than lubricant baths or spraying.

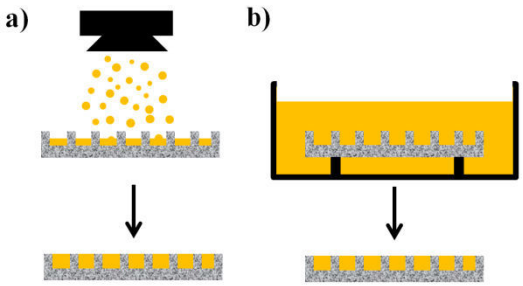

Figure 2.8.3: a) Lubricating the porous substrate with the help of spraying the lubricant onto the texture. b) Impregnating the substrate with the help of a lubricant bath.

Improved and accelerated internal lubricant distribution can be achieved with the help of internal fluidic networks, *i.e.*microchannels[168]. Internal fluidic networks can be established either via drilling internal lubricant distribution channels into the substrate material[168] or via utilizing vascularization methods[31,180]. Lubricant distribution channels can be placed underneath the porous substrate used to establish the liquid-infused surface[168]. Encased networks are an example of a vascularization method; they can be created using 3D molds[31]. Direct embedding of networks can also serve as a vascularization network[180]. Subsequent infusion of the encased or embedded network establishes the liquid-infused surface. However, the time scales required to facilitate lubrication are not specified. It is speculated that they are considerable since they rely on capillarity and diffusion.

Independent of the presence or absence of internal fluidic networks to aid the distribution of lubricant and their level of sophistication, all presented approaches for lubricant-replenishment (except lubricant bath and spraying) rely on a lubricant reservoir present underneath (or in close vicinity to) the surface of the liquid-infused surface. Capillarity (hemiwicking, section 2.4) and diffusion are needed to assist in the replenishment of lubricant, making lubrication potentially slow. If such a lubricant reservoir is absent, no lubricant-replenishment can be accomplished. Within the framework of this thesis, a novel strategy of lubricant-replenishment, which does neither rely on a lubricant-reservoir within the structure nor relies on capillarity or diffusion, is devised (Chapter 6).

2.9 Summary, Contributions of the Author, and Outlook

Despite the abundance of literature on the topics involving liquid-infused surfaces, many unanswered questions and challenges remain. The character of the thesis is to advance human knowledge on liquid-infused surfaces on multiple fronts. This thesis aims at extending this body of knowledge on some of the aspects concerning liquid-infused surfaces, namely fabrication of liquid-infused surfaces, drop mobility on liquid-infused surfaces, lubricant-depletion, and lubricant-replenishment (Figure 2.5.1).

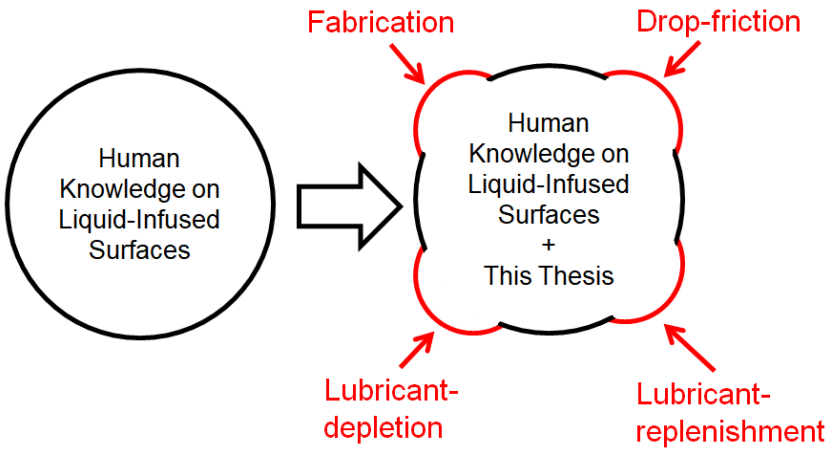

Figure 2.5.1: Aim of the thesis. The circle on the left-hand side of the chart symbolizes the body of human knowledge on liquid-infused surfaces. A successful thesis will hopefully extend the body of knowledge on liquid-infused surfaces in the way suggested on the right-hand side of the chart.

In particular, the four parts of the thesis are addressing the following unanswered questions:

- How can transparent liquid-like surfaces, a sub-class of liquid-infused surfaces, be produced at room temperature in an environmentally friendly way without the use of solvents and the formation of potentially hazardous by-products? What are their characteristics and performance (Chapter 3)?

- Is there a universal scaling behavior of the friction of drops on liquid-infused surfaces (Chapter 4)? The mobility of drops placed on liquid-infused surfaces is the basis of most applications of liquid-infused surfaces. However, the interaction of a drop with a liquid-infused surface is not fully understood yet, also because a consistent formalism describing drop friction on liquid-infused surfaces has not been developed yet.

- How does lubricant-depletion progress and can be quantified on liquid-infused surfaces consisting of a solid texture coated and covered with a swollen hydrogel when subjected to continuous flows of oil (Chapter 5)? Liquid-infused surfaces whose lubricant is water are less understood than their more conventional counterpart lubricated with (nonvolatile) oil despite their occurrence in nature (not limited to the *Nepenthes* pitcher plant) and their potential in tissue engineering or related fields due to the improved biocompatibility. Furthermore, this part of the thesis constitutes an approach, which combines gels and a rough texture.

- How can lubricant-replenishment be facilitated *in-situ* based on the flow of oil-in-water emulsions (Chapter 6)? Lubricant-replenishment strategies are limited to *ex-situ* methods, such as lubricant baths and spraying, or built-in lubricant-reservoirs. Once a reservoir is drained, the lubricant has to be replenished *ex-situ*, which means additional working steps and efforts owed to removing the liquid-infused surface from its site of action and subsequent lubricant-replenishment. Using flow conditions to overcome shear-induced depletion constitutes an entirely novel concept to facilitate lubricant-replenishment *in-situ*. So far, a conceptual understanding and realization are missing.

The first question does only concern the liquid-infused surface itself. The second question addresses the interaction and phenomena of single discrete drops with liquid-infused surfaces. The remaining questions address continuums of fluids (dynamic fluid environment) in contact with liquid-infused surfaces. The second to last question concerns neat oil. The last question concerns oil-in-water emulsions.

The primary experimental tool utilized in this dissertation was laser scanning confocal microscopy (LSCM).

In the following, the results obtained in each part of the thesis are summarized. The contributions of the author of this thesis are explained in detail.

In the **first part of the thesis**, the author aims at contributing to the fabrication of environmentally safe and sustainable liquid-like surfaces, sub-class of liquid-infused surfaces. The preparation is based on the spontaneous and stable bonding of methyl-terminated polydimethylsiloxane (PDMS) to glass and other surfaces, offering silicon oxide surface chemistry. The bonding takes place at room temperature. The excessive use of environmentally hazardous and toxic solvents, as well as the formation of potentially hazardous by-products, can be avoided. In particular, the lubrication of the surfaces does not require additional infusion steps, unlike more conventional approaches to prepare liquid-infused surfaces, whose preparation, in general, requires a two-step procedure consisting of the fabrication of the solid substrate followed by the infusion of lubricant. The cleaning procedure followed after the grafting step determines the extent of the lubrication of the surface. Extensive characterization of the resulting transparent and nm-thick liquid-infused surfaces is performed. The potential for industrial and technological applicability is assessed. It is found this 2-5 nm thick coating is transparent and that it successfully repels ice, super glue, polar, and non-polar liquids. The reaction between the PDMS and the material with silicon oxide surface chemistry is based on the hydrolysis of the siloxane bonds of PDMS via nucleophilic attack of the oxygen contained in ambient water.

This work has been submitted and is currently *in revision*:

Teisala, H., **Baumli, P.**, Weber, S. A. L., Butt, H.-J., Vollmer, D., Grafting silicone films on glass at room temperature, *Langmuir*, *in revision* (ID la-2019-032236).

The **contributions of the author** of the thesis are as follows:

The author of this thesis is a **co-author** of this work. The author of the thesis assisted the first author Dr. H. Teisala in the preparation of the sample surfaces and the preparation of figures (photography). Furthermore, the author of the thesis designed, performed, and elaborated the X-ray Photoelectron Spectroscopy study of the sample surfaces. Professor S. A. L. Weber performed the atomic force microscopy (AFM) measurements. The responsibility of the overall supervision of the work lay with Professor H.-J. Butt and Professor D. Vollmer.

The **second part of the thesis** deals with the mobility and friction of drops (immiscible with the infused lubricant) deposited on liquid-infused surfaces. Concerning the friction laws of drops on liquid-infused surfaces, the crucial role of the meniscus (wetting ridge) under conditions when friction predominantly takes place in the oil-phase has already been elucidated (section 2.6). However, the works of Keiser *et al.*[47] and Daniel *et al.*[54], although both works make use of the Landau-Levich formalism, have, in part, reached different conclusions. So far, it is unclear whether there is a universal scaling law describing drop friction on liquid-infused surfaces and how it could accurately capture and describe experimental findings. In the work of Daniel *et al.*[54], it is postulated that the friction force (called dissipative force F_d in that work) acting on drops scales linearly with the capillary number ($F_d \sim Ca$) on liquid-infused surfaces equipped with tall micropillars (several tens of μm, exceeding the film thickness predicted by the Landau-Levich law), a situation in which Landau-Levich films are absent[54]. In contrast, on liquid-infused surfaces equipped with short micropillars (several μm), Landau-Levich films are present, and the friction force scales with the power 2/3 of the capillary number ($F_d \sim Ca^{2/3}$) leading to a thickness of the oil film in agreement with the Landau-Levich law[54]. In contrast, the work of Keiser *et al.*[47] postulates that the friction force F_η is scaling with the power 2/3 of the capillary number ($F_\eta \sim Ca^{2/3}$) in the event of friction predominantly taking place in the oil-phase. In this part of the thesis, these conflicting results are reconciled. For that purpose, the configuration of a drop moving on a liquid-infused surface is separated into six different dynamic regions. The wetting ridge (also called meniscus or oil foot) is considered in a 2D-picture and is separated into a front and back meniscus. The front and back menisci are further separated into an advancing and receding part each. The advancing parts of the front and back menisci are considered equivalent. Likewise, the receding parts of the front and back menisci are considered equivalent. The remaining two dynamical regions are the drop and the lubricant film underneath the drop[181]. The role of the height of the micropillar features is elucidated. It is found that the velocity of a drop descending on a liquid-infused surface shows the same scaling behavior independent of the micropillar height. Only the prefactors depend on the height of the micropillars owed to the presence (short micropillars) or absence (tall micropillars) of Landau-Levich films[181]. In Keiser *et al.*[47], the Landau-Levich framework only concerns the receding parts of the wetting ridge. In contrast, the advancing parts are modeled, relying on the assumption of a dynamic contact angle described by Tanner´s law[47]. The dynamic nature of the advancing parts of the meniscus, in particular of the front meniscus, is investigated and confirmed with the help of laser scanning confocal microscopy. It is found that the friction force F_η of drops on liquid-infused surfaces does indeed scale universally with the power of 2/3 of the capillary number ($F_\eta \sim Ca^{2/3}$) on both short and tall micropillars. The author and his close collaborator (Dr. Armelle Keiser, ESPCI Paris and EPFL) tested the generality of this result for two additional configurations. Drops confined in Hele-Shaw cells consisting of two liquid-infused surfaces facing each other and bubbles rising on an inclined liquid-infused surface contained in a water bath (inverting the roles of water and air) display the same scaling behavior.

This work has been published:

Keiser, A.[†], **Baumli, P.[†],** Vollmer, D., Quéré, D., Universality of the friction laws on liquid-infused materials, *Phys. Rev. Fluids*, **2020**, 5, 014005.

The **contributions of the author** of the thesis are as follows:

The author of the thesis is the second **co-first author** of this work. He designed, performed, and elaborated the experiments involving drops confined in Hele-Shaw cells, including the development of a method to obtain transparent surfaces and building the experimental setup. The author of the thesis carried out a systematic study on the influence of different parameters across wide parameter spaces

based on scaling laws developed and presented in an earlier work by Dr. A. Keiser and compared the results obtained for drops in Hele-Shaw cells with the results published in Keiser *et al*[47]. Furthermore, the author investigated and visualized the shape of the dynamic meniscus (advancing part of the front meniscus in the 2D-representation of the meniscus) at different velocities with the help of laser scanning microscopy (supported by A. Naga and Dr. A. Kaltbeitzel) confirming the validity of the model (assuming a dynamic nature of the meniscus) based on which drop friction on liquid-infused surfaces is explained in this work and the earlier work of Keiser *et al*[47]. The author of the thesis and Dr. A. Keiser wrote the draft version of the manuscript. The author has been involved in the entire process of writing and revising the manuscript. The responsibility of the overall supervision of the work lay with Professor D. Vollmer and Professor D. Quéré (ESPCI Paris).

The **third part of the thesis** combines aspects concerning the fabrication/preparation of liquid-infused surfaces and lubricant-depletion. Most of the literature presented on the topic of lubricant-depletion concerns oil-based liquid-infused surfaces (section 2.7). The potential of hydrogel-bound water to act as a lubricant on liquid-infused surfaces is interesting for applications encountering biological tissue or living systems. In this work, the well-established (in the field of liquid-infused surfaces) roles of water and oil are reversed. To the best of the knowledge of the author of this thesis, this situation has only received little attention in the literature. In this project, the lubricant is water, and it is held in place with the help of a hydrogel-coating covalently attached to the micropillar array. Two different kinds of hydrogels are utilized in this work, namely, the temperature –sensitive Poly(N-isopropylacrylamide) (PNIPAm) and the weak polyelectrolyte Poly(acrylic acid) (PAA). The swollen hydrogel-coating is then subjected to a shear-flow of neat oil. The influence of varying flow velocities, oil viscosities have been investigated for the two different hydrogel-coatings. The lubricant-depletion (the loss of water) is monitored with the help of laser scanning confocal microscopy. Advanced image processing reveals that depletion progresses linearly within the whole range of parameters investigated. The diffusion of water into the oil (not water-saturated) is the basis for the observed depletion kinetics, which is modeled with the help of an extended diffusion model. The control experiment involving a shear flow of water-saturated silicone oil across the swollen hydrogel-coating confirmed the hypothesis.

This work is close to submission:

Baumli, P.[†], Lorusso, E.[†] , Hauer, L.[†], Sharifi-Aghili, A., Hegner, K., D´Acunzi, M., Gutmann, J., Dünweg, B., Vollmer, D.*, Depleting Hydrogels with Oil Flows, *in preparation*.

The **contributions of the author** of the thesis are as follows:

The author of the thesis is the first **co-first author** of this work. He teamed up with other researchers (Lukas Hauer, Max Planck Institute for Polymer Research, and Emanuela Lorusso, Deutsches Textilforschungszentrum Nord-West Öffentliche Prüfstelle GmbH (DTNW), Krefeld, Germany). The method to prepare hydrogel-coatings on micropillar arrays has been developed by the second co-first author E. Lorusso (under the guidance and supervision of Dr. M. d´Acunzi). The micropillar arrays have been prepared by A. Sharifi-Aghili and K. Hegner. The author of the thesis designed and carried out the depletion experiments relying on laser scanning confocal microscopy. The modifications to the flow cells necessary to successfully perform the depletion experiments were realized by the author. The systematic assessment of the depletion behavior in terms of the influence of oil viscosity, flow velocity, and nature of the hydrogel-coating was performed by the author. The third co-first author L. Hauer assisted the author of the thesis in image processing and developed the extended diffusion model. The author of the thesis wrote the draft version of the manuscript and prepared the figures. The author has been involved and coordinated the entire process of writing and revising the manuscript.

The responsibility of the overall supervision of the work lay with Professor J. Gutmann (DTNW), Professor B. Dünweg, and Professor D. Vollmer.

The **fourth and last part of this thesis** concerns lubricant-replenishment on liquid-infused surfaces. To the best knowledge of the author, it is the first approach published in the literature that does not rely on built-in lubricant-reservoirs or unsustainable lubricant baths or spraying (section 2.8). A strategy to facilitate lubricant-replenishment based on the flow of oil-in-water emulsions across a chemically compatible porous texture is devised. The starting point is a hydrophobic porous texture contained in a water-filled microfluidic flow cell. The starting situation represents the worst-case scenario of a liquid-infused surface completely devoid of lubricant. The charge repulsion between the negatively charged oil drops contained in the emulsion is overcome via the addition of the positively charged surfactant CTAB (cetyltrimethylammonium bromide) at concentrations in a narrow range (500 – 1000 µg/L) around the point of charge reversal (*pcr*) corresponding to approximately 0.14 % of the critical micelle concentration (CMC). Overcoming the charge repulsion enables the coalescence of oil drops. As the flow of the emulsion across the texture is started, oil drops attach to the top portions of micropillars in a systematic way and predominantly in the flow direction. The oil drops attached to the micropillars subsequently grow in size due to the coalescence with newly arriving oil drops. A micropillar can repeatedly accommodate (multiple) drops. Since oil drops also attach and spread on the bottom substrate, the growing oil drops attached to the top portions of the micropillars eventually coalesce with this oil film on the bottom substrate and descend to the bottom substrate, filling the interstitial spaces in-between micropillars. Gravity is not responsible for that process (length scales below the capillary length). The water contained in-between the micropillars is gradually replaced by oil. The flow conditions established facilitate fast transport (faster than hemiwicking presented in section 2.2 and diffusion) of lubricant directly to the porous substrate. Above a threshold velocity, lubricant-depletion induced by shear flows is always dominated by flow-induced filling of the texture with oil. The filling of the porous substrate initially devoid of any lubricant is observed and quantified with the help of laser scanning confocal microscopy. Oil and water are fluorescently labeled. The drops keep their spherical shape during the growth at the pillar tops. The approach works for a wide variety of solid-liquid combinations. The filling process has been demonstrated for silicone oil (PDMS, viscosities ranging from 5 – 500 cSt), Poly-α-Olefin (PAO), Krytox® 103, and FC-70. The solid texture has to be hydrophobic (standard case is the Chemical Vapor Deposition of octadecyltrichlorosilane, OTS), but for successful filling, it is extraneous whether the texture is "just" hydrophobic, or whether it is fluorinated, or superhydrophobic. With the choice of the topography of the textured substrate, there is ample flexibility. Successful filling of the texture with oil has been demonstrated for smooth hydrophobic surfaces, micropillar arrays with different geometries and nanofilament-coatings. Based on the models quantifying lubricant-depletion on grooves surfaces developed by the group of Howard Stone (Princeton University), the stability of the established liquid-infused surface under flow conditions is assessed[97,163]. We find that the filling rate can exceed the shear-induced depletion rate by almost two orders of magnitude.

This work has been published:

Baumli, P.[†], Teisala, H.[†], Bauer, H., Garcia-Gonzalez, D., Damle, V., Geyer, F., D'Acunzi, M., Kaltbeitzel, A., Butt, H.-J., Vollmer, D., Flow-Induced Long-Term Stable Slippery Surfaces. *Adv. Sci.* 2019, 6, 1900019. https://doi.org/10.1002/advs.201900019

The **contributions of the author** of the thesis are as follows:

The author of the thesis is the first **co-first author** of this work. He designed and performed the filling experiments based on laser scanning confocal microscopy published in this work, *i.e.* the author of the

thesis chose the parameters investigated and carried out the systematic study of the conditions under which successful filling can be facilitated. The author of the thesis investigated the influence of flow velocity, the filling process for different oils and their amounts, the influence of the oil viscosity, and the influence of the surface chemistry and topography (including geometry). The influence of the surfactant concentration (presented in the supporting information) has been investigated with the help of D. Garcia-Gonzalez (University of Twente) supervised by the author of the thesis. The author of the thesis designed and supervised the image processing performed by H. Bauer. The sample surfaces were prepared by Dr. F. Geyer and Dr. M. D´Acunzi. Dr. Anke Kaltbeitzel helped the author to optimize the image acquisition using laser scanning confocal microscopy. The author of the thesis rendered these surfaces hydrophobic. The co-first author Dr. H. Teisala had tested the feasibility and practicability of the experimental approach of flowing oil-in-water emulsions across a texture contained in a water-filled flow cell (together with V. Damle, Arizona State University). He introduced and trained the author of the thesis in the methods and experimental skills utilized in this work. Furthermore, he helped the author of the thesis with the modeling of the stability of the established liquid-infused surfaces under flow conditions. The author of the thesis has optimized the experimental approaches. The author of the thesis wrote the manuscript and prepared the figures in close collaboration with Dr. H. Teisala. The author has been involved and coordinated the entire process of writing and revision of the manuscript (in close collaboration with Dr. H Teisala). The responsibility of the overall supervision of the work lay with Professor H.-J. Butt and Professor D. Vollmer.

A lot of unanswered questions remain, independent whether one considers the liquid-infused texture exclusively, or whether one extends the picture to single discrete drops and continuums of fluids interacting with liquid-infused surfaces. In the following, a brief outlook suggesting future lines of research and projects concludes this section.

Concerning the preparation of liquid-infused surfaces, the mechanical durability of the underlying (solid) texture remains a matter of pressing urgency despite many different solids and liquids can be flexibly combined.

The dynamic shape of the menisci formed by single discrete drops (laterally) moving on liquid-infused surfaces at velocities orders of magnitude larger than the drop descending velocities investigated in this work (Chapter 4) remains to be elucidated with the help of laser scanning confocal microscopy possibly involving the modification of the current setups available. The visualization of the advancing front meniscus with the help of laser scanning confocal microscopy (Chapter 4, Figure 4.3c) revealed that the dynamic contact angles are considerably larger than assumed in the description, making use of the Huh-Scriven approximation of small angles. This is the weak point of the model describing the friction of drops on liquid-infused surfaces. A detailed study of the evolution of the dynamic contact angles in dependence of drop velocity (possibly with the help of laser scanning confocal microscopy) and the considerations of possible corrections to the model has to be left to future efforts.

Although it is known that the lateral adhesion of drops moving on a liquid-infused surface is weak, it remains to be elucidated how strong the vertical adhesion of drops to liquid-infused surfaces is. An interesting continuation of this thesis would be to investigate (possibly combined with laser scanning confocal microscopy imaging utilizing a novel custom-build setup mounted onto the microscope) the vertical adhesion of drops placed on liquid-infused surfaces and to investigate the dissipation associated with vertically lifting off drops from liquid-infused surfaces. Furthermore, the influence solid contaminants present on a liquid-infused surface have on drop mobility would constitute an interesting line of research addressing the self-cleaning properties of liquid-infused surfaces.

Lubricant-depletion continues to be a hot topic in the research field of liquid-infused surfaces. On grooved substrates[97,162,163] and hydrogel-coated micropillar arrays (Chapter 5), lubricant-depletion has been studied. It remains, however, to elucidate lubricant-depletion behavior on infused substrates equipped with micropillars, possibly in dependence on the geometry of the micropillars and/or flow velocities. Combining experiments with simulations could be an asset. Furthermore, the author speculates that the presence or absence of lubricant-reservoirs will have a strong influence on the observed lubricant-depletion behavior. The existence of a *steady-state length*[97,162,163] across the texture remains lubricated, although the flow-induced shear-forces may be a direct consequence of the lubricant-reservoir present in these works. Perhaps, transition regimes between different depletion scenarios can be identified and described as well.

Lubricant-replenishment relying on the flow of emulsions has been successfully demonstrated (Chapter 6). Whether the same approach works in environments of high salinity remains unclear. Moreover, it would be interesting to know whether a flow is indispensable for lubricant-replenishment utilizing emulsions. So far, the effect of buoyancy has not been considered. Whether one can rely on surface chemistry and buoyancy to facilitate the lubrication of a solid texture with emulsions remains to be investigated. Furthermore, the author speculates that an interesting line of research would be opened up by relying on flows of Pickering emulsions filling the structure. The particles used to stabilize the emulsion could further stabilize the oil within the texture, making the liquid-infused surface even more resistant to shear-induced depletion.

3 Grafting Silicone at Room Temperature – a Transparent, Scratch-Resistant Non-Stick Molecular Coating

Hannu Teisala,[a,] Philipp Baumli,[a] Stefan A. L. Weber,[a,b] Doris Vollmer[a,]* and Hans-Jürgen Butt[a]*

[a]Max Planck Institute for Polymer Research, Department of Physics at Interfaces, Ackermannweg 10, D-55128 Mainz, Germany

[b]Johannes Gutenberg University, Department of Physics, Staudingerweg 10, D-55128 Mainz, Germany

*teisala@mpip-mainz.mpg.de, vollmerd@mpip-mainz.mpg.de

This work is currently *in revision* (*Langmuir*, ID la-2019-032236).

Keywords: PDMS brush, hydrophobic, oleophobic, slippery, anti-icing

Silicones are usually considered to be inert, and thus not reactive with surfaces. Here we show that the most common silicone, methyl-terminated polydimethylsiloxane, spontaneously and stably bounds on glass – and any other material with silicon oxide surface chemistry – even at room temperature. As a result, a 2–5 nm thick and transparent coating, which shows extraordinary non-stick properties towards polar and non-polar liquids, ice, and even super glue, is formed. 10 µL drops of various liquids slide off a coated glass when the sample is inclined by less than 10°. Ice adhesion strength on a coated glass is only 2.7±0.6 kPa, *i.e.* more than 98% less than ice adhesion on an uncoated glass. The mechanically stable coating can be easily applied by painting, spraying, or roll-coating. Notably, the reaction does not require any excess energy, solvents, nor does it induce hazardous by-products, which makes it an ideal option for environmentally sustainable surface modification in a myriad of technological applications.

3.1 Introduction

Silicones are colorless, non-toxic, and generally considered to be biocompatible materials. Silicones are frequently used in industry and a broad range of consumer products worldwide[182-184]. The global market for silicones is rapidly increasing and is expected to reach 20 billion US dollars in 2021[185]. The unique properties of silicones include excellent thermal stability, thermal and electrical insulation, and water repellency. Important fields of applications of silicones cover medical technology, construction, automotive, and paper industry. Typical examples are top coatings for medical devices, electronics, solar cells, optical lenses, window panes, release layers for adhesive labels, containers, and food packages[182,183,186]. The unique properties of silicones result from the inorganic–organic composite structure of siloxane molecules.

The most common silicone is trimethylsiloxy-terminated linear polydimethylsiloxane (PDMS). It has an inorganic silicon (Si)–oxygen (O) backbone with two organic methyl side groups ($-CH_3$) attached to each silicon atom (Supporting Information, Figure S3.1)[182]. The organic/inorganic molecular structure gives PDMS its unique properties. For example, the low electronegativity of Si leads to a highly polarized Si–O bond in the PDMS backbone (Supporting Information, Table S3.1). The large bond energy of 452 kJ mol^{-1} gives PDMS its high thermal stability[182]. The hydrophobic methyl side groups provide low surface energy and shield the inorganic Si–O backbone, thereby lowering intermolecular interactions within PDMS. Because of its low surface tension $\gamma \approx 20$ mN m^{-1} PDMS easily wets most materials[182]. The wide bond angle $\approx 150°$ between Si−O−Si atoms yield nearly vanishing torsional barriers[187]. As an instructive example, the rotation energy around a $(CH_3)_2Si–O$ bond in PDMS is only 3.3 kJ mol^{-1} whereas around a $CH_2–CH_2$ bond in polyethylene it is 13.8 kJ mol^{-1} [182]. The low glass transition temperature T_g at −127°C[182] ensures excellent lubricating properties over a wide range of temperatures.

It is common knowledge that silicones tend to stick to surfaces. It has been shown that treating PDMS on oxide surfaces by heat[188,189] yields strongly bound, polymer brush[190,191] like PDMS films. Such films show remarkable liquid-repellency and exhibit a low contact angle hysteresis $\leq 10°$ for various polar and non-polar liquids. In comparison, other hydrophobic coatings like fluorosilanes[192] and Teflon[193] (polytetrafluoroethylene, PTFE) typically show water contact angle hysteresis of about 20–30°. In addition to using heat, PDMS can be bound on metal oxide photocatalysts by illuminating with UV light[194]. For example, Eifert et al.[195] applied PDMS on various substrates, including glass, and baked the samples for 1–3 min at 300°C to attach PDMS to the surfaces. Thereafter they impregnated the samples with PDMS to achieve liquid repelling oil-infused surfaces. Xue et al.[196] fabricated a superhydrophobic PDMS/Octadecylamine coating on fabrics that showed self-healing ability after both mechanical and chemical damage. Yang et al.[197] applied drop coating, curing and abrasion to fabricate a superhydrophobic ZnO/PDMS coating with ice repelling properties. Besides coating applications, interactions between PDMS and solids[198] are of fundamental and practical importance, for instance in binding inorganic filler particles used to reinforce silicone rubbers[199]. Other sophisticated applications based on organosilica architecture include environmental sensors[200] and filtration of nanoparticles[201].

Despite the abundant use of PDMS, its reactions with oxides are not clear. The first paper pointing out the heat-activated reaction of PDMS with glass was published already in 1947 by Hunter et al.[202] In 1969, Willis[203] wrote: “We have observed greatly enhanced reaction at metal surfaces. Decomposition of the polydimethylsiloxanes can occur at temperatures as low as 90–100°C, resulting in the formation of extremely thin polymeric films.” He pointed out that the reaction only occurs on metal oxide

surfaces, not on noble metals, and that the reaction was not observed under inert gas atmospheres of nitrogen and argon. These early works, however, did not get wide attention because PDMS was considered to be unreactive on oxides, *i.e.* not capable of forming any covalent bonds with the substrate, as it does not contain any reactive groups such as chlorine (–Cl) or hydroxyl (–OH) groups. Adsorption of PDMS was explained by hydrogen bonding with the substrate[204]. The possibility of a chemical surface reaction was not considered until 2010 when Krumpfer and McCarthy[188,189] and, 4 years later, Graffius et al.[205] proposed that PDMS can adsorb to silicon oxide *via* acid-catalyzed surface reaction, which involves scission of the siloxane backbone of PDMS and condensation with the surface silanols (≡Si−OH) at elevated temperatures at 100–300°C.

It has been proposed that surface silanols are favorable sites for chemical bonding of PDMS on silicon oxide[188,189,205]. Fully hydroxylated silicon dioxide surface has a considerable amount of surface silanols, about 5 OH nm^{-2} [205-207]. Despite these silanol groups, spontaneous formation of a high-quality coating film from PDMS without adding reagents or catalysts seems surprising at first sight as PDMS does not contain any reactive groups. The reaction is of particular industrial interest because producing molecular PDMS coatings typically releases toxic chemicals[182,208] or consumes energy[189,195]. On thicker cross-linked PDMS coatings liquid drops pin to the surface. This problem has been overcome by infiltrating PDMS with silicone oil, giving rise to lubricant-infused surfaces[1,2,105,195,209]. The drawback of such an approach is that the sliding drops take the lubricant along, ruining the properties in the course of time (Supporting Information, Video S3.1)[210,211].

Here we overcome the problems related to production of PDMS surfaces and the adhesion of drops by introducing an easy but unexplored strategy. We show that PDMS spontaneously reacts with silicon oxide surfaces over a wide range of temperatures; even at room temperature and below. We propose that grafting reaction of PDMS to silicon oxide at room temperature is induced by attachment of linear PDMS chains to the surface *via* hydrolysis and condensation reactions. Notably, the reaction yields a 2–5 nm thick, high-quality coating, which shows contact angle hysteresis below 10° for water and a variety of organic liquids on both glass and silicon wafers (Figure 3.1). The PDMS film thus enables easy sliding of various polar and non-polar liquids on its surface. Gravity or a gentle blow easily removes the drops, thus helping the surface to stay clean (Figure 3.1a and Supporting Information, Video S3.2). Notably, this environmentally friendly, one-step synthesis yields a liquid-repellent, transparent, mechanically stable, and non-stick coating which is capable of repelling ice, spray-paints, and adhesives, including super glue. Solid and porous surfaces of any shape can easily be coated including paper and textiles (Supporting Information, Video S3.3).

3.2 Materials and Methods

3.2.1 Materials

The substrate materials were 170 µm thick borosilicate cover glass slides (Menzel-Gläser, Thermo Scientific) and mirror polished silicon wafers (Si-Mat). Additionally, 1 mm thick soda-lime laboratory glass (Menzel-Gläser, Thermo Scientific) was used as a substrate for demonstrating stability and easy-to-clean properties of the coating. Linear polydimethylsiloxanes (PDMS) with molecular weights (MW) of 770 and 49 350 g mol^{-1} were purchased from Gelest, Inc., and MW 2 000, 6 000, 14 000, 28 000, 63 000, and 117 000 g mol^{-1} from Alfa Aesar. The cyclic PDMS, decamethylcyclopentasiloxane (D5), MW 371 g mol^{-1}, was purchased from Sigma Aldrich. Milli-Q water was used for the experiments. All technical probe liquids were purchased from Sigma Aldrich and used as received.

3.2.2 Sample Preparation

The glass and silicon wafer substrates were washed with ethanol and water, dried under nitrogen flow, and if not otherwise stated, oxygen plasma cleaned at 300 W for 10 min (Femto low-pressure plasma system, Diener electronic). Few drops of PDMS (*i.e.* a silicone oil with a defined molecular weight), about 30–50 µL in total, were dropped on the substrate surface after which the drops were spread with another glass slide to form a < 1 mm thick PDMS film. We used a PDMS with a molecular weight of 6 000 g mol^{-1} (viscosity = 95 mPa s) in all the experiments, if not otherwise stated. After spreading the PDMS films on the substrates, the samples were placed in plastic polystyrene containers at a temperature of 22−23°C and relative humidity of 30−60% for 24 h to let it react with the sample surface, if not otherwise stated. The containers were not sealed gas proof. Some samples were grafted at varying temperatures. Therefore, the PDMS films were spread on the samples as described above, after which the samples were placed in oven, fridge, or freezer for 24 h. The PDMS grafting at varying humidity at room temperature was carried out in a custom-made chamber, where the relative humidity (RH) was controlled by circulating dry or moist nitrogen gas. After letting PDMS react with the glass (or silicon wafer) surface, the excess PDMS was washed away by first rinsing with toluene and then sonicating the sample in toluene, ethanol, and water for 10 min in each liquid.

Surface methylation and fluorosilanization were carried out by applying chemical vapor deposition (CVD). The plasma cleaned glass substrates were placed in a desiccator together with 100 µL of the silane, trimethylchlorosilane or 1*H*,1*H*,2*H*,2*H*-perfluorooctyl-trichlorosilane (97% pure, Sigma-Aldrich). The pressure in the desiccator was reduced to about 100–200 mbar for 2 h. Thereafter, the samples were placed in a vacuum oven at 60°C for 2 h to remove any unreacted silane. To compare the grafted PDMS films with a cross-linked PDMS, we prepared cross-linked PDMS surfaces using Sylgard 184 elastomer (Dow Corning). The base component and the cross-linker were mixed at a ratio of 10:1 in weight by manually stirring for 2 min. The solution was degassed in vacuum at 200 mbar for 15 min. After that, about 30 µL of the PDMS solution was deposited on glass substrates of 24 mm × 30 mm in size. The samples were spin-coated at 2 500 rpm for 5 min to form a ≈10 µm thick PDMS film after which the surfaces were cured in an oven at 60°C for 20 h. To compare with a lubricant-infused surface, we infused the cross-linked PDMS film with a PDMS fluid (MW 6 000 g mol^{-1}). Therefore, we deposited a few drops of the PDMS on the sample and let them spontaneously spread over the surface. After letting the film impregnate for 2 h in a horizontal plane, the sample was placed

vertically for 5 h so that the excess PDMS was removed from the surface by gravity. The surface showed a sliding angle of <1° for 10 µL water drops.

To demonstrate PDMS grafting to other materials, which do not have silicon oxide surface chemistry, we coated aluminum, stainless steel, polyester fabric, and paper with PDMS. The metal plates, 50 mm × 50 mm × 1 mm in size, were purchased from Modulor (Germany) and were washed with ethanol and water prior to use. The fabrics were purchased from Karstadt (Germany) and the paper tissues (Kimtech Professional precision wipes, Kimberly-Clark) from Thermo Fisher Scientific. Prior to applying the PDMS films, we coated the substrates with a thin, ~3 nm thick silicon dioxide layer. Therefore, the substrates were first oxygen plasma cleaned (aluminum and stainless steel at 300 W for 10 min, and polyester fabric and paper at 180 W for 2 min). Thereafter, the substrates were placed in a desiccator together with ammonia (3 mL, 25% solution, VWR Chemicals) and TEOS (3 mL, 98% pure, Sigma Aldrich) at atmospheric pressure and room temperature for 4 h to apply a gas-phase Stöber-like reaction[212] to grow the silica layer. Then the samples were oxygen plasma cleaned again using the same parameters that were used prior to growing the silica shell, after which PDMS was grafted to the samples for 24 h at room temperature. To remove unreacted PDMS, the metal plates were sonicated in the solvents using the standard procedure described above. The polyester fabric and paper samples were simply rinsed for about 30 s in each solvent (paper was only rinsed in toluene and ethanol, not in water, to prevent damaging the substrate).

3.2.3 Characterization

Contact angle: Surface wetting was investigated using a DataPhysics OCA 35 goniometer (DataPhysics Instruments). Static contact angles θ and sliding angles α were determined with 10 µL drop volume. The data were collected from at least 3 different positions on each sample. Advancing θ_a and receding θ_r contact angles were determined by increasing and decreasing the drop volume between 10 and 25 µL at the rate of 1 µL s^{-1}.

Ellipsometry: The thickness of the grafted PDMS films was determined by ellipsometry (Nanofilm EP3, 658 nm laser, 50 mW) on silicon wafers. The thickness of the native oxide layer on the wafers was measured to be 3.8±1.5 nm. The thickness of the native oxide layer enters the calculation of the thickness of the PDMS film. Because the refractive index of PDMS (n = 1.42, λ = 500 nm)[213] and native oxide (n = 1.46, λ = 500 nm)[214] are very close, the light is primarily reflected at the interface between the native oxide layer and silicon (n = 4.3, λ = 500 nm).[214]

AFM: The PDMS film thickness and the adhesion force between the PDMS film surface and the AFM tip were investigated by atomic force microscopy (AFM, MFP3D Standalone from Asylum Research). Uncoated Si cantilevers (OMCL-AC240 by Olympus) with force constant between 2.6–3.1 N m^{-1} were used. For each substrate, we used a new cantilever that we calibrated by analyzing the thermal noise spectrum ("Sader method"). Force-distance curves were recorded in a force mapping approach: the tip was repeatedly approached and retracted on a grid of 64 by 64 points (32 by 32 points on the glass reference) on an area of 1 µm × 1 µm. This way, the tip always measured a pristine surface.

XPS: Influence of different grafting times and pre-treatment on the atomic composition on the silicon wafers was investigated by X-ray photoelectron spectroscopy (XPS). XPS analyses were carried out with a Kratos Axis Ultra DLD instrument (Kratos Ltd.) using a monochromatic Al K_α X-ray source

(1486.6 eV, emission current: 10 mA, anode voltage: 15 kV). The instrument base pressure remained below 3.0×10^{-10} Torr. The work function was calibrated to a binding energy of 84.0 eV for metallic gold ($Au4f_{7/2}$). The charge neutralizer system was used for all analyses. The charge neutralization was monitored with the help of the C1s peak for adventitious carbon. Survey spectra and detail scans were recorded at a pass energy of 80 eV with 10 sweeps and an energy step of 1 eV. High-resolution spectra for the transitions C1s, O1s, Si2p, and Si2s were obtained at a pass energy of 20 eV and 5 sweeps each for an energy step of 0.1 eV. The analysis area was ≈ 300 × 700 μm^2. All spectra were recorded in the spectroscopy mode utilizing the hybrid lens mode. For each sample, at least three independent measurements were performed. The calculations of atomic percentage were performed from survey spectra corrected for transmission with the help of the commercial software CasaXPS (version 2.3.16, Casa Software Ltd.). The binding energies were calibrated using the C1s peak for adventitious carbon at a binding energy of 284.8 eV, with an associated error of ≈ 0.1–0.2 eV[215].

FTIR: Fourier-transform infrared spectroscopy (FTIR, Tensor II with Platinum ATR, Bruker) was applied to investigate chemical changes in PDMS, *i.e.* hydrolysis and condensation reactions during the PDMS grafting process at room temperature. To maximize the silicon oxide surface area for the FTIR measurements, we took fumed silica (Aerosil 200, Evonik, surface area = 200 $m^2\ g^{-1}$) and compressed it tight on a glass slide. The compressed powder was oxygen plasma cleaned at 300 W for 10 min. First, pure powder was investigated by FTIR. Thereafter, the powder was removed, and the ATR crystal was cleaned. Second, a film of PDMS (MW 6 000 g mol^{-1}) was spread on the crystal and investigated without the powder. Thereafter, the powder was applied on the PDMS and compressed tight under a glass slide. The chemical changes were monitored by FTIR with time up to 24 h. The experiment was repeated twice to be sure that the results are repeatable. Each spectrum was recorded at a resolution of 1.4 cm^{-1} by taking 200 scans. Recording each single spectrum thus took about 3 min. Penetration depth in the sample is about 1–2 µm at 1000 cm^{-1}. The penetration depth increases by an order of magnitude between 4000 and 400 cm^{-1}. The Bruker software was used to correct the spectra for the absorption of ambient H_2O and CO_2 during the measurements.

UV-Vis: The light transmittance of the PDMS film for wavelengths ranging from 300 to 1 500 nm was measured with an ultraviolet-visible light (UV-Vis) spectrometer (Lambda 900, PerkinElmer).

UV light exposure: The UV stability of the PDMS film was investigated by illuminating the sample by UV-A light (intensity at the sample surface = 2.3 ± 0.3 mW cm^{-2}) from a distance of 8 cm (light source: LQ-400, Dr. Gröbel UV-Elektronik GmbH). The illumination intensity was measured using an UV-radiometer RM-12 with UV-A sensor for a spectral range of 315–400 nm (Dr. Gröbel UV-Elektronik GmbH).

Stability against acid/base solutions: Stability of the PDMS film in acid and base solutions was investigated by immersing the sample in 0.1 M aqueous solution of hydrochloric acid (HCl, pH = 1) or sodium chloride (NaOH, pH = 13), respectively, for 1 h or 24 h.

Tape adhesion: We performed the tape adhesion test following the ASTM D903 standard. As an adhesive tape we used a Tesa fabric tape (Gewebeband blue 2.75 m x 19 mm). The tape was bonded to the substrate using a metallic roller with a diameter of 12.5 cm and a weight of 2.5 kg. After a settling time of 5 min, the tape was removed by pulling backward at a peel angle of 180° at a velocity of 15 cm min^{-1}. The mean adhesion force was recorded using a PCE-DFG N20 force gauge. The average adhesion force was determined from 5 independent measurements.

Ice adhesion: Ice adhesion was measured using a home-built ice adhesion test apparatus. In brief, a force gauge (PCE-DFG N20, max. measurable force of 20 N with an accuracy of ±0.1% of the

measuring range) and a manual linear stage (XR50P/M 50 mm, Thorlabs) to move the sample were attached on an aluminum breadboard (Thorlabs). The whole setup was built in a freezing chamber (Mobicool FR40 compressor cooling system). First, the sample was attached to the linear stage and was let to cool down for 5 min. Thereafter, we carefully deposited 50 µL water drops on the sample surface. After letting the drops cool down for 5 min, their freezing was initiated by touching them with a tiny ice crystal on the tip of tweezers. The drops were let to freeze in the chamber at −8°C for different periods of time, from 10 min up to 16 h. Thereafter, the chamber was opened from the top, and the sample with the ice drops was driven towards the force gauge tip at a velocity of about 50 µm s^{-1}. The temperature at the sample surface remained between −8±1°C during the measurements. The force F required to detach the ice drops from the sample surface was recorded. The contact point between the ice drop and the force gauge tip was set as close as possible to the substrate to be able to determine the shear forces reliably. Contact diameters of 50 µL water drops on different sample materials were determined with a contact angle goniometer. Thus, by knowing the contact area A of the drops on different samples, the lateral adhesion strength of ice was calculated $\tau = \frac{F}{A}$. The average adhesion strength of ice was determined from five individual measurements on each sample. When calculating the shear strength of ice, we assumed circular geometry for the contact line and that the contact area remained unchanged during freezing. We cannot exclude that the contact area expanded slightly during freezing, however, it is included in the given error margins.

3.3 Results and Discussion

3.3.1 Effect of Rinsing Time on Contact Angle

The grafted PDMS film should only contain molecules tightly bound to the substrate. When investigating grafted PDMS films it is important to properly wash away the excess PDMS molecules that are not bound to the surface. Notably, careful rinsing with solvents, *e.g.* with toluene which is a good solvent for PDMS, does not remove all the excess, unbound PDMS molecules from the surface. After 10 s of rinsing the sample in a glass beaker filled with toluene, ethanol and water, respectively, a film of PDMS easily visible by the naked eye remained on the glass surface (Figure S3.2). After 10–30 s of rinsing in the solvents, contact angle hysteresis and sliding angle both kept increasing with increasing rinsing time, and were in the range of 1–6° (Table 3.1). After 20 s of rinsing, the PDMS layer thickness on silicon wafer measured by ellipsometry was 8 nm. For comparison, on the corresponding sample which was sonicated in the solvents and thus unbound PDMS was removed the thickness of the PDMS coating was only about 3 nm. After 30 s of rinsing the contact angle hysteresis and sliding angle were about 5° lower as compared to the corresponding samples sonicated in the solvents (Table 3.2a). Contact angle hysteresis and correspondingly the sliding angle started to saturate at about 10° after 1–2 min rinsing in each of the solvents. This demonstrates that excess PDMS cannot be washed easily by rinsing. Most likely some unbound PDMS remains on the surface after rinsing, and thus the coating remains in its lubricant-infused state[1,2,105,195,209]. The free molecules are held within the film by the grafted PDMS chains and act as a lubricant. Surface properties, therefore, depend on the amount of free PDMS within the film and vary as a function of the rinsing intensity and duration. To remove all unbound PDMS as efficiently as possible, as a standard procedure through the work we first rinsed the samples in toluene and then sonicated them in toluene, ethanol, and water for 10 min in each solvent.

Table 3.1: Water repellency of PDMS films grafted to glass after washing excess PDMS by rinsing in solvents. PDMS films were grafted at room temperature for 24 h, after which the excess PDMS was removed from the samples by rinsing in toluene, ethanol, and water, respectively, for 10–120 s in each solvent. PDMS molecular weight was 6 000 g mol^{-1}.

Rinsing time [s]	θ [°]	θ_a [°]	θ_r [°]	$\theta_a - \theta_r$ [°]	α [°]
10	107±1	107±2	105±2	2	<1
20	109±1	108±1	103±2	5	5±1
30	107±1	109±1	103±4	6	6±5
60	108±1	110±1	98±2	12	10±2
120	107±1	111±1	98±2	13	11±1

3.3.2 Reaction of PDMS with Oxide Surfaces

PDMS starts binding to the glass surface immediately after contacting the substrate at room temperature. Already after 1 min contact time, the initially perfectly hydrophilic glass surface (contact angle $\theta \approx 0°$ for water) becomes slightly water-repellent, displaying an advancing contact angle θ_a = 60±5° and contact angle hysteresis of 31±2°. After 24 h contact time, a hydrophobic PDMS film with θ_a = 109±1° and contact angle hysteresis of 12±2° was formed (Figure 3.1a–d, Table 3.2a). The film thickness was 2.8–3.1 nm; the thickness was measured by ellipsometry on silicon wafers (Table 3.3) and by atomic force microscopy (AFM) on glass from the elastic deformation of the film.

Table 3.2: Water repellency of PDMS films grafted to glass. a) PDMS films were grafted at room temperature for different periods of time. The excess PDMS was washed away by sonicating in toluene, ethanol, and water, respectively. The grafting time 0 min presents wetting of a pristine glass surface after oxygen plasma cleaning. b) PDMS films were grafted at varying temperatures for 24 h. c) PDMS films were grafted at room temperature for 24 h at varying relative humidity (RH). The advancing contact angles θ_a and receding contact angles θ_r were determined by the needle-in-sessile drop method. The sliding angle α is the angle at which 10 µL drops started to move when the substrate was gradually inclined. PDMS molecular weight was 6 000 g mol^{-1}.

a)	Grafting time	θ [°]	θ_a [°]	θ_r [°]	$\theta_a - \theta_r$ [°]	α [°]
	0 min	0	-	-	-	-
	1 min	58±5	60±5	29±6	31	-
	5 min	71±3	73±3	41±1	32	-
	15 min	95±1	97±1	65±1	32	-
	2 h	103±1	106±1	80±1	26	-
	24 h	106±1	109±1	97±1	12	12±2
	5 d	107±1	109±1	99±1	10	7±2

10 d	108±1	109±2	97±2	12	11±2
30 d	107±1	110±1	92±2	18	18±4

b)	Temperature [°C]	θ [°]	θ_a [°]	θ_r [°]	$\theta_a-\theta_r$ [°]	α [°]
	−18	104±1	108±1	83±4	25	-
	10	106±1	109±1	93±1	16	22±4
	22–23 (RT)	106±1	109±1	97±1	12	12±2
	100	105±1	108±1	95±1	13	13±2

c)	RH [%]	θ [°]	θ_a [°]	θ_r [°]	$\theta_a-\theta_r$ [°]	α [°]
	0.1	106±1	109±1	100±1	9	11±1
	30-60	106±1	109±1	97±1	12	12±2
	90	106±1	108±1	94±1	14	11±1
	97-99	95±3	98±3	64±4	34	-

Prolonging the reaction time of PDMS on glass from 1 day to 5 days and 10 days further increased the film thickness from 2.8±1.1 nm to 4.3±0.7 and 5.1±0.7 nm, respectively, as measured by AFM. PDMS film thickness around 4 nm (reaction time of 5 days) appears to yield the best water repellency with contact angle hysteresis of 10±1° and sliding angle of 7±2° for 10 µL drops (Figure 3.1b, c, Table 3. 2a). Higher film thickness yields increased pinning of water drops.

3.3.3 Molecular Weight of PDMS vs. Film Thickness

In addition to the grafting of linear PDMS with molecular weight of 6 000 g mol^{-1}, we grafted significantly lower and higher molecular weight linear PDMS varying from MW 770 g mol^{-1} to MW 117 000 g mol^{-1}. The optimum molecular weight for 24 h room temperature PDMS grafting is of the order of MW 10 000 g mol^{-1} (Figure 3.1e). With lower or higher MW, contact angle hysteresis of water starts to increase, Figure 3.1e and Table 3.3. In the case of low molecular weight, most likely, the attached PDMS chains are too short to be sufficiently flexible and the influence of the underlying glass substrate is still noticeable; contact angle hysteresis was 25–30° after letting the substrate react with a short-chain linear PDMS (MW = 770 g mol^{-1}). In the case of high MW, the chain length is above the threshold where molecule entanglement starts to occur, around MW 6 000–7 000 g mol^{-1} [216]. Entanglement reduces the mobility of the PDMS chains on the surface. It, therefore, increases the contact angle hysteresis and shifts wetting properties of the film towards those of cross-linked PDMS, where the chain mobility is restricted. Indeed, cross-linked silicone typically shows contact angle hysteresis as high as 35–50° for water (Figure 3.1d)[217,218].

PDMS with a molecular weight of 6 000 g mol^{-1} contains about 80 Si–O units per one polymer chain (D number). Thus, the theoretical chain length for PDMS MW 6 000 g mol^{-1} is about 26 nm when Si–O bond length = 0.163 nm, Si–O–Si bond angle = 150°, and dimethylsiloxane monomer weight ($(CH_3)_2SiO$) = 1.23×10^{-22} g. This simplified calculation is solely based on the geometry of the silicon–oxygen bonds[187] in a theoretical case where the polymer chain is fully stretched. In reality, the chains are flexible and rather curly. Furthermore, they may orient parallel to the surface and not perpendicular. For PDMS MW 770 g mol^{-1} and 117 000 g mol^{-1} the theoretical chain lengths are about 3 nm and 500 nm, respectively. Grafting of PDMS film includes scission of the polymer chains by attacking water molecules. Thus, the length of grafted PDMS chains is shorter than the original chain length of the PDMS fluid. In addition, because of the chain scission, the length distribution of individual chains grafted to the substrate is random. Grafted PDMS chains are expected to lie on the surface, and not to stand tall. Therefore, the thickness of the grafted PDMS films (Table 3.3) is much less than the theoretical chain length calculated based on the molecular weight of the used PDMS.

Table 3.3: Water repellency of PDMS films grafted to glass at room temperature for 24 h using different molecular weight (MW) for PDMS. Film thicknesses were measured on silicon wafers by ellipsometry. Please note that the ellipsometry measurements do not contain the systematic error caused by the variations of the thickness of the native oxide layer.

Grafting time [h]	MW [g mol^{-1}]	Ellipsometry thickness [nm]	θ [°]	θ_a [°]	θ_r [°]	$\theta_a-\theta_r$ [°]	α [°]
24	770	1.1±0.3	92±1	95±3	70±2	25	-
24	6 000	3.1±0.2	106±1	109±1	97±1	12	12±2
24	117 000	5.6±0.2	113±1	115±1	75±4	40	-

3.3.4 Sliding Angles of Different Liquids

The degree of pinning of a drop to the surface, *i.e.* the lateral adhesion force F_{adh}, depends on the contact angle hysteresis, *i.e.* the difference between the advancing θ_a and receding θ_r contact angles. For example, for 10 µL water drops (comparable to a volume of a medium-sized rain drop[219]) with a contact width $w = 3.2$ mm and a surface tension γ = 0.073 N m^{-1}, the contact angle hysteresis of 20° yields $F_{adh} \approx w\gamma(\cos\theta_r - \cos\theta_a) \approx 80$ µN[217,220]. Removing the drops from the surface by gravity, $F_G = mgsin\alpha > F_{adh}$, where m is the mass of the drop, g the gravitational acceleration, and α the inclination angle of the substrate, would imply tilting of the substrate by more than 50°. Here, a 10 µL water drop starts to move down the PDMS coated glass surface as soon as the substrate is inclined by about 10° (Table 3.2a) indicating low F_{adh} < 20 µN. The drops move slowly, about 10 µm s^{-1} when the inclination is below 15°. However, with higher inclinations, the drops reach a velocity of the order of a few mm s^{-1} (Supporting Information, Figure S3.3, Table S3.2). In addition to water, a variety of other liquids, including alkanes, oils, solvents, and fluorinated liquids easily slide off from the PDMS coated glass at inclinations below 10° (Figure 3.1f).

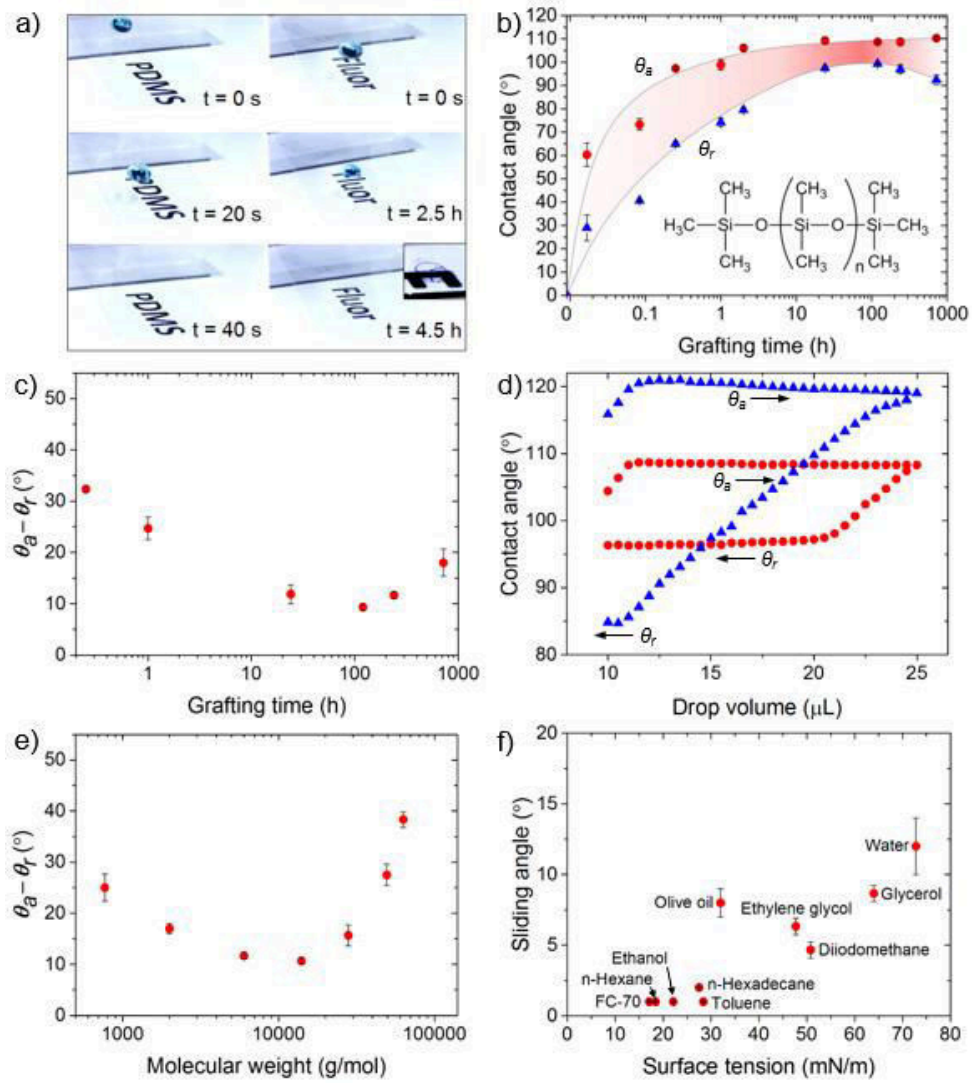

Figure 3.1: PDMS films grafted to glass at room temperature. a) Left: photographs showing a methylene blue dyed water drop (radius ≈ 2 mm) sliding down on the PDMS film. The drop leaves behind a clean surface. The molecular weight of PDMS was 6 000 g mol^{-1} and grafting time was 24 h. Right: the drop is pinned to a chemical vapor deposited (CVD) fluorosilane coating on glass. The drop evaporates and leaves behind a stain (inset). Both surfaces were inclined by 15°. b) Advancing θ_a (red dots) and receding θ_r (blue triangles) water contact angles (inset: molecular formula of PDMS) and c) contact angle hysteresis on the PDMS films after different grafting periods. d) Contact angle versus volume of water drop on the grafted PDMS (red dots) and cross-linked PDMS (blue triangles) on glass when inflating and deflating the drop. Advancing and receding contact angles are consistently defined throughout the work by increasing and decreasing the drop volume between 10 and 25 µL at a constant rate of 1 µL s^{-1} using a standard contact angle goniometer. e) Contact angle hysteresis of water on films grafted with different molecular weights of PDMS. f) Sliding angles for 10 µL drops of different polar and non-polar liquids on the PDMS film. Surface tensions γ of the liquids are: Fluorinert FC-70 17.1 mN m^{-1}; *n*-Hexane 18.4 mN m^{-1}; Ethanol 22.1 mN m^{-1}; *n*-Hexadecane 27.5 mN m^{-1}; Toluene 28.4 mN m^{-1}; Olive oil 32 mN m^{-1}; Ethylene glycol 47.7 mN m^{-1}; Diiodomethane 50.8 mN m^{-1}; Glycerol 64 mN m^{-1}; Water 72.8 mN m^{-1}. In a–d) and f) PDMS molecular weight was 6 000 g mol^{-1}. In a) and d–f) grafting time was 24 h.

3.3.5 Stability and Applicability of the Coating

The PDMS films are stably bound. Water cannot replace the adsorbed PDMS, despite its high polarity and affinity to silicon oxide. Neither can the films be removed by sonicating in organic solvents. This was tested by sonicating the samples for 10 min in water, ethanol, isopropanol, acetone, and toluene, after which contact angle hysteresis of water remained unchanged within the experimental accuracy of ±2°. The films are 100% transparent, as verified by ultraviolet-visible light (UV-Vis) spectroscopy (Supporting Information, Figure S3.4). The reason for the excellent transparency is the small refractive index mismatch of ~3% between PDMS and silicon oxide and the low film thickness. In contrast to porous water-repellent materials[2], the PDMS films do not contain any light reflecting structures. In addition, the films withstand UV illumination. After a 5-day-exposure to UV-A light (intensity at the sample surface = 2.3±0.3 mW cm^{-2}), water repellency of PDMS coated glass remained unchanged (Table 3.4).

Table 3.4: Aging of water-repellent PDMS films grafted to glass at room temperature for 24 h. The samples were aged in the dark at 22–23°C and 30–60% relative humidity or illuminated with UV-A light (intensity = 2.3±0.3 mW cm^{-2}). PDMS molecular weight was 6 000 g mol^{-1}.

Sample	θ [°]	θ_a [°]	θ_r [°]	θ_a–θ_r [°]	α [°]
Pristine PDMS film	106±1	109±1	97±1	12	12±2
Aging 6 months in the dark	105±1	108±1	98±1	10	11±1
Aging 5 days under UV illumination	107±1	109±1	97±1	12	12±1

The PDMS films are resistant to high temperatures due to the strong ionic character of the siloxane backbone. After annealing in an oven at 100°C for 5 h, any changes in the surface wettability could not be observed within the experimental accuracy. After annealing at 400°C for 5 h, the PDMS film still maintained its hydrophobic nature and contact angle hysteresis remained below 30° (Table 3.5). The increased hysteresis during the thermal treatment is associated with partial oxidation of the hydrophobic methyl side groups of PDMS[221]. After annealing at 500°C, the glass surface became completely hydrophilic due to thermal degradation of the PDMS coating.

Immersing the samples in acid or base solutions gradually degrades the PDMS coating (Table 3.6), which is expected considering the acid- and base-catalyzed chain opening and polymerization reactions used in industrial production of PDMS. After storing the PDMS coated glass for 6 months in the laboratory atmosphere, the wetting properties remained unchanged from the freshly prepared sample.

Table 3.5: Temperature stability of water-repellent PDMS films grafted to glass at room temperature for 24 h. The samples were annealed in air in an oven at varying temperatures for 5 h. PDMS molecular weight was 6 000 g mol^{-1}.

Sample	θ [°]	θ_a [°]	θ_r [°]	θ_a−θ_r [°]	α [°]
Pristine PDMS film	106±1	109±1	97±1	12	12±2
Annealing at 100°C	106±1	109±1	98±1	11	12±1
Annealing at 200°C	105±1	108±1	88±1	20	15±2
Annealing at 300°C	104±1	107±1	81±6	26	45±15
Annealing at 400°C	99±1	102±1	74±1	28	47±4
Annealing at 500°C	0	-	-	-	-

Immersing the samples in acid or base solutions gradually degrades the PDMS coating (Table 3.6), which is expected considering the acid- and base-catalyzed chain opening and polymerization reactions used in industrial production of PDMS. After storing the PDMS coated glass for 6 months in the laboratory atmosphere, the wetting properties remained unchanged from the freshly prepared sample.

Table 3.6: Water repellency of PDMS films after immersing in water (pH = 7) or in aqueous acid (0.1 M HCl in water, pH = 1) or base (0.1 M NaOH in water, pH = 13) solutions for 1 h and 24 h. PDMS was grafted to glass at room temperature for 24 h. PDMS molecular weight was 6 000 g mol^{-1}.

Immersion liquid / immersion time	θ [°]	θ_a [°]	θ_r [°]	θ_a−θ_r [°]	α [°]
Pristine PDMS film	106±1	109±1	97±1	12	12±2
H_2O / 1 h	107±1	109±1	99±2	10	11±1
H_2O / 24 h	105±1	109±1	97±1	12	12±1
HCl / 1 h	101±2	104±1	88±3	16	40±2
HCl / 24 h	51±6	55±7	26±5	29	-
NaOH / 1 h	47±9	54±10	33±5	21	-
NaOH / 24 h	40±5	44±2	0	44	-

Furthermore, we tested the PDMS films without applying any solvents even in the washing step. Therefore, after applying PDMS on plasma cleaned glass for 24 h, we polished the sample surface with a paper tissue, so that all visible PDMS was removed (Video S3.4). The coating displayed even lower water contact angle hysteresis, 7±1°, than the sonicated samples. It is likely that a small amount of unbound PDMS remained on the sample surface after polishing, which is desirable in many applications as the liquid repellency of the coating further improves.

Because the 6 000 g mol^{-1} PDMS used here has a low viscosity (0.1 Pa s), thin PDMS films can be applied easily by a multitude of standard methods suitable for coating large surface areas, including painting, spraying, or roll-coating (Video S3.4). Complex objectives and heat sensitive components can be coated as the low surface tension $\gamma \approx 20$ mN m^{-1} allows PDMS to easily wet almost all materials[182] and thermal energy is not needed for the coating formation. Therefore, PDMS can react and bound to the substrate spontaneously even during storage or transport from production site to customer. To demonstrate the large-scale applicability to our approach in potential applications, we coated different types of glass. In addition to the borosilicate glass used in the experiments, we coated soda-lime laboratory glass and glass vials with the PDMS films (Supporting Information, Video S3.5). In addition, other materials such as aluminum, stainless steel, polyester fabric, and paper can be coated after silica modifying the substrates. To obtain the siloxane chemistry, we applied a nanometer-thin silica layer on the substrates by a gas-phase Stöber-like reaction[212] prior to applying the PDMS film (Supporting Information, Figure S3.5, Table S3.3, and Video S3.3).

The PDMS films on glass withstand cleaning with a cleaning tissue, abrasion with a rubber glove, scratching with a razor blade or a metal scouring sponge, and even repeated attachment and detachment of adhesive tape (Figure 3.2a, Video S3.6). Therefore, the PDMS films are mechanically stronger than most superhydrophobic or superoleophobic coatings (Supporting Information, Video S3.7)[212,222]. Lubricant-infused surfaces fail after the lubricant is depleted from the surface by, for example, continuous flow of water drops (Supporting Information, Video S3.1). The films show low adhesion to solids and liquids and can repel even super glue (Video S3.8), permanent markers (Figure 3.2b, Video S3.9), and spray paints (Figure 3.2c**,** Video S3.10). The excellent mechanical stability and the non-stick properties make grafted PDMS coatings a potential option to be used in anti-fouling and easy-to-clean applications.

The PDMS films can function as release layers for adhesive films and labels enabling their easy detachment and re-attachment without losing adhesive properties of the glue. This was demonstrated by attaching and measuring the force required to detach a Tesa fabric tape (180° peel angle) on a sample surface. The mean force required to move the tape from an uncoated glass was 3.7±0.1 N. On the PDMS coated glass the mean adhesion force was significantly lower, only 0.22±0.02 N. That is, the PDMS coating lowered the adhesion force of the tape to glass by 94%. After removing the tape from the PDMS coated sample and re-attaching it to the uncoated glass, the adhesion force was 3.8±0.1 N. This implies that the properties of the glue were not altered by the PDMS coating (Figure 3.3a).

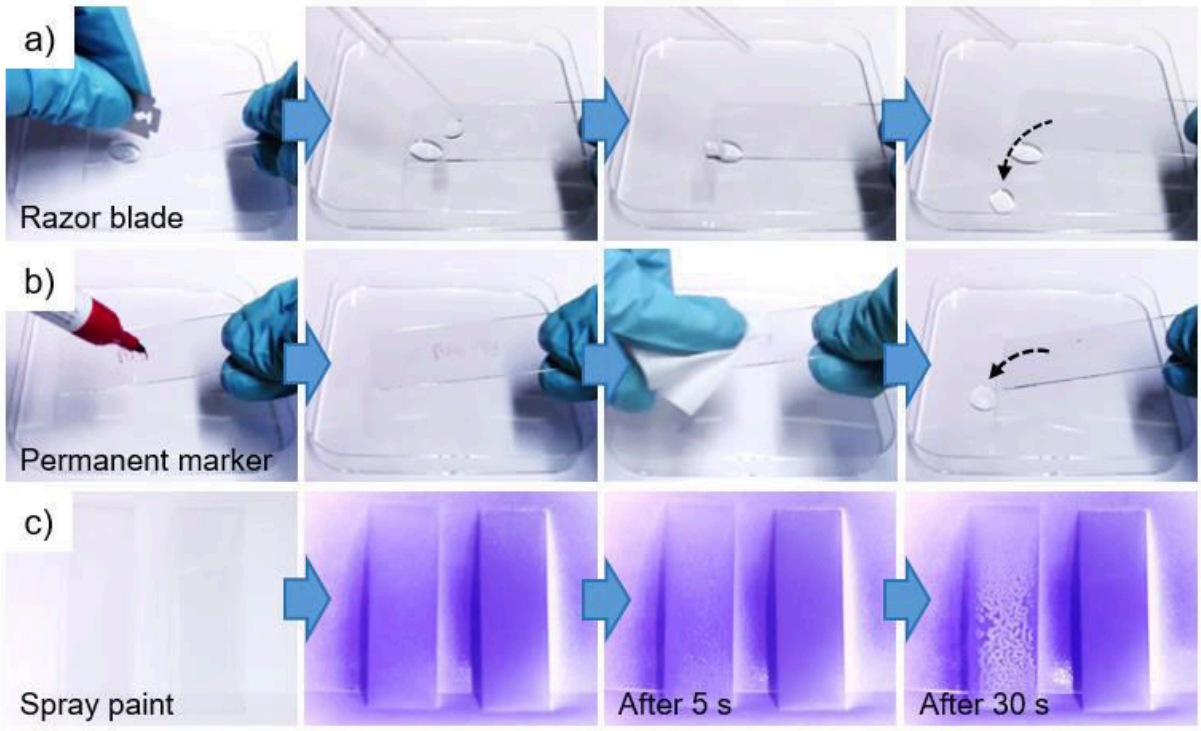

Figure 3.2: Photographs demonstrating stability and easy-to-clean properties of the PDMS films grafted to 1 mm thick soda-lime glass slides. a) The films are tolerant against scratching with a razor blade (Supporting Information, Video S3.6) and b) repel permanent markers allowing the surface to be cleaned with a paper tissue (Supporting Information, Video S3.9). The PDMS films allow easy sliding of water drops on their surface after the scratching or polishing with the tissue. c) The PDMS films repel spray paint. 30 s after spraying; the paint dewets the PDMS coated glass (PDMS coated glass on the left, uncoated glass on the right, Supporting Information, Video S3.10). The PDMS films were grafted at room temperature for 24 h. PDMS molecular weight was 6 000 g mol^{-1}.

The PDMS coatings significantly reduce ice adhesion on glass. Shear strength of ice drops on the PDMS coated glass was as low as 2.7±0.6 kPa, *i.e.* more than 98% less than ice adhesion on an uncoated glass, which was measured to be 155±17 kPa. Freezing of 50 µL drops that were used in the experiments takes only a few minutes. With our ice adhesion measurement setup full ice adhesion is reached already after freezing time of 10 min. We measured ice adhesion strength on the PDMS coated glass repeatedly 20 times on 5 individual spots. We marked target positions for the drops underneath the glass sample so that the drops could be placed at the same location each time. Within the 20 experiments, the ice adhesion strength remained unchanged within the experimental accuracy (Figure 3.3b, inset). Also, among other water-repellent test surfaces, including fluorinated materials and cross-linked PDMS, the grafted PDMS coatings showed remarkably low ice adhesion. For example, ice adhesion strength on cross-linked PDMS (Sylgard 184) was 104±25 kPa, *i.e.* almost 40 times higher as compared to our grafted PDMS films (Figure 3.3b and Supporting Information, Figure S3.6 and Table S3.4).

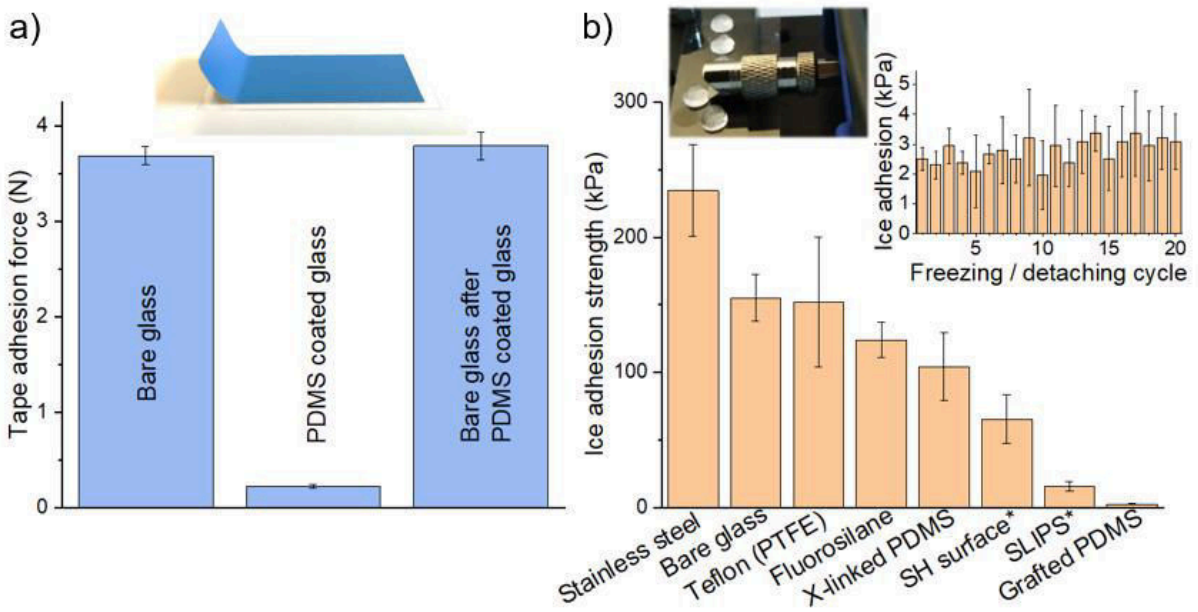

Figure 3.3: Tape and ice adhesion on grafted PDMS films on glass and on reference materials. a) Mean adhesion force required to detach a 19 mm wide Tesa fabric tape (180° peel test) from uncoated glass, PDMS coated glass, and from uncoated glass after the tape was first detached from the PDMS coated glass and re-attached to uncoated glass. Inset: test tape attached to bare glass. The tape was bonded to the substrate using a metallic roller with diameter of 12.5 cm and weight of 2.5 kg. After a settling time of 5 min the tape was removed by pulling backward at a peel angle of 180° at a velocity of 15 cm min^{-1}. b) Ice adhesion strength measured on different materials at −8°C. Ice adhesion strength for superhydrophobic (SH) and slippery liquid-infused porous surface (SLIPS) were taken from Ref.[83,223] (*measured at −10°C). Insets: a photograph of the force gauge tip and ice drops on the PDMS coated glass and ice adhesion strength results over 20 repeated freezing and detaching cycles of ice on the PDMS coated glass. The PDMS films were grafted at room temperature for 24 h. PDMS molecular weight was 6 000 g mol^{-1}.

3.3.6. PDMS Grafting Mechanism

The advantageous properties of the grafted PDMS films require that PDMS strongly binds to the substrate. PDMS itself does not contain reactive groups. However, siloxane bonds (Si–O) can be hydrolyzed by water molecules to form reactive terminal hydroxyl groups. Therefore, for example, silicon dioxide is soluble in water[224-226]. Dissolution of silicon dioxide in water is, however, relatively slow, of the order of 10 nm/year at room temperature[225,226]. The good resistivity of silicon dioxide against an attack of water molecules arises from its structure where Si^{4+} ions are in tetrahedral coordination with oxygen ions. Four water molecules are required to break the bonds to form fully hydrated silicic acid $Si(OH)_4$[208,225,226]. In addition, high connectivity of the glass network makes structural rearrangement difficult. With PDMS, attack of a single water molecule is enough to break the Si–O bond to produce OH-terminated PDMS to initiate the grafting reaction *via* condensation with the surface OH-groups. That is, hydrolyzing the siloxane backbone of PDMS to form hydroxyl-

terminated PDMS chains enables the reaction with the surface silanols to form a stable, covalently bound PDMS film.

Considering the reactivity of PDMS with silicon oxide, one might question the ability of water to hydrolyze PDMS chains and claim that the surface reactions are due to the small amounts of residues that are left in PDMS from the manufacturing process. These residues may contain terminal OH-groups that could theoretically cause the observed surface reactivity with silicon oxide. However, our results rule out that the PDMS surface reactions are due to the OH-terminated residues. Prolonged direct contact even with water slowly degrades the PDMS film (Table 3.7): nucleophilic attack of water molecules gradually breaks the siloxane bonds at the top of the film. The cleaved PDMS chains can restore the siloxane bonds *via* condensation, or the free ends of the cleaved chains can drift away from the surface. The degradation is extremely slow. Complete degradation of a few nm thick films takes several months. Thus, the degradation of grafted PDMS films in water is a strong indication that PDMS is hydrolyzed by the attack of water molecules. Eventually, prolonged direct contact with water will completely degrade the PDMS coatings.

Table 3.7: Water repellency of PDMS films after immersing in water for 1–3 months. PDMS was grafted to glass at room temperature for 24 h. PDMS molecular weight was 6 000 g mol^{-1}.

Immersion [months]	θ [°]	θ_a [°]	θ_r [°]	$\theta_a - \theta_r$ [°]	α [°]
0	106±1	109±1	97±1	12	12±2
1	96±2	98±2	59±2	39	19±8
2	82±6	86±3	31±3	55	-
3	76±1	79±1	29±4	50	-

We propose a reaction that takes place at room temperature and does not require an acid catalyst. Our results hint that the reaction between PDMS and silicon oxide is initiated by hydrolysis of the siloxane bonds of PDMS *via* a nucleophilic attack of the oxygen contained in water according to Eq. (1). The two Si–OH terminated chain ends can then link to surface silanol groups or to another cleaved PDMS chains (Figure 3.4). An example of such a hydrolysis reaction is the dissolution of silicon dioxide in water at room temperature[224-226].

$$(\equiv Si{-}O{-}Si\equiv) + H_2O \underset{condensation}{\overset{hydrolysis}{\rightleftarrows}} (\equiv Si{-}OH) + (OH{-}Si\equiv) \qquad (1)$$

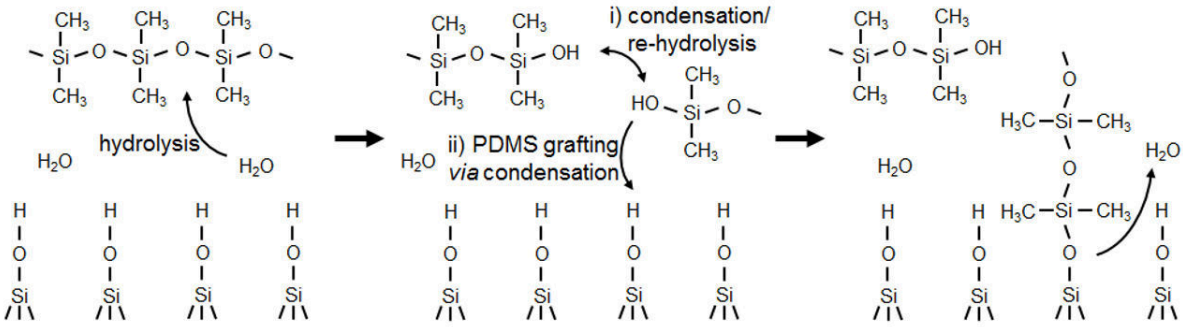

Figure 3.4: Proposed grafting reaction of PDMS to silicon oxide at room temperature. Covalent attachment of linear PDMS chains to the surface occurs *via* hydrolysis and condensation reactions. The scission of a single PDMS chain by hydrolysis consumes a single water molecule. Ideally, if both of the hydrolyzed chain ends react with the oxide surface, two water molecules are released.

Notably, the reaction is reversible, *i.e.* the silanol groups formed by hydrolysis can condense to restore the siloxane bond and release a water molecule. Indeed, the condensation reaction is known in the context of silicon wafer bonding[225,227-229]. Thus, it can be expected that surface exposed siloxane bonds of PDMS hydrolyze by the surface-bound water to form two reactive silanol groups. These silanol groups then readily condense with the surface silanols to covalently bond PDMS to the substrate. Our data consistently support that this happens at room temperature and below (Table 3.2b).

3.3.7 The Effect of Grafting Temperature on the Coating Quality

We also tested how ambient temperature affects the coating properties. Therefore, we fabricated control PDMS films at varying temperatures between −18 and +100°C (Table 3.2b)[188,189,205]. PDMS binding to the glass substrate is pronounced even at temperatures significantly below the room temperature. The adsorption is, however, faster at higher temperatures[189,195]. For example, contacting glass with PDMS at 10°C for 24 h yields a 4° higher contact angle hysteresis as compared to the corresponding sample prepared at room temperature. One reason for the faster reaction at high temperatures is likely removal of excess molecular water from the surface. A too high amount of surface-bound water blocks the surface silanols and thus prevents hydrolyzed PDMS from establishing chemical bonds at the surface. However, after 24 h of grafting time, contact angle hysteresis on the films prepared at 100°C[188,189] did not deviate from the samples prepared at room temperature (Table 3.2b and Table 3.8). It is worth pointing out, that at higher temperatures above 200°C used by other groups[195], the grafting reaction may be different from the room temperature grafting and may include thermal degradation of the methyl side groups of PDMS.

Table 3.8: Water repellency of PDMS films grafted to glass and silicon wafer at room temperature and 100°C for 24 h. PDMS molecular weight was 6 000 g mol^{-1}.

Substrate	Grafting T [°C]	θ [°]	θ_a [°]	θ_r [°]	$\theta_a - \theta_r$ [°]	α [°]
Glass	22-23	106±1	109±1	97±1	12	12±2
Glass	100	105±1	108±1	95±1	13	13±2
Si wafer	22-23	106±1	109±1	99±1	10	17±2
Si wafer	100	106±1	108±1	101±1	7	10±1

3.3.8 Grafting with Cyclic PDMS

If our explanation is correct, cyclic PDMS should also bind to glass. Therefore, we used low molecular weight cyclic PDMS (decamethylcyclopentasiloxane, D5, molecular weight = 371 g mol^{-1}, Supporting Information, Figure S3.7) to investigate whether the terminal methyl groups of PDMS play a role in the reaction with silicon oxide. A few drops of the cyclic PDMS were deposited on the sample surface and were let to spread spontaneously. The sample was stored in a plastic container in a similar way to the samples with linear PDMS. Despite the fact that the cyclic PDMS was volatile, even after 24 h, some PDMS remained at the sample surface as the container slowed down the evaporation. The surface reaction appears to be analogous to the linear PDMS, *i.e.* water repellency of the glass surface starts to increase immediately after contact with the PDMS (Table 3.9). After 24 h of grafting time, the contact angle hysteresis with low MW linear PDMS (770 g mol^{-1}) was about 25° and with the cyclic PDMS about 30°. Likely, in both cases, the grafted PDMS molecules are too short to fully cover the surface or to be sufficiently flexible. Indeed, the analogy of the surface reaction between the linear and cyclic PDMS indicates that the reaction occurs *via* hydrolysis of the siloxane backbone of PDMS, followed by condensation with the surface silanols. Possible hydrolysis of the methyl side groups can be excluded, as such a reaction would rapidly turn the PDMS film completely hydrophilic when contacting with water.

Table 3.9: Water repellency of glass surface after grafting of cyclic silicone decamethylcyclopentasiloxane (D5) at room temperature. *Glass surface after oxygen plasma cleaning and without any D5 grafting. Water perfectly spreads on the surface. **Glass surface after oxygen plasma cleaning and sonicating in toluene, ethanol, and water, 10 min in each solvent, respectively, without any D5 grafting. θ_a and θ_r cannot be determined on bare glass surfaces due to the spontaneous spreading of water drops.

Grafting time	θ [°]	θ_a [°]	θ_r [°]	θ_a−θ_r [°]	α [°]
15 min	65±2	71±1	41±3	30	-
24 h	79±2	82±6	52±4	30	-
*	~0	-	-	-	-
**	8±1	-	-	-	-

3.3.9 Grafting PDMS to Dehydroxylated Silicon Oxide

To get more information on the relevance of the surface silanols in the grafting of PDMS, we investigated the formation of coatings on partially dehydroxylated silicon oxide surfaces. Fully hydroxylated silicon dioxide surface has a hydroxyl group density of about 5 OH nm^{-2} [206]. Dehydroxylation of silicon dioxide surface, *i.e.* removal of surface OH-groups, starts at about 200°C *via* associative desorption of the OH-groups (Figure 3.5) leading to the formation of siloxane bridges (≡Si−O−Si≡) and water condensation at the surface[206]. We annealed silicon wafers in air at 500°C and at 900°C for 5 h to reduce the number of surface silanols. At first, physically adsorbed water is removed. This is followed by condensation of surface silanols to siloxane bridges. According to Agzamkhodzhaev et al.[230], the surface OH-group density is only 0.66 OH nm^{-2} after annealing in air at 900°C. Recovery of the surface OH-groups occurs *via* dissociative adsorption of water (Figure 3.6). The process involves the breaking of the siloxane bridges and is typically extremely slow at room temperature.

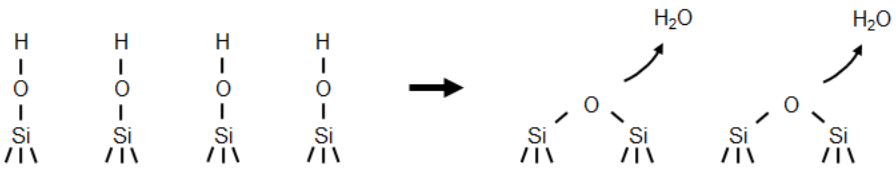

Figure 3.5: Dehydroxylation of silicon oxide surface *via* associative desorption of surface silanols at temperatures above 200°C.

Figure 3.6: Recovery of surface silanols on silicon oxide *via* dissociative adsorption of water.

Recovery of the surface OH-groups can take even 5 years[206]. Even so, room temperature grafting of PDMS on dehydroxylated surfaces is pronounced: after 24 h of grafting the sample that was annealed at 500°C exhibited similar or even better water repellency as compared to the corresponding oxygen plasma cleaned sample, *i.e.* the contact angle hysteresis was < 10° (Table 3.10). The sample annealed at 900°C displayed reduced, but still good water repellency with θ = 103±1° and contact angle hysteresis of 26±1° (Table 3.11a) after PDMS grafting. The reason for the lower water repellency of the sample annealed at 900°C is the reduced density of grafted PDMS chains at the surface, which was verified by X-ray photoelectron spectroscopy (XPS) from the amount of elemental carbon, which originates from the methyl side groups of grafted PDMS (Table 3.11b and Table 3.12), on the samples. Furthermore, XPS analysis on partially dehydroxylated (annealed in air at 900°C for 5 h) and hydroxylated (oxygen plasma cleaned) silicon oxide surfaces show that increasing the grafting time from 1 day to 5 days increased the amount of bound PDMS by about 10% on both samples (Table 3.11). This is a clear indication that the grafting density on one surface compared to the other remained unchanged and thus the already attached PDMS chains appear to grow linearly.

Table 3.10: Water repellency of PDMS films grafted to glass and silicon wafers at room temperature. Different pre-treatments were applied to the substrates prior to PDMS grafting: the substrates were either hydroxylated by oxygen plasma cleaning or partially dehydroxylated by annealing in air in an oven at 500°C for 5 h. PDMS molecular weight was 6 000 g mol^{-1}.

Substrate	Treatment	Grafting time [days]	θ [°]	θ_a [°]	θ_r [°]	θ_a−θ_r [°]	α [°]
Glass	O_2 plasma	1	106±1	109±1	97±1	12	12±2
Glass	Annealing at 500°C	1	106±1	108±1	101±1	7	12±2
Si wafer	O_2 plasma	1	106±1	109±1	99±1	10	17±2
Si wafer	Annealing at 500°C	1	107±1	108±1	100±1	8	14±2

Table 3.11: PDMS films grafted to hydroxylated and dehydroxylated silicon oxide at room temperature. a) Water repellency of PDMS films grafted to silicon wafers for 1 and 5 days. Different pre-treatments were applied to the substrates prior to the PDMS grafting: the substrates were either hydroxylated by oxygen plasma cleaning or partially dehydroxylated by annealing in air in an oven at 900°C for 5 h. b) Elemental composition of silicon wafer surfaces before and after the PDMS grafting. The relative percentages of elemental carbon (C), oxygen (O), and silicon (Si) were determined from the C1s, O1s, and $Si2p_{3/2}$ peaks, respectively, by XPS. PDMS molecular weight was 6 000 g mol^{-1}.

a)	Substrate	Treatment	Grafting time	θ [°]	θ_a [°]	θ_r [°]	$\theta_a - \theta_r$ [°]	α [°]
	Si wafer	O_2 plasma	No	0	-	-	-	-
	Si wafer	O_2 plasma	1 d	106±1	109±1	99±1	10	17±2
	Si wafer	O_2 plasma	5 d	106±1	108±1	100±1	8	8±1
	Si wafer	Annealing at 900°C	1 d	103±1	106±1	80±1	26	-
	Si wafer	Annealing at 900°C	5 d	107±1	109±2	96±2	13	27±3

b)	Substrate	Treatment	Grafting time [days]	C [%]	O [%]	Si [%]	C/(O+Si)
	Si wafer	O_2 plasma	No grafting	5.6±0.4	44.3±0.7	50.1±0.8	0.06
	Si wafer	O_2 plasma	1	19.9±0.4	31.4±0.6	48.7±0.2	0.25
	Si wafer	O_2 plasma	5	21.6±0.1	28.8±0.4	49.7±0.3	0.28
	Si wafer	Annealing at 900°C	1	14.5±0.2	43.4±0.2	42.1±0.3	0.17
	Si wafer	Annealing at 900°C	5	16.1±0.4	41.1±0.2	42.8±0.3	0.19

Table 3.12: Elemental composition of silicon wafer surfaces before and after PDMS grafting at room temperature for 24 h. Different pre-treatments were applied to the substrates prior to PDMS grafting: the silicon wafer surfaces were either oxygen plasma cleaned, or annealed in air in an oven at 500°C or 900°C for 5 h. The relative percentage for elemental carbon (C), oxygen (O), and silicon (Si) were determined from C1s, O1s, and $Si2p_{3/2}$ peaks by XPS. PDMS molecular weight was 6 000 g mol^{-1}.

Substrate	Treatment	Grafting time [days]	C [%]	O [%]	Si [%]
Si wafer	-	No grafting	9.7±0.3	26.6±0.1	63.6±0.3
Si wafer	O_2 plasma	No grafting	5.6±0.4	44.3±0.7	50.1±0.8
Si wafer	O_2 plasma	1	19.9±0.4	31.4±0.6	48.7±0.2
Si wafer	Annealing at 500°C	1	21.2±0.3	36.4±1.0	42.4±0.9
Si wafer	Annealing at 900°C	1	14.5±0.2	43.4±0.2	42.1±0.3

3.3.10 Growth of the Coating

To determine the PDMS film thickness, we used AFM force spectroscopy. On the pure glass reference surface, the tip directly jumped into the solid surface (red line in Figure 3.7a). On the PDMS coated surfaces, however, the tip could still move at a negative force over a couple of nanometers before the force turned repulsive again. The shape of the force curves is typical for liquid polymer films.[231-233] The PDMS film thickness was estimated from the distance between the first snap-in position during the approach and the next crossing of the x-axis (dashed vertical lines in Figure 3.7b–d). The elastic deformation of the remaining PDMS under the tip and the exact shape of the meniscus after the snap-in adds a systematic error of ±1 nm to the measured distances. The AFM experiments show that the PDMS film thickness grows from 2.8±1.1 nm after 1 day of grafting to 5.1±0.7 nm after 10 days of grafting and the adhesion force between the sample surface and the silicon tip of the AFM cantilever is suppressed from 7.1±0.7 nN to 2.6±0.4 nN, respectively (Figure 3.7a–d). To analyze the chemical nature of the bond we carried out Fourier-transform infrared (FTIR) measurements on densely packed silicon oxide particles (surface area = 200 m^2 g^{-1}) immersed in PDMS (Figure 3.8 and Supporting Information, Figure S3.8). The absorption band from the siloxane bonds of PDMS at 1000–1130 cm^{-1} first reduce and then increase in line with the proposed hydrolysis and condensation reactions of PDMS at the oxide surface.

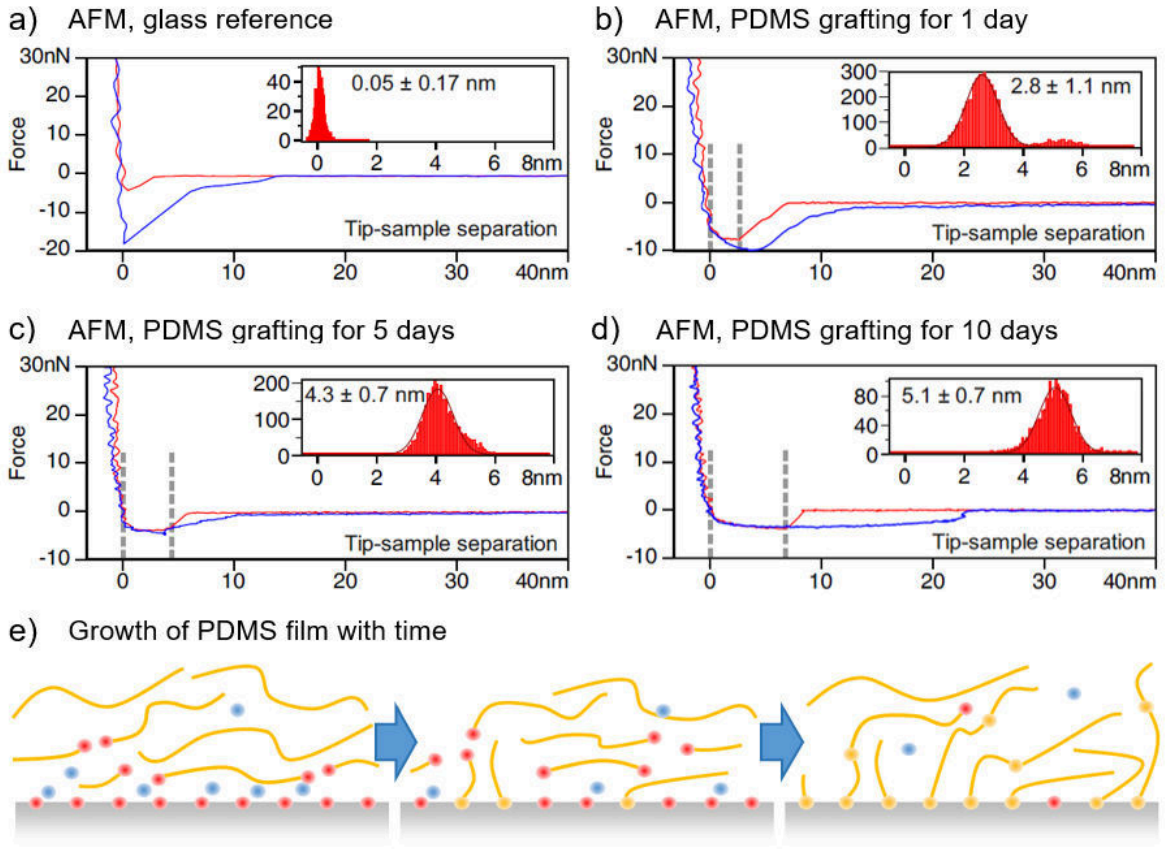

Figure 3.7: Grafting PDMS to silicon oxide. a) Representative AFM force curves recorded while approaching to (red color) and retracting from (blue color) pristine oxygen plasma cleaned glass, adhesion force = 17±3 nN, and room temperature grafted PDMS films on glass for b) 1 day, film thickness = 2.8±1.1 nm, adhesion force = 7.1±0.7 nN; c) 5 days, film thickness = 4.3±0.7 nm, adhesion force = 3.3±0.3 nN; and d) 10 days, film thickness = 5.1±0.7 nm, adhesion force = 2.6±0.4 nN. Insets: histogram and average of PDMS film thickness after the different grafting periods. In total 4096 force curves were recorded on each PDMS coated sample. e) Schematic of the PDMS film growth mechanism. Yellow strings indicate PDMS molecules. Blue dots indicate molecular water and red dots indicate hydroxyl groups at the substrate or the chain ends of hydrolyzed PDMS. Yellow dots indicate established chemical bonds *via* condensation of hydroxyl groups. In a–d) PDMS molecular weight was 6 000 g mol^{-1}.

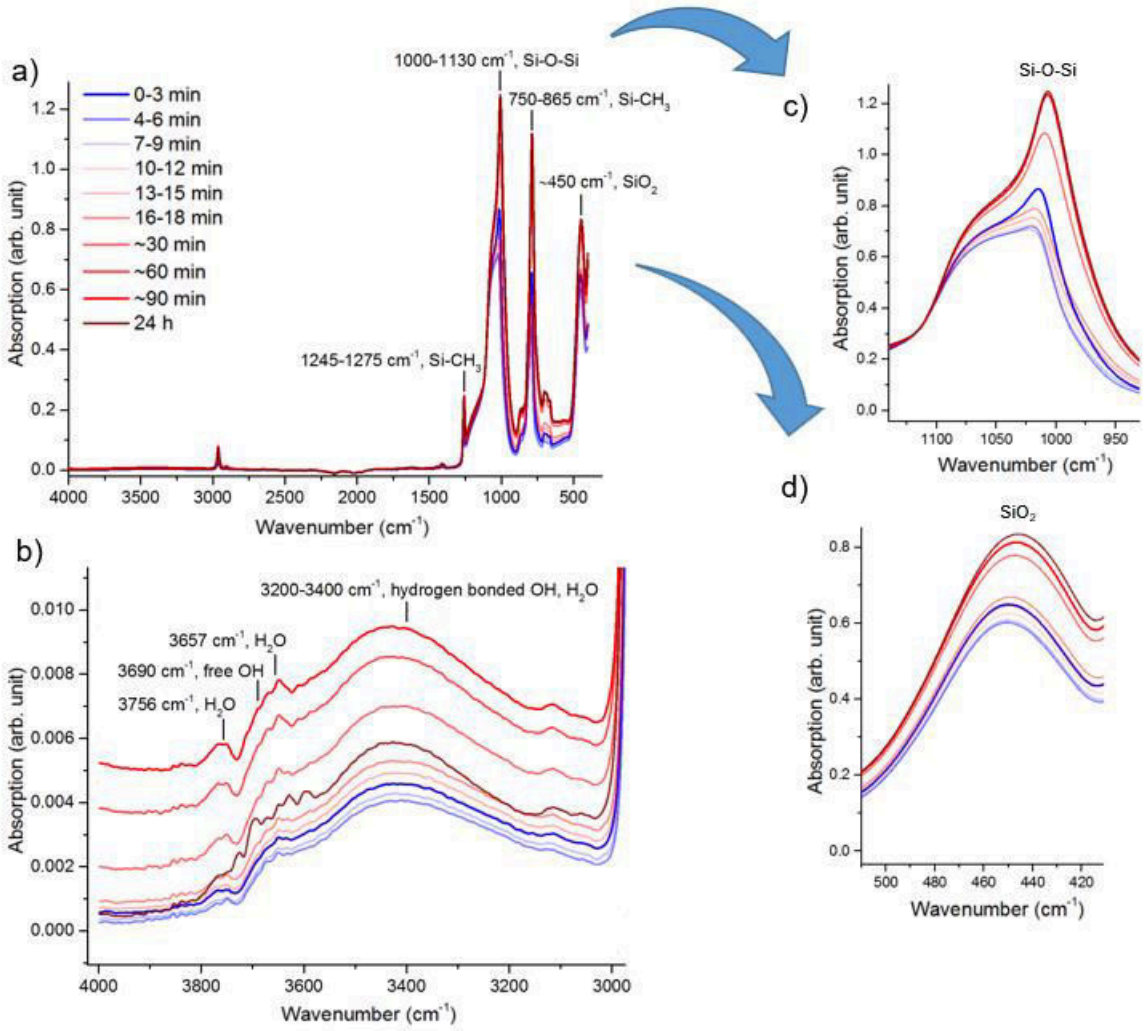

Figure 3.8: Monitoring chemical changes by FTIR during PDMS grafting to silicon oxide particles at room temperature. a) Evolution of the FTIR absorption spectrum after contacting PDMS with silicon oxide particles. b) Evolution of the absorption bands from hydroxyl groups and water during the grafting reaction. c, d) Magnifications of the characteristic bands of Si–O–Si and SiO_2 shown in a). Prior to the experiments the particles were densely packed and oxygen plasma cleaned to provide a sufficiently large surface area for the grafting reaction to enable detection of the chemical changes in PDMS during the reaction. PDMS molecular weight was 6 000 g mol^{-1}.

Surface-bound water plays an important role in the beginning of the reaction by hydrolyzing PDMS in the vicinity of the oxide surface. Since PDMS contains about 100 ppm molecular water[205] capable of diffusing through the film[182], indeed, the grafting reaction should not be limited to the vicinity of the oxide surface. Instead, as indicated by our results, the growth of the bound PDMS chains should continue at the distance of several nm above the surface *via* random hydrolysis and condensation reactions (Figures 3.4 and 4.7e, Table 3.11).

Another hint of the reactions between PDMS and silicon oxide was given by Sun et al.[198], who investigated the interaction of an AFM tip and a silicon oxide surface immersed in a PDMS fluid. They observed that, initially, an oscillatory interaction became monotonically repulsive after 10 h.

Such a repulsive force is an indication for the bound PDMS chains. Indeed, the reaction of PDMS and silicon oxide is generic. Breaking a single PDMS chain *via* hydrolysis – to create two hydroxyl-terminated PDMS chains readily reactive with the surface silanols – only requires a single water molecule. Sufficient amount of molecular water to initiate the grafting reaction at room temperature is always available at the silicon oxide surface as a layer of physisorbed water[205,206]. In addition, when a hydrolyzed PDMS chain binds to the oxide surface *via* condensation water is released (Figure 3.4). Thus, the availability of molecular water does not limit the grafting reaction even at a very low relative humidity (Table 3.2c).

Furthermore, our strategy does not require a fully hydroxylated or clean silicon oxide surface. The grafting reaction yields a drastic decrease in contact angle hysteresis down to about 10° also on partially dehydroxylated surfaces (Tables 3.10–3.12) and even on surfaces on which the silanol groups are covered by a contaminant layer, for example, hydrocarbons adsorbed from air (Table 3.13 and Supporting Information, Table S3.5).

The amount of grafted PDMS on the dehydroxylated surfaces does not correlate with the number of surface hydroxyl groups. The data reveal that the difference in the amount of elemental carbon detected on the surfaces, which originates from the methyl side groups of PDMS, is much less than the difference in the OH-group density at the fully hydroxylated and annealed surfaces. On the sample annealed at 500°C the amount of elemental carbon was even higher, 21.2±0.3%, than on the corresponding oxygen plasma cleaned sample on which the amount of carbon was 19.9±0.4% (Table 3.12). Likely, in this case, the removal of excess physisorbed water by annealing facilitated the PDMS grafting. In line with this result, both on glass and silicon wafer substrates contact angle hysteresis of water was 2–5° lower on the annealed samples at 500°C as compared to the oxygen plasma cleaned samples (Table 3.10). This indicates that the room temperature grafting reaction of PDMS on dehydroxylated silicon oxide surfaces involves siloxane bridge opening followed by covalent bonding of hydrolyzed PDMS to the surface (Figure 3.9). That is, surface hydroxyl groups are not necessarily needed for the grafting reaction on silicon oxide. Thus, the results indicate that hydrolyzed PDMS can open siloxane bonds at silicon oxide surfaces (Figure 3.9) and even replace chemisorbed contaminants (Figure 3.10) due to the far stronger ionic character of the Si–O bonds (50%) as compared to the C–O bonds (22%, Supporting Information, Table S3.1).

On both the plasma-cleaned and the annealed samples extended grafting time from 1 day to 5 days further increases the amount of grafted PDMS. In both cases, the amount of carbon increased by about 10%. This indicates that the grafting density ratio between the samples remains unchanged, and the increase in the amount of carbon is primarily due to the linear growth of the already attached PDMS chains (Table 3.11). A likely reason is that on a dehydroxylated surface, the opening of a siloxane bridge and bonding of a hydrolyzed PDMS does not release any water (Figure 3.9) and, therefore, PDMS hydrolysis in the vicinity of the surface – and thus establishing new grafting sites – is limited by the availability of molecular water.

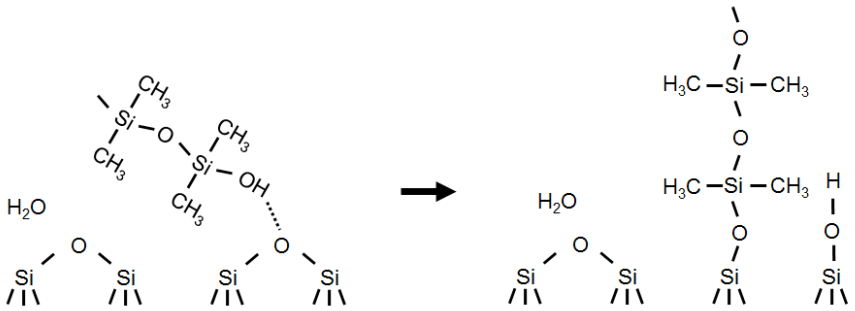

Figure 3.9: Proposed mechanism of PDMS grafting to dehydroxylated silicon oxide surface at room temperature. The opening of the siloxane bridges at the surface is initiated by hydroxylated PDMS. The bonding reaction on the dehydroxylated surface does not release molecular water. Thus, lack of molecular water at the surface slows down the grafting reaction as compared to the hydroxylated surface presented in Figure 4. Graffius et al.[205] explained bonding of PDMS on dehydroxylated silicon oxide at an elevated temperature of 100°C by a direct reaction between the PDMS backbone and siloxane bridges at the surface. Due to the extremely slow recovery of surface silanols at room temperature[206], we propose an alternative mechanism to explain the PDMS grafting to dehydroxylated silicon oxide surfaces.

3.3.11 Grafting PDMS to Contaminated Glass Surface

To investigate whether PDMS can also be grafted to surfaces where silanols are covered by organic impurities, we applied PDMS on glass which was not exposed to oxygen plasma cleaning. The glass surface thus contained a native contamination layer of low-surface-energy species, such as hydrocarbons. Such contaminations adsorb to the surface from the atmosphere[207], cover the surface silanols and thus lower the surface energy. Therefore, prior to grafting, water drops on the glass displayed a finite static contact angle θ = 43±3°. After 24 h of PDMS grafting at room temperature, the surface became water-repellent with θ = 103±1° and contact angle hysteresis of 26±1° (Table S3.5). After prolonged grafting time of 5 days and 10 days, contact angle hysteresis decreased to 14±2° and 10±2°, respectively (Table 3.13). That is, the hysteresis became as low as on plasma cleaned glass after PDMS grafting.

PDMS can also be grafted to a glass surface pre-treated with chemical vapor deposition (CVD) of trimethylchlorosilane. Prior to PDMS grafting, the surface silanols on the CVD coated sample were occupied by methyl groups. Therefore, the surface was repellent to water with θ = 84±1°. After 5 days of PDMS grafting at room temperature, the contact angle increased to θ = 100±1° (Table 3.14). These data indicate that PDMS can even substitute part of the methyl groups on the oxide surface. That is likely caused by the lower electronegativity of silicon as compared to carbon, *i.e.* oxygen–carbon bonds are replaced by more ionic oxygen–silicon bonds (Figure 10 and Supporting Information, Table S3.1).

Table 3.13: Water repellency of PDMS films grafted to contaminated glass at room temperature for 1–10 days. The glass surface was not cleaned by oxygen plasma prior to the grafting, *i.e.* most of the surface silanols were occupied by atmospheric contaminants such as hydrocarbons. PDMS molecular weight was 6 000 g mol^{-1}.

Grafting time [days]	θ [°]	θ_a [°]	θ_r [°]	$\theta_a - \theta_r$ [°]	α [°]
1	103±1	107±1	81±1	26	-
5	106±1	108±1	94±2	14	17±10
10	106±1	109±1	99±1	10	16±6

Table 3.14: Water repellency of PDMS films grafted to methylated glass surface at room temperature. The grafting time = 0 days presents wetting of a glass surface after CVD of trimethylchlorosilane. PDMS grafting was applied on the pristine methylated surface where surface silanols are occupied by the methyl groups. PDMS molecular weight was 6 000 g mol^{-1}.

Grafting time [days]	θ [°]	θ_a [°]	θ_r [°]	$\theta_a - \theta_r$ [°]	α [°]
0	84±1	86±1	67±1	19	-
1	88±1	92±1	66±1	26	-
5	100±1	103±1	75±2	28	-

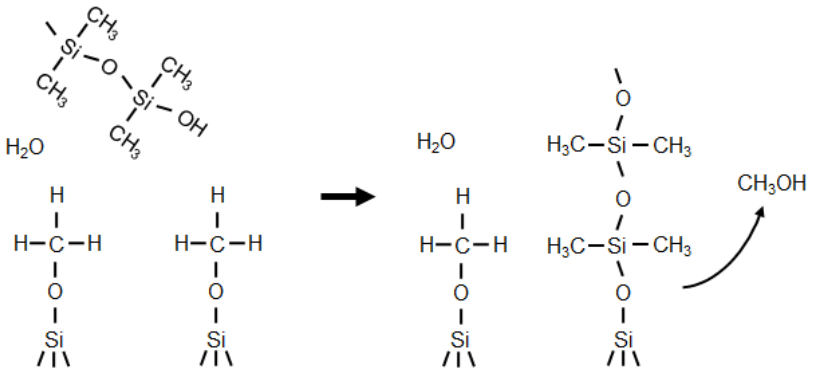

Figure 3.10: Proposed mechanism of PDMS grafting to a contaminated silicon oxide surface at room temperature.

3.4 Summary

In summary, our environmentally friendly method to fabricate transparent liquid-, adhesive-, and ice-repellent coatings which are mechanically stable and can be easily applied on a large scale does not require the use of any solvents nor does it release any chemicals or hazardous by-products to the environment. The coating shows advantageous properties including low sliding angles below 10° for various liquids, extremely low ice adhesion strength of 2.7±0.6 kPa, and easy cleanability. Therefore, we anticipate our work to open new avenues in tailoring surfaces with silicones. Indeed, knowledge on the reactivity of PDMS is crucial in understanding the formation of PDMS coatings and their properties, polymer filler interactions, degradation of silicone rubber in humid environments[199], or degradation of PDMS in nature[234].

3.5 Supporting Information

3.5.1 Supplementary Discussion

Characterizing wetting of surfaces by water

Surface water repellency is commonly characterized by measuring static contact angles θ after a water drop is deposited on a surface or by measuring advancing contact angles θ_a and receding contact angles θ_r when the water drop is inflated or deflated. The difference between θ_a and θ_r is termed contact angle hysteresis. It describes the adhesion force of the drop to the surface[217,220,235]. Additionally, sliding angle or roll-off angle, *i.e.* the angle at which a drop of certain size starts to move when the substrate is inclined, is used to characterize the wetting properties of surfaces. High receding contact angle and low sliding angle are required to shed drops easily and to keep surfaces clean.

Sliding drops

Hydrophobicity alone is not a sufficient condition to induce self-cleaning of a surface. Shedding of liquids, leaving the surface dry, is crucial. Otherwise, particle contamination on the surface cannot be collected by drops or contaminants from evaporating drops are left on the surface (Figure 3.1a and Video S3.2).

Both the velocity and the contact angle hysteresis of sliding water drops depend on the inclination angle of the sample (Table S3.2). At an inclination of 15° of a PDMS grafted glass surface, the drop velocity is about 10 µm s^{-1} and the contact angle hysteresis measured from the moving drops was only 4±1° (Figure S3.3). On the same sample surface, at an inclination of 45°, the drop velocity was of the order of 2.6 mm s^{-1}, and the contact angle hysteresis increased to 15°. That is, θ_a and θ_r are not absolute values but are dependent on the velocity of the moving three-phase contact lines in the front and the rear of the drop, respectively[236-239].

Organic liquids start to slide on the PDMS films much more easily than water. Typically, 10 µL drops start to slide at inclinations even below 5° (Figure 3.1f). In addition, the sliding velocity generally is much faster as compared to that of water. Already at inclinations below 10°, the sliding velocity of organic liquids is typically of the order of mm s^{-1}.

Light transmittance

The PDMS films are 100% transparent as verified by UV-Vis spectroscopy (Figure S3.4). This is due to the small refractive index mismatch, only about 3%, between PDMS and silicon oxide and because the coating film is only a few nm thick and does not contain any light reflecting surface structures which hinder light transmission.

Coating different substrates

Additionally to the borosilicate glass substrate used in the experiments, we grafted PDMS MW 6 000 g mol^{-1} to soda-lime laboratory glass and a glass vial (Video S3.5). After applying a thin silica layer (~3 nm thick) onto the substrate surface by the gas-phase Stöber-like reaction, we managed to PDMS-coat aluminum and stainless steel plates, and porous surfaces of polyester fabric and paper, Figure S3.5, Table S3.3, and Video S3.3.

PDMS films as anti-icing coatings

The PDMS films significantly reduce ice adhesion on glass. On the PDMS coated glass, ice adhesion strength was only 2.7±0.6 kPa, whereas on uncoated, clean glass surface the ice adhesion strength was 155±17 kPa. That is, the PDMS coating reduced the ice adhesion by more than 98% as compared to the uncoated glass surface.

Freezing of 50 µL drops that were used in the experiments takes only a few minutes. Therefore, with our ice adhesion measurement setup full ice adhesion is reached already after freezing time of 10 min. With large ice blocks that are typically used in ice adhesion measurements, freezing times of several hours (overnight) are required. Another advantage of the small drop size is that several independent measurements can be carried out on a small sample area (Figure S3.6). Therefore, our setup allows fast and repeated ice adhesion strength measurements. We measured ice adhesion strength on the PDMS coated glass repeatedly 20 times on 5 individual spots. We marked target positions for the drops underneath the glass sample so that the drops could be placed at the same location each time. Within the 20 experiments, the ice adhesion strength remained unchanged within the experimental accuracy (Figure 3.3b, inset).

In addition, we measured ice adhesion on some other, commonly used materials to verify our results with the results obtained by other groups with different ice adhesion measurement setups. We measured ice adhesion of 152±48 kPa on Teflon (PTFE), 104±25 kPa on cross-linked PDMS, 657±49 kPa on aluminum, and 235±34 kPa on stainless steel. The ice adhesion strength values measured on the reference materials in this work are of the same order of magnitude that other researchers have reported previously, Table S4[83,87,223,240-246].

FTIR monitoring of PDMS reactions at silicon oxide surface

We monitored the room temperature grafting reaction of PDMS *in-situ* by FTIR (Figures 3.8 and S3.7). To maximize the surface area for the reaction, we contacted PDMS (MW 6 000 g mol^{-1}) with densely packed silicon dioxide particles (surface area = 200 m^2 g^{-1}). Evolution of the whole spectrum after contacting PDMS with the particles is shown in Figure 3.8a and magnification of the absorption bands from hydroxyl groups and water at 3 000–4 000 cm^{-1} in Figure 3.8b. Magnifications of the characteristic bands for PDMS[247] and silicon dioxide[248] are shown in Figure 3.8c–d. At the beginning of the reaction, the bands from the methyl groups (Si–CH_3) and the siloxane backbone (Si–O–Si) of PDMS reduce. These changes are associated with the hydrolysis of PDMS by the physisorbed water at the silicon dioxide surface, *i.e.* the regular structure of PDMS chains containing the methyl groups and

siloxane bonds, $–Si(CH_3)_2–O–Si(CH_3)_2–$, is converted to hydroxyl terminated chains, $–Si(CH_3)_2–OH$. When the reaction proceeds, both the bands from the siloxane bonds and the methyl groups start to increase, indicating growth of attached PDMS chains *via* condensation of hydrolyzed PDMS. Notably, the increment in the signal from the siloxane bonds and the methyl groups during the grafting process does not arise solely from establishing new siloxane bonds while grafting the PDMS chains, but the replacement of the initial physisorbed water layer at the silicon dioxide surface also contributes to the increased signal.

It is possible that the changes shown by the FTIR spectra are also partially caused by capillary driven rearrangements within the particle–PDMS fluid system during the experiment. In addition, we cannot exclude that some air remained trapped between the particles. Nevertheless, the differences in the relative changes of the bands from the siloxane bonds and the methyl groups indicate chemical changes in PDMS, which are associated with the hydrolysis and condensation reactions during the room temperature grafting of PDMS on silicon oxide. For example, after 24 h of grafting the band from siloxane bonds still slightly increased (Figure 3.8c) while the bands from the methyl groups remained unchanged or even decreased. FTIR spectra for the neat PDMS fluid and the neat silicon dioxide particles are shown in Figures S3.7a and S3.7b, respectively.

Large-scale application of PDMS films

The PDMS films can be applied using well-established coating techniques suitable for large-scale production. To demonstrate the easy applicability of the coatings, we used a multitude of different approaches to deposit the coatings including painting, spraying, and roll-coating (Video S3.4). In large-scale production, it is desirable to avoid using solvents in all steps of the coating procedure. Therefore, we tested producing PDMS films without using any solvents, even in the washing step. After letting PDMS MW 6 000 g mol^{-1} react with the glass substrate for 24 h at room temperature, we simply polished the surface with a paper tissue so that all visible PDMS was removed (Video S3.4). After polishing, a tiny amount of unbound lubricating PDMS remains on the surface held in place by the grafted PDMS chains. Although the free PDMS can still continue reacting with the grafted PDMS, the anti-wetting properties of the film remained good after 1 month storing in laboratory air, *i.e.* contact angle hysteresis of water was 12±2° and the sliding angle for 10 µL water drops was 7±2°.

3.5.2 Supplementary Figures

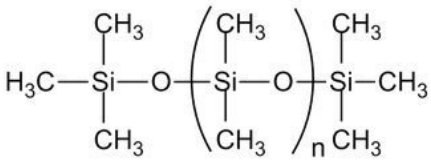

Figure S3.1: Molecular formula of trimethylsiloxy-terminated linear polydimethylsiloxane (PDMS).

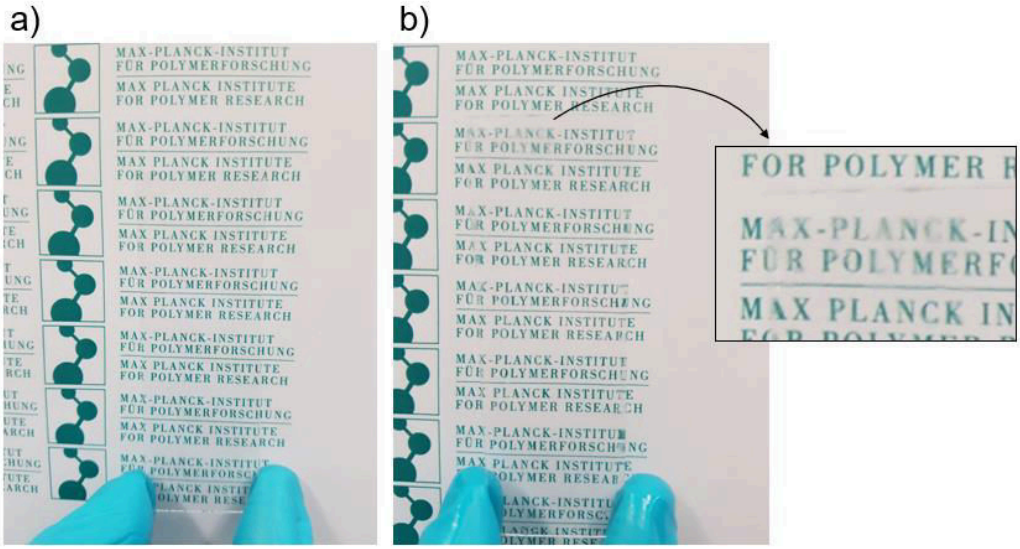

Figure S3.2: Unmodified and PDMS modified glass after insufficient rinsing. a) Undisturbed view to printed letters below an unmodified glass. b) Blurry view due to unbound, thick layer of PDMS remaining on glass after insufficient rinsing in solvents. The sample was rinsed in toluene, ethanol, and water for 10 s in each liquid.

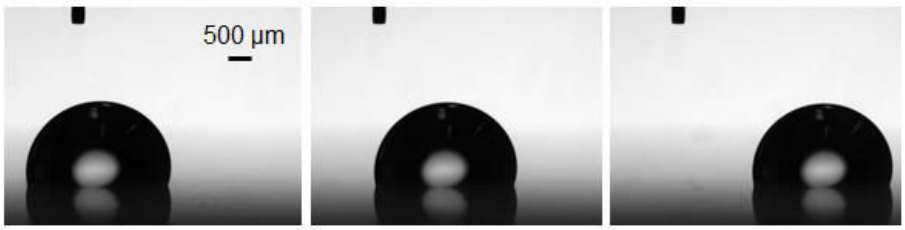

Figure S3.3: Water drop (10 µL) sliding down on a PDMS film grafted to glass at room temperature for 24 h. The sample was inclined by 15°, and the drop had a velocity of 10 µm s^{-1}. Contact angle hysteresis, *i.e.* the difference between θ_a in the front and θ_r in the rear of the drop, respectively, is 4°. PDMS molecular weight was 6 000 g mol^{-1}.

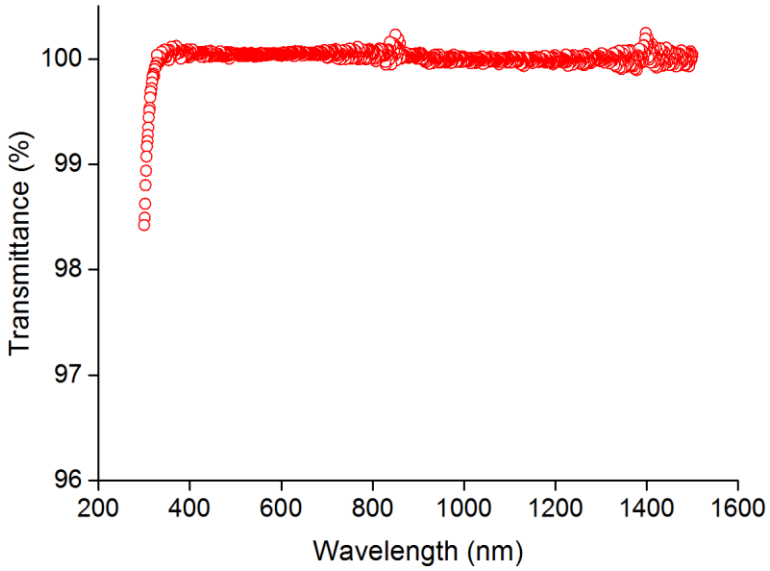

Figure S3.4: Light transmittance of PDMS film grafted to glass at room temperature for 24 h. PDMS molecular weight was 6 000 g mol^{-1}. Light transmittance is normalized to the transmittance of the uncoated glass substrate.

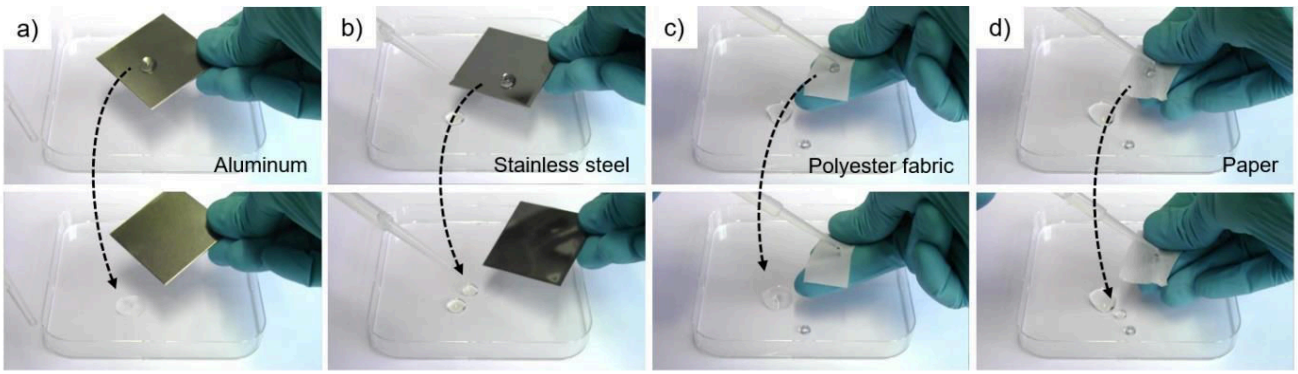

Figure S3.5: Water repellent PDMS films grafted to silica modified substrates. a) Aluminum, b) stainless steel, c) polyester fabric, and d) paper tissue grafted with PDMS at room temperature for 24 h. PDMS molecular weight was 6 000 g mol^{-1}.

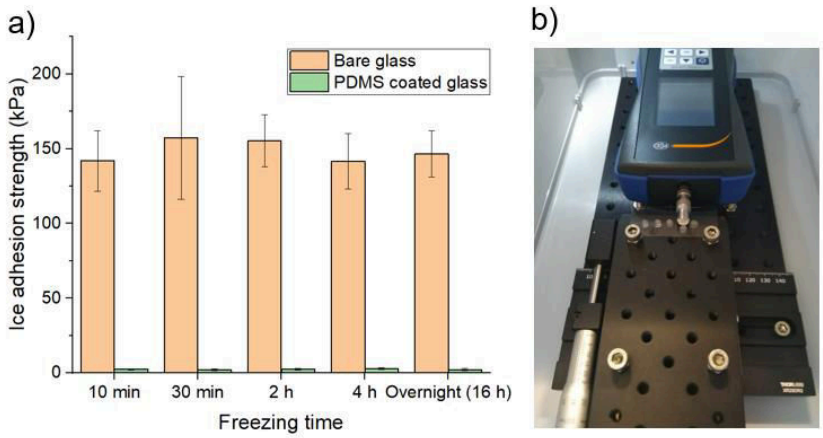

Figure S3.6: Characteristics of the home-built ice adhesion measurement device. The whole setup is built in a portable cooling chamber. The temperature inside the chamber remains at –8°C during the measurements. Drop size and wettability of the sample surface, *i.e.* the static contact angle, decide the drop/sample contact area. Therefore, the contact area for the 50 µL drop size that was used in the experiments was determined for each sample material independently prior to the force measurements. a) Ice adhesion strength with varying freezing time measured on uncoated glass and on PDMS films grafted to glass. Full ice adhesion strength on both sample materials is achieved already after 10 min of freezing. b) A photograph of the ice adhesion measurement setup. The small drop size allows rapid freezing and multiple parallel measurements on a small sample area. The PDMS films were grafted at room temperature for 24 h. PDMS molecular weight was 6 000 g mol^{-1}.

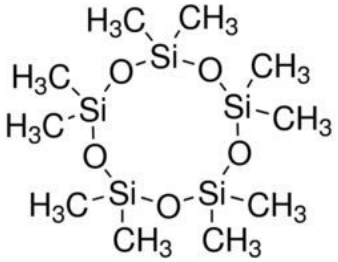

Figure S7. Molecular formula of decamethylcyclopentasiloxane (D5).

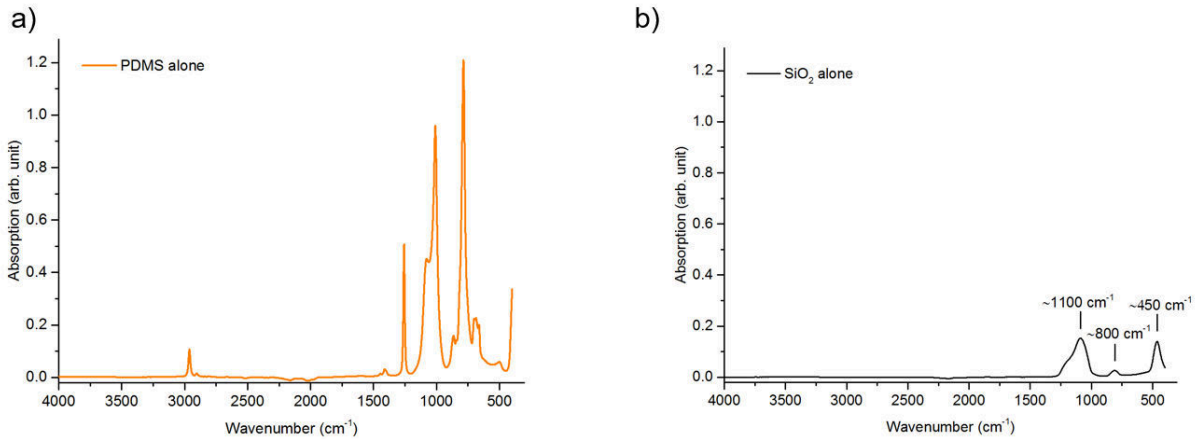

Figure S3.8: Absorption spectra from a) neat PDMS fluid and b) neat silicon dioxide particles.

3.5.3 Supplementary Tables

Table S3.1: Physicochemical properties of Si-X and C-X bonds[182].

Element [X]	Bond length [Å]		Ionic character [%]	
	Si-X	C-X	Si-X	C-X
Si	2.34	1.88	-	12
C	1.88	1.54	12	-
H	1.47	1.07	2	4
O	1.63	1.42	50	22

Table S3.2: Contact angle hysteresis for 10 µL water drops sliding down on a PDMS film grafted to glass at room temperature for 24 h. Drop velocity and contact angle hysteresis increase with increasing tilt angle of the substrate. PDMS molecular weight was 6 000 g mol^{-1}.

Tilt angle [°]	Velocity [µm s^{-1}]	θ_a [°]	θ_r [°]	θ_a–θ_r [°]
15	10	107±1	103±1	4
30	600	107±1	99±1	8
45	2600	109±2	94±3	15

Table S3.3: **Water repellency of PDMS films grafted to silica modified surfaces of aluminum, stainless steel, polyester fabric, and paper tissue at room temperature. PDMS molecular weight was 6 000 g mol^{-1}. Prior to the PDMS grafting, the aluminum and stainless steel plates showed water contact angle hysteresis of 104±3° and 54±2°, respectively. Before the grafting, the polyester fabric showed a static water contact angle θ of about 55°. However, θ continuously decreased as water spread within the surface structure *via* capillary wicking. Prior to the PDMS grafting, the paper tissue showed perfect wetting (θ = 0°) and absorption of water. Note, θ continuously decreased as water was sucked into the tissue *via* capillary wicking.**

Grafting time [h]	Substrate	θ [°]	θ_a [°]	θ_r [°]	$\theta_a - \theta_r$ [°]	α [°]
24	Aluminum	113±1	116±4	89±3	27	-
24	Stainless steel	108±1	111±1	101±1	10	12±2
24	Polyester fabric	143±4	147±2	134±4	13	40±5
24	Paper tissue	124±10	-	-	-	-

Table S3.4: Wettability and ice adhesion strength on different test materials. In the present work aluminum, stainless steel, bare glass, and Teflon were cleaned with ethanol and water and dried under nitrogen flow prior to measurements. Ice adhesion strength was measured at −8°C. The PDMS films were grafted at room temperature for 24 h. PDMS molecular weight was 6 000 g mol^{-1}.

Material	θ [°]	θ_a [°]	θ_r [°]	$\theta_a - \theta_r$ [°]	Ice adh. strength [kPa]
Aluminum	97±3	104±3	0	104	657±49; 317±25[223]
Stainless steel	86±1	91±1	38±2	53	235±34; 172±17[245]
Bare glass	53±1	58±1	16±1	42	155±17
Teflon (PTFE)	105±1[249]	110±1[249]	78±2[249]	32[249]	152±48; 268±13[249]; 44±3[244]
Fluorosilane coating	119±1	126±1	85±3	41	124±13
Cross-linked PDMS	116±1	119±1	95±1	24	104±25
Superhydrophobic surface	163±2[223]	-	-	6[223]	65.4±18[223]

Slippery liquid-infused surface	-	117±3[83]	115±3[83]	2[83]	15.6±3.6[83]
Grafted PDMS on glass	106±1	109±1	97±1	12	2.7±0.6

Reference ice adhesion values from Refs[223, 245, 249, 244, 83] were measured at the temperatures between −5°C and −10°C.

Table S3.5: Water repellency of PDMS films grafted to contaminated glass at room temperature for 1–24 h. The glass surface was not cleaned by oxygen plasma prior to the grafting. Thus, most of the surface silanols were occupied by atmospheric contaminants such as hydrocarbons. Therefore, the glass surface was less hydrophilic than plasma cleaned glass. PDMS molecular weight was 6 000 g mol^{-1}.

Grafting time [h]	θ [°]	θ_a [°]	θ_r [°]	θ_a−θ_r [°]	α [°]
1	85±1	87±1	55±1	32	-
2	92±1	97±1	62±1	35	-
24	103±1	107±1	81±1	26	-

3.5.4 Supplementary Videos

Video S3.1. Flow of water drops over lubricant-infused cross-linked PDMS film and grafted PDMS film (24 h grafting at room temperature, the molecular weight of PDMS was 6 000 g mol^{-1}). The cross-linked PDMS (Sylgard 184) was infused with PDMS fluid of molecular weight of 6 000 g mol^{-1}. The surfaces were inclined by 30° and water drops, about 150 drops/min with a volume of 50 µL per drop, were continuously sliding over the samples.

Video S3.2. Colored water drop (radius ≈ 2 mm, the drop was dyed with methylene blue) sliding down on the PDMS coated glass. The drop leaves behind a clean surface. The sample was inclined by 15°, and the drop was released to the surface from the height of 1 cm. On a fluorosilane coated glass the drop pins and leaves behind a stain. PDMS was grafted at room temperature for 24 h. PDMS molecular weight was 6 000 g mol^{-1}.

Video S3.3. PDMS coatings on different substrates. The coated materials are silica modified aluminum, stainless steel, polyester fabric, and paper. PDMS was grafted at room temperature for 24 h. PDMS molecular weight was 6 000 g mol^{-1}. The liquid used to demonstrate repellency was water.

Video S3.4. Grafting PDMS to glass. PDMS can be applied to surfaces by well-established methods. After the grafting reaction, excess PDMS was removed from the substrate with a paper tissue. PDMS molecular weight was 6 000 g mol^{-1}. The liquids used to demonstrate repellency were water, ethanol, *n*-hexadecane, and diiodomethane.

Video S3.5. Different types of glass coated with PDMS films. The coatings were applied on a 170 µm thick borosilicate cover glass slide, a 1 mm thick soda-lime laboratory glass, and a glass vial. PDMS was grafted at room temperature for 24 h. PDMS molecular weight was 6 000 g mol^{-1}. The liquid used to demonstrate repellency was water.

Video S3.6. Mechanical stability of the PDMS coatings. The coated glass withstands polishing with a cleaning tissue, rubbing, abrasion, scratching, and repeated attachment and detachment of an adhesive tape. The substrate was 1 mm thick soda-lime laboratory glass. PDMS was grafted at room temperature for 24 h. PDMS molecular weight was 6 000 g mol^{-1}. The liquid used to demonstrate repellency was water.

Video S3.7. Abrading a superamphiphobic coating with a rubber glove. The liquid used to demonstrate repellency was water.

Videos S3.8. The PDMS coated glass repels super glue. PDMS was grafted at room temperature for 24 h. PDMS molecular weight was 6 000 g mol^{-1}. The liquid used to demonstrate repellency was water.

Video S3.9. The PDMS coated glass repels permanent markers and provides easy-to-clean properties. The substrate was 1 mm thick soda-lime laboratory glass. PDMS was grafted at room temperature for 24 h. PDMS molecular weight was 6 000 g mol^{-1}. The liquid used to demonstrate repellency was water.

Video S3.10. The PDMS coated glass shows dewetting of spray paint. The substrate was 1 mm thick soda-lime laboratory glass. PDMS was grafted at room temperature for 24 h. PDMS molecular weight was 6 000 g mol^{-1}.

4 Universality of Friction Laws on Liquid-Infused Materials

Armelle Keiser[1,†], Philipp Baumli[2,†], Doris Vollmer[2], David Quéré[1]

† These two authors have contributed equally to this work.

[1] Armelle Keiser, David Quéré

Physique et Méchanique des Milieux Hétérogène, UMR 7636, CNRS, PSL Research University, ESPCI, 75005 Paris, France.

[2] Philipp Baumli, Doris Vollmer

Max Planck Institute for Polymer Research, Ackermannweg 10, 55128, Mainz, Germany. E-mail: vollmerd@mpip-mainz.mpg.de

Reprinted with permission from *Physical Review Fluids*, 5, 014005 (**2020**).

Liquid-infused surfaces (LISs) make drops remarkably mobile. However, the dynamics of those drops proved to be subtle, due to the numerous phases at stake (lubricating liquid, drop, solid texture, and air). In this article, we highlight the role played by a feature specific to LISs, namely, the "foot" of oil surrounding the drops and drawn by their surface tension. Consequently, viscous dissipation can be localized in four distinct regions, which we tune independently through various experimental setups. Despite this complexity, we evidence a universal scaling for the friction law and reconcile recent results produced on this topic.

4.1 Introduction

So-called liquid-infused surfaces (LISs) recently have attracted a lot of attention due to the extremely low adhesion of water or aqueous solutions to them. These materials are covered by a microscopic texture in which oil is infused so that another liquid deposited on them faces an impregnated porous-like substrate on which it barely pins[1,2,45,143]. Hence, the liquid (hereafter generically called water) is highly mobile, yet with some friction[28,45,47,54,160,250,251], whose nature is still under debate, owing to the complexity of the situation[45,47,54,160,250].

We focus here on the generic case of a drop facing a liquid of higher viscosity, which corresponds to water on nonvolatile oils. Smith *et al.*[45] showed that friction then occurs in the oil meniscus (or foot) surrounding the drop [sketched in Figure 4.1a]. If this friction were dominated by the bulk of the foot (assumed to have a constant shape), it would have a classical Stokes nature, evidenced by a linear relationship between friction and speed. However, Daniel *et al.*[54] and Keiser *et al.*[47] suggested that the shape of the meniscus is speed dependent, leading to a nonlinear relationship between friction and speed. It is worth discussing the generality of these ideas. A natural parameter, for instance, is the height of the underlying texture. Daniel *et al.* argued that the scaling between the friction and speed might depend on this height, with a linear relationship for tall pillars and a nonlinear relationship for short ones[54]. This change was attributed to the possibility of generating Landau-Levich oil films above short pillars, as drops move, while such films are absorbed by a tall texture[48,49]. We provide here experiments in a broad range of velocity, allowing us to discuss the role of the menisci front in the dissipation process, with the aim of establishing the scaling form(s) of the friction.

Our main conclusion is that the scaling law for the friction is surprisingly universal, varying as the power 2/3 of speed on both short and tall pillars. However, the prefactor in the law does depend on the pillar height, a consequence of the existence or absence of Landau-Levich films beneath the moving drop. A transition regime thus exists, depending on the pillar height and/or drop speed, where the scaling law is transiently lost. We finally confirm the generality of our results by studying two supplementary configurations, that of a drop confined in a Hele-Shaw cell and that of a bubble rising along an inclined LIS plunged in a water bath.

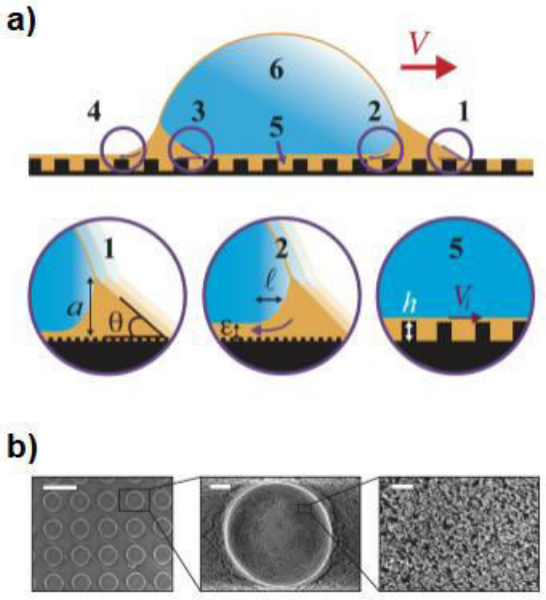

Figure 4.1: a) Schematic of a drop moving at a speed V on a liquid-infused material. Water (or aqueous phase) is blue, while the lubricating oil is orange. Six main dynamical regions can be defined. Four of them concern the oil foot around the drop, with advancing (regions 1 and 3) and receding (regions 2 and 4) sides. The two other regions are the drop itself (region 6) and the oil film with thickness h within the texture (region 5). The oil foot (size a) is supposed asymmetric, with an advancing angle θ at the front (region 1) and a film of thickness ε at the rear (region 2). V_i is the water/oil interface velocity (close-up in region 5). b) SEM images of the texture made of (Norland Optical Adhesive (NOA)) on a glass slide and treated with colloidal particles. Left: Top view of the pillar network (scale bar, 40 µm). Middle: Close-up on one pillar (scale bar, 4 µm). Right: Close-up on the nanoroughness at the pillar top (scale bar 400 nm).

4.2 Mobility of Drops on LIS

We consider micropillars (with density ϕ =23−25%) etched in SU-8 resin after photolithography, then coated with nanometric colloids (Glaco Mirror Coat, Soft 99). This double scale of roughness is visible in Figure 1b and it provides an ultralow hysteresis once the oil is infused[47,148]. Details on the preparation of the samples are given in Appendix A. The lubricating liquid is a silicone oil with surface tension γ_O = 20 mN/m and viscosity η_O = 100 mPa s while the drop is made of a water/glycerol mixture with η_w = 2 mPa s ($\eta_w << \eta_O$). After tilting the liquid-infused surfaces by an angle α, we measure the constant drop velocity V (reached after a few millimeters of descent) using a videocamera. In this stationary regime, the friction F is known, since it balances the weight $\rho g \Omega \sin\alpha$, where ρ is the water density, Ω the drop volume, and g the gravitational acceleration. Varying the tilting angle α from 1° to 40° increases friction by about two decades, which makes it possible to investigate the relationship between friction and speed thoroughly.

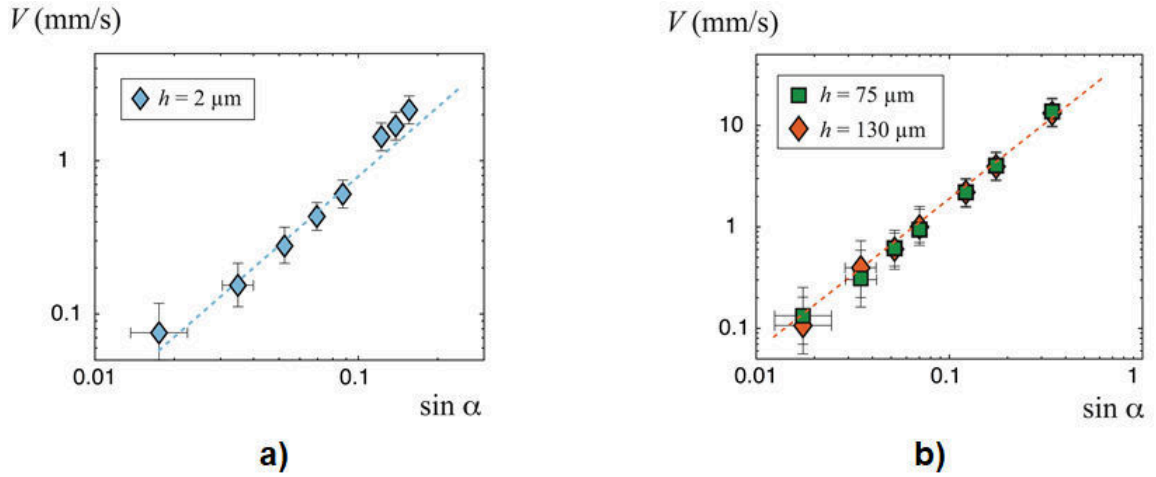

Figure 4.2: Speed V of water-glycerol drop (η_w = 2 mPa s, Ω = 20 µL) running down an impregnated, textured material (η_O = 100 mPa s), tilted by an angle α, as a function of the slope sinα. We compare what happens on (a)) short pillars (h = 2 µm) and (b)) tall pillars (h = 75 and 130 µm), two situations for which the physics is quite different: Landau-Levich films are expected on short pillars while they get absorbed in the tall texture. However, scaling laws with the same exponent (3/2, shown by dashes) are observed in both cases.

In Figure 4.2a, we plot the drop velocity V as a function of $sin\alpha$, the slope of the liquid-infused material having small pillars (h = 2 µm). As reported in the literature[47], the graph evidences a scaling behavior and we deduce from the slope of 3/2 drawn across the data that velocity increases as the power 2/3 of the driving force, confirming the nonlinear character of the mobility on a LIS. A second series of experiments is performed on much taller pillars (h = 75 and 130 µm). This situation is less explored despite its practical interests: the reservoir of oil inside the pillars is then about 50 times larger than previously. As observed in Figure 4.2b, a scaling law is also observed. The dashes show a slope similar to that in Figure 4.2a. This result appears robust, being valid for two pillar heights and a variation of the drop velocity by two orders of magnitude. But it is also surprising since switching from short to large pillars should manifest in the presence or absence of Landau-Levich films, respectively, making the hydrodynamics of the films and thus friction different in both cases.

We now discuss a possible origin for the universal scaling observed for the drop mobility on LIS and further explore differences between the two experiments reported in Figure 4.2.

4.3 The Complex Nature of Interfaces on a LIS

As sketched in Figure 4.1a, the existence of four phases (solid, oil, water, and air) in the wetting of LISs generates multiple kinds of interfaces close to which dissipation can take place. We wonder whether all these regions equally contribute to the total friction F and how the texture topology affects friction. In the following, we use the notation F_i to refer to the friction in region i. As pointed out by Daniel *et al.*[54] and by Keiser *et al.*[47], oil feet should be dynamically reshaped, which generates original sources of friction compared to more usual cases.

(1) Oil films may form at the rear of the feet (regions 2 and 4 in Figure 4.1a). In the Landau-Levich (LL) framework[49], a foot is deformed by a distance $l \sim RCa^{1/3}$, leading to a film thickness $\varepsilon \sim RCa^{2/3}$, where R is the drop radius and Ca is the capillary number at deposition ($Ca = \eta_o V/\gamma_{ow}$ in region 2, $Ca = \eta_o V/\gamma_o$ in region 4, with γ_{ow} and γ_o the oil-water and oil-air tensions, respectively). This classical result can be markedly corrected on pillars, depending on the ratio between the thickness ε and the pillar height h: as shown by Seiwert *et al.*[48], a LL film is expected only for $h < \varepsilon$, while slippage induced in the opposite limit ($h > \varepsilon$) prevents oil deposition above tall pillars. This criterion can be expressed in terms of velocity: LL films exist if the drop velocity V is larger than $V^* \sim (\gamma/\eta_o)(h/R)^{3/2}$. On short pillars, this criterion is always satisfied, while it can never be met on tall ones, V^* increasing by a factor 1000 when multiplying h by 100. Using interferometric measurements, Daniel *et al.* directly observed this wetting transition for drops on LIS, with a prefactor of order 3 for a pillar density $\phi = 25\%$[54]. It should be noted though, that this prefactor decreases as the pillar density increases, as recently observed for droplets confined in Hele-Shaw cells[155]. Coming back to the experiments in Figure 4.2 (with $\phi = 25\%$), V^* is 13 mm/s for $h \approx 100$ µm, a speed comparable to the maximal speed reached in our experiments. Hence, we do not expect LL films on such tall pillars. Conversely, V^* falls to 40 µm/s for $h \approx 2$ µm, so that LL deposition should concern the whole range of explored velocities for short pillars. In the latter case, the corresponding friction F_2 and F_4 scales as $2\pi(\eta_o V/\varepsilon)lR$, that is, $F_2 \sim 2\pi\gamma_{ow}RCa^{2/3}$ in region 2 and $F_4 \sim 2\pi\gamma_o RCa^{2/3}$ in region 4. These two quantities of similar amplitudes are not linear in velocity, a consequence of the difference in speed dependency of l and ε. Conversely, LL-friction can be simply neglected on tall pillars (or below V^*), which does not explain the scaling observed in that case.

(2) Yet, Keiser *et al.* reported that friction depends on the pillar density ϕ[47], which does not appear in (1). Oil feet move on a mixture of solid and oil (regions 1 and 3 in Figure 4.1a), which generates a dynamic angle θ at the front[147,154,252-255]. At small θ, the viscous force there can be written $\int(\eta_o V/\theta x)Rdx$, where θx is the wedge thickness at a distance x from its tip. Introducing the meniscus size a (typically 50 µm) and a molecular size b as cut-off distances, we deduce a friction $F_{1/3} \sim (\eta_o V/\theta)R\ ln(a/b)$[254,255]. The logarithmic factor, typically ~10, reflects the enhancement of the viscous force at contact lines. The model must be corrected on infused materials: the foot can slip on the thick oil layer between pillars so that dissipation mainly takes place on the pillar tops. Restricting friction to these tops provides: $F_{1/3} \sim (\eta_o V/\theta)\phi R\ ln(a/b)$. Balancing $F_{1/3}$ with the capillary force $\gamma R(1 - cos\theta) \approx \gamma R\theta^2/2$ yields Tanner's law, $\theta \sim Ca^{1/3}$ [154], and an explicit formula for the friction, $F_{1/3} \sim \phi^{2/3} ln^{2/3}(a/b)\ \gamma RCa^{2/3}$, with $\gamma = \gamma_o$ in region 1 and $\gamma = \gamma_{ow}$ in region 3. This friction being independent of the pillar's height, it is relevant on any kind of LIS – in particular on tall pillars, where there is no film deposition: this may explain the non-linear character of the scaling observed in Figure 4.2a. It should also be noted that the presence of LL-films on small pillars (or for $V > V^*$) may significantly reduce this friction in region 3.

Still, other dissipation mechanisms can be discussed. For instance, the friction in the subjacent film (region 5 in Figure 4.1a) turns out to be negligible, owing to the modest value of the velocity V_i at the oil/water interface. The stress balance at this interface writes $\eta_w V/R \sim \eta_o V_i/h$, which yields: $V_i \sim V\ \eta_w h/\eta_o R$. The corresponding force is $(\eta_o V_i/h)\ R^2 \sim \eta_w VR$, indeed much smaller than other viscous frictions for $\eta_w << \eta_o$. Smith *et al.*[45] finally considered the friction in the bulk of the foot (with size a), obtained by integrating the viscous stress $\eta_o V/a$ over the

surface area $2\pi aR$ [45]. The corresponding friction $F \sim 2\pi\eta_o VR \sim 2\pi R\gamma Ca$ is linear in velocity and thus expected to be negligible compared to the line friction in $Ca^{2/3}$ at small Ca.

4.4 Back to Experiments

We showed that dissipation at the foot fronts (regions 1 and 3) always needs to be considered, while friction in rear sides (regions 2 and 4) can be switched on and off by varying pillar height h or drop velocity V. Despite different physical contents, both frictions at the front and rear sides of the foot scale as $\gamma RCa^{2/3}$, which explains why the total friction F most generally scales as the power 2/3 of V (Figure 4.2). We can test the model more accurately by comparing our data to expected behaviours, as done in Figures 4.3a and 4.3b, where we also include data obtained by Daniel *et al.* with a similar texture.

These graphs allow us not only to test the scaling but also to compare friction on short and tall pillars. All data nicely collapse on a line of slope 1 (dashes) but the numerical coefficient depends on the category of pillars: friction is increased by about 60% on short pillars, compared to that on tall ones. These facts agree with our model. We indeed expect an additional LL friction on short pillars; and the coefficient of the front friction, $[\phi ln(a/b)]^{2/3}$ (that reflects both the composite nature of the substrate and the amplification of viscous effects in a wedge), should be of order unity, that is, comparable to the coefficient in the rear friction. We can finally complete these findings by two supplementary experiments:

(1) Since dissipation in the foot front was assumed to be always at stake, it is essential to show the reality of dynamic angles in regions 1 and 3. To that end, we visualize the moving menisci using laser scanning confocal microscopy, as described in the appendix. A water drop ($\Omega \approx 20$ µL) placed on a liquid-infused surface (h = 20 µm) is moved with a needle, parallel to the substrate, in the range of capillary numbers explored in Figure 4.3a. Figure 4.3c shows three successive images of region 1 at $Ca = 5.10^{-3}$ and $Ca = 10^{-2}$. Incorporating a fluorescent dye in the oil makes it grey in the image and visible both in the texture and in the foot, while water, pillars, and air appear in black[10]. Two major observations can be made. Firstly, the oil meniscus is stationary, even at the larger velocity. This assumption in the model was not obvious since flows might redistribute oil from the front to the rear of the drop, making, for instance, the foot globally smaller when velocity is higher and/or with size a varying along with the motion. Second, the foot is asymmetric, as we assumed: the rear (region 2) meets tangentially the substrate (and the resolution of the technique even confirms the absence of Landau-Levich deposition on these high pillars), while the flow stiffens the front (region 1) and produces a dynamic contact angle whose value increases with the drop speed. This also shows that viscous dissipation in region 2 (and 4) is not large enough to deform an oil meniscus on tall pillars from its quasi-static configuration, which justifies that we do not consider this dissipation in our balance.

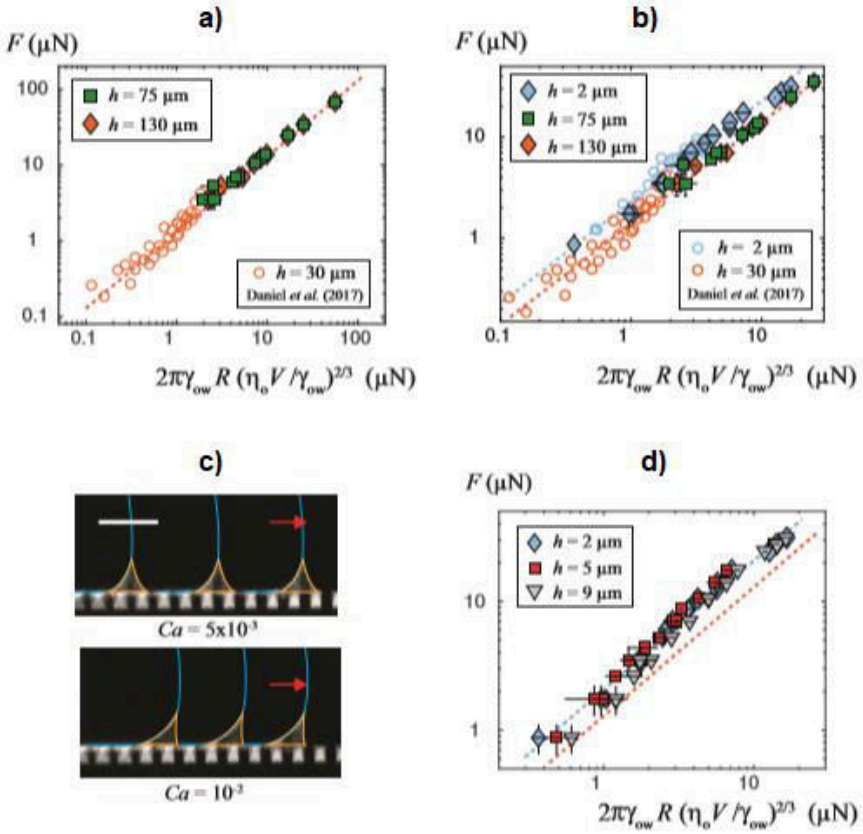

Figure 4.3: Friction of drops (η_w = 2 mPa s) running down tilted LIS (η_O = 100 mPa s). a) Friction F as a function of the scaling when dissipation is localised in the front foot, as expected for tall pillars (h = 75 µm, green squares; h = 130 µm, orange diamonds; h = 30 µm, orange circles, data by Daniel *et al.*[54]). Dashes show a slope 1. b) Comparison between the friction on short (h = 2 µm, blue diamonds, our data, and empty circles, data from Daniel *et al.*[54]) and tall pillars (h = 75 µm, green squares; h = 130 µm, orange diamonds). Orange and blue lines have a slope 1 with respective prefactors of 1.4 and 2.3 that stress the augmented friction on short pillars. c) Chronophotographs of the front foot of a moving drop. Laser scanning confocal microscopy and fluorescent dye allow us to distinguish the oil (in grey) from the rest (water, solid and air), in black. Images are respectively separated by 11.7 s (first picture, drop velocity V = 10 µm/s) and 1.7 s (second picture, V = 200 µm/s). The contour of the drop is highlighted in blue, and that of the meniscus in orange. The scale bar is 100 µm. d) For pillars with intermediate size (h = 5 µm and 9 µm), we observe a transition between the two regimes of friction (drawn with the orange and blue lines), a consequence of the Landau-Levich transition at sufficiently large capillary number.

(2) We can also consider pillars with intermediate height. Contrasting with the previous asymptotic situations, we then expect a transition to Landau-Levich deposition within the range of explored speed ($V^* \approx$ 300 µm/s for h = 9 µm), which should impact the friction. As seen in Figure 4.3d, data for h = 9 µm (grey triangles) leave the regime of "high friction" at large Ca for the regime of "low friction" at small Ca. The drop speed at the transition is $V^* \approx$ 200 µm/s, in reasonable agreement with our expectation. Interestingly, the transition is found to be shifted to smaller Ca for shorter pillars (h = 5 µm, red squares) – in agreement with the fact that LL-films

appear at a lower velocity on smaller texture. Hence varying the texture height allows us to control the resistance (and thus the speed) of drops on infused materials. This action is efficient since shortening the pillars roughly doubles the friction, without modifying its non-linear character in velocity.

4.5 Drops Confined in a Hele-Shaw Cell

In order to test the universality of the scaling laws, we now observe drops moving in a Hele-Shaw cell (with gap $H = 1110$ µm) whose both plates are textured and impregnated. Drops adopt a pancake shape[256-258], as sketched in Figure 4.4a. Increasing the tilt angle of the cell, we can vary the drop velocity from 0.01 mm/s to 20 mm/s, allowing us to measure the relationship between friction and velocity by more than three decades in speed.

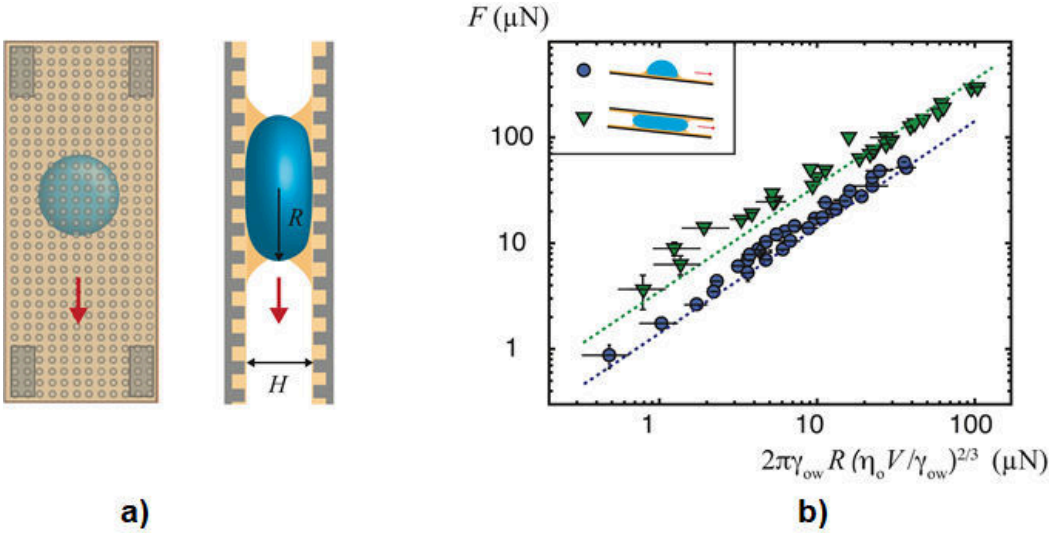

Figure 4.4: a) Front and side views of a Hele-Shaw LIS. A drop with radius R is confined between two LIS impregnated with silicon oil and separated by a distance $H < R$. The cell is tilted by an angle α ($\alpha = 90°$ in the schematics). b) Friction F of drops as a function of the scaling form $2\pi\gamma_{ow}R\,(\eta_o V/\gamma_{ow})^{2/3}$ on LIS (blue circles) and in Hele-Shaw LIS ($H = 1110$ µm, green triangles). All surfaces have the same texture (square lattice of circular pillars, $h = 20$ µm, $\phi = 23\%$). Oil and water viscosities are respectively $\eta_o = 100$ mPa s and $\eta_w = 2$ mPa s. Drop volumes are varied between 10 and 30 µL and tilt angles between 1° and 90°. Lines have a slope 1 and numerical factors of 1.4 (blue line), as in Figure 4.3, and 3.5 (green line). The small deviation at small speed (tilting angle < 5°) may be attributed to some residual adhesion, enhanced in this configuration.

Our results are displayed in Figure 4.4b. When plotting the friction as a function of the scaling form $2\pi\gamma_{ow}R(\eta_o V/\gamma_{ow})^{2/3}$, we observe that data align along two well-separated lines of slope 1. The numerical coefficient provided by the fit is 3.5 (green dashes) in the Hele-Shaw cell, that is,

about twice larger than on a LIS (blue dashes, where the numerical factor is 1.4). Even if the Hele-Shaw configuration strongly modifies the drop geometry, the foot dissipation should indeed simply double in a cell, that is when doubling the number of feet.

4.6 Bubbles on a LIS

We finally consider a gas bubble running up a tilted liquid-infused surface immersed in water (Figure 4.5a). Then, water and air are inverted, compared to the previous configurations.

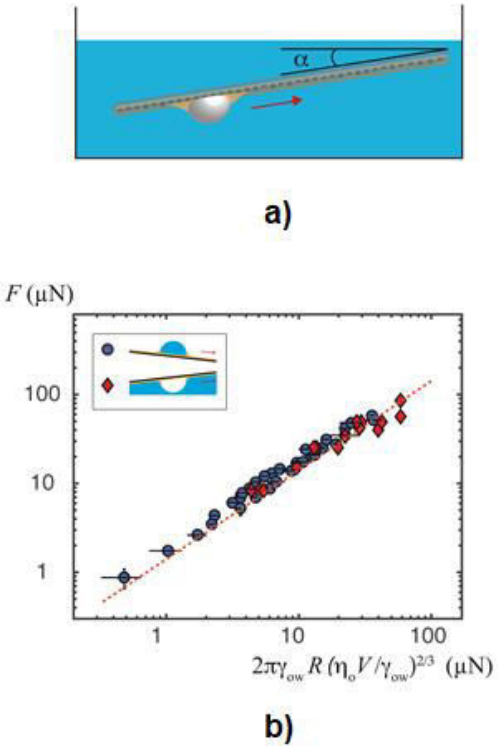

Figure 4.5: a) Air bubble with volume Ω rising on a tilted LIS immersed in water. Water and air are inverted, compared to Figure 4.1a. b) Friction F of drops or bubbles as a function of the scaling form $2\pi\gamma_{ow}R\,(\eta_o V/\gamma_{ow})^{2/3}$ for drops (blue circles) or bubbles (red diamonds) on a LIS with h = 20 µm and ϕ = 23%. Water viscosity is η_w = 2 mPa·s, and oil viscosity is η_o = 100 mPa s for the drop and η_o = 10, 100 or 1000 mPa s for the bubble. Drop and bubble volumes are 20 µL and 10 µL, respectively, and tilt angle is varied between 1° and 30°. The line has a slope 1 and a numerical factor of 1.4, as in Figure 4.3.

This is reminiscent of the historical experiment of Bretherthon[259], where a bubble confined in a capillary tube of radius R is driven by pressure. Then, the friction in the liquid wedge at the front of the drop was shown to scale as $\gamma RCa^{2/3}$. Non-confined bubbles moving on smooth immersed solids have also been discussed[260-262]. In that case the deposition of a film between the bubble and the solid substrate generates a wedge friction still scaling as $Ca^{2/3}$. The situation of bubbles moving on immersed LIS might induce differences: the presence of oil menisci generates two extra dissipative terms, in regions 1 and 4; in addition, the solid surface is not smooth but textured.

Yet, data for drops and bubbles are found to be superimposed (Figure 4.5b), contrasting with what we would find if we did the same inversion on a regular, hydrophobic solid. This confirms the negligible role of water and air viscosity in the viscous dissipation and eventually provides independent proof of the role of the oil meniscus (equally present for drops and bubbles) in the dissipation associated with the fluid motion.

4.7 Summary

On the whole, the friction force on a LIS most generally scales as $V^{2/3}$, a unique behaviour despite the multiple possible causes of dissipation – that eventually condense in a universal friction law. In addition, the numerical coefficient in the friction (and thus the drop speed) can be efficiently tuned by the pillar height, which shows that the use of texture is not only relevant for diminishing the liquid adhesion, but also to adjust its friction.

4.8 Acknowledgments

This work has received the support of Institut Pierre-Gilles de Gennes (équipement d'excellence Investissements d'avenir, programme ANR-10-EQPX-34), and the European Union's Horizon 2020 research and innovation program ITN LubISS No 722497. The authors thank A. Kaltbeitzel and A. Naga for taking the confocal images and for stimulating discussions.

4.9 Appendix A: Fabrication of the Fabrication of the Surfaces and Imaging

Textured surfaces are obtained using SU-8 photolithography. A layer of SU-8 resin is spin-coated on the surface of a clean, dehydrated silicon wafer. The rotating speed imposes the deposited thickness and thus the pillar height. Reticulation of pillars is performed by UV-light through a mask, and the obtained texture consists of square arrays of either circular or rectangular pillars. The second scale of roughness is added by dipping the microtextured material in a solution of Glaco Mirror Coat (Soft 99). After evaporation of the solvent (drying at 70°C for 30 min.), both the substrate and the pillars are coated with a layer of hydrophobic nanobeads (typical size 30 nm), as shown in Figure 4.6.

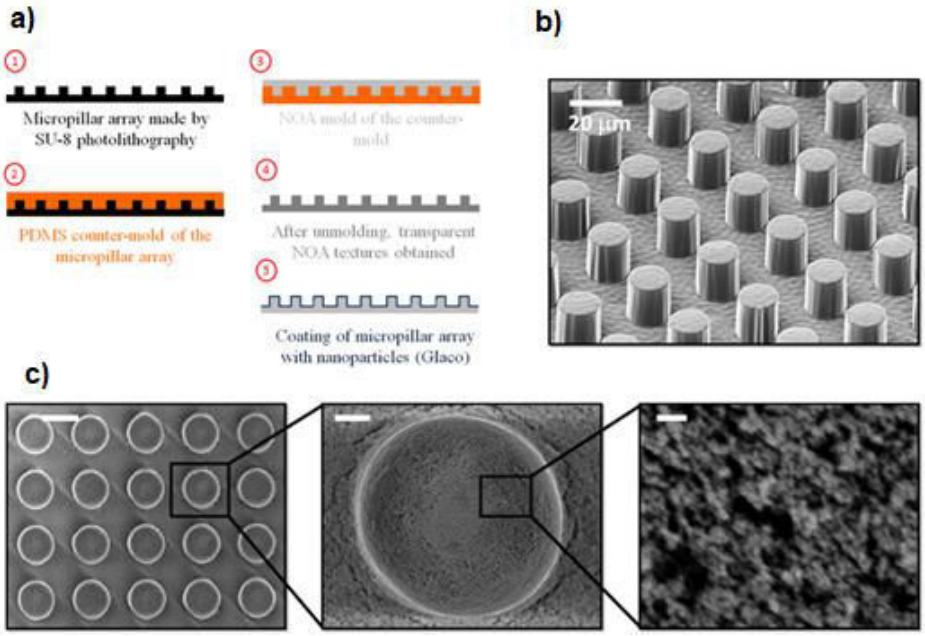

Figure 4.6 a) Schematic of the main steps to obtain transparent textured surfaces in NOA optical adhesive on a glass slide. b) SEM images of the textures made of NOA optical adhesive on a glass slide. c) Close-up on the nano-roughness at the pillar tops on the Glaco-treated surfaces. Left: top view of the pillar network (bar: 40 µm). Middle: close-up on one pillar (bar: 4 µm). Right: close-up on the pillar top (bar: 400 nm).

The procedure is repeated three times to ensure a homogeneous coating. Impregnation of the surfaces is then achieved by capillarity, taking special care not to over-impregnate the surfaces. To that end, surfaces are tilted with their lower side in contact with a bath of silicone oil of viscosity η_o so that oil rises within the texture. Transparent surfaces (necessary for the experiments in the Hele-Shaw cell) are obtained by two additional steps: 1) fabrication of a PDMS counter-mold of the SU-8 texture; 2) mold of this counter-mold with a transparent optical adhesive (NOA, Norland Optical Adhesive) on a glass slide. This protocol is shown in Figure 4.6a, and SEM images of the transparent surfaces obtained (60 mm x 24 mm, thickness: ≈ 170 µm) with the NOA optical adhesive before and after the coating with nanobeads are shown in Figures. 4.6b and 4.6c, respectively.

Silicone oil does not completely wet neither SU-8 nor NOA in an aqueous environment. Thus, direct contact between the drop and the pillar tops exists if no Glaco-treatment is made[47], which explains why the two scales of roughness are necessary to provide an ultra-low adhesion of water with roll-off angles below 1° for a 20 µL drop[47,148]. The impregnation method must also be stressed. Beyond introducing a layer of oil of uncontrolled thickness, over-impregnation will profoundly affect the dissipation of the front menisci (through the logarithm factor discussed in the main paper). As this thickness is not controllable over an extended period of time, over-impregnation will lead to scattered measurements of the friction force.

An inverted laser scanning confocal microscope (Leica TCS SP8 SMD) equipped with a 40x/1.11 water immersion objective lens (Olympus) was employed to image the oil meniscus surrounding the aqueous drop. The free working distance of the objective is 0.65 mm. The drop is moved by a glass capillary that pins the liquid and entrains it. Scanned areas are 400 x 400 µm^2, if not stated otherwise. Horizontal and vertical resolutions are ~500 nm and ~1 µm, respectively, and the time span between successive images is 0.78 s (1.29 fps). The scanning frequency is 400 Hz. Images are

acquired at different heights with respect to the bottom surface of the micropillar substrate. The silicone oil is dyed with a TDI-derivative (terrylene diimide-based dye[263], or NileRed from Sigma Aldrich). After impregnation, the fluorescence of the silicone oil within the texture and in the meniscus appears in grey, while pillars, water and air remain black. All chemicals were used as received. Processing of the confocal images is done with the Java-based open-source image processing software IMAGEJ/FIJI. Contrast and brightness are optimized, and smoothening algorithms are applied to further improve the image quality by minimizing the number of intensity variations.

4.10 Appendix B: Complements in Hele-Shaw Cells

Due to the confined geometry, the experiments in the Hele-Shaw cell show scaling laws that slightly differ from the one derived in Keiser *et al.*[47] . We present here supplementary results about this special geometry (Figure 4.7).

First, the viscosity of the drop has been varied to explore regions not only with $\eta_o >> \eta_w$ but also with $\eta_o << \eta_w$. Two main regimes appear (Figure 4.7), showing that dissipation is either localized in the oil (when $\eta_o >> \eta_w$) or in the drop (when $\eta_o << \eta_w$), as known for non-confined drops[47,250].

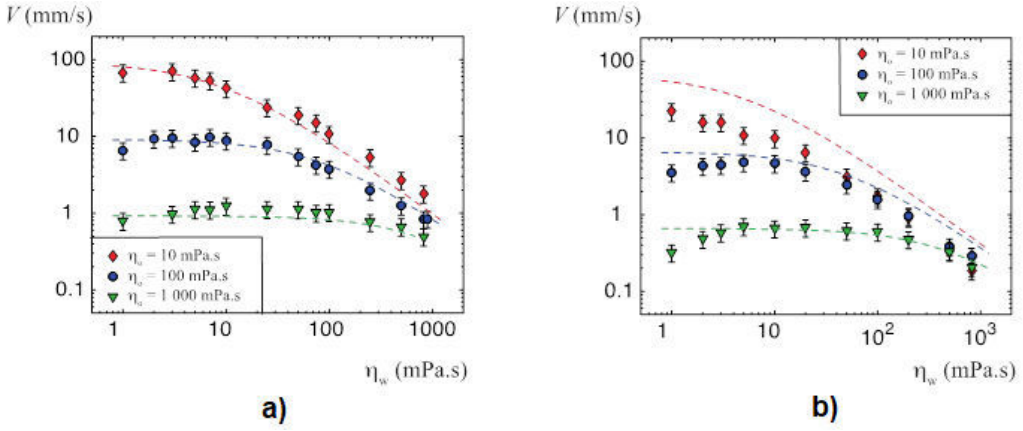

Figure 4.7: Speed V of water/glycerol mixtures (Ω = 10 µL, viscosity η_w) confined in a vertical Hele-Shaw cell of thickness 1110 µm (a) or 720 µm (b). The cell walls are LIS impregnated by silicone oil with viscosity η_o = 10 mPa s (red diamonds), 100 mPa s (blue circles) or 1000 mPa s (green triangles). At low η_w, the speed is nearly independent of η_w. At large η_w, the speed becomes inversely proportional to η_w. Dashes show the speed obtained by balancing gravity with the total friction in the drop and in the menisci (see main text). For the Hele-Shaw cell of thickness 720 µm, the agreement between experiments and model is less convincing at low oil viscosity. The drops then become slightly elliptic, that is, of larger perimeter, which might contribute to increase the viscous dissipation and thus lower the velocity.

At high drop viscosity ($\eta_w >> \eta_o$), dissipation takes place in the drop and the friction is proportional to the speed (Figure 4.8a).

In this simplified configuration (compared to the case of a non-confined drop, explore by Keiser *et al.*[47]), we can exactly express the prefactor in the Poiseuille force, which yields: $F_\eta = 12\pi R^2 \eta_w V/H$. Balancing this friction with the driving force $\rho g \pi R^2 H \sin\alpha$, we get:

$$V = \rho g H \sin\alpha / 12 \eta_w$$

Due to the pancake shape of the drop in this geometry, the velocity is found to be independent of the drop radius (and volume), which is indeed observed in Figure 4.8b.

In the opposite limit ($\eta_o >> \eta_w$), the dissipation localizes in the oil foot, as described in the main text, leading to a non-linear relation between the friction force and speed (Figure 4.8c). Balancing the driving force $\rho g \pi R^2 H \sin\alpha$ with the friction force $F_\eta = 2\pi R \phi \gamma Ca^{2/3} L$ leads to a new expression for the drop speed:

$$V = (\rho g \sin\alpha / 2\phi L)^{3/2} (\Omega H/\pi)^{3/4} / \eta\gamma^{1/2}$$

Both the scaling of the speed V with the driving force and with the volume are verified in the Figures 4.3c and 4.3d, where the dashes show the slopes 3/2 and 3/4, respectively.

A general relationship between drop velocity and viscosity can finally be obtained by solving the implicit equation $\rho g \Omega \sin\alpha = 2(2\pi R \gamma Ca^{2/3} \phi^{2/3} \ln^{2/3}(a/b)) + 12\pi R^2 \eta_w V/H$, the balance of gravity with the total friction (in both oil menisci and in the drop). Doing so, we find a very good agreement (without any adjustable parameters other than the logarithm factor taken as 10, its expected value) between the model and the whole set of data, as seen in Figure 4.7.

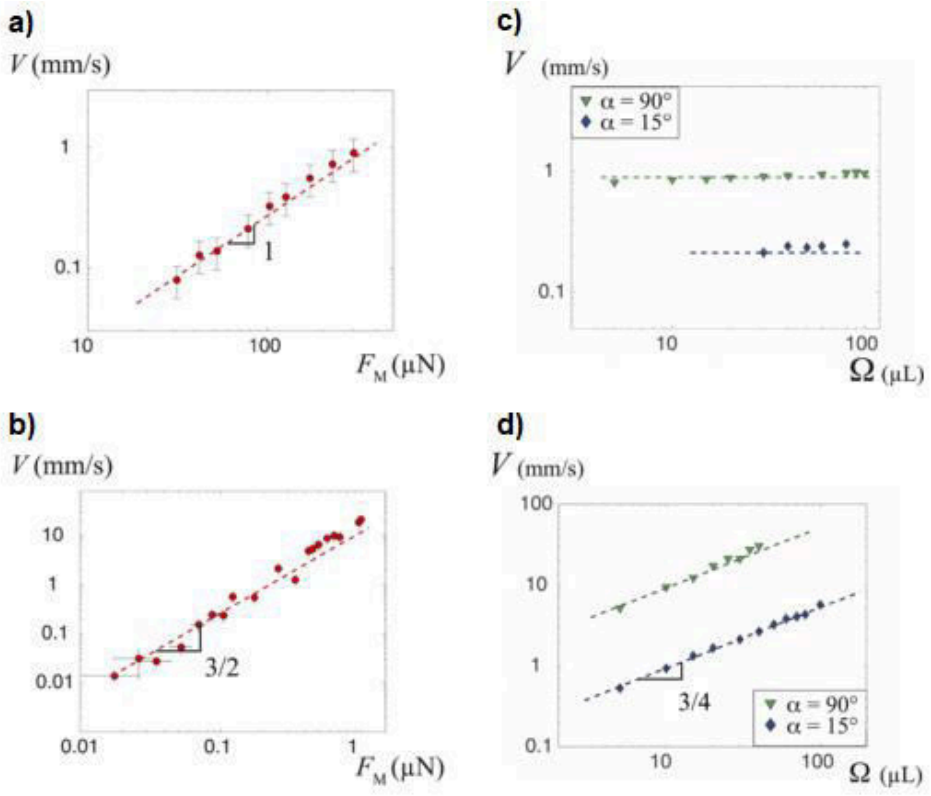

Figure 4.8 : a) Speed V of a drop (Ω = 30 µL, η_w = 900 mPa s) in a Hele-Shaw cell impregnated with silicone oil with viscosity η_o = 100 mPa s as a function of the driving force $F_M = \rho g \Omega \sin\alpha$. For $\eta_w >> \eta_o$, dissipation localizes in the drop, which makes the friction linear in speed. b) Then, the speed is observed to be independent of the drop volume Ω, as predicted by our model. c) Same experiment as in (a) for η_w = 2 mPa s and η_o = 100 mPa s ($\eta_w << \eta_o$). Then dissipation localizes in the oil and the dependency between friction with speed becomes non-linear. d) In this case, the speed varies as the power ¾ of Ω again in accord with our expectations.

5 Depleting Hydrogels with Oil Flows

P. Baumli[1,†], E. Lorusso[2,†], L. Hauer[1,†], A. Sharifi-Aghili[1], K. Hegner[1], M. d´Acunzi[1], J. Gutmann[2], B. Dünweg[1], and D. Vollmer[1,*]

† Contributed Equally

* Corresponding Author: vollmerd@mpip-mainz.mpg.de

1 Max Planck Institute for Polymer Research, Ackermannweg 10, 55128 Mainz, Germany.

2 Deutsches Textilforschungszentrum Nord-West ÖP GmbH, Adlerstraße 1, 47798 Krefeld, Germany.

This work is currently in the final stages of preparation and is close to *submission*.

Hydrogels are well-known for their outstanding performance to bind and hold aqueous solutions. Research focused on a discussion of the polymer conformation both under static and dynamic conditions to understand this unique phenomenon. However, little is known about the interaction of hydrogels with oil. How resilient are hydrogels to shear flows of oil? Here we investigate the depletion dynamics of a hydrogel by confocal laser scanning microscopy. As model gels, we use a weak polyelectrolyte (PAA) and a thermo-responsive hydrogel (PNIPAm). The water-swollen hydrogels are subjected to a shear flow of neat silicone oil. Notably, dehydration and shrinking of the hydrogel-coating progress linearly independent of investigated flow conditions and hydrogel-coating. The depletion mechanism is quantitatively modelled by an adjusted diffusion model.

5.1 Introduction

Hydrogels are ubiquitous in our daily lives. Everyday applications range from jelly pudding and diapers to contact lenses and scaffolds in tissue engineering[264-266]. Hydrogels are three-dimensional networks of hydrophilic polymers, facilitated by chemical (covalent interactions) or physical crosslinking (noncovalent interactions), such as entanglements. Chemical or physical crosslinking provides physical and structural integrity. All hydrogels have in common that they can bind large amounts of water, even as much as 99%[267-269]. Enthalpic and/or entropic gains are the driving forces for swelling of the polymer network in water. Entropic gains are dominated by the gain in translational entropy of dissociated counterions. The response of a hydrogel to external stimuli depends on its bulk structure, characterized by the polymer fraction in the swollen state, the crosslinking density, and the corresponding mesh size[270-272]. In most cases, swelling/deswelling is induced by a variation in an external stimulus, including pH[273], salt, temperature[274,275], and light[276,277]. Then, swelling is generally reversible[278-280].

A neutral hydrogel immersed in a fluid experiences two opposing forces[268]. The thermodynamic force of mixing is opposed by the elastic contractive forces[281,282] of polymer chains that balance upon establishing the equilibrium swelling state[283,284]. Hydrogels based on Poly(N-isopropylacrylamide) (PNIPAm) are among the most prominent cases of neutral, albeit temperature-sensitive hydrogels[285,286]. The degree of swelling of PNIPAm can conveniently be tuned by changing the temperature because it displays a lower critical solution temperature (LCST) of 32°C.

In the case of charged hydrogels (cationic or anionic), one distinguished between strong and weak polyelectrolytes. For strong polyelectrolytes, the maximum counterion concentration and the related maximum degree of swelling are determined by Manning condensation. For weak polyelectrolytes, the maximum counterion concentration can be tuned by the pH. Both for strong and weak polyelectrolytes, the degree of swelling depends on the ionic strength, reflected in the Debye screening length.

For polyelectrolytes, the Donnan equilibrium dictates that upon an increasing ionic strength of the swelling agent, the concentration of ions within the hydrogel must increase[287,288]. The electrostatic interactions between the ions contribute to the osmotic pressure, which is the driving force for swelling[283]. Hydrogels based on poly(acrylic acid) (PAA), are known to show *pH*- and ionic strength-dependent swelling kinetics in these gels[289].

Polyelectrolyte multilayers are swelling in a humid atmosphere (≈ 40% RH at room temperature). The water contact angle formed by a sessile drop on the polyelectrolyte reflects the swelling state of the multilayer. It depends on the nature of the outermost exposed layer of the polyelectrolyte[290 291-293], *i.e.* drops spread (vanishing contact angle) in a water-saturated atmosphere[290].

The swelling state achieved in a water-saturated atmosphere differs from the swelling state in liquid water[290]. In liquid water, the polyelectrolyte multilayers generally reach greater thicknesses than only in contact with water-saturated vapor, independent of the nature of the outermost layer (polycation or polyanion)[294]. The swelling kinetics of hydrogels are either diffusion-controlled (Fick´s Law) or relaxation-controlled[283]. The swelling kinetics is diffusion-controlled, provided that the water diffusion into the hydrogel occurs much faster than the relaxation of the polymer chains[295]. In the case of polymer networks of extremely poor chain mobility, the characteristic time of relaxation exceeds the characteristic time scale of diffusion[296,297].

We demonstrate that the hydrogel-based coating dehydrates linearly upon shear-flow of oil for a wide variety of flow conditions independent of the exact nature of the hydrogel-coating. Dehydration of the hydrogel-coating is followed by confocal laser scanning microscopy. Dehydration progresses linearly and independent of the flow velocity, oil viscosity, and the chemical nature of the hydrogel. The model system considered is the polyelectrolyte PAA (poly(acrylic acid)) sheared with silicone oil. Our findings are generalized by comparing the results obtained for poly(acrylic acid)-based hydrogels to subjecting the strongly temperature-sensitive hydrogel PNIPAm (poly(N-isopropyl acrylamide)) to identical shearing conditions.

5.2 Results and Discussion

We are inspired by fish skin whose structure (micro-and nanostructure), in combination with the high water content, facilitates oil-repellent properties when submerged in water[298,299]. To achieve a homogeneous hydrogel coating, it turned out that micropillar arrays facilitated the binding of the hydrogel. The micropillar arrays consisting of the transparent photoresist SU-8 were first functionalized with allylamine and subsequently coated with an acrylic acid-based hydrogel solution (Methods, Supporting Information). Coating the micropillar array with hydrogel is achieved via doctor blading the hydrogel solution. Subsequent UV-illumination facilitated chemical crosslinking and covalent attachment (Figure S5.1a). Scanning Electron Microscopy (SEM) confirms the presence of a homogeneous hydrogel coating (Figure S5.1b).

After the hydrogel was swollen in dyed water and the steady-state thickness of the swollen equilibrated hydrogel has been reached a flow of neat silicon oil (polydimethylsiloxane, PDMS, 50 cSt, 500 cSt) was applied (average velocity: 5 mm/s, 50 mm/s), Figure 5.1. We monitored the stability of the swollen hydrogel under flow conditions utilizing Laser Scanning Confocal Microscopy (LSCM, Figure S5.2).

We conducted all experiments using rectangular flow cells having plastic side and top walls. The flow cells have a volume of 30 μL, a height of H = 500 μm, a length of L = 17 mm, and a width of W = 3.8 mm. The flow profile is approximately parabolic through its depth since the height of the flow cell greatly exceeds the height of micropillars and the hydrogel coating. The volumetric flow rates Q established through the flow channel using a peristaltic pump ranged from Q = 0.48 mL/min to 4.8(0.2) mL/min, which resulted in average flow velocities ranging from 5.3 mm/s to 53(2) mm/s. Image acquisition was performed in the middle of the horizontal flow cell with respect to the lateral direction parallel to the flow. The swollen structure was left to equilibrate for 30 min to ensure homogeneous swelling (Figure 5.2a and Figure S5.3a, S5.4a). Hydrogels prepared of PAA swell to a larger thickness than hydrogels prepared from PNIPAm (Figure S5.3a, S5.4a).

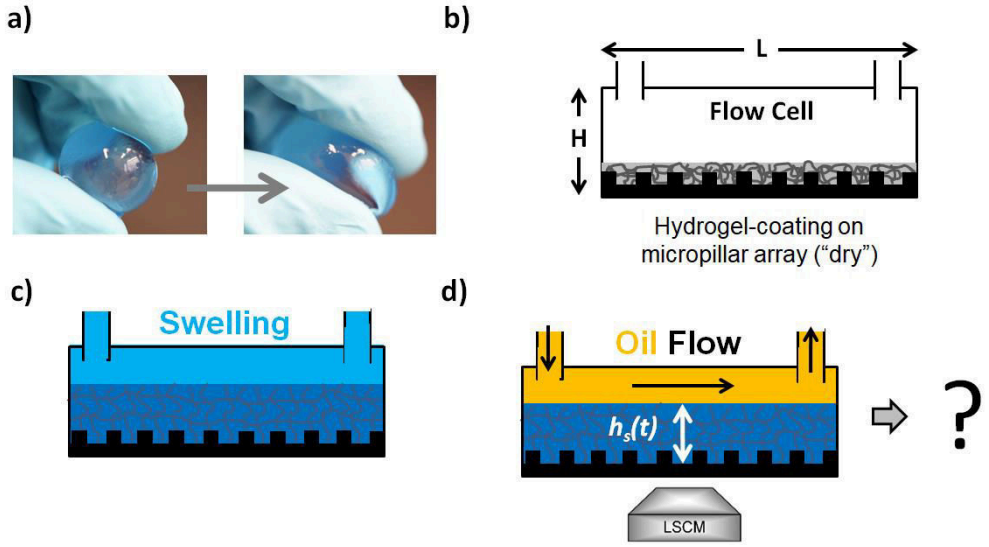

Figure 5.1: Experimental Approach. a) Manual squeezing of a colored hydrogel bead; the hydrogel beads prove resilient to mechanical deformation and maintains the imbibed water. But how resilient are hydrogels to shear flows of oil? Is the water bound strong enough within the hydrogel to resist shear flows of oil? b) hydrogel-coated micropillar arrays contained in a microfluidic flow cell. c) The hydrogel is swollen with MilliQ water containing fluorescent dye (Atto 488 NHS-Ester, 1µg/g. This low concentration ensures that the interfacial tensions remain unmodified. d) Depletion experiment: a flow of silicone oil (yellow) is applied across the hydrogel-coating, which leads to shear stresses acting on the hydrogel coating. The evolution of the thickness height of the hydrogel coating above the substrate, in the following denoted by $h_s(t)$, is monitored by Laser Scanning Confocal Microscopy (LSCM).

The difference in color intensity between the excess water and the water contained in the hydrogel may be attributed to different affinities of the dye to unbound water and bound water within the hydrogel. The height of the initial swelling (>100 µm for PAA, >50 µm for PNIPAm) is much larger than the pillar height (10 µm), as well as the dry thickness of the hydrogel. The flow of silicone oil leads to progressive dehydration of the hydrogel-coating, *i.e.* water-depletion of the coating (Figure 5.2b, Figure S5.3b-k). As dehydration progresses, the remaining portions of swollen hydrogel adapt to the shape of the micropillar array (Figure 5.2c, Figure S5.3j-r). Eventually, the remaining swollen portions of the hydrogel reach a steady-state retention thickness, which remains unchanged as the flow of oil continues (Figure 5.2d, Figure S5.3k-r). The same observations can be made when relying on hydrogel-coatings based on PNIPAm subjected to the same dehydration experiment (Figure S5.4).

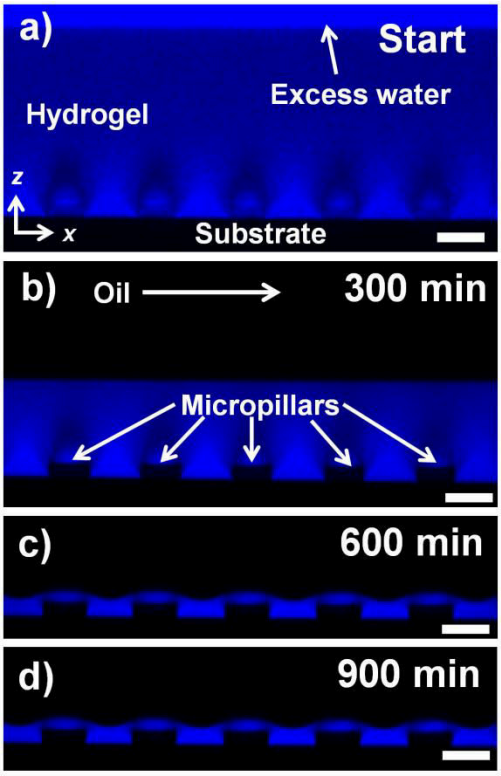

Figure 5.2: Depletion of Hydrogels with Oil Flows. Time evolution of side view (xz-scan) laser scanning confocal images (40x/1.1 water immersion objective) demonstrating dehydration of a hydrogel-coating consisting of PAA (poly(acrylic acid)) on a micropillar array (based on SU-8). Flow direction from left to right. a) Initially, the hydrogel coating with swollen with fluorescently labeled MilliQ-water and left to equilibrate for 30 min. Dye concentration: 1 µg/ml. The substrate and the micropillars appear black since they have not been dyed. b) Silicone oil (viscosity: 50 cSt, density: 0.96 g/mL) is then continuously circulated over the hydrogel-coated micropillar array at an average flow velocity of 5.3 mm/s. The undyed silicone oil appears black. The excess water not contained within the hydrogel leaves the flow cell. c) Eventually, the hydrogel reaches a steady-state thickness, d) which remains unchanged although oil continues to circulate continuously over the hydrogel-coating. The fluorescence signal of the fluorescently labeled water persists. Hence, water is retained within the hydrogel. Image acquisition was performed in the middle of the flow channel. Pillar dimensions: diameter d = 30 µm, center-to-center spacing p = 60 µm, and pillar height h = 10 µm. All scale bars are 30 µm.

Quantification of the hydrogel dehydration was performed by extracting the mean height $h_s(t)$ of the hydrogel coating above the substrate *via* a costume-written Matlab script (Methods). The hydrogel coating thickness, *i.e.* hydrogel depletion, progresses linearly with time (Figure 5.3a). A linear decrease of the thickness is also found for PNIPAm-based hydrogel coatings (Figure 5.3a, Figure S5.4, and Figure S5.5). At a first glance, linear dehydration kinetics is surprising since hydrogels undergo structural changes during dehydration[300,301].

The depletion of the hydrogel-coating progresses until the steady-state retention thickness is reached. There is an abrupt transition ("kink in the curve") in the time evolution of the depletion (Figure 5.3a, inset).

Regardless of the hydrogel-coating considered and the flow characteristics that were chosen (flow velocity and oil viscosity), the depletion kinetics (represented by the slopes of the curve) hardly show any variations (Figure 5.3b). These results in the retention of infused water are expected to depend on the degree of hydration. The thickness of the hydrogel coating levels and remains stable after some point in time of the depletion experiment has been surpassed.

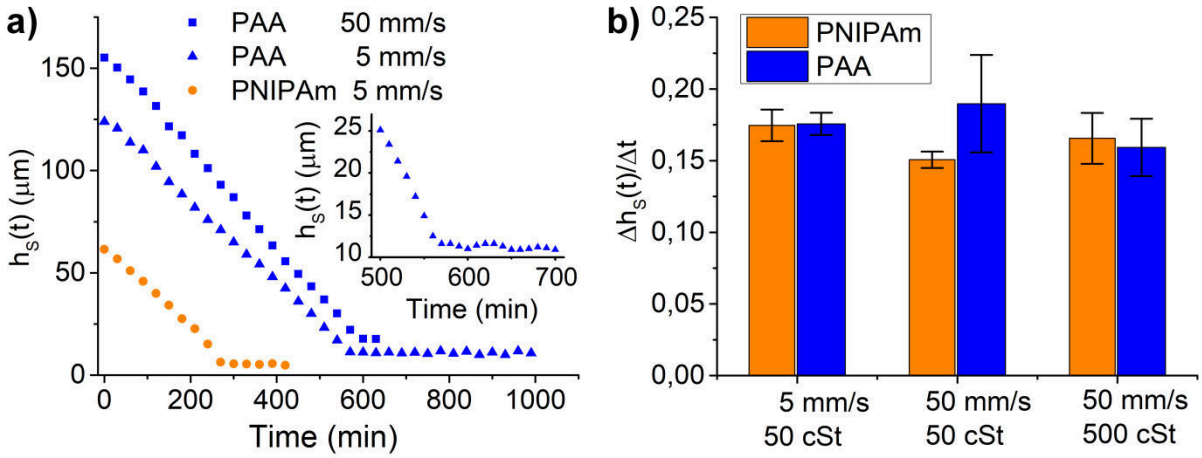

Figure 5.3: Linear Depletion of Hydrogels. a) Representative examples of hydrogels based on PAA (blue) and PNIPAm (orange) linearly depleted of water by a shear flow of silicone oil (50 cSt). The establishment of the retention thickness takes place abruptly (inset). Oil viscosity: 50 cSt. Flow velocities: 5 mm/s or 50 mm/s. b) Changes in the flow characteristics, *i.e.* flow velocity (limited by the experimental feasibility, utilization of LSCM, image definition limited due to vibrations imposed by higher flow velocities) and oil viscosity (limited by the fact that oil has to be efficiently pumped across the swollen hydrogel-coating), do not alter the slope of the depletion kinetics, independent of the hydrogel considered (blue: PAA, orange: PNIPAm).

The slopes decrease if the hydrogel coatings were swollen in aqueous solutions containing large amounts of salt, 6 M NaCl (Figure S5.6).

Up to now, image acquisition (LCSM) has been conducted in the middle of the flow channel exclusively. The progress of dehydration is faster, *i.e.* more pronounced, close to the inlet than close to the outlet at any given time during a depletion experiment (Figure S5.7, S5.8).

What causes the linear decrease of the thickness with time? A possible instability of the hydrogel-oil interface requires that we have a water layer separating the hydrogel and the oil film. However, contact angle measurements[290,302-304] reveals that silicone oil spreads on a dry as well as on a swollen PAA-based hydrogel-coating. The water contact angle on a dry PAA-based hydrogel-coating amounted to 27(2)°, which indicates that the hydrogel-air interface is slightly hydrophobic, making the presence of a water layer in-between the hydrogel and the oil-phase and hence an instability unlikely.

Another possibility is that the thickness decreases because of water diffusing into silicone oil. Water reaching the oil phase is taken along by the oil flow. We developed an extended diffusion model explained below. The experimental findings can accurately be modeled with the extended diffusion model (Figure 5.4a).

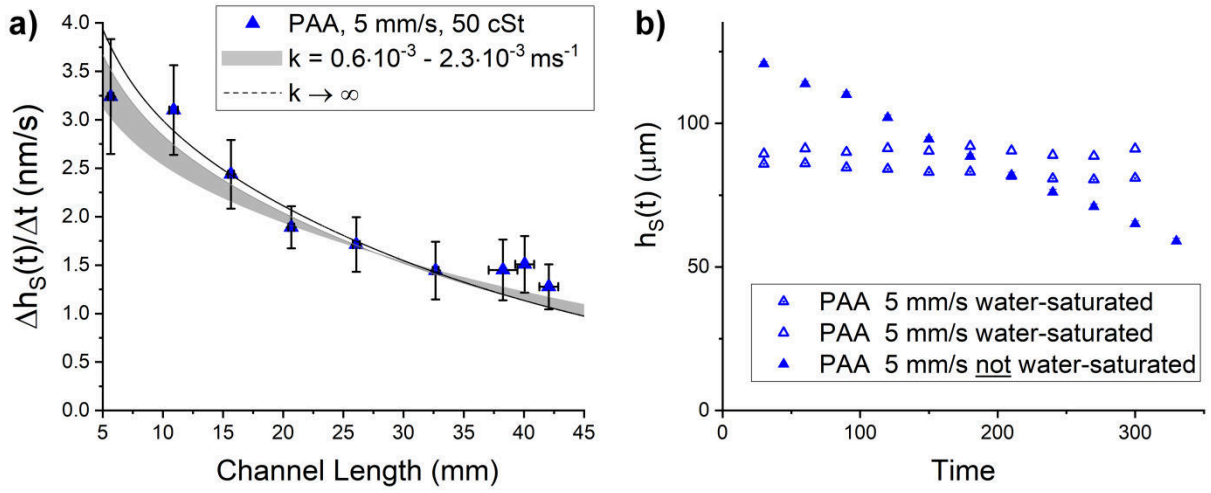

Figure 5.4: Diffusion model – water-saturation. a) Change of the thickness of the hydrogel coating with time (slopes of the linear depletion curves) $\Delta h_s(t)/\Delta t$ at different positions along a microfluidic flow channel in the downstream direction. Extended diffusion model superimposed onto experimental data (blue triangles) for a range of Sherwood numbers. b) Absence of depletion on swollen hydrogel-coatings subjected to a shear-flow of water-saturated silicone oil.

For diffusion-dominated depletion, it is important to note that silicone oil can take up 30 – 40 mM (up to 4-wt%) [305] of water. The oil which enters the flow channel holds no water. Therefore, a gradient of the chemical potential between the entering silicone oil and the hydrogel prevails. To equilibrate this difference in chemical potential water migrates from the hydrogel into the oil. The rate of water migration in the oil can be expressed with a kinematic relation of first order [306], namely:

$$\frac{dc_{H_2O,l}}{dt} = k\left(c_{H_2O,hg} - c_{H_2O,l}\right) \qquad (5.1)$$

The concentration of water in the oil and the hydrogel are denoted with $c_{H_2O,hg}$ and $c_{H_2O,l}$, respectively. Note that water in the hydrogel is always saturated, in contrast to the water in the oil. Thus, the water concentration in the hydrogel stays spatially and temporally constant. The coefficients k describe the kinematic transfer coefficient. The flow of the oil across the hydrogel-coating imposes an advective transport on the water in the oil. The total transport of water concentration in the lubricant reads [307]:

$$\boldsymbol{u}\nabla c_{H_2O,l} = D\nabla^2 c_{H_2O,l} \qquad (5.2)$$

The diffusivity D of water in oil is around $4x10^{-8}$ m^2/s. The imposed advection velocity field $\boldsymbol{u}$ is characterized by the mass averaged velocity of the lubricant flow. To find the diffusion rate of water into the oil, the advection-diffusion equation (5.2) is solved, together with the momentum transport of the flow. Therefore, the transport equations are solved numerically for the velocity $\boldsymbol{u}$ and the concentration field $c_{H_2O,l}$ with a finite element scheme, utilizing COMSOL Multiphysics ® 5.4. The flow domain is well resolved in a structured, cartesian mesh[308]. After a small inlet length of around 100 µm, the computed velocity profile develops a parabolic form, which is typical for channel flows. The velocity field, $\boldsymbol{u}$, is coupled to the advection-diffusion equation. Equation (5.1) imposes a water flux at the shared interface between oil and hydrogel as a boundary condition for equation (5.2). To

match the model with the experimental data, we tuned the kinematic coefficient k within a range of $0.6 \times 10^{-3} - 2.3 \times 10^{-3}$ m/s. The computed migration rate of water into the oil is strong at the inlet and becomes weaker over the channel length. Measurements of the rate at different positions along the flow channel excellently match the simulated lines (Figure 5.4 a). Since water contained in the oil is advected downstream with the flow, the water concentration in the oil over the shared interface rises over the channel length. Hence, higher water concentration gradients prevail in the vicinity of the inlet. This enables higher migration rates near the inlet compared to rates at the channel outlet. Note that in the direct vicinity of the channel inlet, the migration rate can deviate from the measured values. This is due to the complicated real inflow into the flow channel of the actual microfluidic flow cell. The inlet length of the real-world system is comparatively small, considering the whole channel length[309]. To justify an advection-diffusion transport of the water in the oil, the depletion experiments were conducted with water-saturated oil. According to our model, the height stayed nearly constant over 300 minutes. No significant changes in the thickness of the hydrogel coating beyond sample inhomogeneity are observed (Figure 5.4b). Therefore, depletion can be avoided by subjecting the swollen hydrogel to a shear flow of water-saturated oil. This indicates no water migration.

The depletion of water in a swollen hydrogel coated onto a micropillar array due to shear flows of oil progresses linearly owed to the diffusion of water into the non-water-saturated oil for a large parameter space, *i.e.* flow velocity and oil viscosity, for PAA- and PNIPAm-based hydrogel-coatings. Deviations from linear depletion behavior can be observed upon re-using the same flow channel after a depletion experiment has already been conducted (Figure S5.9). However, it is possible to re-swell depleted hydrogel-coatings by resupplying water after a depletion experiment was performed (Figure S5.10). We speculate that our approach contributes to the development of liquid-infused surfaces lubricated with water, which stay lubricated under shear flows of oil. Our approach may potentially be useful in the field of secondary or enhanced oil recovery.

5.3 Methods

Materials. The SU-8 photoresist was purchased from MicroChem Corp. Trichloro(octadecyl)silane (OTS, >90%), N-Isopropylacrylamide (NIPAm, 97%), Acrylic Acid (AA, 99%), N,N'-methylenebisacrylamide (NMBA, 99%), 2-Hydroxy-4′-(2-hydroxyethoxy)-2-methylpropiophenone (Irgacure D-2959) and Allylamine (AlAm, 99,5%) were purchased from Sigma-Aldrich. The fluorescent dye was ATTO 488 NHS-ester (ATTO-TEC GmbH, Germany, diluted in MilliQ water, concentration: 1 µg/g). As lubricants, silicone oils (PDMS, Sigma-Aldrich, viscosity: 50 cSt and 500cSt at 25 °C) were used.

All chemicals were used as received. The flow cells (Sticky-Slide VI0.4) were ordered from ibidi GmbH (Germany). The flow cells were connected to a peristaltic pump (Reglo-Analog MS4/8, Cole-Parmer GmbH) via polyvinyl chloride (PVC)-tubes (internal diameter = 1.42 mm, Novodirect GmbH Labor und Meßgeräte) and tightly sealing linkers. The fluorescent dye ATTO 488 NHS-ester offers excellent water solubility, strong absorption, high fluorescence quantum yield, and high photostability. The fluorescence is excited most efficiently in the range of 480 and 1515 nm. The 488 nm line of the argon laser was used for excitation. The used dye concentrations did not change the interfacial tension of water.

Preparation of Hydrogel-Coating. The preparation of the neat/non-functionalized SU-8 micropillar arrays is described elsewhere.[310] [10] The SU-8 micropillars arrays were coated with a hydrogel. Double functional groups were first introduced onto the SU-8 photoresist-based micropillar array surface via a reaction involving allylamine (ALAm). A 5%v/v solution of allylamine in water was prepared and put under stirring for 10 minutes. The as-prepared solution was poured into a glass box containing the SU-8 micropillar arrays and left for 30 minutes. The amino-groups of AlAm react with the epoxy groups of SU-8 in an SN_2-type reaction, therefore, exposing the allyl-group to the surface.[311] After 30 minutes, the samples were then extensively rinsed with water and left to dry. After the pre-modification, UV-induced radical photopolymerization was used to grow the hydrogel network on SU-8 micropillar arrays. For that purpose, 10% v/v aqueous solutions of NIPAm and AA were prepared by adding a 2% w/w NMBA, with respect to the monomer content, as the crosslinker. Finally, 20mg Irgacure D-2959 as initiator was added to the solutions. The micropillar arrays were wetted with 1 mL of hydrogel solution. A glass slide was gently positioned onto the arrays forming a ''sandwich structure'' by doctor blading in order to spread the solution drop, avoiding the formation of bubbles. The arrays were positioned under a UV lamp at a distance of 7.5 cm (6,0 mW/cm^2) and irradiated for 20 minutes. After polymerization, the glass slide was removed. The hydrogel formed had more affinity with the micropillars arrays; therefore, only this surface resulted in being coated. The as-obtained hydrogel-functionalized micropillar arrays were washed with water and left to dry. Coating with acrylic acid-based hydrogel solution establishes PAA-based hydrogel coatings. In contrast, with an N-isopropylamide-based hydrogel solution establishes the PNIPAm-hydrogels.

Preparation of saturated silicone oil. 12 mL of MilliQ water was added to 40 mL of 50 cSt silicone oil and stirred at 300 rpm for 72 h. The separation was performed with a separation funnel. Care was taken to seal the vessel during the experiments using paraffin tape.

Setup of Flow Cell Experiments. The micropillar arrays containing the hydrogel coatings were stuck onto sticky microfluidic flow cells. Great care was taken to avoid oil spillage and leakage onto and into the components of the microscope. For that purpose, the individual flow channels were also sealed off with the help of super glue. The flow cell consists of 6 individual rectangular channels. The individual channels are 0.4 mm high, 17 mm long, and 3.8 mm wide, which amount to a coverable area of 64.6 mm^2 per channel. Each channel has a volume of 30 μL. The rectangular flow cells have plastic side and top walls based on epoxy resin. The flow cells are mounted to the sample surface by an adhesive layer, which adds 0.1 mm to the overall height of the flow channel, i.e. H = 500 μm. The flow cell with the affixed micropillar array was connected to PVC tubes via rectangular linkers. The tubes were fixated on a peristaltic pump and immersed into the oil. The peristaltic pump used allowed to tune the flow velocities (5 mm/s and 50 mm/s). The flow is laminar since the Reynolds number (*Re*) lay below unity. The flow cell setup was mounted onto the commercial laser scanning confocal microscope (Leica TCS SP8 SMD). The tubes were sufficiently long to connect to the flask containing the oil reservoir. The container of the oil was sealed with paraffin film subsequently. Before starting the experiment with the oil flow, the channels were filled with dyed water (1 μg/mL) to ensure proper swelling of the hydrogel and to make sure that there are no air bubbles left and to tune the confocal image acquisition parameters. The swollen hydrogel-coating was allowed to equilibrate for 30min prior to starting the experiment. Before each experiment, the connecting tubes were rinsed multiple times with MilliQ water and dried with pressurized nitrogen.

Laser Scanning Confocal Microscopy. An inverted laser scanning confocal microscope (LSCM, Leica TCS SP8 SMD) with a 40x/1.11 water immersion objective lens (Olympus) was employed to image the lubricant-depletion, *i.e.* dehydration of the hydrogel. The scanned areas in the cross-section images (*xz*-scans) were normally 290.62 x 145.17 μm^2 (1024 x 256 pixel^2), if not otherwise

mentioned. The horizontal resolution was ~500 nm, the vertical resolution was ~1 μm, and the time span in-between successive images was 10 min – 30 min. The scanning frequency was 600 Hz. A line average of 8 was used to improve image quality. For imaging procedures requiring the simultaneous acquisition of images at different positions, the acquisition routine contained programmed pre-defined positions (along the flow channel from inlet to outlet), which were manually adjusted for each acquisition in order to minimize positional deviations.

Scanning Electron Microscopy. The micropillar arrays were characterized via scanning electron microscopy (SEM) using a LEO 1530 Gemini scanning electron microscope (Zeiss, Germany). The samples were tilted (45°) to best visualize a micropillar array.

Image Processing. Utilizing laser scanning confocal microscopy, we capture cross-sectional views of the hydrogel during the depletion process. The confocal images have been evaluated and processed using a custom-written MATLAB script. The aim of image processing was to elucidate the correct heights of the hydrogel coating above the substrate and the micropillar array, including correcting for the refractive index mismatches. We used the fluorescence signal of the obtained data and transferred them into grayscale images. The images were smoothed. The upper and the lower edge of the hydrogel were tracked. The difference between the average position of the upper and lower edge yielded the hydrogel height.

5.4 Authors' Contributions

E. L. prepared the hydrogel coatings. P.B. designed and performed the experimental setups and the laser scanning confocal experiments. E. L. and M.D. developed the process of preparing the hydrogel-coatings. E. L. prepared the hydrogel-coatings. L.H. performed the analysis of the experimental data and performed the numerical analysis. A. S. and K.H. assisted in the sample preparation. B.D. supported the numerical analysis. P.B., E.L., H.-J.B., J. G., and D.V. designed the structure of the manuscript. P.B, H.-J., B., and D.V. wrote the manuscript with the support of E.L., L.H., and B.D. All authors approve of the final version of the manuscript. The authors declare that there are no financial conflicts of interest.

5.5 Acknowledgements

The authors acknowledge the funding received from the European Union's Horizon 2020 research and innovation program under the Marie Skłodowska-Curie grant agreement No 722497, the ERC Advanced Grant No. 340391-SUPRO, the Collaborative Research Center (SFB) 1194. The authors thank Dr. Thomas Vilgis (MPIP), Professor Harald Pleiner (MPIP) Professor Lou Kondic (New Jersey Institute of Technology), Professor Walter Richtering (RWTH Aachen), and Professor Detlef Lohse (University of Twente) for helpful and stimulating discussions. The authors are grateful to Alexandre Laroche (Airbus) for assisting in photography.

5.6 Supporting Information

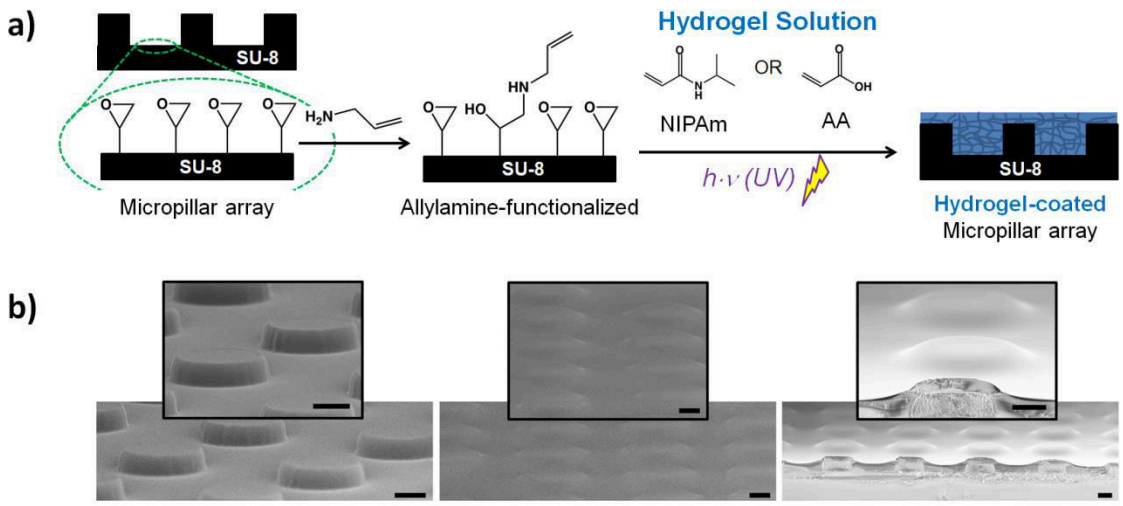

Figure S5.1: Sample Preparation. a) Preparation of Hydrogel-Coating on SU-8 photoresist-based micropillar arrays (pillar diameter: 30 µm, center-to-center spacing: 60 µm, Pillar height: 10 µm). The hydrogel solution consisting of either N-isopropylamide (NIPAm) or Acrylic Acid (AA) monomers, initiator, and crosslinker is applied via doctor blading, followed by UV-illumination (see Experimental Section 3.2.3). b) SEM images of neat unfunctionalized pillars (left), pillar array coated with hydrogel, dry state (middle), and the cross-section through hydrogel coating (right). All scale bars are 10 µm.

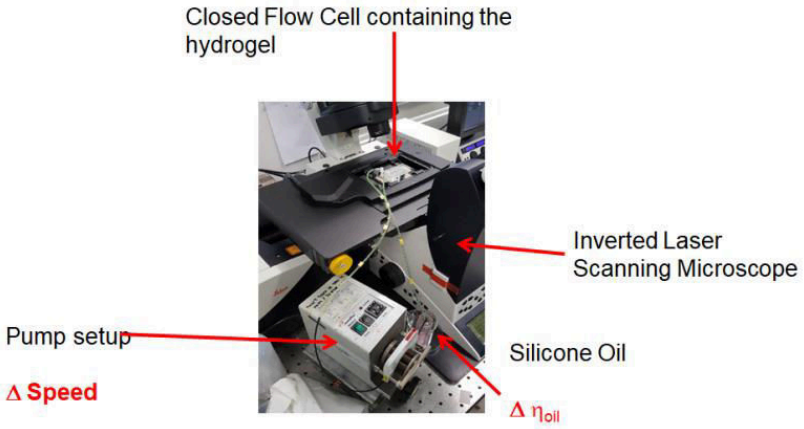

Figure S5.2: Experimental Setup. The key components are the inverted laser scanning confocal microscope (Leica TCS SP8 SMD), the peristaltic pump, and the hydrogel-coatings contained in flow cells. The system is not open to the atmosphere, the vials containing the oil and the flow cells are sealed.

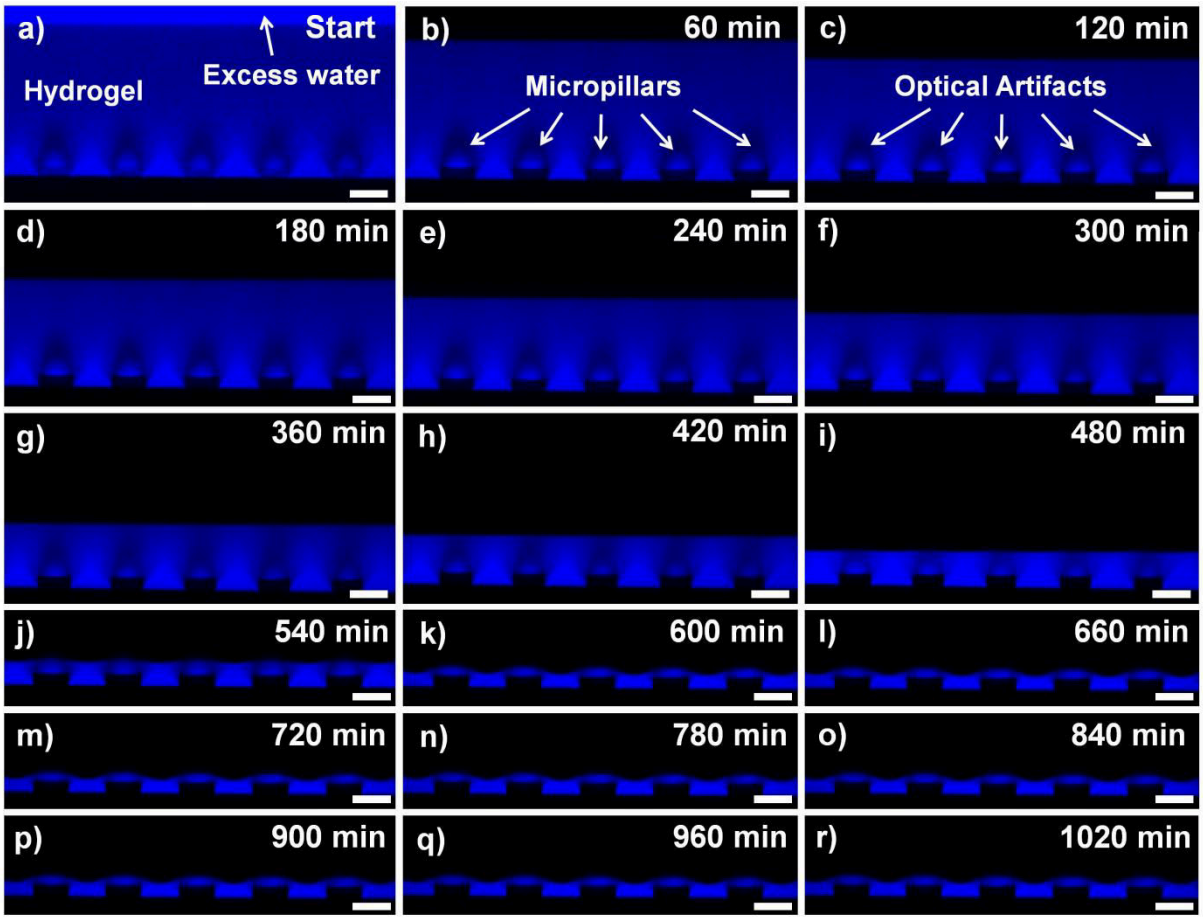

Figure S5.3: Depletion of Hydrogels with Oil Flows. Time evolution of side view (xz-scan) laser scanning confocal images (40x/1.1 water immersion objective lens) demonstrating progressive dehydration of the hydrogel-coating consisting of PAA on a micropillar array (based on SU-8) due to the flow of oil across the coating (flow direction from left to right). The time series consists of images acquired in the fluorescence channel. Only the water (blue) contained in the hydrogel was dyed using a fluorescent dye (ATTO 488 NHS-Ester, concentration: 1 μg/g). The dye concentration is sufficiently low, not to change the interfacial tension. Image acquisition was performed in the middle of the flow channel using a line average of 8 and a scanning frequency of 600 Hz. a) Initially, the hydrogel coating with swollen with fluorescently labeled MilliQ-water and left to equilibrate for 30 min. b-j) Silicone oil (viscosity: 50 cSt, density: 0.96 g/mL) is then continuously circulated over the hydrogel-coated micropillar array at an average flow velocity of 5.3 mm/s. The continuous flow leads to progressive dehydration, *i.e.* lubricant-depletion, of the hydrogel, evidenced by the decreasing thickness of the fluorescence emission signal detected, which represents the thinning of the hydrogel coating. The water leaving the hydrogel-coating moves too fast to be monitored. Hence, only the water remaining within the hydrogel contributes to detected fluorescence. k - r) Eventually, the hydrogel reaches a steady-state thickness, which remains unchanged although oil continues to circulate continuously over the hydrogel-coating. Pillar dimensions: diameter d = 30 μm, center-to-center spacing p = 60 μm, and pillar height h = 10 μm. All scale bars are 30 μm.

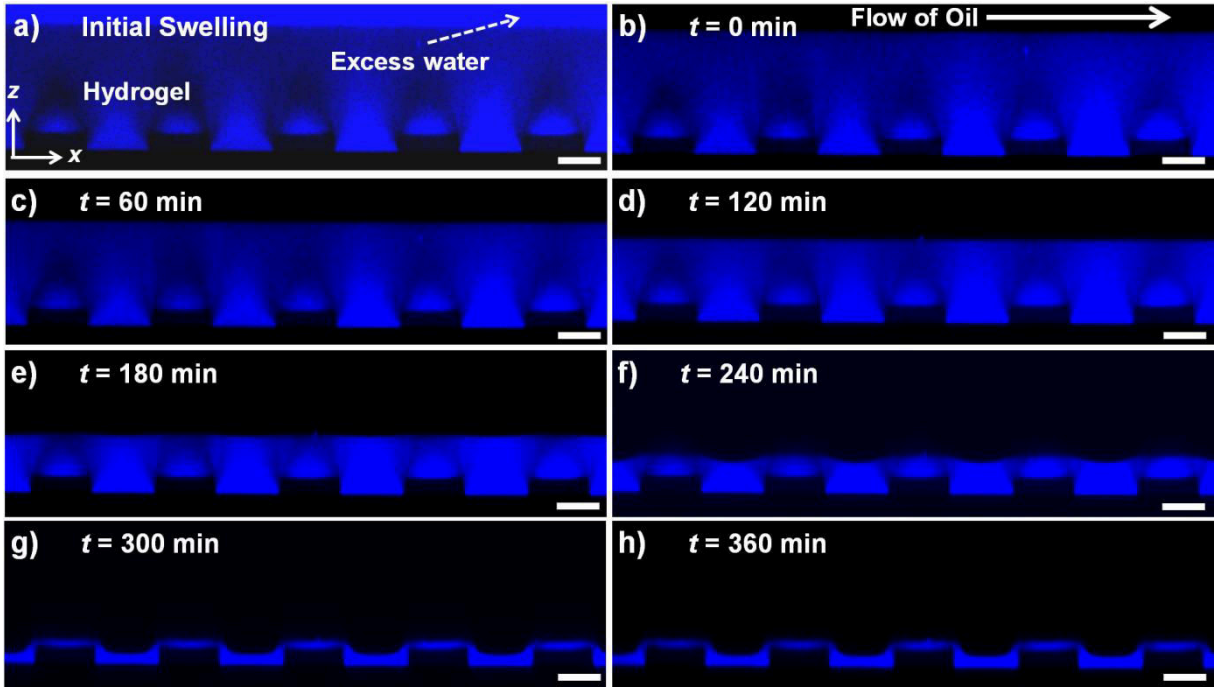

Figure S5.4: Depleting of Hydrogels with Oil Flows. Depletion Experiments Conducted for PNIPAm-based Hydrogel-Coating. Time evolution of side view (xz-scan) laser scanning confocal images (40x/1.1 water immersion objective lens) demonstrating progressive dehydration of the hydrogel-coating consisting of PNIPAm with 20% crosslinking density on a micropillar array due to the flow of oil across the coating (flow direction from left to right). The time series consists of images acquired in the fluorescence channel. Only the water (blue) contained in the hydrogel was dyed using a fluorescent dye (ATTO 488 NHS-Ester, concentration: 1 μg/g). The dye concentration is sufficiently low, not to change the interfacial tension. Image acquisition was performed in the middle of the flow channel using a line average of 8 and a scanning frequency of 600 Hz. a) Initially, the hydrogel coating with swollen with fluorescently labeled MilliQ-water and left to equilibrate for 30 min. b-g) Silicone oil (viscosity: 50 cSt, density: 0.96 g/mL) is then continuously circulated over the hydrogel-coated micropillar array at an average flow velocity of 5.3 mm/s. The continuous flow leads to progressive dehydration, *i.e.* lubricant-depletion, of the hydrogel, evidenced by the decreasing thickness of the fluorescence emission signal detected, which represents the thinning of the hydrogel coating. The water leaving the hydrogel-coating moves too fast to be monitored. Hence, only the water remaining within the hydrogel contributes to detected fluorescence. g, h) Eventually, the hydrogel reaches a steady-state thickness, which remains unchanged although oil continues to circulate continuously over the hydrogel-coating. Pillar dimensions: diameter d = 30 μm, center-to-center spacing p = 60 μm, and pillar height h = 10 μm. All scale bars are 20 μm.

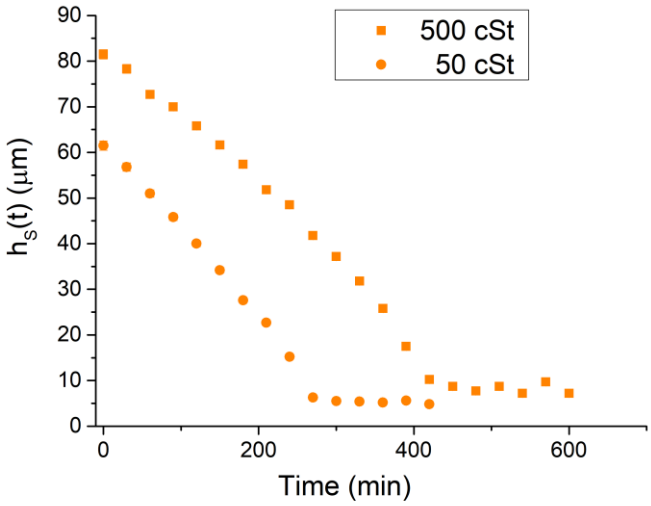

Figure S5.5: Representative depletion experiments conducted on PNIPAm-based hydrogel-coating. Time evolution of the height of the hydrogel coating above the substrate. The time evolution of the height of the hydrogel coating, *i.e.* $h_s(t)$. Flow velocity: 5 mm/s. Oil viscosities: 500 cSt and 50 cSt.

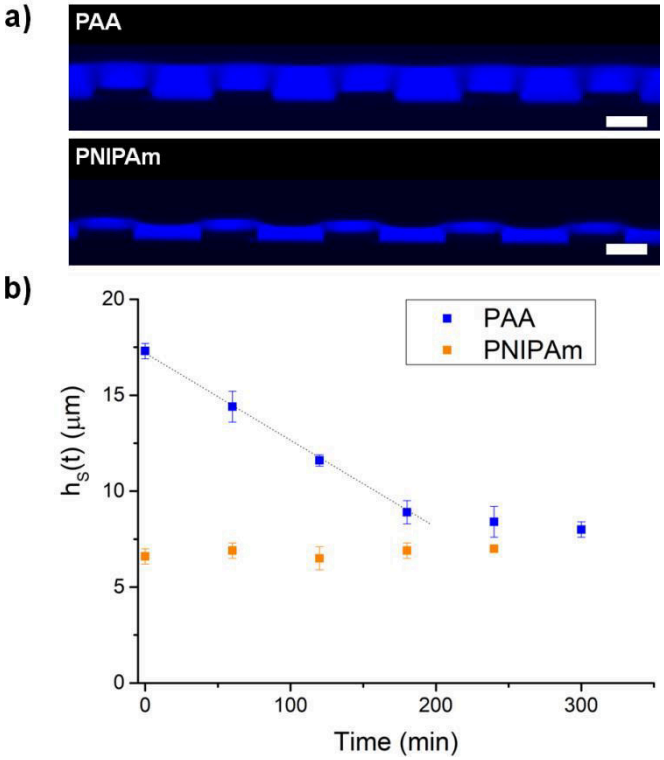

Figure S5.6: a) PAA-based hydrogel-coating (top) and PNIPAm-based hydrogel-coating (bottom) swollen in 6M NaCl(aq). PAA is the stronger electrolyte than PNIPAm. Hence, PAA-based hydrogel-coatings can swell stronger and can cope better with a large amount of salt. Scale bar: 20 µm, b) Nevertheless, the depletion kinetics, although remaining linear, change significantly upon the addition of large amounts of salt.

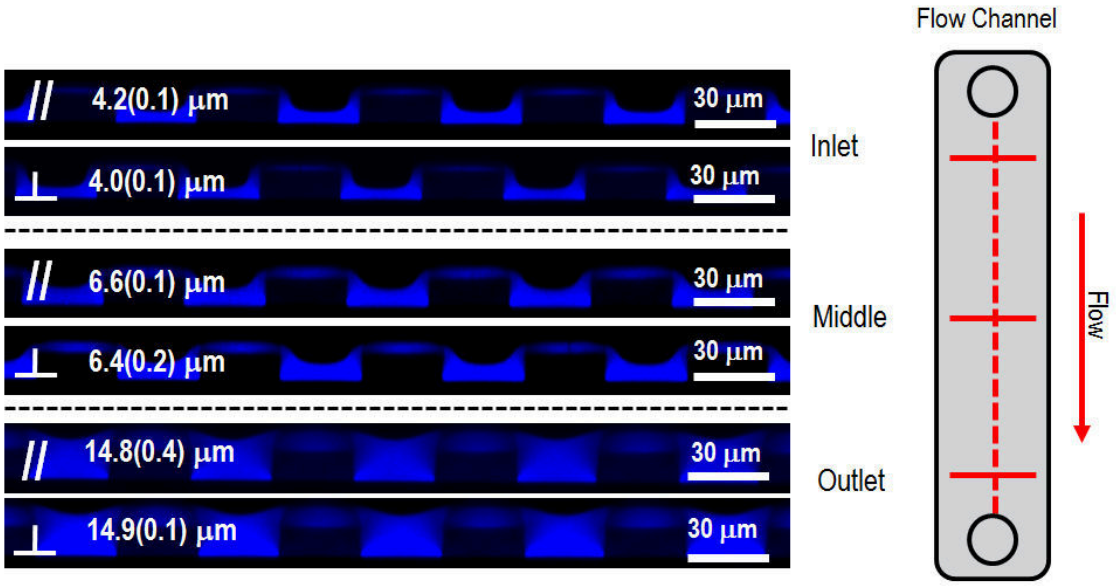

Figure S5.7: Progress of Depletion. The progress of dehydration close to the inlet is faster than close to the outlet. For the same lateral positions (perpendicular to the flow direction), the progress of dehydration slows down in the downstream direction.

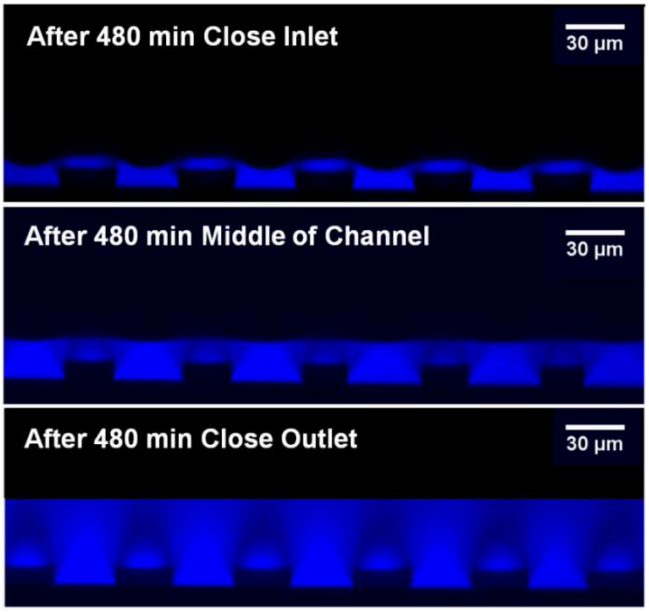

Figure S5.8: Progress of Depletion for PAA-based hydrogels in the downstream direction. The progress of dehydration close to the inlet is faster than close to the outlet. After running the depletion experiment for 8 hours (480 min, Figure 2i), depletion is more advanced close to the inlet than close to the outlet of the flow channel. Close to the inlet, the thickness of the hydrogel coating measured above the substrate amounts to 8.8(0.5) µm. In contrast, in the middle of the flow channel and close to the outlet of the flow channel, the obtained thicknesses of the hydrogel-coating amounted to 21(2) µm and 48.4(0.9), respectively.

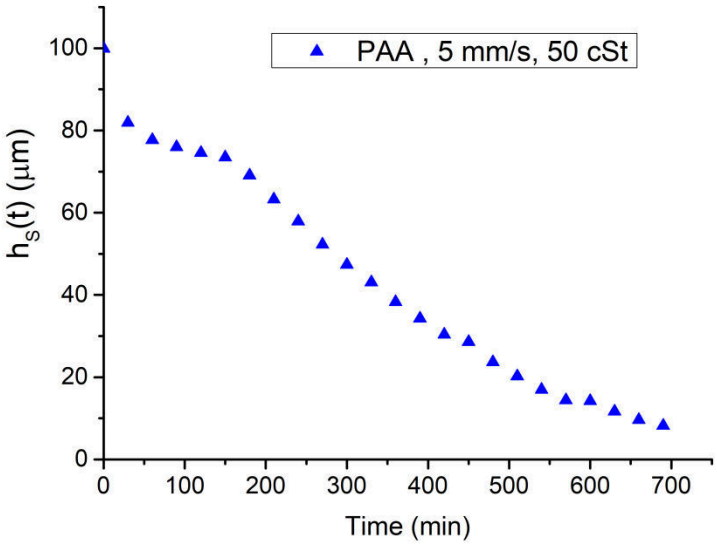

Figure S5.9: Repeated depletion experiment on re-swollen hydrogel-coating. Significant deviations from linear depletion kinetics are observed for re-swollen PAA-based hydrogel-coating subjected to a depletion experiment.

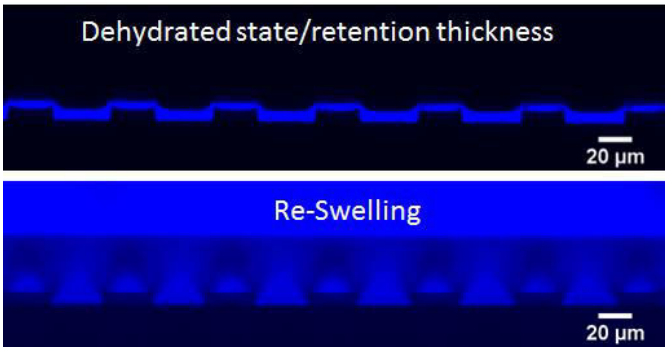

Figure S5.10: Concept of Re-Swelling. A hydrogel-coating that has reached the retention thickness of the coating can be re-swollen. Re-Swelling is achieved via flushing the channel with dye-containing water, analogous to initial swelling.

6 Flow-Induced Long-Term Stable Slippery Surfaces

Philipp Baumli†, Hannu Teisala†, Hoimar Bauer, Diana Garcia-Gonzalez, Viraj Damle, Florian Geyer, Maria d´Acunzi, Anke Kaltbeitzel, Hans-Jürgen Butt, and Doris Vollmer*

† These two authors have contributed equally to this work.

P. Baumli, Dr. H. Teisala, H. Bauer, F. Geyer, Dr. M. d´Acunzi, Dr. A. Kaltbeitzel, Prof. Dr. H.-J. Butt, Prof. Dr. D. Vollmer

Max Planck Institute for Polymer Research, Ackermannweg 10, 55128, Mainz, Germany. E-mail: vollmerd@mpip-mainz.mpg.de

D. Garcia-Gonzalez
Physics of Fluids Group, University of Twente, Drienerlolaan 5, 7522NB, Enschede, The Netherlands.

Dr. V.Damle
School for Engineering of Matter, Transport and Energy, Arizona State University, Tempe, Arizona 85287-1604, United States.

Reprinted with permission from Advanced Science, **2019**, 6, 1900019.

Keywords: porous surfaces, emulsions, flow, confocal microscopy, wetting

Slippery lubricant-infused surfaces allow easy removal of liquid droplets on surfaces. They consist of textured or porous substrates infiltrated with a chemically compatible lubricant. Capillary forces help to keep the lubricant in place. Slippery surfaces hold promising prospects in applications including drag reduction in pipes or food packages, anti-corrosion, anti-biofouling, or anti-icing. However, a critical drawback is that shear forces induced by flow lead to depletion of the lubricant. In this work, a way to overcome the shear-induced lubricant depletion by replenishing the lubricant from the flow of emulsions is presented. The addition of small amounts of positively charged surfactant reduces the charge repulsion between the negatively charged oil droplets contained in the emulsion. Attachment and coalescence of oil droplets from the oil-in-water emulsion at the substrate surface fills the structure with the lubricant. Flow-induced lubrication of textured surfaces can be generalized to a broad range of lubricant-solid combinations using minimal amounts of oil.

6.1 Introduction

From everyday experience, we know that friction is significantly reduced when driving on a wet street or moving over a slippery plank. The reason is that the rough surface is infiltrated with a liquid, also termed lubricant. For Slippery Lubricant-Infused Porous Surfaces (SLIPS)[1,2] an immobilized lubricant surface is established through capillary forces which keep the lubricant in place within the texture[10,45]. As a consequence, a smooth lubricant surface is formed. Slippery lubricant-infused surfaces, however, are by no means fully explored. Complexity arises from the 4-component nature of the system (solid substrate, lubricant, liquid to be repelled, and air).

A significant challenge for applications[15,28,68,72,75,77,83-85,94,100,106,312,313] of lubricant-impregnated slippery surfaces is the depletion of lubricant[97,98,161,163,166]. Drag reduction is no longer in effect on lubricant-depleted surfaces. Depletion of lubricant due to gravitational drainage, evaporation or cloaking can be prevented or minimized by well-thought choice of lubricant and surface design. However, no solution against shear-induced depletion of lubricant has been presented, yet[45,97]. Hydrodynamics necessitate that a moving liquid takes lubricant along due to the requirement of continuity of the interfacial velocities and shear stresses across the liquid-lubricant interface. This gives rise to depletion of lubricant and loss of the surface functionality. Therefore, being able to replenish the lubricant is vital; to which besides spraying, dipping or painting no strategy exists yet. These strategies require *ex-situ* accessibility. Here, we introduce the first *in-situ* approach of replenishing lubricant utilizing flow of oil-in-water emulsions.

Emulsion- and surfactant-based products are ubiquitous. Emulsions constitute a large proportion of liquids that we interact with. Examples include emulsified food such as milk and yogurt, cosmetic products such as creams and lotions, or crude oils that are often delivered as water-in-oil emulsions.

We demonstrate the formation of a slippery surface via the flow of an emulsion over a fully water-filled micropillar array, *i.e*. starting replenishing lubricant from the worst-case scenario of a completely lubricant-depleted surface. Intuitively, replenishing lubricant with emulsions does not seem to be possible because of hydrodynamics (no-slip boundary conditions); a stable water film surrounds the pillars, preventing coalescence of the oil drops with the surface. In addition, buoyancy drives many lubricants away from the solid. We overcome these issues by manipulating the wettability properties of the oil drops. Laser scanning confocal microscopy (LSCM) reveals that above a threshold velocity the oil droplets attach to the pillar walls, grow larger, and finally coalesce and descend to fill the structure.

6.2 Results and Discussion

We conducted all experiments using rectangular flow cells having plastic side and top walls, Figure 6.1 (and Figure S6.1, Supporting Information).

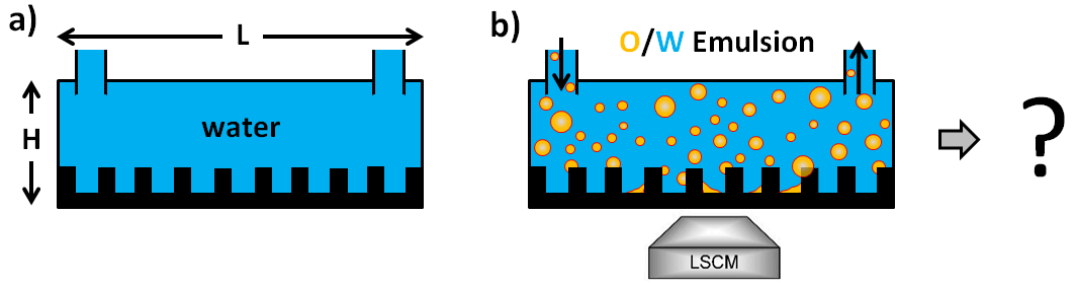

Figure 6.1: Experimental Setup. a) An initially water-filled flow channel containing a micropillar array, b) is subjected to a continuous flow of an oil-in-water (O/W) emulsion. Can the oil gradually replace the water in-between the micropillars leading to the formation of a slippery surface? The filling process is monitored using an inverted laser scanning confocal microscope (LSCM).

If not stated otherwise, the glass bottom of the flow cells contains uniform and regular SU-8 photoresist micropillar arrays (Figure 6.2j, k, Experimental Section for details) hydrophobized by chemical vapor deposition (CVD) of trichlorooctylsilane (OTS, $C_8H_{17}SiCl_3$). The flow cells have a height of H = 500 µm, a length of L = 17 mm and a width of W = 3.8 mm, thus they are much deeper than the 10 -25 µm high pillars. Hence, the flow profile is approximately parabolic through its depth. The maximal volumetric flow rate Q established through a flow channel using a peristaltic pump amounted to $Q = 7.0 \pm 0.2$ mL min^{-1}, which resulted in average flow velocity of 77 ± 2 mm s^{-1} (Figure S6.1 and S6.2, and Table S6.1, Supporting Information). We investigated the attachment and growth of drops to the pillar walls using an inverted laser scanning confocal microscope (Leica TCS SP8 SMD). Imaging was performed in the middle of the horizontal flow cell with respect to the lateral direction parallel to the flow.

In the beginning, the micropillar array is completely filled with water (blue), representing the worst-case scenario of a slippery surface completely devoid of lubricant (Figure 6.1a, Figure 6.2a). Subsequently, an oil-in-water emulsion is circulated over the micropillar array (Figure 6.1b). The emulsification was done using a tip sonicator (SONIFIER® W-450D) for 2 minutes (see Experimental Section and Figure S6.3a, Supporting Information, for details). The diameter of the polydisperse oil droplets was determined by laser scanning confocal microscopy as well as microscopy and rarely exceeds 4 µm (Figure S6.3b, c, Supporting Information).

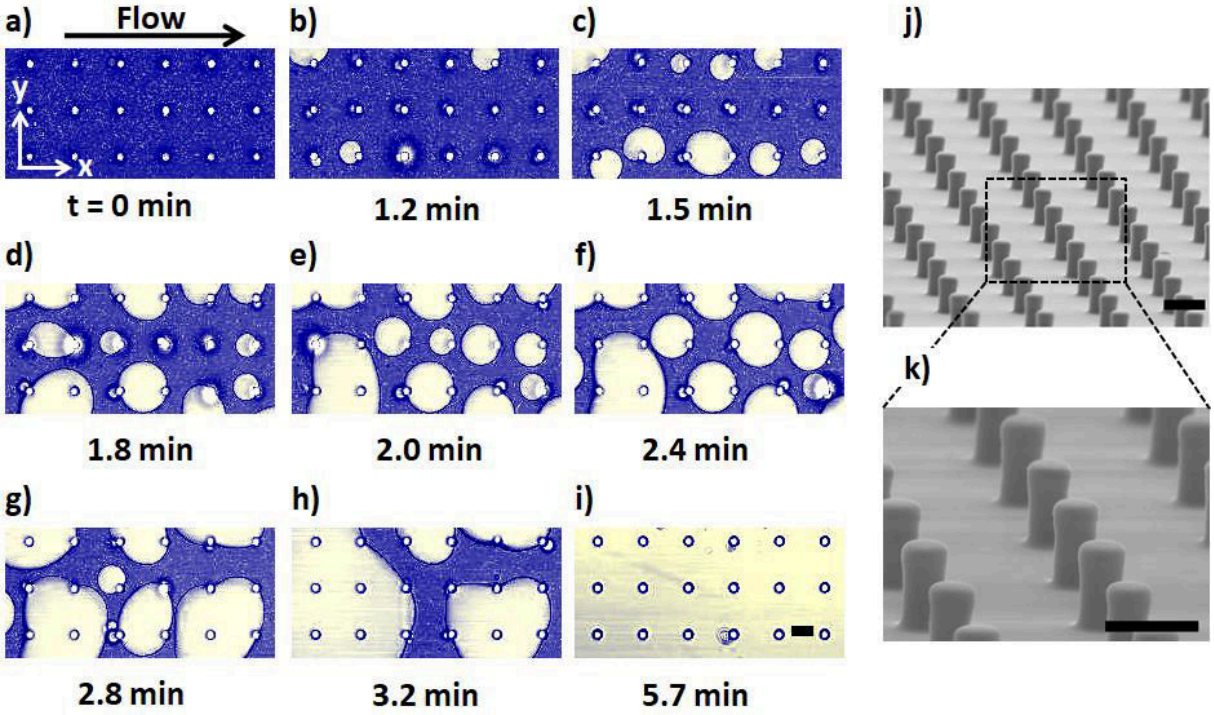

Figure 6.2: Time evolution of top view laser scanning confocal images. (40×/1.11 water immersion objective lens) demonstrating complete filling (flow direction from left to right) of a micropillar array. The time series consists of an overlay of the transmission and fluorescence channel images which were simultaneously recorded. The confocal microscope imaging was focused roughly 5 µm above the bottom of the micropillar structure. An oil-in-water emulsion (2 wt.-% of silicone oil, viscosity: 50 cSt, density: 0.96 g mL^{-1}) is circulated over the micropillar array at an average flow velocity of 77±2 mm s^{-1}. 500 µg L^{-1} CTAB or approximately 0.14% of critical micelle concentration (CMC) was added to the water phase before emulsification. a) Starting from an initially water-filled (blue) channel the continuous flow of emulsion b)-i) leads to the attachment of oil droplets (yellow) to the pillars and the bottom substrate leading to gradual filling of the structure with oil. The water is dyed with 1 µg g^{-1} Atto 488 NHS-Ester. The dye concentration is sufficiently low, not to change the interfacial tension. The pillars (grey) are added based on their position and size given by the transmission image. j, k) SEM images of micropillar arrays. Pillar dimensions: diameter *d* = 5 µm, center-to-center spacing *P* = 20 µm, and pillar height *h* = 10 µm. All scale bars are 10 µm.

After the flow was started, the oil drops circulated with the emulsion through the micropillar array refused to attach to the pillar walls. To test whether this was caused by electrostatic repulsion between the drops and the surface, we added different surfactants (see Supporting Information 6.5.5.1 and 6.5.5.2) to the emulsion. Indeed, after the addition of tiny amounts of the positively charged surfactant cetyltrimethylammonium bromide (CTAB, 500µg L^{-1}) drops attached to the pillars. This is in line with the observation that silicone oil-water interfaces are negatively charged[314-317]. The surfactant reduces the electrostatic repulsion between the oil droplets (Figure S6.3d, e, Figure S6.4, Figure S6.5, Figure S6.6, and Video S6.1, Supporting Information) which prevented their attachment and coalescence. Top view images demonstrate that droplets (yellowish domains) quickly begin to attach to the micropillars (encircled white dots, Figure 6.2b). The free emulsion droplets move too fast to be monitored. After 1.5 min almost every pillar has oil droplets attached to it (Figure 6.2c). As the

experiment progresses, the attached drops grow in size due to coalescing with newly arriving and already attached neighboring droplets, Figure 6.2d – i. Eventually, the drops descend and cover the underlying solid substrate (Videos S6.2 and S6.3, Supporting Information).

Three-dimensional laser scanning confocal microscopy images demonstrate that the growing drops keep their shape spherical during the whole growth process, pointing out that the Laplace pressure, $\Delta P = 2\,\gamma/R$ dominates shear-induced deformations (Figure 6.3a and Video S6.4, Supporting Information). Here, R is the radius of an attached oil drop and γ the interfacial tension. The green rectangles highlight that multiple drops can attach to the same pillar (Figure 6.3b, Figure S6.7, Supporting Information). Notably, micropillars can repeatedly accommodate droplets also when portions underneath the pillar are already filled (see the red and white circles in Figure 6.3, Figure S6.8, Supporting Information). This is confirmed by side view images revealing detailed information on the height and position along the pillar where droplets attach, Figure 6.3b and Figure 6.3c for a sketch of the time evolution.

The emulsion droplets (black in Figure 6.3b, yellow in Figure 6.3c) preferentially attach to the pillars' front side, *i.e.* in the flow direction (Figure S6.9 and S6.10, Supporting Information). Attached drops grow via coalescence with newly arriving droplets and neighboring drops along the pillar walls and tops. If the droplet touches the bottom surface, capillary forces pull the drop down, causing it to spread within the microstructure. The red circles highlight examples of drops just before descending. Gradually, the whole space in-between the micropillar gets filled with oil, and a lubricant-impregnated slippery surface is established. Note that gravity does not cause descending of drops because the silicone oil has a lower density (ρ_O = 0.96 g mL^{-1}) than water (ρ_w = 1.00 g mL^{-1}). After lubricating the structure by the emulsion, water drops could easily slide on the surface when the substrate was inclined by less than 10° (Video S6.5, Supporting Information).

Quantitative data on the attachment and filling process is obtained using *xy*-image sequences acquired in the fluorescence channel. The orientation of the drops attached to the pillars concerning the flow direction of the emulsion is defined via an orientation angle (Figure 6.4a). An orientation angle of zero means that the drops attach to the pillars precisely in the flow direction of the emulsion. The orientation angle has been measured for every drop in every frame of the image sequence. Angles vary between 0° and 180°, assuming that attachment is symmetric with respect to the flow direction. In the initial stage of the filling experiment, the first third of the experiment, over 86% of the droplets attached at angles below 45° (Figure 6.4b, S6.9, and S6.10, Supporting Information). The inset visualizes the preferred attachment of drops in the flow direction (higher magnification shown in Figure S6.10, Supporting Information). As the filling progresses further, the occurrence of a preferred direction of drop attachment in flow direction is progressively lost (the successive two-thirds of the filling experiment, Figure 6.4b (and Figure S6.11, Supporting Information). Newly arriving drops preferentially attach to the pillars tops because these regions are more accessible to the flowing oil droplets. The individual drops do not change their position during their whole lifetime (Figure S6.12, Supporting Information). Indeed, the lateral adhesion greatly exceeds the shear-induced depinning force (see Supporting Information 6.5.3.5). For the vast majority of droplets, the projected surface area remained below 50 μm^2 before they descend to the bottom substrate, corresponding to a drop diameter below 8 μm (Figure S6.13, Supporting Information).

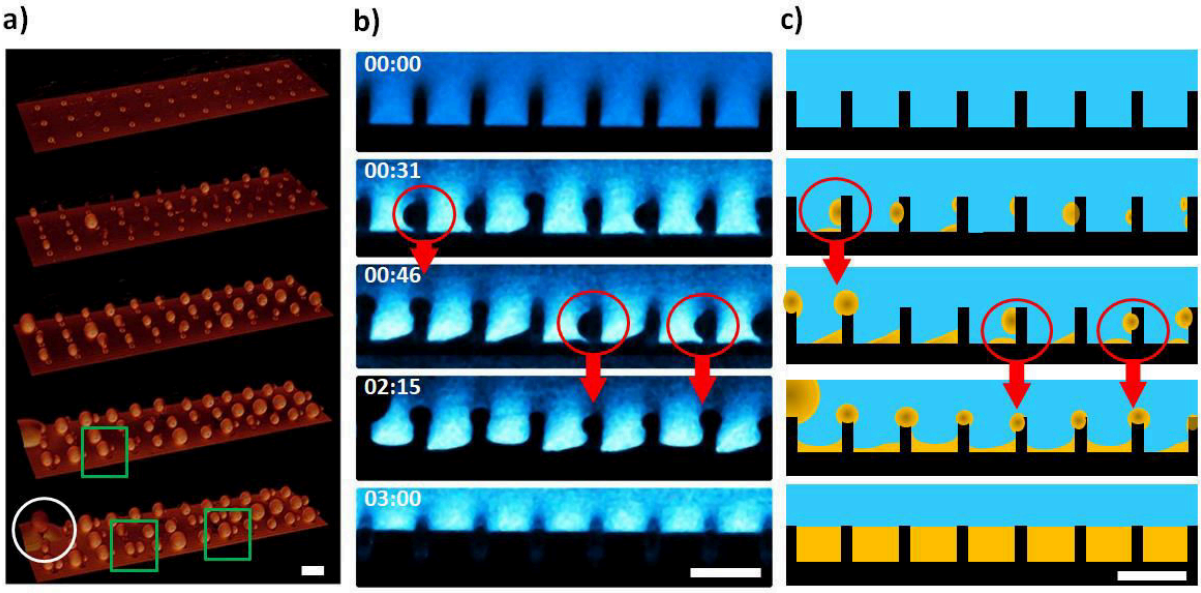

Figure 6.3: Filling of a micropillar array with lubricant. An oil-in-water emulsion (2 wt.-% of silicone oil, 500 µg L^{-1} CTAB) is circulated over the micropillar array at an average flow velocity of 77 mm s^{-1}. Pillar dimensions: diameter *d* = 5 µm, center-to-center spacing *P* = 20 µm, and pillar height *h* = 10 µm. a) 3D laser scanning confocal images recorded in the reflection channel are visualizing the time evolution of the filling process (40×/1.11 water immersion objective lens). Multiple oil droplets can attach to the same pillar (green rectangles), and the drops can repeatedly be accommodated (white circle). For this experiment, the oil has been dyed with Coumarin 6 with subsequent image inversion. b) Laser scanning confocal side view images recorded in the fluorescence channel. Starting from an initially water-filled micropillar array, the oil (black) gradually replaces the water (blue) in-between micropillars (black). Red circles: Droplets just before coalescing with the oil film. Red arrows: After coalescence, newly arriving droplets attach to the same pillars. The water is dyed with 1 µg g^{-1} Atto 488 NHS-Ester. The images give the impression that the pillars are sticking out of the lubricant phase. This false impression is caused by a combination of errors due to the mismatch of the refractive indices and a lens effect because of the top face of the pillars is not completely flat. c) Schematic illustration of the filling process. Oil is colored in yellow, water in blue, and the pillars in black. The scale bar is 20 µm.

The temporal evolution of the filling kinetics of individual filling experiments varies as shown in Figure 6.4c, where the time evolutions of the oil coverage of the underlying bottom substrate are shown. Often a slowing down of the filling can be observed in the course of time (Figure S6.14, Supporting Information). Likely, this is caused by the accumulation of repulsive charges at the surface of oil droplets and replenished films. Coalescence requires that electrostatic repulsion between oil droplets needs to be overcome. Indeed filling works best for surfactant concentrations between 500 and 1000 µg L^{-1}. For the concentration range of 500–1000 µg L^{-1} of CTAB, the surfactant molecules cover ≈ 0.03–0.06% of the surface area of the drops (Figure S6.6, Supporting Information 6.5.3.2). For increasing surfactant concentration, droplets preferentially attach at the pillars´ base and the bottom substrate. For high concentrations of CTAB > 4000 µg L^{-1} (1.1% CMC), the oil droplets in the emulsions become sufficiently positively charged that electrostatic repulsion of the charged oil-water interface again impedes coalescence of droplets and filling of the structure (see Supporting Information).

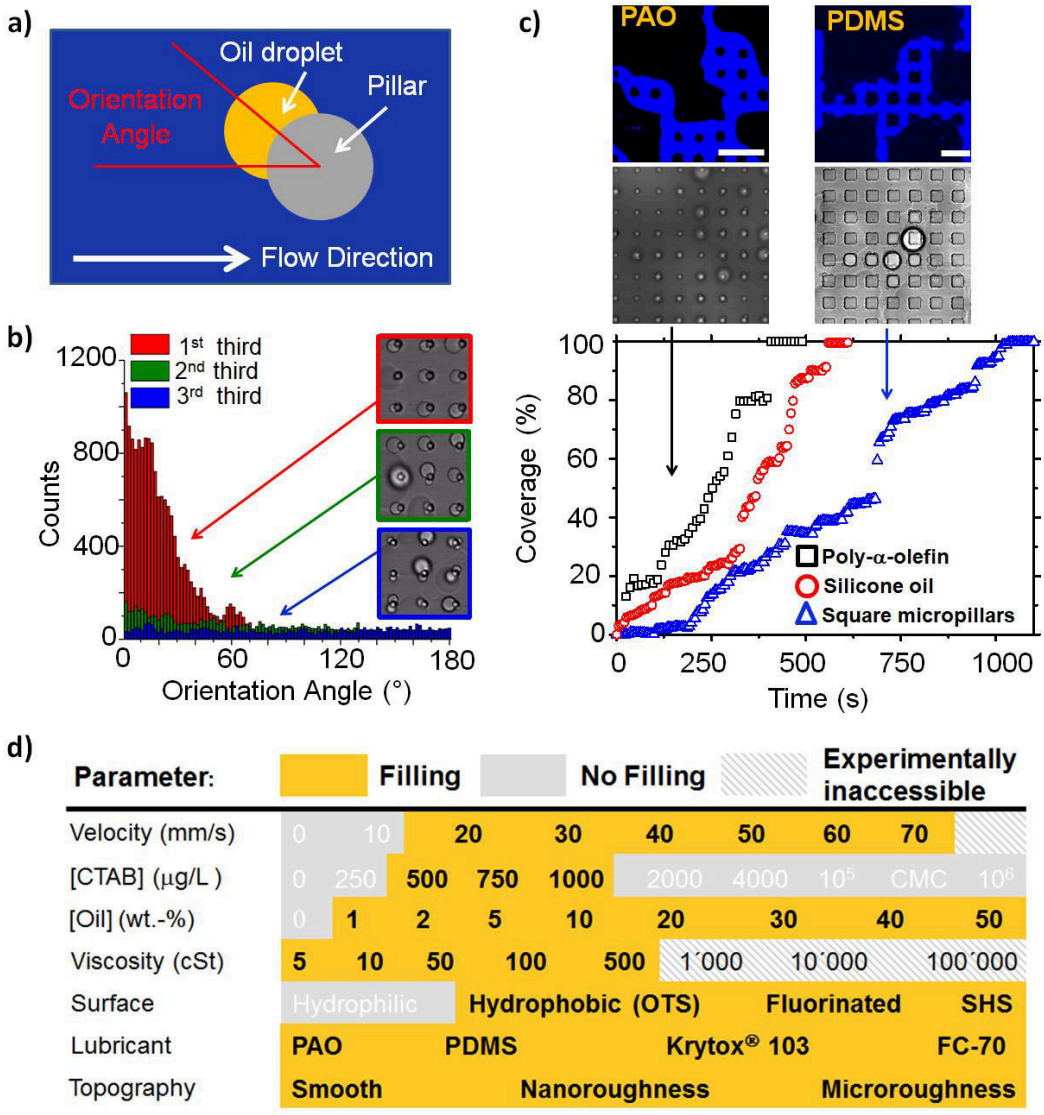

Figure 6.4: Drop orientation and filling process. a) The *Orientation Angle* is defined as the angle between the horizontal flow direction and the connecting line between the center of the projected area of the pillar and the droplet´s center of mass. Drops attaching at an angle of *e.g.* 10° and -10° are counted together as they can be treated to be equivalent. b) Orientation angle at the first, second and last third of the filling process. Insets: transmission channel images of drops attached to the pillars at different phases of filling. Cylindrical pillar dimensions: diameter d = 5 µm, center-to-center spacing P = 20 µm, and pillar height h = 10 µm. c) Time evolution of the coverage for three different filling experiments using the industrially relevant poly-α-olefin (black squares, fluorescence channel (top) and transmission channel (bottom) snapshot of filling process on the upper left, scale bar: 50 µm) and biocompatible silicone oil with cylindrical (standard case, red circles) and quadratic (blue triangles, fluorescence channel (top) and transmission channel (bottom) snapshot of filling process on the upper right, scale bar: 50 µm) micropillars. Quadratic pillar dimensions: edge length = 20 µm, center-to-center spacing P = 40 µm, pillar height h = 10 µm. Apart from changing the oil and pillar, geometry, the experimental conditions were identical.

d) Phase diagram showing parameter windows for successful filling experimentally verified in this work (yellow) and conditions at which successful filling is not achieved (grey). The experiments where the velocity and CTAB concentration were not varied were performed at a constant average velocity of 77±2 mm s^{-1} and a CTAB concentration of 500 µg L^{-1}. The different parameters can be varied independent of each other.

The filling mechanism works for a wide range of velocities, oil concentrations, and viscosities, Figure 6.4d. The maximum accessible velocity and viscosity were given by the setup. To investigate whether the filling works analogously for different surface structures and emulsions we first filled arrays of quadratic pillars of larger size (edge length: 20 µm, blue triangles, Figure S6.15, Supporting Information). The structures can be filled, showing that the filling does not depend on details of the flow profile. The lubricant can also be replenished on fluorosilane coated micropillars and using nanostructured, porous surfaces, for example, glass coated with silicone nanofilaments[318] (Figure S6.16, S6.17, and S6.18 and Video S6.6, Supporting Information).

Also, the oil used to prepare the emulsion can be replaced. We tested the industrially widely used poly-α-olefin (PAO, ρ = 0.78-0.82 g mL^{-1}), Figure 6.4c, black squares (and Figure S6.18a, Supporting Information), and the fluorinated oils[2,9,16,25,161], Krytox® 103 and Fluorinert™ FC-70 (FC-70), which are commonly used lubricants for slippery surfaces (Figure S6.19, Supporting Information). In all cases, the negative charge of the emulsion drops had to be compensated by adding 500 µg L^{-1} of CTAB to the water phase before emulsification. This also indicates that a flow-induced separation of the less viscous component to the walls is unlikely to be the cause of the filling. Whereas PAO contains many components of greatly varying molecular weights and viscosities, silicone oil, Krytox® 103 and FC-70 are fairly monodisperse (Figure S6.20, Supporting Information).

The generality of the phenomenon poses the question, whether flow-induced but shear-resistant lubrication is to be expected. No, because continuity of interfacial velocities v_i and shear stresses τ_{xy} across the interface takes lubricant along. The shear stress induced by the flowing emulsion can be estimated from the geometry and flow rate. It is safe to assume laminar flow since the Reynolds number ($Re = \rho_e \cdot v \cdot H/\eta_e$) is 0.1 for this flow condition. Here, $\rho_e \approx 1$ g mL^{-1} is the density of the emulsion, $\eta_e = \eta_w \cdot (1 + 5/2 \cdot \phi)$ is the viscosity of the emulsion, η_w = 1 mPa s is the viscosity of water and ϕ is the fraction of oil present in the emulsion[319-324]. As the height of the surface structures is more than an order of magnitude less than the height of the flow cell, the flow profile is parabolic through its depth, and the flow rate Q imposes a shear stress τ_{xy} on the top face of the micropillars[97,163]:

$$\tau_{xy} = \frac{6 \cdot \eta_e \cdot Q}{W \cdot H^2} \qquad (6.1)$$

This yields $\tau_{xy} = 0.8$ Pa for the model emulsion $\phi = 0.02$, $\eta_e = 1.05$ mPa·s, and $Q = 7$ mL min^{-1}. The amount of lubricant sheared off by the flow has been estimated assuming completely filled simple rectangular groove geometry. In that case, shear-induced depletion per unit of time along single grooves can be estimated to be[163]:

$$q = c \frac{wh^2}{\eta} \tau_{xy} \qquad (6.2)$$

Here, the constant $c \approx 0.15$ accounts for the hydrodynamic resistance created by the walls of the grooves and is dependent on the aspect ratio of width $w = P - d$ and the height h of the grooves. The

total shear-induced depletion of lubricant within a flow channel made of N grooves is $q_d = N \cdot q$. Assuming that a row of micropillars resembles a groove the amount of sheared off lubricant can be estimated as $q_d = 6.6 \cdot 10^5$ µm^3 s^{-1} for the model emulsion and flow channel with w = 15 µm, h = 10 µm, and $N = 190$.

Theoretically the hydrodynamic drag force of water (viscosity η_w = 1 mPa s) F_{hyd} should prevent coalescing of the oil drops and filling of the structure[317,325-327]. For spheres $F_{hyd} = -\frac{6\pi\eta_w v R^2}{x}$ diverges if the distance x between the oil droplets of radius R and the surface approaches zero. Because drops are deformable, no analytical expression exists. Still, only at sufficiently high velocity v or long contact times; the water film separating the drop and the pillar is sufficiently thinned during the impact that a defect can induce rupturing of the water film[328-330]. One might speculate whether diffusion of oil and nucleation of drops might give rise to faster filling. Both processes can safely be ignored because the solubility of silicone oil in water is negligible, < 1 part per billion (ppb)[331].

Beside of a minimum flow rate, experimentally found to be $Q \approx 1$ mL min^{-1} corresponding to an average flow velocity $v \approx 10$ mm s^{-1}, Figure 6.4d (and Figure S6.21, Supporting Information), good chemical compatibility of the emulsion drops and the surface is essential. Analogous to oil capture underwater[332], hydrophilic arrays (neat SU-8 micropillars and plasma-activated micropillar arrays) cannot be filled as oils avoid hydrophilic surfaces when surrounded by water, Figure 6.4d (and Figure S6.22, Supporting Information). Different from underwater oil capture, here the oil drops are freely circulated within the surface structure of the substrate by a flow. The filling of surface structure by oil is solely based on attachment and merging of drops.

To fill the structure, the lubricant sheared off from the surface needs to be compensated by the coalescing droplets at the surface structure. This implies that the filling rate $\dot{V}$ has to exceed the amount of sheared off lubricant, $\dot{V} > q_d$. An upper limit of the filling rate is given by:

$$\dot{V}_{max} = Q \cdot \phi \cdot \frac{h}{H} \tag{6.3}$$

As the filling rate and the shear stress at the surface are both dependent on the flow rate Q, $\dot{V}_{max}$ always exceeds the amount of depleted lubricant q_d independently on the flow velocity (Figure S6.23, Supporting Information 6.5.3.5, 6.5.3.9 and 6.5.3.10).

6.3 Conclusions

In conclusion, lubricant-infused surfaces can be facilitated on a broad range of solid-lubricant combinations. In contrast to all ex-situ approaches, the presented in-situ replenishing strategy does not rely on spraying, dipping or painting. The dispersed phase acts as an autonomously replenishing lubricant. Also, high-viscosity oils can be transported quickly in a diluted oil/water emulsion. The generic nature of the filling mechanism and the successful use of different lubricants demonstrate the potential for industrial applications. Basically, for every commercial product involving the flow or movement of emulsions over a porous surface, *i.e.* the walls of the container containing an emulsion-based product, our approach could be applied.

6.4 Experimental Section

Materials: The surfactant cetyltrimethylammonium bromide (CTAB) was purchased from Sigma-Aldrich. Trichlorooctylsilane (TCMS), trichlorooctylsilane (OTS) and fluorosilane, 1*H*,1*H*,2*H*,2*H*-perfluorooctyl-trichlorosilane were purchased from Sigma-Aldrich. The SU-8 photoresist was purchased from MicroChem Corp. The fluorescent dyes were *ATTO 488 NHS-ester* (ATTO-TEC GmbH, Germany, diluted in MilliQ water) and Coumarin 6 (Sigma-Aldrich). As lubricants silicone oil (PDMS, SIGMA-ALDRICH, viscosity: 50 cSt at 25 °C), poly-α-olefin (PAO, Durasyn® 166, Tunap Industry, Canada), Krytox® 103 (DuPont) were used. All chemicals were used as received. The flow cells (Sticky-Slide VI$^{0.4}$) were ordered from ibidi GmbH. The flow cells were connected to a peristaltic pump (Reglo-Analog MS4/8, Cole-Parmer GmbH) via PVC-tubes (internal diameter = 1.42 mm, Novodirect GmbH Labor- und Meßgeräte) and tightly sealing linkers. The fluorescent dye *ATTO 488 NHS-ester* offers excellent water solubility, strong absorption, high fluorescence quantum yield, and high photostability. The fluorescence is excited most efficiently in the range of 480 nm and 1515 nm. The 488 nm line of the argon laser was used for excitation[333]. To visualize replenishment of the lubricant within the nanofilament coating, Coumarin 6 with the concentration of 50 µg g^{-1} was used to label the silicone oil. The 476 nm line of the argon laser was used for excitation. The used dye concentrations did not change the interfacial tension of water. Before preparing the emulsion, the dyed oil was sonicated for 2 h and filtered through a 0.22 µm syringe filter to remove possible aggregates of the dye.

Setup of Flow Cell Experiment: The OTS-coated micropillar arrays were stuck onto flow cells (Figure S6.1 and Table S6.1, Supporting Information). To ensure tight sealing a ferrule was used. The flow cell consists of 6 individual rectangular channels. The individual channels are 0.4 mm high, 17 mm long and 3.8 mm wide, which amount to a coverable area of 64.6 mm^2 per channel. Each channel has a volume of 30 µL. The rectangular flow cells have plastic side and top walls based on epoxy resin (Figure S6.1, Supporting Information). The flow cells are mounted to the sample surface by an adhesive layer, which adds 0.1 mm to the overall height of the flow channel, *i.e.* H = 500 µm. The flow cell with the affixed micropillar array was connected to PVC tubes via rectangular linkers. The tubes were fixated on a peristaltic pump and immersed into the emulsion (Figure S6.2, Supporting Information). By choosing the pumping speed at the peristaltic pump, the volume flow rate of emulsion flowing through the channel could be adjusted at our discretion. The volumetric flow rate established through the channel was to amount to Q = 7 ± 0.2 mL min^{-1}, which results in an average velocity of 77 ± 2 mm s^{-1}. This implies that the flow is laminar ($Re = \rho_e \cdot v \cdot H / \eta_e$ = 0.1 < 1). Figure S6.2, Supporting Information, shows a photograph of the experimental setup (top) and a schematic of the filling experiment (bottom). The flow cell setup was mounted onto the commercial laser scanning confocal microscope (Leica TCS SP8 SMD). The tubes were sufficiently long to connect to the flask containing the emulsions. Before starting the experiment with the emulsion, the channels were filled with dyed water (1 µg mL^{-1}) to ensure that there are no air bubbles left and to tune the confocal image acquisition parameters. The prevenient filling of the channel with water does establish the situation of a porous structure (micropillar array) being completely devoid of lubricant, *i.e.* it establishes the situation of complete lubricant depletion from which we start the filling experiment. Before each experiment, the connecting tubes were rinsed multiple times with MilliQ water and dried with pressurized nitrogen. The hydrophobic PVC tubes prefer oil over water. As a consequence, the tubes can be wetted by oil and an oil drop might form. In some of the experiments, the oil droplet is taken along with the emulsion, entering the flow cell and interfering with the measurements. These data were excluded from further considerations.

Preparation of Emulsions/Facilitating Coalescence: A volume of 19.4 mL of MilliQ water containing a concentration of 500 µg L^{-1} of cetyltri-methylammonium bromide (CTAB) was added to 0.4 g of the silicone oil. Furthermore, 0.2 mL of MilliQ water containing the fluorescent dye at a concentration of 100 µg mL^{-1} was added so that the total concentration of the dye in the emulsion was 1 µg mL^{-1}. The emulsification was done using a tip sonicator (SONIFIER® W-450D, G. Heinemann Ultraschall- und Labortechnik) for 2 minutes (70% amplitude, 20 s. pulse duration, 10 s. of pause between pulses). During the sonication, the emulsion was kept in an ice bath. Silicone oil droplets in an aqueous environment are negatively charged[317], which gives rise to a repulsive force between the drops and good stability of the emulsion. The concentration of the positively charged surfactant CTAB[314,315] was chosen in such a way to allow the drops to attach and coalesce at the micropillar array still having good stability within the emulsion. The concentration of the surfactant = 1.4 µM is selected close at the point of charge reversal (*pcr*), orders of magnitude below the CMC of CTAB (1 mM). Pendant drop and Tensiometer (Wilhelmy plate) measurements evidence that, within the experimental accuracy, the surface tension values measured at this surfactant concentration do not deviate from the value for pure water. When observed with the Laser Scanning Confocal Microscope (LSCM) it is revealed that the emulsion is very polydisperse, having oil droplet diameters up to approximately 4 µm (Figure S6.3b and c, Supporting Information).

Preparation of Micropillar Arrays: The preparation of the neat/non-functionalized SU-8 micropillar arrays is described elsewhere[10,310]. The regular and uniform SU-8 photoresist micropillar arrays were fabricated on 170 µm thick coverslip glass slides (Thermo Fisher Scientific). Prior to photolithography, the glass slides were plasma-activated (Femto, Diener electronic GmbH + Co. KG) with for 1 min. (oxygen plasma, 65% of the max. intensity of 300 W, pressure below 0.3 mbar). Subsequently, the samples were subjected to chemical vapor deposition (CVD) at ~ 200 mbar for 2 h to deposit a trichlorooctylsilane (or fluorosilane) monolayer onto the substrates (100 µL of silane together with the samples were placed in the desiccator) to render the surfaces more hydrophobic[334,335]. After the CVD-process, the samples were put into a vacuum oven (2 h, 60 °C, VTR5022, Heraeus) to get rid of residual unreacted silane and volatile contaminants.

Preparation of Silicone Nanofilaments: A solution containing trichloromethylsilane (TCMS) and toluene, having a water content of 85 ± 5 ppm (200 µL TCMS per 100 mL n-hexane), was prepared by stirring for 60 s in a reaction container. The water content was evaluated using a Karl Fischer coulometer (Mettler Toledo C20 Compact KF coulometer). Coverslips cleaned by ultrasonication in ethanol were subsequently immersed in the solution, and the reaction container was sealed. After 2 d the coverslips coated with silicone nanofilaments (TCMS) were rinsed with n-hexane (Fisher Chemical) and dried under a nitrogen stream. More detailed information on the preparation of silicone nanofilaments can be found elsewhere[336-338].

Homogeneity of OTS-coating: The homogeneity of the OTS-coating has been confirmed by checking the static water contact angle on flat glass substrates at 24 different points for at least one sample of each batch. The static water contact angle averaged over all samples investigated amounts to 105 ± 2°. The value of the standard deviation (± 2°) does not exceed the experimental accuracy of the contact angle goniometer, which proves the homogeneity of the OTS-coating. Note that filling of the structure is not observed for the case of a hydrophilized, oxygen plasma activated, micropillar substrate. However, for the case of a fluorinated substrate, the filling mechanism works as observed for the case of OTS-coated substrates.

Confocal imaging: An inverted laser scanning confocal microscope (LSCM, Leica TCS SP8 SMD) with a 40x/1.11 water immersion objective lens (Olympus) was employed to image the oil

replenishment process. The scanned areas were normally 400 x 400 μm^2, if not otherwise mentioned. The horizontal resolution was ~500 nm, the vertical resolution was ~1 µm and the time span in-between successive images was 1.29 s. The scanning frequency was 400 Hz. Images were acquired at different heights with respect to the bottom of the micropillar substrate.

Contact Angle and Interfacial Tension Measurements: Contact angles were measured at different solid-liquid-air/solid-liquid-liquid combinations with a standard goniometer (OCA35, DataPhysics) using the sessile drop method. Interfacial and surface tensions were measured using the contact angle goniometer (OCA35, DataPhysics) with the pendant drop method and a tensiometer (DCAT 11EC, DataPhysics) using the Wilhelmy plate method. The silicone oil-water interfacial tension $\gamma_{ow} = 39.8 \pm 0.3$ mN m^{-1} does not change measurably due to the addition of CTAB at a concentration of 500 µg L^{-1} (0.15 % of CMC). Silicone oil droplets on a smooth OTS-coated surface immersed in MilliQ-water showed a static contact angle $\theta = 96°$, an advancing contact angle $\theta_a = 113 \pm 2°$ and a receding contact angle $\theta_r = 0°$. The vanishing receding contact angle does indicate strong pinning of the three-phase contact line, which means that lateral adhesion is strong and large shear forces would be required to shear off droplets from the surface. To check whether the surface is slippery, we aimed to compare the mobility of water drops before and after infiltrating the structure using the emulsion. However, it turned out to be impossible to disassemble the flow cell. Therefore, we used an OTS-coated micropillar arrays (cylindrical pillars, diameter = 5 µm and center-to-center spacing = 20 µm) in open air and let an identically prepared emulsion (2 wt.-% of silicone oil, 500 µg L^{-1} of CTAB) flow over the micropillar array. Before the emulsion was flowing over the surface, water drops pinned to the surface (Video S6.5, Supporting Information). After the flow of emulsion over the structure, water drops deposited on the surface could easily slide/roll-off the surface. 10 µL water drops started to move downwards the surface as soon as the substrate was inclined by 8 ± 1° determined by the contact angle goniometer at the constant inclination rate of 1° s^{-1}.

Scanning Electron Microscopy (SEM): The micropillar arrays were characterized via scanning electron microscopy (SEM) using a LEO 1530 Gemini scanning electron microscope (Zeiss, Germany). The samples were tilted to best visualize a micropillar array.

Image Processing: The confocal images have been evaluated and processed using the Java-based open-source image processing software ImageJ® (Fiji) and Python™ scripts. The statistical evaluation and the extraction of quantitative data on the behavior of the individual droplets with the aim of further elucidating the filling mechanism in detail were the principle aims of image processing. The primary focus lied on the images and videos obtained in the fluorescence channel. Low signal-to-noise ratios (noise), horizontal banding in the image and poor contrast were frequent problems which had to be dealt with in the image analysis. The poor contrast originated from the fact that, since in many of the experiments the oil has remained undyed, pillars and oil droplets both appear black in the fluorescence channel. The workflow is described shortly in the following. The image processing and evaluation started with the help of adapted built-in Fiji plugins. At first, frames were duplicated for further evaluation. Then, the individual pillars were stacked on top of each other to simplify further processing. The areas occupied with pillars were filled with background signal. A mean filter has been applied to reduce the noisiness in the data, *i.e.*, to smoothen the images by reducing the amount of intensity variation. Subsequently, Python scripts have been used. At first, all droplets per micropillar and frame were consolidated. Then, the centers of the pillars and the droplets have been listed. To determine the orientation of the droplets with respect to the center of the pillar towards the flow direction of the emulsion in the flow channel the respective centers of the pillars and the droplets attached to the pillars have been listed. After correcting for the sample flow channel´s rotation angle against the horizontal direction, the angles obtained between the horizontal line and the straight line

connecting the centers of the pillars and the droplets, referred to as orientation angle in the following, have been recorded. The orientation angles were used to quantify the orientation of the droplets with respect to the center of the pillar towards the flow direction of the emulsion in the flow channel. These orientation angles were averaged over all frames to provide quantitative data on the average orientation of the droplets with respect to the pillars and the flow direction. Furthermore, the orientation angle immediately before to the sinking of the droplet, referred to as the last angle, has been logged. In addition to the orientation of the droplets, quantitative data on the droplet sizes (projected area) and their growth were extracted. To this end, the droplets were considered spherical and the contours of the droplets, which have been assumed to represent the equatorial circumference of the droplet considered, were recorded. The averaged distances between selected points on the contour to the center of the droplets provided the radius of the spherical droplets. The projected area of the droplet, *i.e.* the droplet size, was obtained with the help of elementary geometry. The droplet sizes were listed for each frame of the image sequence. The droplet size immediately before the sinking event, referred to as the last area, was of particular interest. The image processing algorithms also took into account the possibilities of droplet shrinking and detachment from pillars.

6.5 Supporting Information

6.5.1 Flow Cell Specifications and Main Experimental Setup

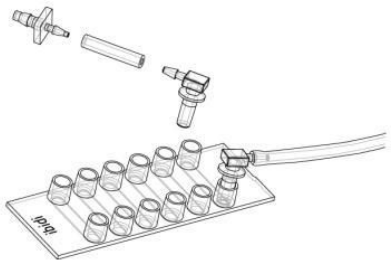

Figure S6.1: The flow cells used throughout this work. The technical specifications of the flow cells are presented in Table S1. (© ibidi GmbH)

Table S6.1: Technical specifications of the flow cells.

Volume per reservoir	60 µL
Number of channels	6
Volume of each channel	30 µL
Height of channels	0.4 mm
Length of channels	17 mm
Width of channels	3.8 mm

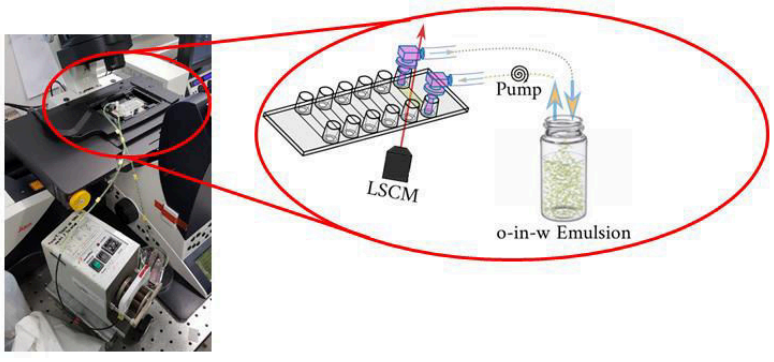

Figure S6.2: A photograph of the experimental setup (top) and a schematic of the filling experiment (bottom).

6.5.2 Supplementary Videos

This section contains a list of videos (.avi).

Video S6.1: Silicone oil droplets in aqueous environment refusing to coalesce even if the contact line gets deformed considerably.

Video S6.2: Top view of filling of micropillar structure.

Video S6.3: Side view of filling of micropillar structure.

Video S6.4: Early stages of filling experiment in 3D.

Video S6.5: Lubricating micropillar structure by flow of emulsion in open air. The sample was inclined by 15°.

Video S6.6: Lubricant-replenishment on a nanofilament coating depleted with lubricant.

6.5.3 Additional Measurements/Supplementary Experiments

6.5.3.1 Charging of Oil Droplets

The conceptual idea behind the addition of a positively charged surfactant is illustrated in Figure S6.3. The emulsions remain sufficiently stable over the time scales of hours to days, also upon the addition of positively charged surfactant. In Figure S6.3a we present photographs of the emulsions taken immediately after preparation, 1h after preparation, 5h after preparation, and 24 after preparation. In both cases (without CTAB and with CTAB), the emulsions remain turbid. Visual inspection hardly reveals any differences. In Figure S6.3b and S6.3c, it is shown that the polydisperse character of the emulsion not containing CTAB (Figure S6.3b) is preserved upon the addition of CTAB (Figure S6.3c). Both, negative as well as positive charges on the oil droplets do stabilize an emulsion (Figure S6.4)[317,339]. Addition of the cationic surfactant reduces the effective charge of the droplet, resulting in a decrease of electrostatic repulsion. As long as the charge repulsion between the charges on the oil droplet does not become too pronounced, the filling of the structure can progress. If no surfactant is added, the emulsions are very stable, but no attachment and coalescence on the solid is observed (Figure S6.5).

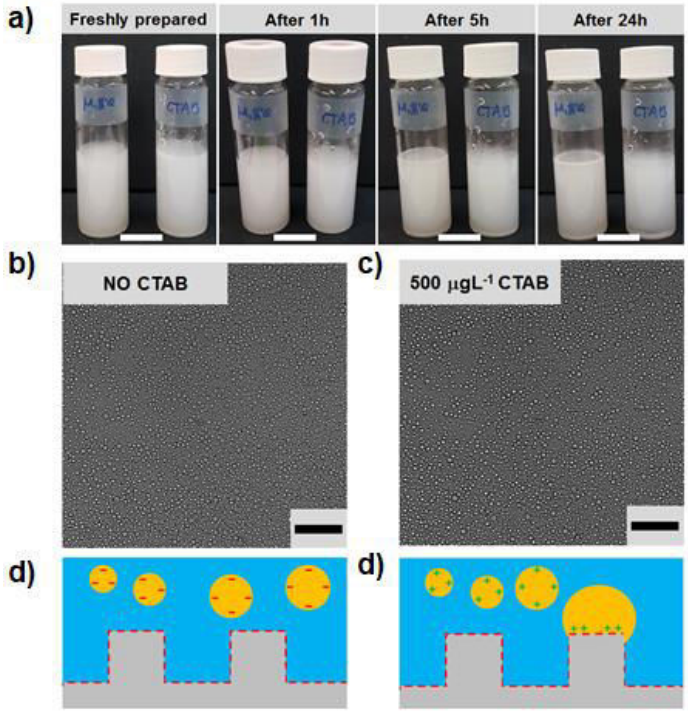

Figure S6.3: Negatively charged oil droplets. a) Visual inspection of emulsion stability. The emulsions remain stable long beyond the time scale of the filling experiments conducted in this work since turbidity is maintained. The scale bar is 2 cm. b) and c) Representative micrographs recorded in the transmission channel (40x/1.11 water immersion objective) showing the polydispersity of the oil-in-water emulsion c) not containing CTAB. and c) containing 500 µgL^{-1} of CTAB. Scale bar: 50 µm. d) Negative charges on the oil droplets lead to charge repulsion and no oil film formation, and filling takes place. e) Weakly charged droplets lead to attachment of oil droplets on the pillars and the bottom substrate and their growth via coalescence with newly arriving droplets, eventually leading to the filling of the structure with oil.

Figure S6.4 and Video S6.1 show that without the addition of positively charged surfactant (CTAB) the negative charges on the oil droplets are sufficiently strong to prevent coalescence in an aqueous environment even when the droplets are pushed into one another.

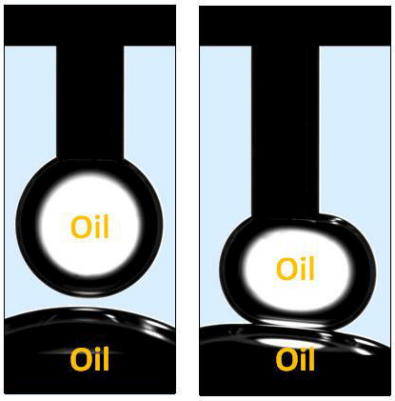

Figure S6.4. Negatively charged oil droplets in aqueous environment preferring deformation over coalescence.

At the later stages of the filling experiment; the filling process does slow down (Figure S6.14). We expect that this is due to progressive accumulation of charges at the surface of the deposited oil film, which eventually leads to charge repulsion ending the filling process. The addition of a negatively charged surfactant (SDS, sodium dodecyl sulfate) and neutral surfactant Pluronic® F-127 is not effective since it does not decrease the electrostatic repulsion between the emulsion drops.

Since a suitable content of a cationic surfactant has been added to reduce the electrostatic repulsion between the drops, the coalescence of droplets at the micropillar surface and thus formation of droplet bridges from pillar tops over the pillar walls to the bottom of the substrate depends on the flux of newly arriving drops. The flow of the emulsion facilitates the transport of the oil droplets.

The primary size or the size distribution of the arriving droplets is not relevant since the success of the filling process does not depend on either of them. The key element to the successful lubricant replenishment is the amount of cationic surfactant that is used. Also, surfaces in aqueous environments are typically negatively charged[317]. The interaction between the oil drops and the micropillar is the first event in any filling experiment. However, negatively charged oil droplets and a negatively charged surface lead to charge repulsion and droplet attachment to the micropillar array is not observed. After addition of 0.14% CMC of CATB, the emulsions are still stable for hours, *i.e.* enough for the timespan of the filling experiments which is typically ~1 h. If the concentration of CTAB is too high (> 1000 µg L^{-1}), there is only a thin oil film formed on the surface with very little subsequent coalescence of oil droplets since the charge density of positive charges becomes too high. In this case, the charge repulsion between the positive charges in the oil droplets dominates and hence prevents the filling.

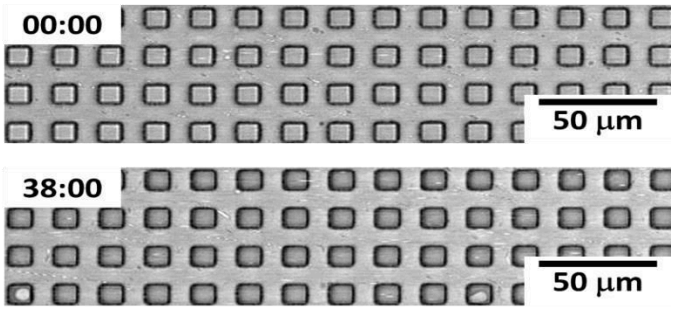

Figure S6.5. Without the addition of a surfactant, electrostatic repulsion between oil droplets prevents filling of the micropillar array. Even after 38 minutes (bottom) the spaces between the pillars remained water filled with no coalescence of oil droplets and filling taking place.

An upper limit of the number of CTAB molecules per drop can be estimated as follows: the molecular weight of CTAB is $M_w = 364.45$ g mol^{-1}. For a CTAB concentration = 500 µg L^{-1} (1.4 µM) this corresponds to $x = 8.4 \cdot 10^{17}$ molecules per liter. Assuming an average radius of $R = 2$ µm for the oil drops, the number of drops per liter of emulsion $N_d = \frac{0.02}{V_d} = 6.6 \cdot 10^{13}$, where 0.02 is the volume fraction of oil in the emulsion and $V_d = \frac{4\pi R^3}{3}$ is the volume of one drop. Thus, each drop is covered by $\frac{x}{N_d} = 12.7 \cdot 10^3$ surfactant molecules. Full coverage of the surface of oil drops by CTAB $\frac{A_{drop}}{A_{CTAB}} = \frac{4 \cdot \pi \cdot R^2}{A_{CTAB}}$ would imply $5 \cdot 10^7$ molecules per drop assuming area per single CTAB molecule[340,341] $A_{CTAB} \approx 1$ nm^2. In reality, the number of CTAB molecules per drop will be less because not all the

surfactant molecules go to the drop surface but also to the water/air interface and walls of the vessel during the preparation of the emulsions.

6.5.3.2 Influence of Surfactant Concentration

The standard CTAB concentration used in this work (500 µg L^{-1}), an amount of 2 wt.-% oil and assuming an average radius of R = 2 µm for the oil drops, each drop is covered by less than $13 \cdot 10^3$ surfactant molecules. Full coverage of the drop surface by CTAB would imply $5 \cdot 10^7$ molecules per drop assuming each CTAB molecule covers[340,341] ≈ 1 nm^2. Hence, the surfactant molecules cover less than 0.03% of the surface area of the drops.

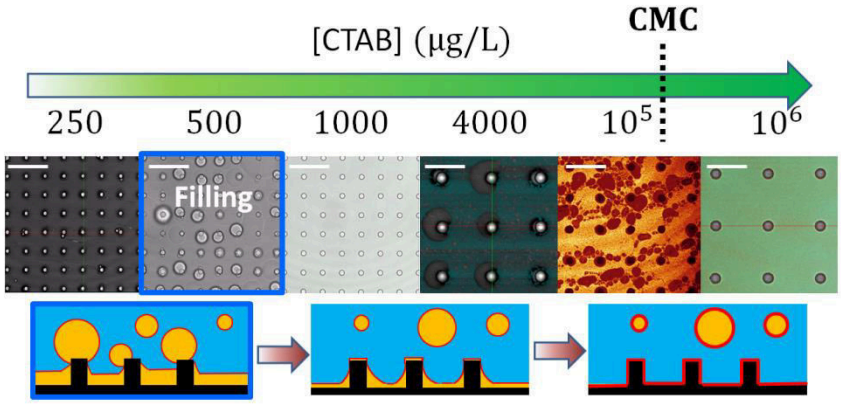

Figure S6.6: Filling mechanisms in dependence on the concentration of the positively charged surfactant CTAB. The concentration of 500 µg L^{-1} enables successful filling of the structure. A concentration below 500 µg L^{-1} does not overcome the charge repulsion between the negatively charged oil droplets. Hence, no coalescence and consequently no droplet attachment and droplet growth is possible. Above concentrations of 500 µg L^{-1} which remain well below the CMC of CTAB (1 mM) droplet attachment predominantly takes place on the bottom substrate, and the structure gets partially filled starting from the bottom substrate, but droplet attachment at pillars and droplet growth on pillars does no longer take place. As soon as an oil layer is formed on the bottom substrate, which may also embrace the pillars, the filling stops due to charge repulsion and increased emulsion stability. The addition of more CTAB above a concentration of 500 µg L^{-1} has led to the increased repulsion of positive charges, which dominates upon further increasing the CTAB-concentration. For CTAB concentrations approaching and exceeding the CMC, no droplet attachment is observed anymore since in these cases the strong presence of CTAB leads to strong charge repulsion between the individual oil droplets as well as between the oil droplets and the bottom substrate. Since surfactant is always present on the bottom substrate, the strong presence of CTAB leads to a positively charged surface which repels the now positively charged oil droplets.

Among the surfactant (CTAB) concentrations used in this work, the concentration of 500 µg L^{-1} (≈ 1.4 µM, 0.14% of critical micelle concentration CMC = 1 mM ≈ $3.35 \cdot 10^5$ µg L^{-1}) led to successful filling of the structure. In this work, we investigated several CTAB-concentrations. In addition to the selected CTAB-concentration of 500 µg L^{-1} we worked with CTAB-concentrations of 250 µg L^{-1} (≈ 0.7 µM,

0.07% CMC), 1000 μg L^{-1} (≈ 2.7 μM, 0.3% CMC), 4000 μg L^{-1} (≈ 11 μM, 1.1% CMC), 10^5 μg L^{-1} (≈ 274 μM, 27.4% CMC), and 10^6 μg L^{-1} (≈ 2.74 mM, 274% CMC). As the surfactant concentration exceeds the concentration of 500 μg L^{-1}, the stability of the emulsions increases (less coalescence). As the surfactant concentration increases above 500 μg L^{-1}, droplet attachment to pillars is less prominent, but droplet attachment to the bottom substrate dominates. Droplet coalescence and partial filling of the structure does occur from the bottom substrate. In contrast to the case of a surfactant concentration of 500 μg L^{-1}, droplet attachment to pillars, droplet growth on pillars and descent of droplets to the bottom substrate is no longer observed. Complete filling of the structure is no longer observed. These results indicate good spreading of the oil on the substrate with increased CTAB concentrations, however, positive charge accumulation in the oil film ends the filling process. For CTAB-concentrations above 4000 μg L^{-1} droplet attachment to the bottom substrate gradually reduces. Above a concentration of 10^5 μg L^{-1} hardly any droplets still attach to the bottom substrate. No droplet attachment at all is observed above the CMC. This is expected to happen due to the surfactant accumulation at the solid substrate, thus preventing attachement of any surfactant covered oil drops. Figure S6.6 summarizes our observations.

6.5.3.3 Attachment of Oil Droplets

As can be seen in Figure 6.3a multiple oil droplets can attach to the same pillar and repeatedly accommodate droplets even after some portions of the underlying bottom substrate around a pillar have already been filled with oil. Figure S6.7 and S6.8 show magnified versions of the area marked by green squares and a white circle in Figure 6.3a.

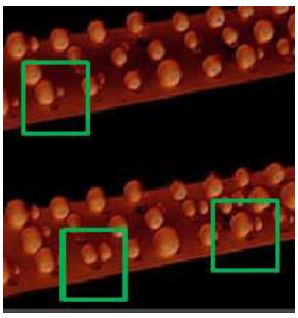

Figure S6.7: Magnification of the area encircled by a square in Figure 6.3a. Two droplets can attach to the same pillar.

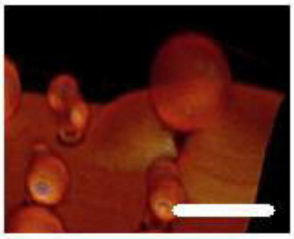

Figure S6.8. Magnification of the area encircled by a white circle in Figure 6.3a. A micropillar repeatedly accommodates a growing droplet. Portions around the micropillars are already surrounded by oil. The scale bar is 10 μm.

6.5.3.4 Orientation of Droplets with Respect to the Micropillar and Size of Descending Droplets

At the early stages of the filling procedure, droplets are oriented towards the flow direction, as shown in Figure S6.9, S6.10, and S6.11. Lifetime of drops and their growth is presented in Figure S6.12 and S6.13.

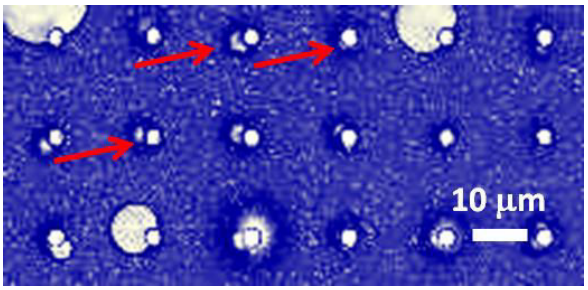

Figure S6.9: Droplets preferentially attach at the front side of the micropillars. Blue: water; light yellow: oil. The cylindrical micropillars are colored in white. They can be discriminated from the oil by the regular arrangement.

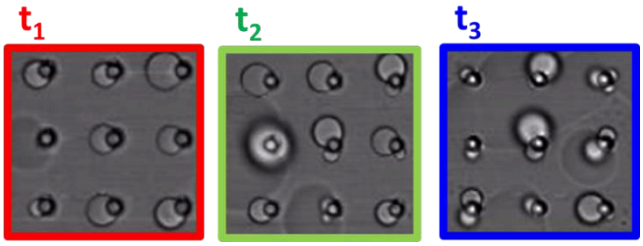

Figure S6.10: Magnified view of the orientation of droplets with respect to the pillars. t_1: First third of the filling (after 5.3 min.), t_2: second third of the filling (10.6 min.), t_3: last third of the filling procedure (15.9 min.). Pillar diameter = 5 µm and center-to-center spacing = 20 µm.

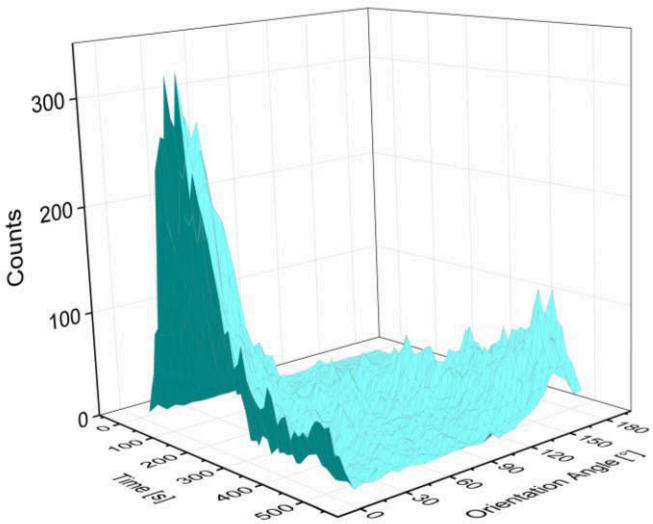

Figure S6.11: Temporal development of the orientation of attached droplets with respect to the center of the pillar. The majority of droplets attached to pillars are found facing the flow direction of the emulsion.

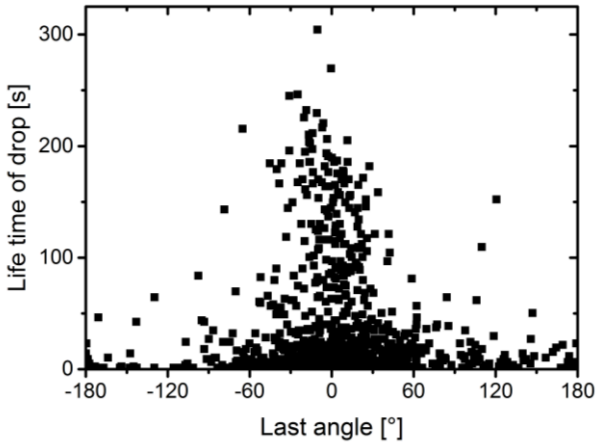

Figure S6.12: Orientation of the droplet just before it sank down with respect to the center of the pillar. Droplets oriented in flow direction stay on the pillars the longest before they sink down.

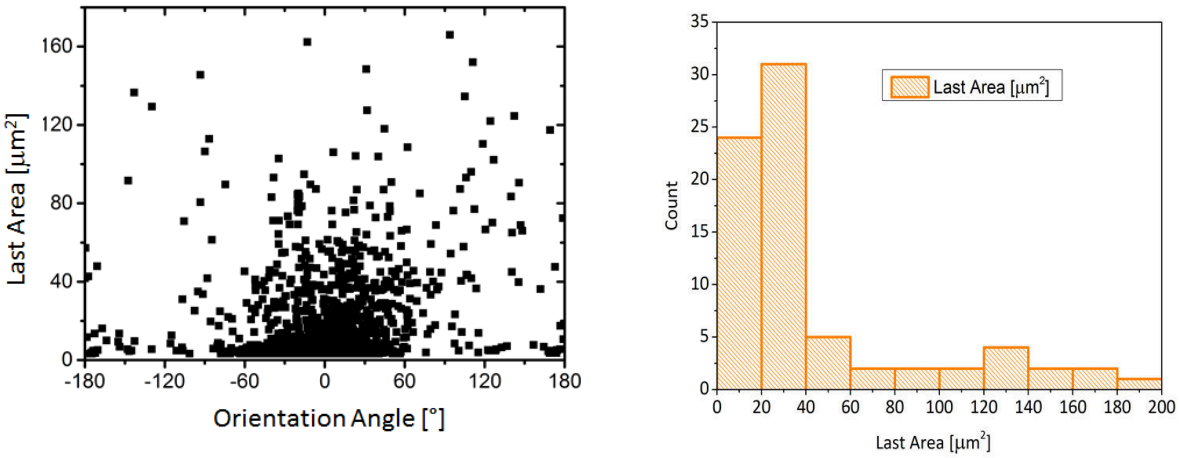

Figure S6.13: Left: The projected area of the droplets before they sink to the pillar substrate and their corresponding final orientation (last angle). Droplet attachment on the portions of the pillars turned away from the flow of emulsion is less frequent than droplet attachment in the flow direction. Right: The projected area to which each of the droplets had grown before it sank to the bottom substrate, the so-called *last area* is given. The data recorded in the fluorescence and transmission channel corresponding to the projected area 9 µm above the bottom substrate. The majority of droplets grew to sizes not exceeding 50 µm². There is no preferred droplet size to which the droplets grow before descending to the bottom substrate. Towards the end of the filling procedure droplets primarily attach at the pillars' top faces. Now, the center of the droplets can be to the left or right of the center of the pillars, reflected in an orientation angle larger than 90°.

6.5.3.5 Lateral Adhesion versus Shear-Induced Depinning

After attachment of a single oil drop to a pillar wall, continuity of shear stresses across the interface might remove the droplet from the wall. However, after attachment, the droplets do not leave the pillar nor do not change their position. This implies that the lateral adhesion force needs to overcome the depinning force and the shear force.

The lateral adhesion force of attached oil drops on pillar walls[342,343] can be estimated as $F_{adh} = k \cdot L \cdot \gamma_{ow} \cdot (\cos\theta_r - \cos\theta_a)$, where $k \approx 1$ is a dimensionless factor accounting for the precise shape of the solid-liquid-oil three-phase contact line of the drop. The drop contact width is designated by L, θ_a = 113 ± 2° is the advancing contact angle and θ_r = 0° is the receding contact angle of silicone oil in water on smooth OTS coated SU-8 surface. Assuming a drop contact width of 5 µm (representing the width of a pillar) and the value of unity for the dimensionless factor k, the lateral adhesion force can be estimated to be $F_{adh} = 1 \cdot 5 \cdot 10^{-6}\, m \cdot 38.9 \cdot 10^{-3} \frac{N}{m} \cdot (1 - \cos(113°)) \approx 2.7 \cdot 10^{-7}$ N. The adhesion force per area is then: $F_{adh}/\pi R^2 \approx 1.4 \cdot 10^4$ Pa. This value needs to be compared to the shear force $\tau_{xy} \approx 0.8$ Pa acting at the surface (Equation (6.1) in main text), which is four orders of magnitude lower.

The shear stress required to depin a sessile droplet from a flat surface surrounded by an immiscible fluid is estimated by[163,344]:

$$\tau_{depin} = \frac{\gamma_{ow}}{R}(0.28)\theta_a^{4/3}(\theta_a - \theta_r). \qquad \text{(S6.1)}$$

With R = 2.5 µm for the small and R = 50 µm for the large droplets, the required yield stress would amount to $7.6 \cdot 10^4$ Pa and $0.4 \cdot 10^4$ Pa, respectively, more than three orders of magnitude larger than the flow induced shear stress τ_{xy} at the surface. Thus, consistently with the experiments, the calculations suggest that the droplets remain in place after attaching the pillar walls.

6.5.3.6 Slowing Down of Filling

Without the addition of a surfactant, the underlying structure will not be filled with oil. Likely, accumulation of the surfactant molecules in the oil film causes the slowing down of the filling process with time (Figure S6.14).

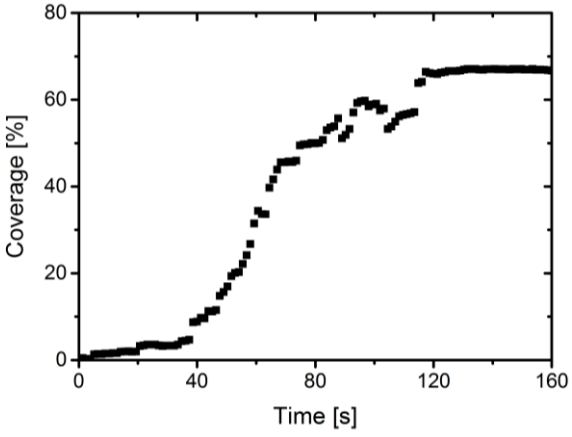

Figure S6.14: Temporal development of the filling of a micropillar array: the coverage saturates after 2 minutes.

6.5.3.7 Quadratic Pillars

As a next step, the droplet distribution (number of droplets) around big rectangular pillars (40 µm edge length) has been elucidated to compare it to the droplet orientation found for the situation of cylindrical pillars (see main text, Figure 6.4a, b). The definition of an *orientation angle* is not appropriate for the case of rectangular pillars owed to the presence of sharp edges. In Figure S6.15 the time evolution of the droplet distribution is presented for a filling experiment conducted with a micropillar array consisting of large rectangular pillars. The standard experimental conditions were established (see main text). Owed to geometry three cases need to be distinguished. There is no radial symmetry. The side of the rectangle facing the flow direction (black curve, in Figure S6.15), the side turned away from the flow direction (blue curve, in Figure S6.15) and the two equivalent sides parallel to the flow direction (red curve, in Figure S6.15). Analogous to the case of the cylindrical micropillar arrays, the number of attached droplets is larger in the early stage of the filling experiment. As more and more portions of the bottom substrate get filled, the number of recorded attached droplets decreases. The three curves show very similar disposal. The disposal of the curves is connected to the

filling kinetics of the individual experiment, which may vary significantly for individual filling experiments performed under identical conditions. There is no preferred orientation for droplet deposition.

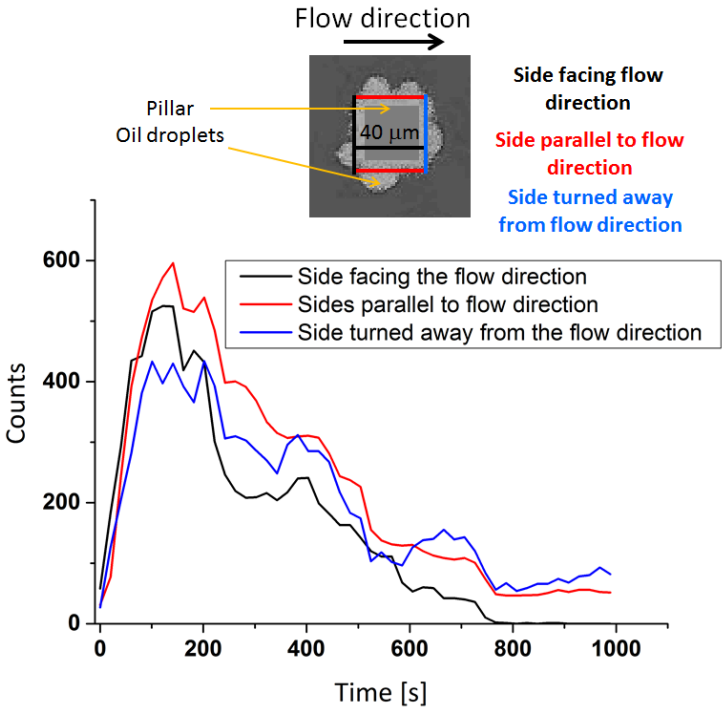

Figure S6.15: Time evolution of droplet distribution around large rectangular micropillars (40 µm side length) during a filling experiment (flow direction from left to right). Three cases need to be distinguished (see sketch on top): the side facing the flow direction (black), the side turned away from the flow direction (blue) and the two sides parallel to the flow direction being equivalent (red). The three curves show very similar disposals. The side facing the flow direction is not preferred over the side turned away from the flow direction regarding more frequent drop attachment.

6.5.3.8 Filling of Porous Substrates of Varying Geometry and with Different Oils

The approach used in this work can potentially be extended to various other porous substrates different from micropillar substrates. To find out whether the mechanism also applies to nanoscopic, porous structures and whether lubricant can be replenished, we investigated glass coated with silicone nanofilaments[318], Figure S6.16. Silicone nanofilaments consist of a fibrous structure of filaments having a diameter of approximately 70 nm.

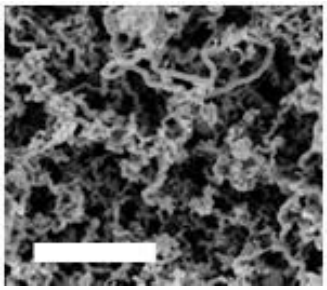

Figure S6.16: SEM image of a glass substrate coated with silicone nanofilaments (Scale bar = 3 μm).

In Figure S6.17, top row, in the fluorescence channel images the level from which the fluorescence signal from the oil-containing dyed water (blue) can be detected changes within the course of the experiment (left: beginning of the filling experiment, right: end of filling experiment), which indicates that the porous substrate gets infiltrated with the emulsion. In Figure S6.17, on the middle row, in the reflection channel images, the large refractive index mismatch leads to pronounced reflection signal at the beginning of the filling experiment (left) since pores in-between nanofilaments are void of oil or water and only contain air. At the end of the filling experiment (right), the pores are filled with the emulsion. Hence, the reflection signal decreases due to the less pronounced refractive index mismatch, which demonstrates the generality of the filling mechanism.

Figure S6.17, bottom row, reveals lubricant replenishment on partially oil-depleted nanofilaments coating (SEM image on the left). On the middle parts overlays of laser scanning confocal images consisting of images recorded in the reflection channel and the fluorescence channel are presented. The nanofilament-coated glass slide stuck onto the flow cell and pre-filled with undyed silicone oil. The amount of oil was then reduced by blowing lubricant away using a flow of nitrogen (middle left). The filling experiments were conducted with an emulsion containing silicone oil dyed with a hydrophobic fluorescent dye Coumarin 6 and the surfactant. As the filling experiment progresses, more and more dyed oil coming from the flow of the emulsion replenishes the depleted lubricant leading to a bright yellow signal corresponding to the replenished oil in the fluorescence channel (middle right, sketch on the right, Supplementary Video S6.5).

So far only silicone oil was used. This poses the question whether the filling mechanism works analogously for different lubricating oils. Figure S6.18a shows the filling of a micropillar structure with the lubricant poly-α-olefin (PAO, ρ = 0.78-0.82 g mL^{-1}). The key strength of PAO lies in its compatibility with many essential lubricant additives, such as antioxidants, anti-wear additives, anti-corrosion agents, friction modifiers or viscosity modifiers[345]. Again, 500 μg L^{-1} CTAB was added to the water phase before emulsification (2 wt.-% of PAO). The top row shows the fluorescence channel (water in blue, oil and pillars in black) and the bottom row the corresponding image in the transmission channel. The filling kinetics resembles those observed for silicone oil. Also, with a fluorinated lubricant Krytox® 103[2,9,16,25,161], which is a commonly used lubricant for slippery surfaces, the same mechanism of droplet attachment to the pillars walls, growth, coalescence and descending by droplet-bridging was observed (Figure S6.19). Analogously to the case of using silicone oil as lubricating oil, filling of the structure with PAO and Krytox® 103 did not occur without added surfactant, hinting that PAO and Krytox emulsions are negatively charged.

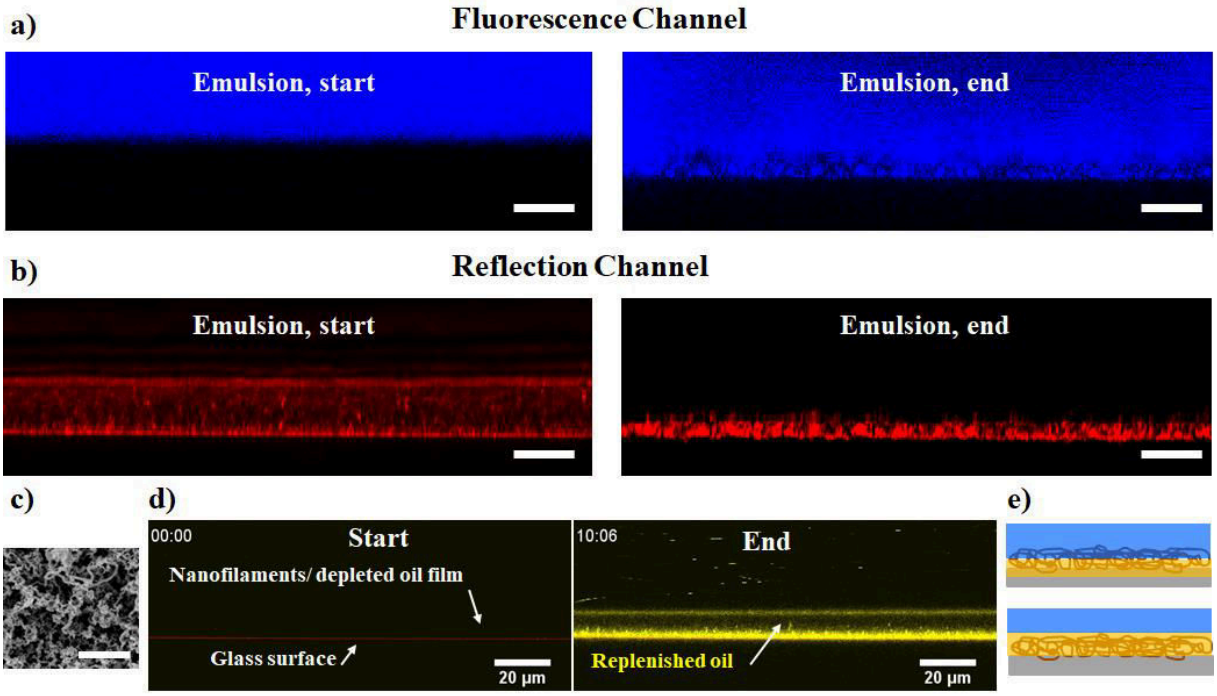

Figure S6.17: Filling of a porous and unordered nanofilament coating with emulsion. a) fluorescence channel (water in blue, oil undyed, scale bar is 20 µm), b) reflection channel (scale bar is 20 µm). c) SEM image of the nanofilament coating, scale bar is 3 µm. d) depleted oil film in nanofilament coating on a glass substrate (left) can be replenished with silicone oil (dyed yellow, right). The laser scanning confocal microscopy side view images consist of an overlay of the reflection and fluorescence channel. At the beginning of the experiment, only the reflection signal owed to the mismatch in the refractive indices of emulsion/filament/oil/glass substrate interfaces are shown. Within the course of the experiment, the depleted oil layer (not dyed in the left part of b)) within the nanofilament coating gets replenished with fresh oil (dyed yellow in the right part of part b)) from the emulsion. The bright fluorescence signal at the top of the oil film and at the glass substrate is due to a tendency of the dye to accumulate at the interfaces. e) Sketch of the start and end of the experiment.

To test the generic nature of flow-induced filling, we investigated the influence of the surface structure. Figure S6.18b shows the top view of the time evolution of a pillar array consisting of square pillars (edge length: 20 µm, center-to-center spacing: 40 µm, pillar height: 10 µm). Again, the top row depicts the fluorescence channel, and the bottom row the transmission channel. The transmission channel image sequence demonstrates that the droplet growth and coalescence take place analogously to the case of cylindrical pillars and the pillar substrate gets filled with oil in an approximately square-like pattern[346]. Different from the cylindrical pillars (Figure 6.2 and Figure 6.3); here each pillar accommodates several droplets due to the large pillar size. Moreover, droplets also attach to the side walls and the pillars backsides, Figure S6.15. The side facing the flow direction is not preferred over the side turned away from the flow direction regarding more frequent drop attachment. Figure S6.18c compares the filling kinetics observed with cylindrical pillars with the filling kinetics for square micropillars. Change of oil or pillar geometry naturally leads to different filling velocities. The sharp steps in the time evolution of the coverage are caused by coalescence of oil patches outside the field of view. The coalesced oil domains spread onto the bottom substrate within the field of view.

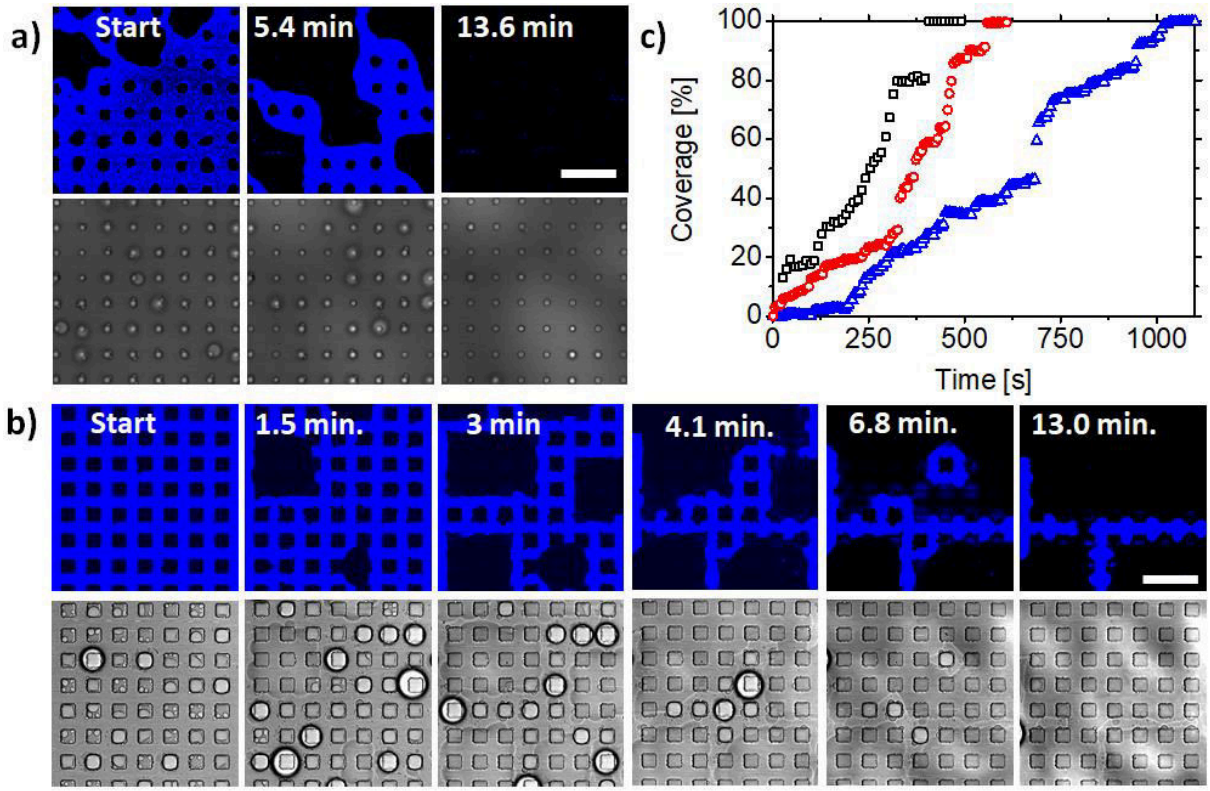

Figure S6.18: The generic nature of the filling and lubricant replenishment mechanism. a) Filling of an initially water-filled (blue = water) micropillar array (black) with the commercial lubricant (black) poly-α-olefin (PAO). The oil gradually replaces the water. Top row: fluorescence channel time evolution image sequence. Bottom row: transmission channel time evolution image sequence. Pillars' geometry: diameter = 5 μm, center-to-center spacing *P* = 20 μm, pillar height *h* = 10 μm. Scale bar: 50 μm. b) A substrate of square micropillars is filled with silicone oil. Top row: The fluorescence channel time evolution image sequence. Bottom row: The transmission channel time evolution image sequence. Pillars' geometry: width = 20 μm, center-to-center spacing *P* = 40 μm, pillar height *h* = 10 μm. Scale bar: 80 μm. The imaging plane lied 2 μm above the bottom surface of the micropillar array. c) Time evolution of the coverage for three different filling experiments with poly-α-olefin (red circles) and silicone oil with cylindrical (standard case, black squares) and square (blue triangles) micropillars. Apart from changing the oil and pillar geometry, the experimental conditions were identical. Flow velocity: 77 mm s^{-1}.

In the main text successful filling of the micropillar structure with silicone oil and PAO is demonstrated. The structure can also be successfully filled with Krytox® 103 and Fluorinert™ FC-70 as is shown in Figure S6.19 showing droplet attachment and growth to the micropillars. Successful filling is also observed in the case of customary food-grade olive oil (not shown).

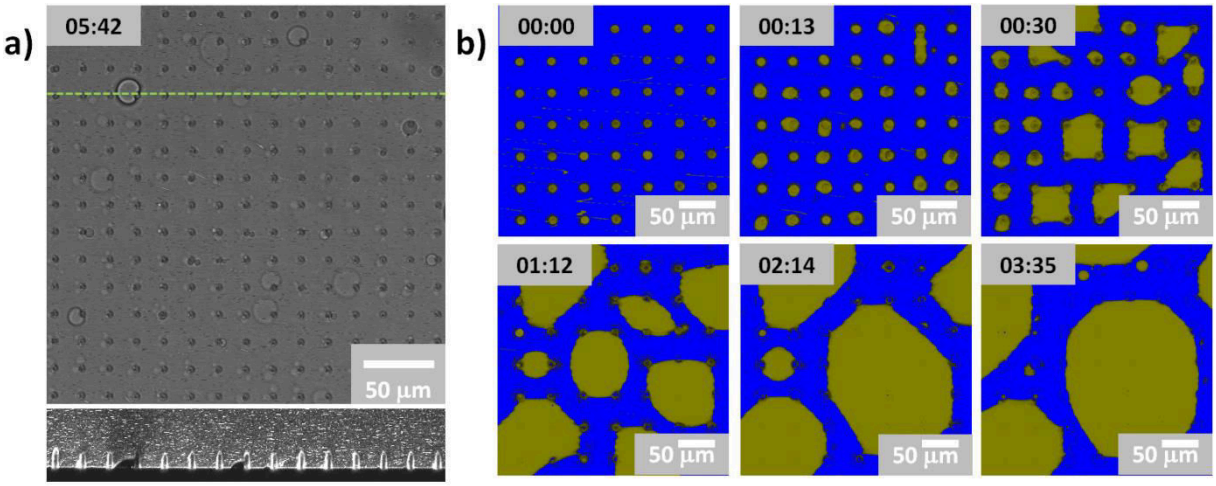

Figure S6.19: a) Filling of micropillar array with Krytox® 103. The filling mechanism works analogously to the case of using silicone oil or PAO as lubricating oil. The upper image shows a transmission channel top-view snapshot of the filling process at 5.42 min. after starting the filling experiment; the image on the bottom shows a transmission channel side view snapshot along the green line drawn above at the same time. b) Filling of a micropillar array with Fluorinert™ FC-70. The images display a time evolution of the filling process in the form of overlay images originating from the fluorescence channel (water: blue, oil: yellow).

For all the lubricants contained in the oil-and-water emulsions used for the filling experiments in this work (silicone oil, PAO, Krytox® 103, Fluorinert™ FC-70), the negative charge of the oil drops had to be compensated by adding 500 μgL^{-1} of CTAB to the water phase before emulsification. In the main text, it is stated that a flow-induced separation of the less viscous component to the walls is unlikely to be the cause of the successful filling.

Below, in Figure S6.20, an experiment supporting this expectation is presented. In the standard filling experiments reported in this manuscript based on an oil-in-water emulsion containing 2 wt.-% 50 cSt silicone oil as well the positively charged surfactant CTAB at a concentration of 500 μgL^{-1}, the viscosity ratio of the lubricant to aqueous phase is $\eta_{oil}/\eta_{water} \approx 50$. To test whether the viscosity ratio matters, we conducted the same experiment using a ratio $\eta_{oil}/\eta_{water} \approx 50$, by exchanging pure water as the aqueous phase by a water-glycerol mixture having a viscosity of ≈ 100 mPa·s; a change by a factor of 100. Still, the filling mechanism works analogously, *i.e.* oil droplets (dyed yellow) attach to pillars, growth through coalescence, and descend onto the substrate. Water is replaced by oil at the pillars.

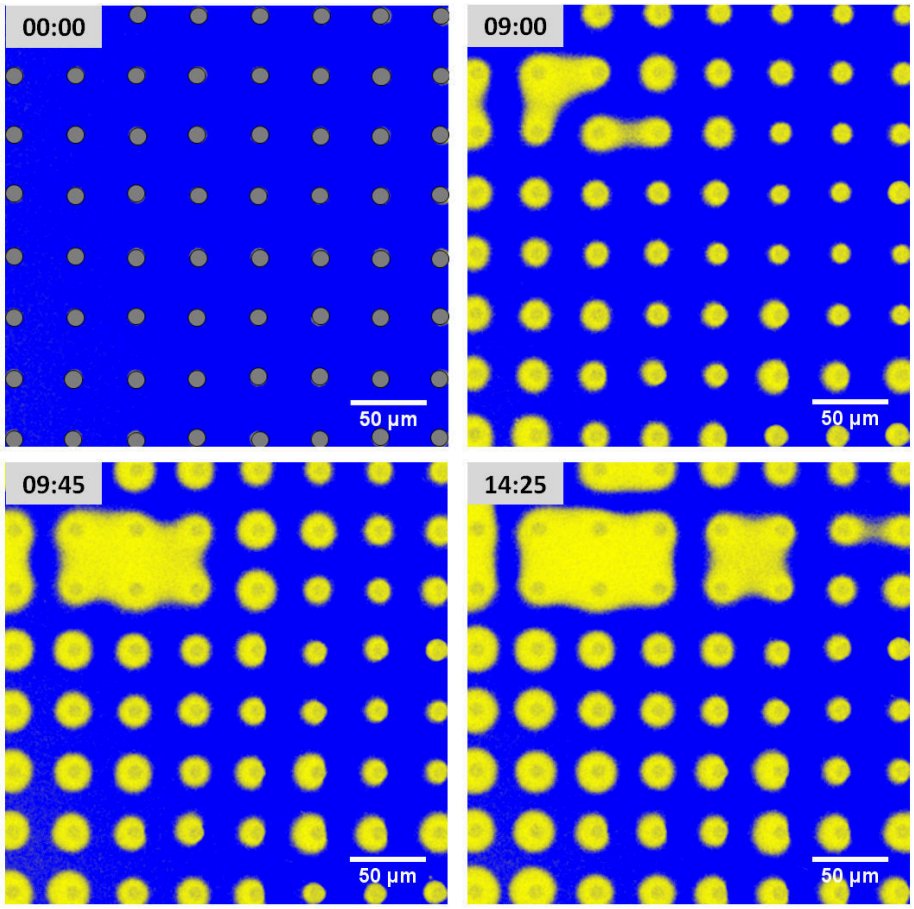

Figure S6.20: Filling experiment conducted with an emulsion whose continuous phase consisting of a water-glycerol mixture having a viscosity of 100 cSt. The concentration of CTAB was kept at 500 µgL^{-1}. The discontinuous/dispersed phase consists of 50 cSt silicone oil (PDMS), η_{oil}/η_{water} = 0.5. The filling takes place analogously to the standard case of oil-in-water emulsions, η_{oil}/η_{water} = 50, whose continuous phase is water. This supports that a flow-induced separation of the less viscous component to the walls of the micropillars or a certain viscosity ratio of the working fluid to the viscosity of the working fluid is unlikely to be the decisive factor for the successful filling of the structure.

6.5.3.9 Generic Nature of Flow-Induced Lubricant-Replenishment from Emulsions

Lubricant-replenishment from the flow of emulsions works analogously for a broad range of lubricant-solid combinations and flow velocities. However, flow and positively charged surfactant are crucial. Firstly, the presence of flow is necessary to facilitate the attachment and growth of droplets, Figure S6.21. At some point, the flow in the filling experiment was stopped (indicated by time 00:00 in upper image) and droplets attached to pillar have remained unchanged for 15 minutes; they neither grow, nor detach, nor descend to the bottom substrate. It has to be noted that in the case of a lubricating oil less dense than water, buoyancy will keep the oil from contacting the bottom substrate as well as pillars. Secondly, without the addition of a surfactant, the underlying structure will not be filled with oil.

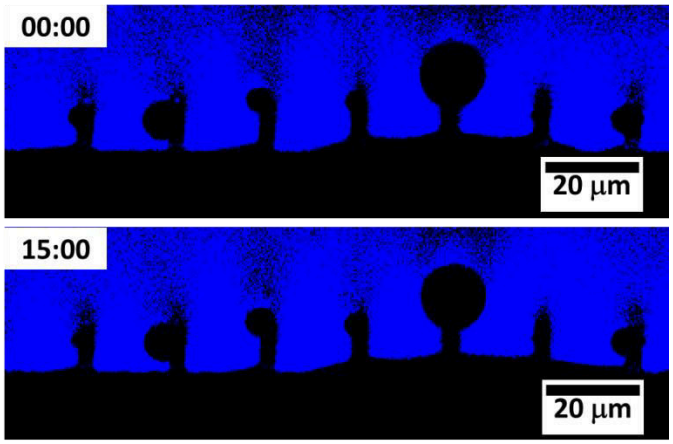

Figure S6.21: Influence of flow on the filling kinetics. After partially filling an OTS-coated micropillar array with silicone oil (contained in an oil-in-water emulsion, 2 wt.-% of silicone oil, 500 µg L^{-1} of CTAB) the flow was turned off. Even after 15 minutes, the filling did neither progress nor change.

For hydrophilic substrates, filling does not take place. The hydrophobic (oleophilic) nature of the underlying solid substrate needs to be preserved, as is shown in Figure S6.22, in order to facilitate filling.

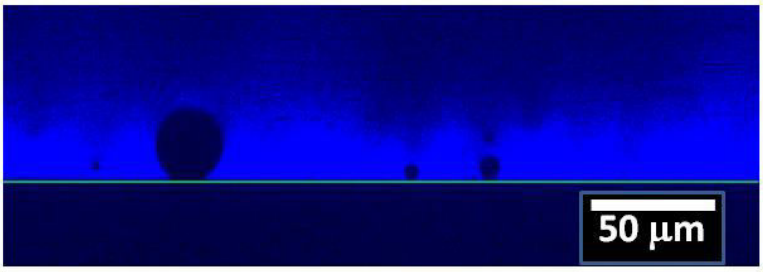

Figure S6.22: Side view fluorescence channel image (blue = water, black = oil droplets and bottom substrate, green line = boundary between solid substrate and emulsion) recorded in-between pillars reveals that on a hydrophilic substrate consisting of oxygen-plasma-activated glass slides coated with SU-8 the oil droplets do not spread. Hence, no filling takes place.

When circulating the emulsion over the micropillar array, the number of drops adhering to the surface or merging with other drops or the oil film cannot be reliably predicted. However, we can estimate it from the filling rate and the amount of lubricant sheared off by the flow. The total volume of oil required to fill the structure completely is $6.1 \cdot 10^8$ µm^3. With a total filling time of 4 min the filling rate is thus $2.5 \cdot 10^6$ µm^3 s^{-1}. Assuming an average drop radius of 2 µm the filling rate is $7.6 \cdot 10^4$ drops s^{-1}. The amount of depleted lubricant, Equation 6.2 in the main text, in the flow cell is $6.6 \cdot 10^5$ µm^3 s^{-1} corresponding to $2 \cdot 10^4$ drops s^{-1}. At a flow rate of 7 mL min^{-1}, which corresponds to an average flow velocity = 77 mm s^{-1}, and an oil concentration of 2 wt.-% approximately $7 \cdot 10^7$ drops s^{-1} pass the flow channel. The flow of oil drops thus exceeds the amount of depleted lubricant by more than three orders of magnitude. Both the shear-induced depletion and the amount of oil droplets passing through the flow channel are equally dependent on the flow rate Q. Therefore, the ratio of upper limit of the filling

rate $\dot{V}_{max}$ to the amount of depleted lubricant q_d does not change with the flow velocity, and always remains at a value of the order of 100, *i.e.* the upper limit of the filling rate $\dot{V}_{max}$ remains almost two orders of magnitude higher than the amount of depleted oil (Figure S6.23) q_d. Indeed, within the experimental range, the amount of circulated lubricant is sufficient to fill the structure independently on the flow velocity and even if the flow is reduced between the micropillar arrays[347]. Flow field considerations suggest that a minimum flow velocity is necessary to facilitate transport of oil droplets in-between the pillars and to the bottom substrate[348].

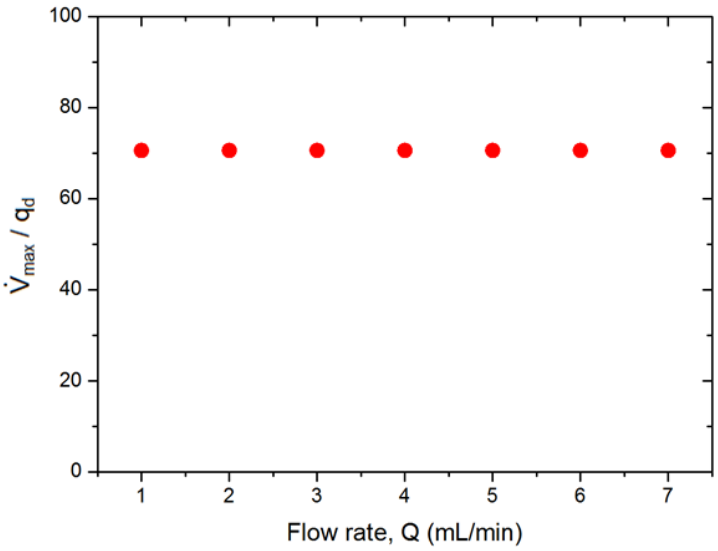

Figure S6.23: Ratio between the upper limit of the filling rate $\dot{V}_{max}$ to the amount of depleted lubricant q_d ($\dot{V}_{max}/q_d$) as a function of flow rate Q.

6.5.3.10 Hydrodynamic Drag Force

Theoretically the hydrodynamic drag force of water (viscosity η_w = 1 mPa s) F_{hyd} should prevent coalescing and filling[317,325-327]. For spheres $F_{hyd} = -\frac{6\pi\eta_w v R^2}{x}$ diverges if the distance x between the particle of radius R and the surface approaches zero. Because drops are deformable, no analytical expression exists. Still, only at sufficiently high velocity v or long contact times; the water film separating the drop and the pillar is sufficiently thinned during the impact that a defect can induce rupturing of the water film[328-330].

6.6 Authors' Contributions

P. B. and H. T. equally contributed to this work. P.B., H.T., H.-J.B. and D.V. designed the structure of the manuscript and planned the experiments. P.B., H.T., D.G.-G., V.D., F.G. and M.D. conducted the experiments. H.B. and A.K. carried out the image analysis. P.B., H.T., H.-J.B. and D.V. wrote the manuscript. The authors declare that there are no financial conflicts of interest.

6.7 Acknowledgements

The authors acknowledge the funding received from the European Union's Horizon 2020 research and innovation program under the Marie Skłodowska-Curie grant agreement No 722497, the ERC advanced Grant No. 340391-SUPRO, the Collaborative Research Center (SFB) 1194. H.T. acknowledges Tekes – the Finnish Funding Agency for Innovation (grant 40365/14), Walter Ahlström Foundation (Tutkijat maailmalle –program), and Alexander von Humboldt Foundation for financial support. D. G.-G. acknowledges the Max Planck –UT Center for Complex Fluid Dynamics for financial support. Dr. Lucas Caire da Silva and Gabriele Schäfer are acknowledged for technical support. We thank Dr. Burkhard Dünweg for fruitful discussions.

7 References

1 Lafuma, A. & Quéré, D. Slippery pre-suffused surfaces. *EPL (Europhysics Letters)* **96**, 56001, doi:10.1209/0295-5075/96/56001 (2011).

2 Wong, T.-S., Kang, S. H., Tang, S. K. Y., Smythe, E. J., Hatton, B. D., Grinthal, A. & Aizenberg, J. Bioinspired self-repairing slippery surfaces with pressure-stable omniphobicity. *Nature* **477**, 443-447, doi:10.1038/nature10447 (2011).

3 Villegas, M., Zhang, Y., Abu Jarad, N., Soleymani, L. & Didar, T. F. Liquid-Infused Surfaces: A Review of Theory, Design, and Applications. *ACS Nano* **13**, 8517-8536, doi:10.1021/acsnano.9b04129 (2019).

4 Bohn, H. F. & Federle, W. Insect aquaplaning: *Nepenthes* pitcher plants capture prey with the peristome, a fully wettable water-lubricated anisotropic surface. *Proceedings of the National Academy of Sciences of the United States of America* **101**, 14138-14143, doi:10.1073/pnas.0405885101 (2004).

5 Bauer, U., Bohn, H. F. & Federle, W. Harmless nectar source or deadly trap: *Nepenthes* pitchers are activated by rain, condensation and nectar. *Proceedings of the Royal Society B: Biological Sciences* **275**, 259-265, doi:doi:10.1098/rspb.2007.1402 (2008).

6 Bauer, U. & Federle, W. The insect-trapping rim of Nepenthes pitchers: surface structure and function. *Plant Signal Behav* **4**, 1019-1023, doi:10.4161/psb.4.11.9664 (2009).

7 Tenjimbayashi, M., Togasawa, R., Manabe, K., Matsubayashi, T., Moriya, T., Komine, M. & Shiratori, S. Liquid-Infused Smooth Coating with Transparency, Super-Durability, and Extraordinary Hydrophobicity. *Advanced Functional Materials* **26**, 6693-6702, doi:10.1002/adfm.201602546 (2016).

8 Ashrafi, Z., Lucia, L. & Krause, W. Nature-Inspired Liquid Infused Systems for Superwettable Surface Energies. *ACS Applied Materials & Interfaces* **11**, 21275-21293, doi:10.1021/acsami.9b00930 (2019).

9 Vogel, N., Belisle, R. A., Hatton, B., Wong, T.-S. & Aizenberg, J. Transparency and damage tolerance of patternable omniphobic lubricated surfaces based on inverse colloidal monolayers. *Nature Communications* **4**, 2176, doi:10.1038/ncomms3176 (2013).

10 Schellenberger, F., Xie, J., Encinas, N., Hardy, A., Klapper, M., Papadopoulos, P., Butt, H.-J. & Vollmer, D. Direct observation of drops on slippery lubricant-infused surfaces. *Soft Matter* **11**, 7617-7626, doi:10.1039/C5SM01809A (2015).

11 Qiu, R., Zhang, Q., Wang, P., Jiang, L., Hou, J., Guo, W. & Zhang, H. Fabrication of slippery liquid-infused porous surface based on carbon fiber with enhanced corrosion inhibition property. *Colloids and Surfaces A: Physicochemical and Engineering Aspects* **453**, 132-141, doi:https://doi.org/10.1016/j.colsurfa.2014.04.035 (2014).

12 Shillingford, C., MacCallum, N., Wong, T.-S., Kim, P. & Aizenberg, J. Fabrics coated with lubricated nanostructures display robust omniphobicity. *Nanotechnology* **25**, 014019, doi:10.1088/0957-4484/25/1/014019 (2013).

13 Wei, Q., Schlaich, C., Prévost, S., Schulz, A., Böttcher, C., Gradzielski, M., Qi, Z., Haag, R. & Schalley, C. A. Supramolecular Polymers as Surface Coatings: Rapid Fabrication of Healable Superhydrophobic and Slippery Surfaces. *Advanced Materials* **26**, 7358-7364, doi:10.1002/adma.201401366 (2014).

14 Tenjimbayashi, M., Park, J.-Y., Muto, J., Kobayashi, Y., Yoshikawa, R., Monnai, Y. & Shiratori, S. In Situ Formation of Slippery-Liquid-Infused Nanofibrous Surface for a Transparent Antifouling Endoscope Lens. *ACS Biomaterials Science & Engineering* **4**, 1871-1879, doi:10.1021/acsbiomaterials.8b00134 (2018).

15 Epstein, A. K., Wong, T.-S., Belisle, R. A., Boggs, E. M. & Aizenberg, J. Liquid-infused structured surfaces with exceptional anti-biofouling performance. *Proceedings of the National Academy of Sciences* **109**, 13182-13187, doi:10.1073/pnas.1201973109 (2012).

16 Brown, P. S. & Bhushan, B. Liquid-impregnated porous polypropylene surfaces for liquid repellency. *Journal of Colloid and Interface Science* **487**, 437-443, doi:https://doi.org/10.1016/j.jcis.2016.10.079 (2017).
17 Li, J., Kleintschek, T., Rieder, A., Cheng, Y., Baumbach, T., Obst, U., Schwartz, T. & Levkin, P. A. Hydrophobic Liquid-Infused Porous Polymer Surfaces for Antibacterial Applications. *ACS Applied Materials & Interfaces* **5**, 6704-6711, doi:10.1021/am401532z (2013).
18 Tonelli, M., Peppou-Chapman, S., Ridi, F. & Neto, C. Effect of Pore Size, Lubricant Viscosity, and Distribution on the Slippery Properties of Infused Cement Surfaces. *The Journal of Physical Chemistry C* **123**, 2987-2995, doi:10.1021/acs.jpcc.8b11221 (2019).
19 Rowthu, S., Balic, E. E. & Hoffmann, P. Molecular dimensions and surface diffusion assisted mechanically robust slippery perfluoropolyether impregnated mesoporous alumina interfaces. *Nanotechnology* **28**, 505605, doi:10.1088/1361-6528/aa974a (2017).
20 Rowthu, S. & Hoffmann, P. Perfluoropolyether-Impregnated Mesoporous Alumina Composites Overcome the Dewetting–Tribological Properties Trade-Off. *ACS Applied Materials & Interfaces* **10**, 10560-10570, doi:10.1021/acsami.8b00061 (2018).
21 Scarratt, L. R. J., Hoatson, B. S., Wood, E. S., Hawkett, B. S. & Neto, C. Durable Superhydrophobic Surfaces via Spontaneous Wrinkling of Teflon AF. *ACS Applied Materials & Interfaces* **8**, 6743-6750, doi:10.1021/acsami.5b12165 (2016).
22 Owais, A., Smith-Palmer, T., Gentle, A. & Neto, C. Influence of long-range forces and capillarity on the function of underwater superoleophobic wrinkled surfaces. *Soft Matter* **14**, 6627-6634, doi:10.1039/C8SM00709H (2018).
23 Ware, C. S., Smith-Palmer, T., Peppou-Chapman, S., Scarratt, L. R. J., Humphries, E. M., Balzer, D. & Neto, C. Marine Antifouling Behavior of Lubricant-Infused Nanowrinkled Polymeric Surfaces. *ACS Applied Materials & Interfaces* **10**, 4173-4182, doi:10.1021/acsami.7b14736 (2018).
24 Wilson, P. W., Lu, W., Xu, H., Kim, P., Kreder, M. J., Alvarenga, J. & Aizenberg, J. Inhibition of ice nucleation by slippery liquid-infused porous surfaces (SLIPS). *Physical Chemistry Chemical Physics* **15**, 581-585, doi:10.1039/C2CP43586A (2013).
25 Kim, P., Kreder, M. J., Alvarenga, J. & Aizenberg, J. Hierarchical or Not? Effect of the Length Scale and Hierarchy of the Surface Roughness on Omniphobicity of Lubricant-Infused Substrates. *Nano Letters* **13**, 1793-1799, doi:10.1021/nl4003969 (2013).
26 Yang, J., Song, H., Ji, H. & Chen, B. Slippery lubricant-infused textured aluminum surfaces. *Journal of Adhesion Science and Technology* **28**, 1949-1957, doi:10.1080/01694243.2014.933563 (2014).
27 Subramanyam, S. B., Azimi, G. & Varanasi, K. K. Designing Lubricant-Impregnated Textured Surfaces to Resist Scale Formation. *Advanced Materials Interfaces* **1**, 1300068, doi:10.1002/admi.201300068 (2014).
28 Solomon, B. R., Khalil, K. S. & Varanasi, K. K. Drag Reduction using Lubricant-Impregnated Surfaces in Viscous Laminar Flow. *Langmuir* **30**, 10970-10976, doi:10.1021/la5021143 (2014).
29 Shirtcliffe, N. J., Aqil, S., Evans, C., McHale, G., Newton, M. I., Perry, C. C. & Roach, P. The use of high aspect ratio photoresist (SU-8) for super-hydrophobic pattern prototyping. *Journal of Micromechanics and Microengineering* **14**, 1384-1389, doi:10.1088/0960-1317/14/10/013 (2004).
30 Amato, L., Keller, S. S., Heiskanen, A., Dimaki, M., Emnéus, J., Boisen, A. & Tenje, M. Fabrication of high-aspect ratio SU-8 micropillar arrays. *Microelectronic Engineering* **98**, 483-487, doi:https://doi.org/10.1016/j.mee.2012.07.092 (2012).
31 Howell, C., Vu, T. L., Lin, J. J., Kolle, S., Juthani, N., Watson, E., Weaver, J. C., Alvarenga, J. & Aizenberg, J. Self-Replenishing Vascularized Fouling-Release Surfaces. *ACS Applied Materials & Interfaces* **6**, 13299-13307, doi:10.1021/am503150y (2014).
32 Tsuruki, Y., Sakai, M., Isobe, T., Matsushita, S. & Nakajima, A. Static and dynamic hydrophobicity of alumina-based porous ceramics impregnated with fluorinated oil. *Journal of Materials Research* **29**, 1546-1555, doi:10.1557/jmr.2014.168 (2014).

33 Takada, Y., Sakai, M., Isobe, T., Matsushita, S. & Nakajima, A. Preparation and hydrophobicity of solid–liquid bulk composite using porous glass and fluorinated oil. *Journal of Materials Science* **50**, 7760-7769, doi:10.1007/s10853-015-9346-9 (2015).
34 Wei, C., Zhang, G., Zhang, Q., Zhan, X. & Chen, F. Silicone Oil-Infused Slippery Surfaces Based on Sol–Gel Process-Induced Nanocomposite Coatings: A Facile Approach to Highly Stable Bioinspired Surface for Biofouling Resistance. *ACS Applied Materials & Interfaces* **8**, 34810-34819, doi:10.1021/acsami.6b09879 (2016).
35 Chen, L., Geissler, A., Bonaccurso, E. & Zhang, K. Transparent Slippery Surfaces Made with Sustainable Porous Cellulose Lauroyl Ester Films. *ACS Applied Materials & Interfaces* **6**, 6969-6976, doi:10.1021/am5020343 (2014).
36 Huang, X., Chrisman, J. D. & Zacharia, N. S. Omniphobic Slippery Coatings Based on Lubricant-Infused Porous Polyelectrolyte Multilayers. *ACS Macro Letters* **2**, 826-829, doi:10.1021/mz400387w (2013).
37 Sunny, S., Vogel, N., Howell, C., Vu, T. L. & Aizenberg, J. Lubricant-Infused Nanoparticulate Coatings Assembled by Layer-by-Layer Deposition. *Advanced Functional Materials* **24**, 6658-6667, doi:10.1002/adfm.201401289 (2014).
38 Liu, Q., Yang, Y., Huang, M., Zhou, Y., Liu, Y. & Liang, X. Durability of a lubricant-infused Electrospray Silicon Rubber surface as an anti-icing coating. *Applied Surface Science* **346**, 68-76, doi:https://doi.org/10.1016/j.apsusc.2015.02.051 (2015).
39 Manna, U. & Lynn, D. M. Fabrication of Liquid-Infused Surfaces Using Reactive Polymer Multilayers: Principles for Manipulating the Behaviors and Mobilities of Aqueous Fluids on Slippery Liquid Interfaces. *Advanced Materials* **27**, 3007-3012, doi:10.1002/adma.201500893 (2015).
40 Zhu, G. H., Cho, S.-H., Zhang, H., Zhao, M. & Zacharia, N. S. Slippery Liquid-Infused Porous Surfaces (SLIPS) Using Layer-by-Layer Polyelectrolyte Assembly in Organic Solvent. *Langmuir* **34**, 4722-4731, doi:10.1021/acs.langmuir.8b00335 (2018).
41 Manabe, K., Kyung, K.-H. & Shiratori, S. Biocompatible Slippery Fluid-Infused Films Composed of Chitosan and Alginate via Layer-by-Layer Self-Assembly and Their Antithrombogenicity. *ACS Applied Materials & Interfaces* **7**, 4763-4771, doi:10.1021/am508393n (2015).
42 Bartz, W. J. Tribology, lubricants and lubrication engineering — a review. *Wear* **49**, 1-18, doi:https://doi.org/10.1016/0043-1648(78)90019-4 (1978).
43 Tomala, A., Karpinska, A., Werner, W. S. M., Olver, A. & Störi, H. Tribological properties of additives for water-based lubricants. *Wear* **269**, 804-810, doi:https://doi.org/10.1016/j.wear.2010.08.008 (2010).
44 Morgese, G., Benetti, E. M. & Zenobi-Wong, M. Molecularly Engineered Biolubricants for Articular Cartilage. *Advanced Healthcare Materials* **7**, 1701463, doi:10.1002/adhm.201701463 (2018).
45 Smith, J. D., Dhiman, R., Anand, S., Reza-Garduno, E., Cohen, R. E., McKinley, G. H. & Varanasi, K. K. Droplet mobility on lubricant-impregnated surfaces. *Soft Matter* **9**, 1772-1780, doi:10.1039/C2SM27032C (2013).
46 Courbin, L., Bird, J. C., Reyssat, M. & Stone, H. A. Dynamics of wetting: from inertial spreading to viscous imbibition. *Journal of Physics: Condensed Matter* **21**, 464127, doi:10.1088/0953-8984/21/46/464127 (2009).
47 Keiser, A., Keiser, L., Clanet, C. & Quéré, D. Drop friction on liquid-infused materials. *Soft Matter* **13**, 6981-6987, doi:10.1039/C7SM01226H (2017).
48 Seiwert, J., Clanet, C. & Quéré, D. Coating of a textured solid. *Journal of Fluid Mechanics* **669**, 55-63, doi:10.1017/S0022112010005951 (2011).
49 Landau, L. & Levich, B. Dragging of a Liquid by a Moving Plate. *Acta Physicochimica U.R.S.S.*, Vol. 17, No. 1-2, pp. 42-54 (1942).
50 Landau, L. & Levich, B. Dragging of a Liquid by a Moving Plate. In *Dynamics of Curved Fronts* (ed. Pierre Pelcé) pp. 141-153 (Academic Press Inc., San Diego, CA, USA, 1988).

51 Derjaguin, B. On the thickness of the liquid film adhering to the walls of a vessel after emptying. *Progress in Surface Science* **43**, 134-137, doi:https://doi.org/10.1016/0079-6816(93)90022-N (1993).
52 Rio, E. & Boulogne, F. Withdrawing a solid from a bath: How much liquid is coated? *Advances in Colloid and Interface Science* **247**, 100-114, doi:https://doi.org/10.1016/j.cis.2017.01.006 (2017).
53 Eifert, A., Paulssen, D., Varanakkottu, S. N., Baier, T. & Hardt, S. Simple Fabrication of Robust Water-Repellent Surfaces with Low Contact-Angle Hysteresis Based on Impregnation. *Advanced Materials Interfaces* **1**, 1300138, doi:10.1002/admi.201300138 (2014).
54 Daniel, D., Timonen, J. V. I., Li, R., Velling, S. J. & Aizenberg, J. Oleoplaning droplets on lubricated surfaces. *Nature Physics* **13**, 1020-1025, doi:10.1038/nphys4177 (2017).
55 Kreder, M. J., Daniel, D., Tetreault, A., Cao, Z., Lemaire, B., Timonen, J. V. I. & Aizenberg, J. Film Dynamics and Lubricant Depletion by Droplets Moving on Lubricated Surfaces. *Physical Review X* **8**, 031053, doi:10.1103/PhysRevX.8.031053 (2018).
56 Wooh, S. & Vollmer, D. Silicone Brushes: Omniphobic Surfaces with Low Sliding Angles. *Angewandte Chemie International Edition* **55**, 6822-6824, doi:10.1002/anie.201511895 (2016).
57 Wang, L. & McCarthy, T. J. Covalently Attached Liquids: Instant Omniphobic Surfaces with Unprecedented Repellency. *Angewandte Chemie International Edition* **55**, 244-248, doi:10.1002/anie.201509385 (2016).
58 Leslie, D. C., Waterhouse, A., Berthet, J. B., Valentin, T. M., Watters, A. L., Jain, A., Kim, P., Hatton, B. D., Nedder, A., Donovan, K., Super, E. H., Howell, C., Johnson, C. P., Vu, T. L., Bolgen, D. E., Rifai, S., Hansen, A. R., Aizenberg, M., Super, M., Aizenberg, J. & Ingber, D. E. A bioinspired omniphobic surface coating on medical devices prevents thrombosis and biofouling. *Nature Biotechnology* **32**, 1134-1140, doi:10.1038/nbt.3020 (2014).
59 Krumpfer, J. W. & McCarthy, T. J. Contact angle hysteresis: a different view and a trivial recipe for low hysteresis hydrophobic surfaces. *Faraday Discussions* **146**, 103-111, doi:10.1039/B925045J (2010).
60 Krumpfer, J. W. & McCarthy, T. J. Rediscovering Silicones: “Unreactive” Silicones React with Inorganic Surfaces. *Langmuir* **27**, 11514-11519, doi:10.1021/la202583w (2011).
61 Cheng, D. F., Urata, C., Yagihashi, M. & Hozumi, A. A Statically Oleophilic but Dynamically Oleophobic Smooth Nonperfluorinated Surface. *Angewandte Chemie International Edition* **51**, 2956-2959, doi:10.1002/anie.201108800 (2012).
62 Liu, P., Zhang, H., He, W., Li, H., Jiang, J., Liu, M., Sun, H., He, M., Cui, J., Jiang, L. & Yao, X. Development of “Liquid-like” Copolymer Nanocoatings for Reactive Oil-Repellent Surface. *ACS Nano* **11**, 2248-2256, doi:10.1021/acsnano.7b00046 (2017).
63 Zhao, T., Wang, G., Hao, D., Chen, L., Liu, K. & Liu, M. Macroscopic Layered Organogel–Hydrogel Hybrids with Controllable Wetting and Swelling Performance. *Advanced Functional Materials* **28**, 1800793, doi:10.1002/adfm.201800793 (2018).
64 Cui, J., Daniel, D., Grinthal, A., Lin, K. & Aizenberg, J. Dynamic polymer systems with self-regulated secretion for the control of surface properties and material healing. *Nature Materials* **14**, 790-795, doi:10.1038/nmat4325 (2015).
65 Yao, X., Wu, S., Chen, L., Ju, J., Gu, Z., Liu, M., Wang, J. & Jiang, L. Self-Replenishable Anti-Waxing Organogel Materials. *Angewandte Chemie International Edition* **54**, 8975-8979, doi:10.1002/anie.201503031 (2015).
66 Damle, V. G., Tummala, A., Chandrashekar, S., Kido, C., Roopesh, A., Sun, X., Doudrick, K., Chinn, J., Lee, J. R., Burgin, T. P. & Rykaczewski, K. “Insensitive” to Touch: Fabric-Supported Lubricant-Swollen Polymeric Films for Omniphobic Personal Protective Gear. *ACS Applied Materials & Interfaces* **7**, 4224-4232, doi:10.1021/am5085226 (2015).
67 Wang, Y., Yao, X., Wu, S., Li, Q., Lv, J., Wang, J. & Jiang, L. Bioinspired Solid Organogel Materials with a Regenerable Sacrificial Alkane Surface Layer. *Advanced Materials* **29**, 1700865, doi:10.1002/adma.201700865 (2017).

68 Cao, M., Guo, D., Yu, C., Li, K., Liu, M. & Jiang, L. Water-Repellent Properties of Superhydrophobic and Lubricant-Infused "Slippery" Surfaces: A Brief Study on the Functions and Applications. *ACS Applied Materials & Interfaces* **8**, 3615-3623, doi:10.1021/acsami.5b07881 (2016).
69 Liu, M., Hou, Y., Li, J., Tie, L. & Guo, Z. Transparent slippery liquid-infused nanoparticulate coatings. *Chemical Engineering Journal* **337**, 462-470, doi:https://doi.org/10.1016/j.cej.2017.12.118 (2018).
70 Luo, J. T., Geraldi, N. R., Guan, J. H., McHale, G., Wells, G. G. & Fu, Y. Q. Slippery Liquid-Infused Porous Surfaces and Droplet Transportation by Surface Acoustic Waves. *Physical Review Applied* **7**, 014017, doi:10.1103/PhysRevApplied.7.014017 (2017).
71 Bjelobrk, N., Girard, H.-L., Bengaluru Subramanyam, S., Kwon, H.-M., Quéré, D. & Varanasi, K. K. Thermocapillary motion on lubricant-impregnated surfaces. *Physical Review Fluids* **1**, 063902, doi:10.1103/PhysRevFluids.1.063902 (2016).
72 Jonathan David Smith, C., MA (US); Rajeev Dhiman, Malden, MA (US); Adam T. Paxson, Cambridge, MA (US); Christopher J. Love, Atlantis, FL (US); Brian R. Solomon, Rockville, MD (US); Kripa K. Varanasi, Lexington, MA (US). SELF-LUBRICATING SURFACES FOR FOOD PACKAGING AND FOOD PROCESSING EQUIPMENT, United States patent US 8,535,779 B1, Sep. 17, 2013.
73 Tesler, A. B., Kim, P., Kolle, S., Howell, C., Ahanotu, O. & Aizenberg, J. Extremely durable biofouling-resistant metallic surfaces based on electrodeposited nanoporous tungstite films on steel. *Nature Communications* **6**, 8649, doi:10.1038/ncomms9649 (2015).
74 Charpentier, T. V. J., Neville, A., Baudin, S., Smith, M. J., Euvrard, M., Bell, A., Wang, C. & Barker, R. Liquid infused porous surfaces for mineral fouling mitigation. *Journal of Colloid and Interface Science* **444**, 81-86, doi:https://doi.org/10.1016/j.jcis.2014.12.043 (2015).
75 MacCallum, N., Howell, C., Kim, P., Sun, D., Friedlander, R., Ranisau, J., Ahanotu, O., Lin, J. J., Vena, A., Hatton, B., Wong, T.-S. & Aizenberg, J. Liquid-Infused Silicone As a Biofouling-Free Medical Material. *ACS Biomaterials Science & Engineering* **1**, 43-51, doi:10.1021/ab5000578 (2015).
76 Yin, J., Mei, M. L., Li, Q., Xia, R., Zhang, Z. & Chu, C. H. Self-cleaning and antibiofouling enamel surface by slippery liquid-infused technique. *Scientific Reports* **6**, 25924, doi:10.1038/srep25924 (2016).
77 Wang, P., Zhang, D., Lu, Z. & Sun, S. Fabrication of Slippery Lubricant-Infused Porous Surface for Inhibition of Microbially Influenced Corrosion. *ACS Applied Materials & Interfaces* **8**, 1120-1127, doi:10.1021/acsami.5b08452 (2016).
78 Keller, N., Bruchmann, J., Sollich, T., Richter, C., Thelen, R., Kotz, F., Schwartz, T., Helmer, D. & Rapp, B. E. Study of Biofilm Growth on Slippery Liquid-Infused Porous Surfaces Made from Fluoropor. *ACS Applied Materials & Interfaces* **11**, 4480-4487, doi:10.1021/acsami.8b12542 (2019).
79 Xiao, L., Li, J., Mieszkin, S., Di Fino, A., Clare, A. S., Callow, M. E., Callow, J. A., Grunze, M., Rosenhahn, A. & Levkin, P. A. Slippery Liquid-Infused Porous Surfaces Showing Marine Antibiofouling Properties. *ACS Applied Materials & Interfaces* **5**, 10074-10080, doi:10.1021/am402635p (2013).
80 Wang, P., Zhang, D. & Lu, Z. Slippery liquid-infused porous surface bio-inspired by pitcher plant for marine anti-biofouling application. *Colloids and Surfaces B: Biointerfaces* **136**, 240-247, doi:https://doi.org/10.1016/j.colsurfb.2015.09.019 (2015).
81 Amini, S., Kolle, S., Petrone, L., Ahanotu, O., Sunny, S., Sutanto, C. N., Hoon, S., Cohen, L., Weaver, J. C., Aizenberg, J., Vogel, N. & Miserez, A. Preventing mussel adhesion using lubricant-infused materials. *Science* **357**, 668-673, doi:10.1126/science.aai8977 (2017).
82 Geyer, F., D'Acunzi, M., Yang, C.-Y., Müller, M., Baumli, P., Kaltbeitzel, A., Mailänder, V., Encinas, N., Vollmer, D. & Butt, H.-J. How to Coat the Inside of Narrow and Long Tubes with a Super-Liquid-Repellent Layer—A Promising Candidate for Antibacterial Catheters. *Advanced Materials* **31**, 1801324, doi:10.1002/adma.201801324 (2019).

83 Kim, P., Wong, T.-S., Alvarenga, J., Kreder, M. J., Adorno-Martinez, W. E. & Aizenberg, J. Liquid-infused nanostructured surfaces with extreme anti-ice and anti-frost performance. *ACS Nano* **6**, 6569-6577 (2012).
84 Subramanyam, S. B., Rykaczewski, K. & Varanasi, K. K. Ice Adhesion on Lubricant-Impregnated Textured Surfaces. *Langmuir* **29**, 13414-13418, doi:10.1021/la402456c (2013).
85 Rykaczewski, K., Anand, S., Subramanyam, S. B. & Varanasi, K. K. Mechanism of Frost Formation on Lubricant-Impregnated Surfaces. *Langmuir* **29**, 5230-5238, doi:10.1021/la400801s (2013).
86 Manabe, K., Nishizawa, S., Kyung, K.-H. & Shiratori, S. Optical Phenomena and Antifrosting Property on Biomimetics Slippery Fluid-Infused Antireflective Films via Layer-by-Layer Comparison with Superhydrophobic and Antireflective Films. *ACS Applied Materials & Interfaces* **6**, 13985-13993, doi:10.1021/am503352x (2014).
87 Kreder, M. J., Alvarenga, J., Kim, P. & Aizenberg, J. Design of anti-icing surfaces: smooth, textured or slippery? *Nat. Rev. Mater.* **1**, 15003, doi:10.1038/natrevmats.2015.3 (2016).
88 Zhang, J., Gu, C. & Tu, J. Robust Slippery Coating with Superior Corrosion Resistance and Anti-Icing Performance for AZ31B Mg Alloy Protection. *ACS Applied Materials & Interfaces* **9**, 11247-11257, doi:10.1021/acsami.7b00972 (2017).
89 Niemelä-Anttonen, H., Koivuluoto, H., Tuominen, M., Teisala, H., Juuti, P., Haapanen, J., Harra, J., Stenroos, C., Lahti, J., Kuusipalo, J., Mäkelä, J. M. & Vuoristo, P. Icephobicity of Slippery Liquid Infused Porous Surfaces under Multiple Freeze–Thaw and Ice Accretion–Detachment Cycles. *Advanced Materials Interfaces* **5**, 1800828, doi:10.1002/admi.201800828 (2018).
90 Juuti, P., Haapanen, J., Stenroos, C., Niemelä-Anttonen, H., Harra, J., Koivuluoto, H., Teisala, H., Lahti, J., Tuominen, M., Kuusipalo, J., Vuoristo, P. & Mäkelä, J. M. Achieving a slippery, liquid-infused porous surface with anti-icing properties by direct deposition of flame synthesized aerosol nanoparticles on a thermally fragile substrate. *Applied Physics Letters* **110**, 161603, doi:10.1063/1.4981905 (2017).
91 Yang, S., Qiu, R., Song, H., Wang, P., Shi, Z. & Wang, Y. Slippery liquid-infused porous surface based on perfluorinated lubricant/iron tetradecanoate: Preparation and corrosion protection application. *Applied Surface Science* **328**, 491-500, doi:https://doi.org/10.1016/j.apsusc.2014.12.067 (2015).
92 Song, T., Liu, Q., Liu, J., Yang, W., Chen, R., Jing, X., Takahashi, K. & Wang, J. Fabrication of super slippery sheet-layered and porous anodic aluminium oxide surfaces and its anticorrosion property. *Applied Surface Science* **355**, 495-501, doi:https://doi.org/10.1016/j.apsusc.2015.07.140 (2015).
93 Song, T., Liu, Q., Zhang, M., Chen, R., Takahashi, K., Jing, X., Liu, L. & Wang, J. Multiple sheet-layered super slippery surfaces based on anodic aluminium oxide and its anticorrosion property. *RSC Advances* **5**, 70080-70085, doi:10.1039/C5RA11263J (2015).
94 Schönecker, C., Baier, T. & Hardt, S. Influence of the enclosed fluid on the flow over a microstructured surface in the Cassie state. *Journal of Fluid Mechanics* **740**, 168-195, doi:10.1017/jfm.2013.647 (2014).
95 Lee, T., Charrault, E. & Neto, C. Interfacial slip on rough, patterned and soft surfaces: a review of experiments and simulations. *Advances in colloid and interface science* **210**, 21-38, doi:10.1016/j.cis.2014.02.015 (2014).
96 Schönecker, C. & Hardt, S. Assessment of drag reduction at slippery, topographically structured surfaces. *Microfluidics and Nanofluidics* **19**, 199-207, doi:10.1007/s10404-015-1565-5 (2015).
97 Wexler, J. S., Jacobi, I. & Stone, H. A. Shear-Driven Failure of Liquid-Infused Surfaces. *Physical Review Letters* **114**, 168301, doi:10.1103/PhysRevLett.114.168301 (2015).
98 Liu, Y., Wexler, J. S., Schönecker, C. & Stone, H. A. Effect of viscosity ratio on the shear-driven failure of liquid-infused surfaces. *Physical Review Fluids* **1**, 074003, doi:10.1103/PhysRevFluids.1.074003 (2016).

99 Wang, Y., Zhang, H., Liu, X. & Zhou, Z. Slippery liquid-infused substrates: a versatile preparation, unique anti-wetting and drag-reduction effect on water. *Journal of Materials Chemistry A* **4**, 2524-2529, doi:10.1039/C5TA09936F (2016).
100 Fu, M. K., Arenas, I., Leonardi, S. & Hultmark, M. Liquid-infused surfaces as a passive method of turbulent drag reduction. *Journal of Fluid Mechanics* **824**, 688-700, doi:10.1017/jfm.2017.360 (2017).
101 Sun, R. & Ng, C.-O. Effective slip for flow through a channel bounded by lubricant-impregnated grooved surfaces. *Theoretical and Computational Fluid Dynamics* **31**, 189-209, doi:10.1007/s00162-016-0414-9 (2017).
102 Scarratt, L. R. J., Zhu, L. & Neto, C. How Slippery are SLIPS? Measuring Effective Slip on Lubricated Surfaces with Colloidal Probe Atmoc Force Microscopy. *Langmuir* **35**, 2976-2982, doi:10.1021/acs.langmuir.8b03767 (2019).
103 Rosenberg, B. J., Buren, T. V., Fu, M. K. & Smits, A. J. Turbulent drag reduction over air- and liquid- impregnated surfaces. *Physics of Fluids* **28**, 015103, doi:10.1063/1.4939272 (2016).
104 Van Buren, T. & Smits, A. J. Substantial drag reduction in turbulent flow using liquid-infused surfaces. *Journal of Fluid Mechanics* **827**, 448-456, doi:10.1017/jfm.2017.503 (2017).
105 Anand, S., Paxson, A. T., Dhiman, R., Smith, J. D. & Varanasi, K. K. Enhanced Condensation on Lubricant-Impregnated Nanotextured Surfaces. *ACS Nano* **6**, 10122-10129, doi:10.1021/nn303867y (2012).
106 Xiao, R., Miljkovic, N., Enright, R. & Wang, E. N. Immersion Condensation on Oil-Infused Heterogeneous Surfaces for Enhanced Heat Transfer. *Scientific Reports* **3**, 1988, doi:10.1038/srep01988 (2013).
107 Rykaczewski, K., Paxson, A. T., Staymates, M., Walker, M. L., Sun, X., Anand, S., Srinivasan, S., McKinley, G. H., Chinn, J., Scott, J. H. J. & Varanasi, K. K. Dropwise condensation of low surface tension fluids on omniphobic surfaces. *Scientific reports* **4**, 4158-4158, doi:10.1038/srep04158 (2014).
108 Anand, S., Rykaczewski, K., Subramanyam, S. B., Beysens, D. & Varanasi, K. K. How droplets nucleate and grow on liquids and liquid impregnated surfaces. *Soft Matter* **11**, 69-80, doi:10.1039/C4SM01424C (2015).
109 Park, K.-C., Chhatre, S. S., Srinivasan, S., Cohen, R. E. & McKinley, G. H. Optimal Design of Permeable Fiber Network Structures for Fog Harvesting. *Langmuir* **29**, 13269-13277, doi:10.1021/la402409f (2013).
110 Lalia, B. S., Anand, S., Varanasi, K. K. & Hashaikeh, R. Fog-Harvesting Potential of Lubricant-Impregnated Electrospun Nanomats. *Langmuir* **29**, 13081-13088, doi:10.1021/la403021q (2013).
111 Yao, X., Hu, Y., Grinthal, A., Wong, T.-S., Mahadevan, L. & Aizenberg, J. Adaptive fluid-infused porous films with tunable transparency and wettability. *Nature Materials* **12**, 529-534, doi:10.1038/nmat3598 (2013).
112 Ma, W., Higaki, Y., Otsuka, H. & Takahara, A. Perfluoropolyether-infused nano-texture: a versatile approach to omniphobic coatings with low hysteresis and high transparency. *Chemical Communications* **49**, 597-599, doi:10.1039/C2CC37576A (2013).
113 Zhang, J., Wang, A. & Seeger, S. Nepenthes Pitcher Inspired Anti-Wetting Silicone Nanofilaments Coatings: Preparation, Unique Anti-Wetting and Self-Cleaning Behaviors. *Advanced Functional Materials* **24**, 1074-1080, doi:10.1002/adfm.201301481 (2014).
114 Zhang, P., Chen, H., Zhang, L., Ran, T. & Zhang, D. Transparent self-cleaning lubricant-infused surfaces made with large-area breath figure patterns. *Applied Surface Science* **355**, 1083-1090, doi:https://doi.org/10.1016/j.apsusc.2015.07.159 (2015).
115 Hou, X., Hu, Y., Grinthal, A., Khan, M. & Aizenberg, J. Liquid-based gating mechanism with tunable multiphase selectivity and antifouling behaviour. *Nature* **519**, 70-73, doi:10.1038/nature14253 (2015).

116 Khalil, K. S., Mahmoudi, S. R., Abu-dheir, N. & Varanasi, K. K. Active surfaces: Ferrofluid-impregnated surfaces for active manipulation of droplets. *Applied Physics Letters* **105**, 041604, doi:10.1063/1.4891439 (2014).
117 Hao, C., Liu, Y., Chen, X., He, Y., Li, Q., Li, K. Y. & Wang, Z. Electrowetting on liquid-infused film (EWOLF): Complete reversibility and controlled droplet oscillation suppression for fast optical imaging. *Scientific Reports* **4**, 6846, doi:10.1038/srep06846 (2014).
118 Bormashenko, E., Pogreb, R., Bormashenko, Y., Aharoni, H., Shulzinger, E., Grinev, R., Rozenman, D. & Rozenman, Z. Progress in low voltage reversible electrowetting with lubricated polymer honeycomb substrates. *RSC Advances* **5**, 32491-32496, doi:10.1039/C4RA15927F (2015).
119 Barman, J., Pant, R., Nagarajan, A. K. & Khare, K. Electrowetting on dielectrics on lubricating fluid-infused smooth/rough surfaces with negligible hysteresis. *Journal of Adhesion Science and Technology* **31**, 159-170, doi:10.1080/01694243.2016.1205245 (2017).
120 Bico, J., Tordeux, C. & Quéré, D. Rough wetting. *Europhysics Letters (EPL)* **55**, 214-220, doi:10.1209/epl/i2001-00402-x (2001).
121 McHale, G., Shirtcliffe, N. J., Aqil, S., Perry, C. C. & Newton, M. I. Topography Driven Spreading. *Physical Review Letters* **93**, 036102, doi:10.1103/PhysRevLett.93.036102 (2004).
122 Courbin, L., Denieul, E., Dressaire, E., Roper, M., Ajdari, A. & Stone, H. A. Imbibition by polygonal spreading on microdecorated surfaces. *Nature Materials* **6**, 661-664, doi:10.1038/nmat1978 (2007).
123 Ishino, C., Reyssat, M., Reyssat, E., Okumura, K. & Quéré, D. Wicking within forests of micropillars. *Europhysics Letters (EPL)* **79**, 56005, doi:10.1209/0295-5075/79/56005 (2007).
124 Xiao, R., Enright, R. & Wang, E. N. Prediction and Optimization of Liquid Propagation in Micropillar Arrays. *Langmuir* **26**, 15070-15075, doi:10.1021/la102645u (2010).
125 Spruijt, E., Le Guludec, E., Lix, C., Wagner, M. & Quéré, D. Liquid filmification from menisci. *EPL (Europhysics Letters)* **112**, 16002, doi:10.1209/0295-5075/112/16002 (2015).
126 Quéré, D. Wetting and Roughness. *Annual Review of Materials Research* **38**, 71-99, doi:10.1146/annurev.matsci.38.060407.132434 (2008).
127 Young, T. III. An essay on the cohesion of fluids. *Philosophical Transactions of the Royal Society of London* **95**, 65-87, doi:doi:10.1098/rstl.1805.0005 (1805).
128 Butt, H.-J., Graf, K., Kappl, M., (2003) Chapter 6 Surface Forces. In: *Physics and Chemistry of Interfaces*, pp. 80-117, Weinheim, Germany, Wiley-VCH Verlag GmbH & Co. KGaA.
129 Semprebon, C., Forsberg, P., Priest, C. & Brinkmann, M. Pinning and wicking in regular pillar arrays. *Soft Matter* **10**, 5739-5748, doi:10.1039/C4SM00684D (2014).
130 Butt, H.-J., Graf, K., Kappl, M., (2003) Chapter 7 Contact Angle Phenomena and Wetting. In: *Physics and Chemistry of Interfaces*, pp. 118-144, Weinheim, Germany, Wiley-VCH Verlag GmbH & Co. KGaA.
131 Quéré, D., Azzopardi, M.-J. & Delattre, L. Drops at Rest on a Tilted Plane. *Langmuir* **14**, 2213-2216, doi:10.1021/la970645l (1998).
132 Shanahan, M. E. R. & Carre, A. Viscoelastic Dissipation in Wetting and Adhesion Phenomena. *Langmuir* **11**, 1396-1402, doi:10.1021/la00004a055 (1995).
133 Carré, A., Gastel, J.-C. & Shanahan, M. E. R. Viscoelastic effects in the spreading of liquids. *Nature* **379**, 432-434, doi:10.1038/379432a0 (1996).
134 Extrand, C. W. & Kumagai, Y. Contact Angles and Hysteresis on Soft Surfaces. *Journal of Colloid and Interface Science* **184**, 191-200, doi:https://doi.org/10.1006/jcis.1996.0611 (1996).
135 Semprebon, C., McHale, G. & Kusumaatmaja, H. Apparent contact angle and contact angle hysteresis on liquid infused surfaces. *Soft Matter* **13**, 101-110, doi:10.1039/C6SM00920D (2017).
136 Sett, S., Yan, X., Barac, G., Bolton, L. W. & Miljkovic, N. Lubricant-Infused Surfaces for Low-Surface-Tension Fluids: Promise versus Reality. *ACS Applied Materials & Interfaces* **9**, 36400-36408, doi:10.1021/acsami.7b10756 (2017).

137 Langmuir, I. Oil Lenses on Water and the Nature of Monomolecular Expanded Films. *The Journal of Chemical Physics* **1**, 756-776, doi:10.1063/1.1749243 (1933).
138 Neumann, A. W., Good, R. J., Hope, C. J. & Sejpal, M. An equation-of-state approach to determine surface tensions of low-energy solids from contact angles. *Journal of Colloid and Interface Science* **49**, 291-304, doi:https://doi.org/10.1016/0021-9797(74)90365-8 (1974).
139 Butt, H.-J., Kappl, M. (2018) Chapter 5 Capillary Forces. In: *Surface and Interfacial Forces*, pp. 131-166, Weinheim, Germany, Wiley-VCH Verlag GmbH & Co. KGaA.
140 Derjaguin B.V., Churaev N.V., Muller V.M. (1987) Disjoining Pressure. In: *Surface Forces*. Springer, Boston, MA.
141 Butt, H.-J., Graf, K., Kappl, M., (2003) Chapter 6 Surface Forces. In: *Physics and Chemistry of Interfaces*, pp. 80-117, Weinheim, Germany, Wiley-VCH Verlag GmbH & Co. KGaA.
142 Brochard-Wyart, F., Di Meglio, J. M., Quere, D. & De Gennes, P. G. Spreading of nonvolatile liquids in a continuum picture. *Langmuir* **7**, 335-338, doi:10.1021/la00050a023 (1991).
143 Quéré, D. Non-sticking drops. *Reports on Progress in Physics* **68**, 2495-2532, doi:10.1088/0034-4885/68/11/r01 (2005).
144 Cheng, N.-S. Formula for the Viscosity of a Glycerol−Water Mixture. *Industrial & Engineering Chemistry Research* **47**, 3285-3288, doi:10.1021/ie071349z (2008).
145 Volk, A. & Kähler, C. J. Density model for aqueous glycerol solutions. *Experiments in Fluids* **59**, 75, doi:10.1007/s00348-018-2527-y (2018).
146 Joanny, J. F. & Gennes, P. G. d. A model for contact angle hysteresis. *The Journal of Chemical Physics* **81**, 552-562, doi:10.1063/1.447337 (1984).
147 Snoeijer, J. H. & Andreotti, B. Moving Contact Lines: Scales, Regimes, and Dynamical Transitions. *Annual Review of Fluid Mechanics* **45**, 269-292, doi:10.1146/annurev-fluid-011212-140734 (2013).
148 Hui Guan, J., Ruiz-Gutiérrez, É., Xu, B. B., Wood, D., McHale, G., Ledesma-Aguilar, R. & George Wells, G. Drop transport and positioning on lubricant-impregnated surfaces. *Soft Matter* **13**, 3404-3410, doi:10.1039/C7SM00290D (2017).
149 Mahadevan, L. & Pomeau, Y. Rolling droplets. *Physics of Fluids* **11**, 2449-2453, doi:10.1063/1.870107 (1999).
150 Bico, J., Ashmore-Chakrabarty, J., McKinley, G. H. & Stone, H. A. Rolling stones: The motion of a sphere down an inclined plane coated with a thin liquid film. *Physics of Fluids* **21**, 082103, doi:10.1063/1.3207884 (2009).
151 Reyssat, E. Drops and bubbles in wedges. *Journal of Fluid Mechanics* **748**, 641-662, doi:10.1017/jfm.2014.201 (2014).
152 Keiser, A., Ph.D. Thesis. Dynamiques sur des surfaces texturées et imprégnées. Dynamique des Fluides [physics.flu-dyn]. Sorbonne Université, 2018. Français. ⟨NNT : 2018SORUS601⟩.
153 Huh, C. & Scriven, L. E. Hydrodynamic model of steady movement of a solid/liquid/fluid contact line. *Journal of Colloid and Interface Science* **35**, 85-101, doi:https://doi.org/10.1016/0021-9797(71)90188-3 (1971).
154 Tanner, L. H. The spreading of silicone oil drops on horizontal surfaces. *Journal of Physics D: Applied Physics* **12**, 1473-1484, doi:10.1088/0022-3727/12/9/009 (1979).
155 Keiser, L., Keiser, A., L'Estimé, M., Bico, J. & Reyssat, É. Motion of Viscous Droplets in Rough Confinement: Paradoxical Lubrication. *Physical Review Letters* **122**, 074501, doi:10.1103/PhysRevLett.122.074501 (2019).
156 Tress, M., Karpitschka, S., Papadopoulos, P., Snoeijer, J. H., Vollmer, D. & Butt, H.-J. Shape of a sessile drop on a flat surface covered with a liquid film. *Soft Matter* **13**, 3760-3767, doi:10.1039/C7SM00437K (2017).
157 Limozin, L. & Sengupta, K. Quantitative Reflection Interference Contrast Microscopy (RICM) in Soft Matter and Cell Adhesion. *ChemPhysChem* **10**, 2752-2768, doi:10.1002/cphc.200900601 (2009).

158 Schilling, J., Sengupta, K., Goennenwein, S., Bausch, A. R. & Sackmann, E. Absolute interfacial distance measurements by dual-wavelength reflection interference contrast microscopy. *Physical Review E* **69**, 021901, doi:10.1103/PhysRevE.69.021901 (2004).
159 Ruiter, J. d., Mugele, F. & Ende, D. v. d. Air cushioning in droplet impact. I. Dynamics of thin films studied by dual wavelength reflection interference microscopy. *Physics of Fluids* **27**, 012104, doi:10.1063/1.4906114 (2015).
160 Sadullah, M. S., Semprebon, C. & Kusumaatmaja, H. Drop Dynamics on Liquid-Infused Surfaces: The Role of the Lubricant Ridge. *Langmuir* **34**, 8112-8118, doi:10.1021/acs.langmuir.8b01660 (2018).
161 Howell, C., Vu, T. L., Johnson, C. P., Hou, X., Ahanotu, O., Alvarenga, J., Leslie, D. C., Uzun, O., Waterhouse, A., Kim, P., Super, M., Aizenberg, M., Ingber, D. E. & Aizenberg, J. Stability of Surface-Immobilized Lubricant Interfaces under Flow. *Chemistry of Materials* **27**, 1792-1800, doi:10.1021/cm504652g (2015).
162 Wexler, J. S., Grosskopf, A., Chow, M., Fan, Y., Jacobi, I. & Stone, H. A. Robust liquid-infused surfaces through patterned wettability. *Soft Matter* **11**, 5023-5029, doi:10.1039/C5SM00611B (2015).
163 Jacobi, I., Wexler, J. S. & Stone, H. A. Overflow cascades in liquid-infused substrates. *Physics of Fluids* **27**, 082101, doi:10.1063/1.4927538 (2015).
164 Muschi, M., Brudieu, B., Teisseire, J. & Sauret, A. Drop impact dynamics on slippery liquid-infused porous surfaces: influence of oil thickness. *Soft Matter* **14**, 1100-1107, doi:10.1039/C7SM02026K (2018).
165 Bazyar, H., Javadpour, S. & Lammertink, R. G. H. On the Gating Mechanism of Slippery Liquid Infused Porous Membranes. *Advanced Materials Interfaces* **3**, 1600025, doi:10.1002/admi.201600025 (2016).
166 Kim, J.-H. & Rothstein, J. P. Delayed lubricant depletion on liquid-infused randomly rough surfaces. *Experiments in Fluids* **57**, 81, doi:10.1007/s00348-016-2171-3 (2016).
167 Seiwert, J., Maleki, M., Clanet, C. & Quéré, D. Drainage on a rough surface. *EPL (Europhysics Letters)* **94**, 16002, doi:10.1209/0295-5075/94/16002 (2011).
168 Damle, V. G., Uppal, A., Sun, X., Burgin, T. P., & Rykaczewski, K. Rapid and scalable lubrication and replenishment of liquid-infused materials. *Surface Innovations* **4**, 102-108, doi:10.1680/jsuin.16.00002 (2016).
169 Zhang, J., Wu, L., Li, B., Li, L., Seeger, S. & Wang, A. Evaporation-Induced Transition from Nepenthes Pitcher-Inspired Slippery Surfaces to Lotus Leaf-Inspired Superoleophobic Surfaces. *Langmuir* **30**, 14292-14299, doi:10.1021/la503300k (2014).
170 Lee, C., Kim, H. & Nam, Y. Drop Impact Dynamics on Oil-Infused Nanostructured Surfaces. *Langmuir* **30**, 8400-8407, doi:10.1021/la501341x (2014).
171 Hao, C., Li, J., Liu, Y., Zhou, X., Liu, Y., Liu, R., Che, L., Zhou, W., Sun, D., Li, L., Xu, L. & Wang, Z. Superhydrophobic-like tunable droplet bouncing on slippery liquid interfaces. *Nature Communications* **6**, 7986, doi:10.1038/ncomms8986 (2015).
172 Zhu, L., Xue, J., Wang, Y., Chen, Q., Ding, J. & Wang, Q. Ice-phobic Coatings Based on Silicon-Oil-Infused Polydimethylsiloxane. *ACS Applied Materials & Interfaces* **5**, 4053-4062, doi:10.1021/am400704z (2013).
173 Okada, I. & Shiratori, S. High-Transparency, Self-Standable Gel-SLIPS Fabricated by a Facile Nanoscale Phase Separation. *ACS Applied Materials & Interfaces* **6**, 1502-1508, doi:10.1021/am404077h (2014).
174 Zhao, H., Sun, Q., Deng, X. & Cui, J. Earthworm-Inspired Rough Polymer Coatings with Self-Replenishing Lubrication for Adaptive Friction-Reduction and Antifouling Surfaces. *Advanced Materials* **30**, 1802141, doi:10.1002/adma.201802141 (2018).
175 Yao, X., Ju, J., Yang, S., Wang, J. & Jiang, L. Temperature-Driven Switching of Water Adhesion on Organogel Surface. *Advanced Materials* **26**, 1895-1900, doi:10.1002/adma.201304798 (2014).

176 Yao, X., Dunn, S. S., Kim, P., Duffy, M., Alvarenga, J. & Aizenberg, J. Fluorogel Elastomers with Tunable Transparency, Elasticity, Shape-Memory, and Antifouling Properties. *Angewandte Chemie International Edition* **53**, 4418-4422, doi:10.1002/anie.201310385 (2014).
177 Urata, C., Dunderdale, G. J., England, M. W. & Hozumi, A. Self-lubricating organogels (SLUGs) with exceptional syneresis-induced anti-sticking properties against viscous emulsions and ices. *Journal of Materials Chemistry A* **3**, 12626-12630, doi:10.1039/C5TA02690C (2015).
178 Mauderly, J. L. & Chow, J. C. Health Effects of Organic Aerosols. *Inhalation Toxicology* **20**, 257-288, doi:10.1080/08958370701866008 (2008).
179 Shiraiwa, M., Ueda, K., Pozzer, A., Lammel, G., Kampf, C. J., Fushimi, A., Enami, S., Arangio, A. M., Fröhlich-Nowoisky, J., Fujitani, Y., Furuyama, A., Lakey, P. S. J., Lelieveld, J., Lucas, K., Morino, Y., Pöschl, U., Takahama, S., Takami, A., Tong, H., Weber, B., Yoshino, A. & Sato, K. Aerosol Health Effects from Molecular to Global Scales. *Environmental Science & Technology* **51**, 13545-13567, doi:10.1021/acs.est.7b04417 (2017).
180 Wu, W., DeConinck, A. & Lewis, J. A. Omnidirectional Printing of 3D Microvascular Networks. *Advanced Materials* **23**, H178-H183, doi:10.1002/adma.201004625 (2011).
181 Keiser, A., Baumli, P., Vollmer, D. & Quéré, D. Universality of friction laws on liquid-infused materials. *Physical Review Fluids* **5**, 014005, doi:10.1103/PhysRevFluids.5.014005 (2020).
182 Colas, A. Silicones: preparation, properties and performance. *Dow Corning Corporation (Form No. 01-3077-01), based on an earlier publication in Chim. Nouvelle* **8**, 847-852 (1990).
183 Eduok, U., Faye, O. & Szpunar, J. Recent developments and applications of protective silicone coatings: A review of PDMS functional materials. *Prog. Org. Coat.* **111**, 124-163, doi:10.1016/j.porgcoat.2017.05.012 (2017).
184 *Encyclopedia.com, https://www.encyclopedia.com/science-and-technology/chemistry/organic-chemistry/silicone*.
185 *Silicone market: Global industry perspective, comprehensive analysis and forecaset 2015-2021, www.zionmarketresearch.com/report/silicone-market*.
186 Rochow, E. G. (1946) Chapter 5: Water-repellent films from organosilicon material. In: *An Introduction to the Chemistry of the Silicones*, pp. 83-88, New York, NY, USA, John Wiley & Sons, Inc.
187 Weinhold, F. & West, R. The nature of the silicon–oxygen bond. *Organometallics* **30**, 5815-5824, doi:10.1021/om200675d (2011).
188 Krumpfer, J. W. & McCarthy, T. J. Contact angle hysteresis: a different view and a trivial recipe for low hysteresis hydrophobic surfaces. *Faraday Discuss.* **146**, 103-111 (2010).
189 Krumpfer, J. W. & McCarthy, T. J. Rediscovering silicones: "Unreactive" silicones react with inorganic surfaces. *Langmuir* **27**, 11514-11519, doi:10.1021/la202583w (2011).
190 Milner, S. T. Polymer brushes. *Science* **251**, 905-914 (1991).
191 Milner, S. T. & Witten, T. A. Theory of the grafted polymer brush. *Macromolecules* **21**, 2610-2619 (1988).
192 Bico, J., Marzolin, C. & Quéré, D. Pearl drops. *Europhys. Lett.* **47**, 220-226 (1999).
193 Tretinnikov, O. N. & Ikada, Y. Dynamic wetting and contact angle hysteresis of polymer surfaces studied with the modified wilhelmy balance method. *Langmuir* **10**, 1606-1614 (1994).
194 Wooh, S., Encinas, N., Vollmer, D. & Butt, H.-J. Stable hydrophobic metal-oxide photocatalysts via grafting polydimethylsiloxane brush. *Adv. Mater.* **29**, 1604637, doi:10.1002/adma.201604637 (2017).
195 Eifert, A., Paulssen, D., Varanakkottu, S. N., Baier, T. & Hardt, S. Simple fabrication of robust water-repellent surfaces with low contact-angle hysteresis based on impregnation. *Adv. Mater. Interfaces* **1**, 1300138, doi:10.1002/admi.201300138 (2014).
196 Xue, C.-H., Bai, X. & Jia, S.-T. Robust, self-healing superhydrophobic fabrics prepared by one-step coating of PDMS and octadecylamine. *Sci. Rep.* **6**, 27262, doi:10.1038/srep27262 (2016).
197 Yang, C., Wang, F., Li, W., Ou, J., Li, C. & Amirfazli, A. Anti-icing properties of superhydrophobic ZnO/PDMS composite coating. *Appl. Phys. A* **122**, 1-10 (2016).

198 Sun, G., Kappl, M. & Butt, H.-J. Confined polymer melts studied by atomic force microscopy. *Colloids Surf. A: Physicochem. Eng. Asp.* **250**, 203-209, doi:10.1016/j.colsurfa.2004.04.083 (2004).
199 Vondráček, P. & Gent, A. N. Slow decomposition of silicone rubber. *J. Appl. Polymer Sci.* **27**, 4517-4523 (1982).
200 El-Safty, S. A., Sakai, M., Selim, M. M. & Alhamide, A. A. One-pot layer casting-guided synthesis of nanospherical aluminosilica@organosilica@alumina core-shells wrapping colorant dendrites for environmental application. *RSC Adv.* **5**, 60307-60321 (2015).
201 El-Safty, S. A., Mekawy, M., Yamaguchi, A., Shahat, A., Ogawa, K. & Teramae, N. Organic-inorganic mesoporous silica nanostrands for ultrafine filtration of spherical nanoparticles. *Chem. Commun.* **46**, 3917-3919 (2010).
202 Hunter, M. J., Gordon, M. S., Barry, A. J., Hyde, J. F. & Heidenreich, R. D. Properties of polyorganosiloxane surfaces on glass. *Ind. Eng. Chem.* **39**, 1389-1395 (1947).
203 Willis, R. F. Thermal decomposition of silicone fluids at metal surfaces. *Nature* **221**, 1134-1135 (1969).
204 Papirer, E. (Ed.) (200) Adsorption on silica surfaces. In: Surfactant Science Series Vol. 90, New York, NY, USA, CRC Press (Copyright © Marcel Dekker, 2000).
205 Graffius, G., Bernardoni, F. & Fadeev, A. Y. Covalent functionalization of silica surface using "inert" poly(dimethylsiloxanes). *Langmuir* **30**, 14797-14807, doi:10.1021/la5031763 (2014).
206 Zhuravlev, L. T. The surface chemistry of amorphous silica. Zhuravlev model. *Colloids Surf. A: Physicochem. Eng. Asp.* **173**, 1-38 (2000).
207 Kanta, A., Sedev, R. & Ralston, J. Thermally- and photoinduced changes in the water wettability of low-surface-area silica and titania. *Langmuir* **21**, 2400-2407 (2005).
208 Arkles, B. Tailoring surfaces with silanes. *Chemtech* **7**, 766-778 (1977).
209 Lafuma, A. & Quéré, D. Slippery pre-suffused surfaces. *Europhys. Lett.* **96**, 56001, doi:10.1209/0295-5075/96/56001 (2011).
210 Kim, J.-H. & Rothstein, J. P. Delayed lubricant depletion on liquid-infused randomly rough surfaces. *Exp. Fluids* **57**, 81, doi:10.1007/s00348-016-2171-3 (2016).
211 Damle, V. G., Uppal, A., Sun, X., Burgin, T. P. & Rykaczewski, K. Rapid and scalable lubrication and replenishment of liquid-infused materials. *Surface Innovations* **4**, 102-108, doi:10.1680/jsuin.16.00002 (2016).
212 Deng, X., Mammen, L., Butt, H.-J. & Vollmer, D. Candle soot as a template for a transparent robust superamphiphobic coating. *Science* **335**, 67-70 (2012).
213 Meichner, C., Schedl, A. E., Neuber, C., Kreger, K., Schmidt, H.-W. & Kador, L. Refractive-index determination of solids from first- and second-order critical diffraction angles of periodic surface patterns. *AIP Advances* **5**, 087135 (2015).
214 *RefractiveIndex.INFO - Refractive index database, https://refractiveindex.info*.
215 Miller, D. J., Biesinger, M. C. & McIntyre, N. S. Interactions of CO2 and CO at fractional atmosphere pressures with iron and iron oxide surfaces: one possible mechanism for surface contamination? *Surf. Interface Anal.* **33**, 299-305, doi:10.1002/sia.1188 (2002).
216 *Polymer Properties Database, https://polymerdatabase.com*.
217 Gao, N., Geyer, F., Pilat, D. W., Wooh, S., Vollmer, D., Butt, H.-J. & Berger, R. How drops start sliding over solid surfaces. *Nat. Phys.* **14**, 191-196, doi:10.1038/nphys4305 (2018).
218 van Poll, M. L., Khodabakhsh, S., Brewer, P. J., Shard, A. G., Ramstedt, M. & Huck, W. T. S. Surface modification of PDMS via self-organization of vinyl-terminated small molecules. *Soft Matter* **5**, 2286-2293, doi:10.1039/b901763a (2009).
219 Laws, J. O. Measurements of the fall-velocity of water-drops and raindrops. *Trans. Am. Geophys. Union* **22**, 709-721 (1941).
220 Frenkel, Y. I. On the behavior of liquid drops on a solid surface. 1. The sliding of drops on an inclined surface. *J. Exptl. Theoret. Phys.* **18**, 658-667 (1948).
221 Camino, G., Lomakin, S. M. & Lazzari, M. Polydimethylsiloxane thermal degradation. Part 1. Kinetic aspects. *Polymer* **42**, 2395-2402 (2001).

222 Quéré, D. Wetting and Roughness. *Annu. Rev. Mater. Res.* **38**, 71-99, doi:10.1146/annurev.matsci.38.060407.132434 (2008).
223 Momen, G. & Farzaneh, M. Facile approach in the development of icephobic hierarchically textured coatings as corrosion barrier. *Appl. Surf. Sci.* **299**, 41-46, doi:10.1016/j.apsusc.2014.01.179 (2014).
224 Paul, A. (1982) Chemical Durability of Glass. In: Chemistry of Glasses. Springer, Dordrecht.
225 Bunker, B. C. Molecular mechanisms for corrosion of silica and silicate glasses. *J. Non-Crystalline Solids* **179**, 300-308 (1994).
226 Hiemstra, T. & van Riemsdijk, W. H. Multiple activated complex dissolution of metal (hydr)oxides: A thermodynamic approach applied to quartz. *J. Colloid Interface Sci.* **136**, 132-150 (1990).
227 Brinker, C. J. Hydrolysis and condensation of silicates: Effects on structure. *J. Non-Crystalline Solids* **100**, 31-50 (1988).
228 Tong, Q.-Y. & Gösele, U. A model of low-temperature wafer bonding and its applications. *J. Electrochem. Soc.* **143**, 1773-1779 (1996).
229 Masteika, V., Kowal, J., Braithwaite, N. S. J. & Rogers, T. A review of hydrophilic silicon wafer bonding. *ECS J. Solid State Sci. Technol.* **3**, Q42-Q54, doi:10.1149/2.007403jss] (2014).
230 Agzamkhodzhaev, A. A., Zhuravlev, L. T. & Kiselev, A. V. Rehydroxylation of surface of amorphous silicas. *Colloid J. USSR* **36**, 1036-1039 (1974).
231 Mate, C. M., Lorenz, M. R. & Novotny, V. J. Atomic force microscopy of polymeric liquid films. *J. Chem. Phys.* **90**, 7550 (1989).
232 Ally, J., Vittorias, E., Amirfazli, A., Kappl, M., Bonaccurso, E., McNamee, C. E. & Butt, H.-J. Interaction of a microsphere with a solid-supported liquid film. *Langmuir* **26**, 11797-11803 (2010).
233 Dehnert, M. & Magerle, R. 3D depth profiling of the interaction between an AFM tip and fluid polymer solutions. *Nanoscale* **10**, 5695-5707 (2018).
234 Graiver, D., Farminer, K. W. & Narayan, R. A review of the fate and effects of silicones in the environment. *J. Polym. Environ.* **11**, 129-136 (2003).
235 Marmur, A. Hydro- hygro- oleo- omni-phobic? Terminology of wettability classification. *Soft Matter* **8**, 6867-6870, doi:10.1039/c2sm25443c (2012).
236 Butt, H.-J., Berger, R., Steffen, W., Vollmer, D. & Weber, S. A. L. Adaptive wetting - Adaptation in wetting. *Langmuir* **34**, 11292-11304, doi:10.1021/acs.langmuir.8b01783 (2018).
237 Blake, T. D. The physics of moving wetting lines. *J. Colloid Interface Sci.* **299**, 1-13, doi:10.1016/j.jcis.2006.03.051 (2006).
238 Schwartz, A. M. & Tejada, S. B. Studies of dynamic contact angles on solids. *J. Colloid Interface Sci.* **38**, 359-375 (1972).
239 Snoeijer, J. H. & Andreotti, B. Moving contact lines: scales, regimes, and dynamical transitions. *Annu. Rev. Fluid Mech.* **45**, 269-292, doi:10.1146/annurev-fluid-011212-140734 (2013).
240 Meuler, A. J., Smith, J. D., Varanasi, K. K., Mabry, J. M., McKinley, G. H. & Cohen, R. E. Relationships between water wettability and ice adhesion. *Appl. Mater. Interfaces* **2**, 3100-3110, doi:10.1021/am1006035 (2010).
241 Ozbay, S., Yuceel, C. & Erbil, H. Y. Improved Icephobic Properties on Surfaces with a Hydrophilic Lubricating Liquid. *ACS Appl. Mater. Interfaces* **7**, 22067-22077, doi:10.1021/acsami.5b07265 (2015).
242 Chen, D., Gelenter, M. D., Hong, M., Cohen, R. E. & McKinley, G. H. Icephobic surfaces induced by interfacial nonfrozen water. *ACS Appl. Mater. Interfaces* **9**, 4202-4214, doi:10.1021/acsami.6b13773 (2017).
243 Niemelä-Anttonen, H., Koivuluoto, H., Tuominen, M., Teisala, H., Juuti, P., Haapanen, J., Harra, J., Stenroos, C., Lahti, J., Kuusipalo, J., Mäkelä, J. M. & Vuoristo, P. Icephobicity of

Slippery Liquid Infused Porous Surfaces under Multiple Freeze-Thaw and Ice Accretion-Detachment Cycles. *Adv. Mater. Interfaces*, 1800828, doi:10.1002/admi.201800828 (2018).
244 Juuti, P., Haapanen, J., Stenroos, C., Niemelä-Anttonen, H., Harra, J., Koivuluoto, H., Teisala, H., Lahti, J., Tuominen, M., Kuusipalo, J., Vuoristo, P. & Mäkelä, J. M. Achieving a slippery, liquid-infused porous surface with anti-icing properties by direct deposition of flame synthesized aerosol nanoparticles on a thermally fragile substrate. *Appl. Phys. Lett.* **110**, 161603, doi:10.1063/1.4981905 (2017).
245 Janjua, Z. A. The influence of freezing and ambient temperature on the adhesion strength of ice. *Cold Regions Sci. Technol.* **140**, 14-19, doi:10.1016/j.coldregions.2017.05.001 (2017).
246 Work, A. & Lian, Y. A critical review of the measurement of ice adhesion to solid substrates. *Prog. Aerospace Sci.* **98**, 1-26, doi:10.1016/j.paerosci.2018.03.001 (2018).
247 Launer, P. J. & Arkles, B. *Infrared analysis of organosilicon compounds: Spectra-structure correlations*. (Reprinted from *Silicon Compounds: Silanes and Silicones,* 3rd Edition, Gelest, Inc., 2013).
248 Hanna, R. Infrared absorption spectrum of silicon dioxide. *J. Am. Ceram. Soc.* **48**, 595-599 (1965).
249 Ozbay, S. & Erbil, H. Y. Ice accretion by spraying supercooled droplets is not dependent on wettability and surface free energy of substrates. *Colloids and Surfaces A: Physicochemical and Engineering Aspects* **504**, 210-218, doi:10.1016/j.colsurfa.2016.05.065 (2016).
250 Daniel, D., Timonen, J. V. I., Li, R., Velling, S. J., Kreder, M. J., Tetreault, A. & Aizenberg, J. Origins of Extreme Liquid Repellency on Structured, Flat, and Lubricated Hydrophobic Surfaces. *Physical Review Letters* **120**, 244503, doi:10.1103/PhysRevLett.120.244503 (2018).
251 Asmolov, E. S., Nizkaya, T. V. & Vinogradova, O. I. Enhanced slip properties of lubricant-infused grooves. *Physical Review E* **98**, 033103, doi:10.1103/PhysRevE.98.033103 (2018).
252 Cox, R. G. The dynamics of the spreading of liquids on a solid surface. Part 1. Viscous flow. *Journal of Fluid Mechanics* **168**, 169-194, doi:10.1017/S0022112086000332 (1986).
253 Voinov, O. V. Hydrodynamics of wetting. *Fluid Dynamics* **11**, 714-721, doi:10.1007/bf01012963 (1976).
254 de Gennes, P. G. Wetting: statics and dynamics. *Reviews of Modern Physics* **57**, 827-863, doi:10.1103/RevModPhys.57.827 (1985).
255 Bonn, D., Eggers, J., Indekeu, J., Meunier, J. & Rolley, E. Wetting and spreading. *Reviews of Modern Physics* **81**, 739-805, doi:10.1103/RevModPhys.81.739 (2009).
256 Huerre, A., Theodoly, O., Leshansky, A. M., Valignat, M.-P., Cantat, I. & Jullien, M.-C. Droplets in Microchannels: Dynamical Properties of the Lubrication Film. *Physical Review Letters* **115**, 064501, doi:10.1103/PhysRevLett.115.064501 (2015).
257 Yahashi, M., Kimoto, N. & Okumura, K. Scaling crossover in thin-film drag dynamics of fluid drops in the Hele-Shaw cell. *Scientific Reports* **6**, 31395, doi:10.1038/srep31395 (2016).
258 Keiser, L., Jaafar, K., Bico, J. & Reyssat, É. Dynamics of non-wetting drops confined in a Hele-Shaw cell. *Journal of Fluid Mechanics* **845**, 245-262, doi:10.1017/jfm.2018.240 (2018).
259 Bretherton, F. P. The motion of long bubbles in tubes. *Journal of Fluid Mechanics* **10**, 166-188, doi:10.1017/S0022112061000160 (1961).
260 Aussillous, P. & Quéré, D. Bubbles creeping in a viscous liquid along a slightly inclined plane. *Europhysics Letters (EPL)* **59**, 370-376, doi:10.1209/epl/i2002-00204-2 (2002).
261 Cantat, I. Liquid meniscus friction on a wet plate: Bubbles, lamellae, and foams. *Physics of Fluids* **25**, 031303, doi:10.1063/1.4793544 (2013).
262 Le Merrer, M., Lespiat, R., Höhler, R. & Cohen-Addad, S. Linear and non-linear wall friction of wet foams. *Soft Matter* **11**, 368-381, doi:10.1039/C4SM01557F (2015).
263 Jung, C., Müller, B. K., Lamb, D. C., Nolde, F., Müllen, K. & Bräuchle, C. A New Photostable Terrylene Diimide Dye for Applications in Single Molecule Studies and Membrane Labeling. *Journal of the American Chemical Society* **128**, 5283-5291, doi:10.1021/ja0588104 (2006).
264 Zhu, J. & Marchant, R. E. Design properties of hydrogel tissue-engineering scaffolds. *Expert Rev Med Devices* **8**, 607-626, doi:10.1586/erd.11.27 (2011).

265 El-Sherbiny, I. M. & Yacoub, M. H. Hydrogel scaffolds for tissue engineering: Progress and challenges. *Glob Cardiol Sci Pract* **2013**, 316-342, doi:10.5339/gcsp.2013.38 (2013).
266 Caló, E. & Khutoryanskiy, V. V. Biomedical applications of hydrogels: A review of patents and commercial products. *European Polymer Journal* **65**, 252-267, doi:https://doi.org/10.1016/j.eurpolymj.2014.11.024 (2015).
267 Peppas, N. A. & Mikos, A. G. (1986) Preparation Methods and Structure of Hydrogels. In: *Hydrogels in Medicine and Pharmacy* Vol. 1. Fundamentals, pp. 1-26, Boca Raton, FL, USA, CRC Press Inc.
268 Flory, P. J. & Rehner J. Jr. Statistical Mechanics of Cross-Linked Polymer Networks II. Swelling. *The Journal of Chemical Physics* **11**, 521-526, doi:10.1063/1.1723792 (1943).
269 Flory, P. J. Statistical Mechanics of Swelling of Network Structures. *The Journal of Chemical Physics* **18**, 108-111, doi:10.1063/1.1747424 (1950).
270 Peppas, N. A. & Mikos, A. G. (1986) Characterization of the cross-linked structure of hydrogels. In: *Hydrogels in Medicine and Pharmacy* Vol. 1. Fundamentals, pp. 27-56, Boca Raton, FL, USA, CRC Press Inc.
271 am Ende, M. T. & Mikos, A. G. Diffusion-controlled delivery of proteins from hydrogels and other hydrophilic systems. *Pharm Biotechnol* **10**, 139-165, doi:10.1007/0-306-46803-4_5 (1997).
272 Canal, T. & Peppas, N. A. Correlation between mesh size and equilibrium degree of swelling of polymeric networks. *J Biomed Mater Res* **23**, 1183-1193, doi:10.1002/jbm.820231007 (1989).
273 Ricka, J. & Tanaka, T. Swelling of ionic gels: quantitative performance of the Donnan theory. *Macromolecules* **17**, 2916-2921, doi:10.1021/ma00142a081 (1984).
274 Nagase, K., Kobayashi, J. & Okano, T. Temperature-responsive intelligent interfaces for biomolecular separation and cell sheet engineering. *Journal of The Royal Society Interface* **6**, S293-S309, doi:doi:10.1098/rsif.2008.0499.focus (2009).
275 Otake, K., Inomata, H., Konno, M. & Saito, S. Thermal analysis of the volume phase transition with N-isopropylacrylamide gels. *Macromolecules* **23**, 283-289, doi:10.1021/ma00203a049 (1990).
276 Kodzwa, M. G., Staben, M. E. & Rethwisch, D. G. Photoresponsive control of ion-exchange in leucohydroxide containing hydrogel membranes. *Journal of Membrane Science* **158**, 85-92, doi:https://doi.org/10.1016/S0376-7388(99)00008-3 (1999).
277 Juodkazis, S., Mukai, N., Wakaki, R., Yamaguchi, A., Matsuo, S. & Misawa, H. Reversible phase transitions in polymer gels induced by radiation forces. *Nature* **408**, 178-181, doi:10.1038/35041522 (2000).
278 Lee, S. J. & Park, K. Synthesis and Characterization of Sol-Gel Phase-reversible Hydrogels Sensitive to Glucose. *Journal of Molecular Recognition* **9**, 549-557, doi:10.1002/(SICI)1099-1352(199634/12)9:5/6<549::AID-JMR299>3.0.CO;2-C (1996).
279 Roy, I. & Gupta, M. N. Smart Polymeric Materials: Emerging Biochemical Applications. *Chemistry and Biology* **10**, 1161-1171, doi:10.1016/j.chembiol.2003.12.004 (2003).
280 Lee, M. C., Kabilan, S., Hussain, A., Yang, X., Blyth, J. & Lowe, C. R. Glucose-sensitive holographic sensors for monitoring bacterial growth. *Analytical Chemistry* **76**, 5748-5755, doi:10.1021/ac049334n (2004).
281 Gordon, M. (1976), The Physics of Rubber Elasticity (Third Edition). L. R. G. Treloar, Clarendon Press, Oxford. 1975 pp. xii + 370. Brit. Poly. J., 8: 39-39. doi:10.1002/pi.4980080107.
282 Flory, P. J., Rabjohn, N. & Shaffer, M. C. Dependence of elastic properties of vulcanized rubber on the degree of cross linking. *Journal of Polymer Science* **4**, 225-245, doi:10.1002/pol.1949.120040301 (1949).
283 Peppas, N. A., Bures, P., Leobandung, W. & Ichikawa, H. Hydrogels in pharmaceutical formulations. *European Journal of Pharmaceutics and Biopharmaceutics* **50**, 27-46, doi:https://doi.org/10.1016/S0939-6411(00)00090-4 (2000).

284 Holback, H., Yeo, Y. & Park, K. (2011) 1 - Hydrogel swelling behavior and its biomedical applications. In: *Biomedical Hydrogels* (ed. Steve Rimmer), pp. 3-24, Woodhead Publishing Limited.
285 Tanaka, T. Collapse of gels and the critical endpoint. *Physical Review Letters* **40**, 820-823, doi:10.1103/PhysRevLett.40.820 (1978).
286 Hirotsu, S., Hirokawa, Y. & Tanaka, T. Volume-phase transitions of ionized N-isopropylacrylamide gels. *The Journal of Chemical Physics* **87**, 1392-1395, doi:10.1063/1.453267 (1987).
287 Stell, G. & Joslin, C. G. The donnan equilibrium: a theoretical study of the effects of interionic forces. *Biophys J* **50**, 855-859, doi:10.1016/s0006-3495(86)83526-3 (1986).
288 Drozdov, A. D. & Christiansen, J. d. Modeling the effects of pH and ionic strength on swelling of anionic polyelectrolyte gels. *Modelling and Simulation in Materials Science and Engineering* **23**, 055005, doi:10.1088/0965-0393/23/5/055005 (2015).
289 Khare, A. R. & Peppas, N. A. Swelling/deswelling of anionic copolymer gels. *Biomaterials* **16**, 559-567, doi:https://doi.org/10.1016/0142-9612(95)91130-Q (1995).
290 Hänni-Ciunel, K., Findenegg, G. H. & von Klitzing, R. Water Contact Angle On Polyelectrolyte-Coated Surfaces: Effects of Film Swelling and Droplet Evaporation. *Soft Materials* **5**, 61-73, doi:10.1080/15394450701554452 (2007).
291 v. Klitzing, R. Internal structure of polyelectrolyte multilayer assemblies. *Physical Chemistry Chemical Physics* **8**, 5012-5033, doi:10.1039/B607760A (2006).
292 Yoo, D., Shiratori, S. S. & Rubner, M. F. Controlling Bilayer Composition and Surface Wettability of Sequentially Adsorbed Multilayers of Weak Polyelectrolytes. *Macromolecules* **31**, 4309-4318, doi:10.1021/ma9800360 (1998).
293 Shiratori, S. S. & Rubner, M. F. pH-Dependent Thickness Behavior of Sequentially Adsorbed Layers of Weak Polyelectrolytes. *Macromolecules* **33**, 4213-4219, doi:10.1021/ma991645q (2000).
294 Wong, J. E., Rehfeldt, F., Hänni, P., Tanaka, M. & Klitzing, R. v. Swelling Behavior of Polyelectrolyte Multilayers in Saturated Water Vapor. *Macromolecules* **37**, 7285-7289, doi:10.1021/ma0351930 (2004).
295 Peppas, N. A. & Colombo, P. Analysis of drug release behavior from swellable polymer carriers using the dimensionality index. *Journal of Controlled Release* **45**, 35-40, doi:https://doi.org/10.1016/S0168-3659(96)01542-8 (1997).
296 Crank, J. & Park, G. S. Diffusion in high polymers: some anomalies and their significance. *Transactions of the Faraday Society* **47**, 1072-1084, doi:10.1039/TF9514701072 (1951).
297 Hong, W., Liu, Z. & Suo, Z. Inhomogeneous swelling of a gel in equilibrium with a solvent and mechanical load. *International Journal of Solids and Structures* **46**, 3282-3289, doi:https://doi.org/10.1016/j.ijsolstr.2009.04.022 (2009).
298 Liu, M., Wang, S., Wei, Z., Song, Y. & Jiang, L. Bioinspired Design of a Superoleophobic and Low Adhesive Water/Solid Interface. *Advanced Materials* **21**, 665-669, doi:10.1002/adma.200801782 (2009).
299 Liu, X., Zhou, J., Xue, Z., Gao, J., Meng, J., Wang, S. & Jiang, L. Clam's Shell Inspired High-Energy Inorganic Coatings with Underwater Low Adhesive Superoleophobicity. *Advanced Materials* **24**, 3401-3405, doi:10.1002/adma.201200797 (2012).
300 Kaklamani, G., Cheneler, D., Grover, L. M., Adams, M. J., Anastasiadis, S. H. & Bowen, J. Anisotropic dehydration of hydrogel surfaces. *Prog Biomater* **6**, 157-164, doi:10.1007/s40204-017-0075-9 (2017).
301 Sekine, Y. & Ikeda-Fukazawa, T. Structural changes of water in a hydrogel during dehydration. *The Journal of Chemical Physics* **130**, 034501, doi:10.1063/1.3058616 (2009).
302 Kolasińska, M., Krastev, R. & Warszyński, P. Characteristics of polyelectrolyte multilayers: effect of PEI anchoring layer and posttreatment after deposition. *Journal of colloid and interface science* **305**, 46-56, doi:10.1016/j.jcis.2006.09.035 (2007).

303 Mohamad, H. S., Neuber, S. & Helm, C. A. Surface Forces of Asymmetrically Grown Polyelectrolyte Multilayers: Searching for the Charges. *Langmuir*, doi:10.1021/acs.langmuir.9b01787 (2019).
304 Tai, F.-I., Sterner, O., Andersson, O., Ekblad, T. & Ederth, T. Interaction Forces on Polyampholytic Hydrogel Gradient Surfaces. *ACS Omega* **4**, 5670-5681, doi:10.1021/acsomega.9b00339 (2019).
305 Watson, J. & Baron, M. The behaviour of water in poly (dimethylsiloxane). *J. Membr. Sci.* **110**, 47-57 (1996).
306 Antoniadis, D., Rodoni, M. & Dutton, R. Impurity Redistribution in SiO2-Si during Oxidation: A Numerical Solution Including Interfacial Fluxes. *J. Electrochem. Soc.* **126**, 1939-1945 (1979).
307 Slattery, J. (1999). Advanced Transport Phenomena. In Advanced Transport Phenomena (Cambridge Series in Chemical Engineering, pp. Xxiii-Xxiv). Cambridge: Cambridge University Press. doi:10.1017/CBO9780511800238.002.
308 Hirsch, C. *Numerical computation of internal and external flows: The fundamentals of computational fluid dynamics*. (Elsevier, 2007).
309 Probstein, R. F. *Physicochemical hydrodynamics: an introduction*. (John Wiley & Sons, 2005).
310 Papadopoulos, P., Mammen, L., Deng, X., Vollmer, D. & Butt, H.-J. How superhydrophobicity breaks down. *Proceedings of the National Academy of Sciences* **110**, 3254-3258, doi:10.1073/pnas.1218673110 (2013).
311 Zhu, Z., Chen, P., Liu, K. & Escobedo, C. A Versatile Bonding Method for PDMS and SU-8 and Its Application towards a Multifunctional Microfluidic Device. *Micromachines (Basel)* **7**, 230, doi:10.3390/mi7120230 (2016).
312 Busse, A., Sandham, N. D., McHale, G. & Newton, M. I. Change in drag, apparent slip and optimum air layer thickness for laminar flow over an idealised superhydrophobic surface. *Journal of Fluid Mechanics* **727**, 488-508, doi:10.1017/jfm.2013.284 (2013).
313 Wang, N., Xiong, D., Lu, Y., Pan, S., Wang, K., Deng, Y. & Shi, Y. Design and Fabrication of the Lyophobic Slippery Surface and Its Application in Anti-Icing. *The Journal of Physical Chemistry C* **120**, 11054-11059, doi:10.1021/acs.jpcc.6b04778 (2016).
314 Gu, Y. & Li, D. An Electrical Suspension Method for Measuring the Electric Charge on Small Silicone Oil Droplets Dispersed in Aqueous Solutions. *Journal of Colloid and Interface Science* **195**, 343-352, doi:https://doi.org/10.1006/jcis.1997.5151 (1997).
315 Gu, Y. & Li, D. Electric charge on small silicone oil droplets dispersed in ionic surfactant solutions. *Colloids and Surfaces A: Physicochemical and Engineering Aspects* **139**, 213-225, doi:https://doi.org/10.1016/S0927-7757(98)00283-0 (1998).
316 Beattie, J. K., Djerdjev, A. M. & Warr, G. G. The surface of neat water is basic. *Faraday Discussions* **141**, 31-39, doi:10.1039/B805266B (2009).
317 Butt, H.-J., Kappl, M. (2018) Chapter 7 Interfacial Forces between Fluid Interfaces and across Thin Films. In: Surface and Interfacial Forces, pp. 191-217, Weinheim, Germany, Wiley-VCH Verlag GmbH & Co. KGaA.
318 Geyer, F., Schönecker, C., Butt, H.-J. & Vollmer, D. Enhancing CO2 Capture using Robust Superomniphobic Membranes. *Advanced Materials* **29**, 1603524, doi:10.1002/adma.201603524 (2017).
319 Taylor, G. I. The viscosity of a fluid containing small drops of another fluid. *Proceedings of the Royal Society of London. Series A, Containing Papers of a Mathematical and Physical Character* **138**, 41-48, doi:doi:10.1098/rspa.1932.0169 (1932).
320 Broughton, G. & Squires, L. THE VISCOSITY OF OIL-WATER EMULSIONS1. *The Journal of Physical Chemistry* **42**, 253-263, doi:10.1021/j100897a010 (1938).
321 Oldroyd, J. G. & Wilson, A. H. The elastic and viscous properties of emulsions and suspensions. *Proceedings of the Royal Society of London. Series A. Mathematical and Physical Sciences* **218**, 122-132, doi:doi:10.1098/rspa.1953.0092 (1953).
322 Sherman, P. The viscosity of emulsions. *Rheologica Acta* **2**, 74-82, doi:10.1007/bf01972558 (1962).

323 Schowalter, W. R., Chaffey, C. E. & Brenner, H. Rheological behavior of a dilute emulsion. *Journal of Colloid and Interface Science* **26**, 152-160, doi:https://doi.org/10.1016/0021-9797(68)90307-X (1968).
324 Palierne, J. F. Linear rheology of viscoelastic emulsions with interfacial tension. *Rheologica Acta* **29**, 204-214, doi:10.1007/bf01331356 (1990).
325 Hardy, W. B. & Bircumshaw, I. *Bakerian Lecture*. - Boundary lubrication. - Plane surfaces and the limitations of Amontons' law. *Proceedings of the Royal Society of London. Series A, Containing Papers of a Mathematical and Physical Character* **108**, 1-27, doi:doi:10.1098/rspa.1925.0056 (1925).
326 Chan, D. Y. C. & Horn, R. G. The drainage of thin liquid films between solid surfaces. *The Journal of Chemical Physics* **83**, 5311-5324, doi:10.1063/1.449693 (1985).
327 Cox, R. G. The motion of suspended particles almost in contact. *International Journal of Multiphase Flow* **1**, 343-371, doi:https://doi.org/10.1016/0301-9322(74)90019-6 (1974).
328 Mugele, F., Bera, B., Cavalli, A., Siretanu, I., Maestro, A., Duits, M., Cohen-Stuart, M., van den Ende, D., Stocker, I. & Collins, I. Ion adsorption-induced wetting transition in oil-water-mineral systems. *Scientific Reports* **5**, 10519, doi:10.1038/srep10519 (2015).
329 Clanet, C., Béguin, C., Richard, D. & D., Q. Maximal deformation of an impacting drop. *Journal of Fluid Mechanics* **517**, 199-208, doi:10.1017/S0022112004000904 (2004).
330 Quéré, D. Water colliding with oil. *Journal of Fluid Mechanics* **702**, 1-4, doi:10.1017/jfm.2012.208 (2012).
331 Graiver, D., Farminer, K. W. & Narayan, R. A Review of the Fate and Effects of Silicones in the Environment. *Journal of Polymers and the Environment* **11**, 129-136, doi:10.1023/a:1026056129717 (2003).
332 Jin, M., Wang, J., Yao, X., Liao, M., Zhao, Y. & Jiang, L. Underwater Oil Capture by a Three-Dimensional Network Architectured Organosilane Surface. *Advanced Materials* **23**, 2861-2864, doi:10.1002/adma.201101048 (2011).
333 ATTO-TEC GmbH, S., Germany. *Atto 488 NHS-Ester data sheet, Recommended Procedures for Labeling*, <http://www.attotec.com/fileadmin/user_upload/Katalog_Flyer_Support/Procedures.pdf > (retrieved in April 2017).
334 Sagiv, J. Organized monolayers by adsorption. 1. Formation and structure of oleophobic mixed monolayers on solid surfaces. *Journal of the American Chemical Society* **102**, 92-98, doi:10.1021/ja00521a016 (1980).
335 Brzoska, J. B., Shahidzadeh, N. & Rondelez, F. Evidence of a transition temperature for the optimum deposition of grafted monolayer coatings. *Nature* **360**, 719-721, doi:10.1038/360719a0 (1992).
336 Artus, G. R. J., Jung, S., Zimmermann, J., Gautschi, H.-P., Marquardt, K. & Seeger, S. Silicone Nanofilaments and Their Application as Superhydrophobic Coatings. *Advanced Materials* **18**, 2758-2762, doi:10.1002/adma.200502030 (2006).
337 Rollings, D.-a. E., Tsoi, S., Sit, J. C. & Veinot, J. G. C. Formation and Aqueous Surface Wettability of Polysiloxane Nanofibers Prepared via Surface Initiated, Vapor-Phase Polymerization of Organotrichlorosilanes. *Langmuir* **23**, 5275-5278, doi:10.1021/la063604a (2007).
338 Zhang, J. & Seeger, S. Superoleophobic Coatings with Ultralow Sliding Angles Based on Silicone Nanofilaments. *Angewandte Chemie International Edition* **50**, 6652-6656, doi:10.1002/anie.201101008 (2011).
339 Jungwirth, P. Spiers Memorial Lecture Ions at aqueous interfaces. *Faraday Discussions* **141**, 9-30, doi:10.1039/B816684F (2009).
340 Babchin, A. J. & Schramm, L. L. Osmotic repulsion force due to adsorbed surfactants. *Colloids and Surfaces B: Biointerfaces* **91**, 137-143, doi:https://doi.org/10.1016/j.colsurfb.2011.10.050 (2012).

341 Qin, L. & Wang, X.-H. Surface adsorption and thermodynamic properties of mixed system of ionic liquid surfactants with cetyltrimethyl ammonium bromide. *RSC Advances* **7**, 51426-51435, doi:10.1039/C7RA08915E (2017).
342 Gao, N., Geyer, F., Pilat, D. W., Wooh, S., Vollmer, D., Butt, H.-J. & Berger, R. How drops start sliding over solid surfaces. *Nature Physics* **14**, 191-196, doi:10.1038/nphys4305 (2018).
343 Frenkel, Y. I. On the behavior of liquid drops on a solid surface 1. The sliding of drops on an inclined surfaceY.I. Frenkel. *J. Exptl. Theoret. Phys. (USSR)* **18** (1948).
344 Dussan V, E. B. On the ability of drops to stick to surfaces of solids. Part 3. The influences of the motion of the surrounding fluid on dislodging drops. *Journal of Fluid Mechanics* **174**, 381-397, doi:10.1017/S002211208700017X (1987).
345 Rudnick, Leslie R. Lubricant additives: chemistry and applications. CRC press, 2017.
346 Pirat, C., Sbragaglia, M., Peters, A. M., Borkent, B. M., Lammertink, R. G. H., Wessling, M. & Lohse, D. Multiple time scale dynamics in the breakdown of superhydrophobicity. *EPL (Europhysics Letters)* **81**, 66002, doi:10.1209/0295-5075/81/66002 (2008).
347 Schäffel, D., Koynov, K., Vollmer, D., Butt, H.-J. & Schönecker, C. Local Flow Field and Slip Length of Superhydrophobic Surfaces. *Physical Review Letters* **116**, 134501, doi:10.1103/PhysRevLett.116.134501 (2016).
348 Osorio-Nesme, A. & Delgado, A. Flow characterization in periodic microchannels containing asymmetric grooves. *Fluid Dynamics Research* **49**, 055502, doi:10.1088/1873-7005/aa7a35 (2017).

8 List of Publications

Baumli, P.[†], Lorusso, E.[†], Hauer, L.[†], Sharifi-Aghili, A., Hegner, K., D´Acunzi, M., Gutmann, J., Dünweg, B., Gutmann, Vollmer, D.*, Depleting Hydrogels with Oil Flows, *in preparation*.

Wong, W. S. Y., Naga, A., **Baumli, P.**, Bauer, H., D´Acunzi, M., Butt, H.-J., Vollmer, D., Super Liquid Repellent Surfaces for Anti-Foaming, *submitted*.

Wong, W. S. Y., Hauer, L., Naga, A., Kaltbeitzel, A., **Baumli, P.**, Berger, R., D´Acunzi, M., Vollmer, D., Butt, H.-J., Adaptive wetting of Polydimethylsiloxane, *submitted*.

Teisala, H., **Baumli, P**., Weber, S. A. L., Butt, H.-J., Vollmer, D., Grafting silicone films on glass at room temperature, *Langmuir*, *in revision* (ID la-2019-032236).

Encinas, N.[‡], Yang, C.-Y. [‡], Geyer, F., Kaltbeitzel, A., **Baumli, P**., Reinholz, J., Mailänder, V., Vollmer, D., Butt, H.-J., Sub-micrometer sized roughness suppresses bacteria adhesion, *ACS Applied Materials & interfaces*, **2020***, XXXX, XXX, XXX-XXX.*

Wong, W. S. Y., Corrales, T., Naga, A., **Baumli, P.**, Kaltbeitzel, A., Kappl, M., Papadopoulos, P., Vollmer, D., Butt, H.-J., Microdroplet Contaminants: When and Why Superamphiphobic Surfaces are Not Self-Cleaning, *ACS Nano*, *ACS Nano,* **2020***, XXXX, XXX, XXX-XXX.*

Keiser, A.[†], **Baumli, P.**[†]**,** Vollmer, D., Quéré, D., Universality of the friction laws on liquid-infused materials, *Phys. Rev. Fluids*, **2020**, 5, 014005.

Klasen, A., **Baumli, P**., Sheng, Q., Johannes, E., Bretschneider, S. A., Hermes, I. M., Bergmann, V. W., Gort, C., Axt, A., Weber, S. A. L., Kim, H., Butt, H.-J., Tremel, W., and Berger, R., Removal of Surface Oxygen Vacancies Increases Conductance Through TiO2 Thin Films for Perovskite Solar Cells, *J. Phys. Chem. C,* **2019** 123 (22), 13458-13466, DOI: 10.1021/acs.jpcc.9b02371

Baumli, P.[†], Teisala, H.[†], Bauer, H., Garcia-Gonzalez, D., Damle, V., Geyer, F., D'Acunzi, M., Kaltbeitzel, A., Butt, H.-J., Vollmer, D., Flow-Induced Long-Term Stable Slippery Surfaces. *Adv. Sci*. **2019**, 6, 1900019. https://doi.org/10.1002/advs.201900019

Geyer, F., D'Acunzi, M., Yang, C.-Y., Müller, M**., Baumli, P**., Kaltbeitzel, A., Mailänder, V., Encinas, N., Vollmer, D., Butt, H.-J., How to Coat the Inside of Narrow and Long Tubes with a Super-Liquid-Repellent Layer—A Promising Candidate for Antibacterial Catheters , *Adv. Mater*. **2019**, 31, 1801324. https://doi.org/10.1002/adma.201801324

9 Appendix

9.1 Acknowledgments

[This section has been removed in the electronic version for data protection reasons.]

9.2 Conference Contributions

93rd ACS Colloid and Surface Science Symposium, June 16th-June 19th , 2019, Atlanta, GA, USA, Conference presentation, title: *Flow-Induced Long-Term Stable Slippery Surfaces*

694. WE-Heraeus-Seminar on Soft and Microstructured Surfaces, April 11th -April 13th , 2019, at Physikzentrum Bad Honnef, Germany, Poster presentation: *Flow-Induced Emulsion-Based Lubricant-Replenishment*

32nd Conference of The European Colloid and Interface Society (ECIS), September 2nd – September 7th, 2018, Ljubljana, Slovenia. Conference presentation, title: *Emulsion-based Lubricant Replenishment Strategies for Lubricant- Impregnated Slippery Surfaces under Flow*

14th Zsygmondy Colloquium 2018, April 9th – April 11th, 2018, Mainz, Germany. Conference presentation, title: *Emulsion-Based Lubricant-Replenishment Strategies for Lubricant-Impregnated Slippery Surfaces*

Gordon Research Seminar (GRS) and Gordon Research Conference (GRC) on Tribology, June 25th – July 1st , 2016, at Bates College, Lewiston, Maine, United States, Poster presentation, title: *Towards Corrosion Inhibition and Optimized Tribological Properties for Stainless Steel Using Binary Mixtures of Trihexyltetradecylphosphonium-Based Ionic Liquids – a Proof of Concept*

611. WE-Heraeus-Seminar on Mechanisms of Tribology, March 29th -April 1st , 2016, at Physikzentrum Bad Honnef, Germany, Poster presentation, Title: *Tribological Properties of Selected Non-Aromatic Ionic Liquids*

9.3 Curriculum Vitae

[This section has been removed in the electronic version for data protection reasons.]